

UNIVERSITY OF SOUTHAMPTON  
FACULTY OF ENGINEERING AND THE ENVIRONMENT  
Energy Technology Research Group

# CFD Modelling of Turbulent Gas-Solid Flows

by

**Recep Kahraman**

Thesis for the degree of Doctor of Philosophy

June 2016



Dedicated to my adorable daughter Sena & my love Kate



UNIVERSITY OF SOUTHAMPTON  
Faculty of Engineering and the Environment

Doctor of Philosophy

## CFD MODELLING OF TURBULENT GAS-SOLID FLOWS

by Recep Kahraman

### ABSTRACT

Turbulent multiphase modelling is essential for improving the efficiency of bubbling (BFB) and circulating (CFB) fluidised beds, heat exchangers, etc. CFBs are widely used in industry, e.g, power plants, cracking and solid fuel combustion, due to their excellent mixing and heat transfer properties. However, the operational efficiency of CFBs needs further improvement in order to reduce harmful emissions which will help mitigate against climate change.

Computational fluid dynamics (CFD), specifically Eulerian two-fluid modelling (TFM), has proven valuable over recent decades for simulating and predicting hydrodynamic processes in fluidised beds. Unfortunately, the combination of dense and dilute structures observed within CFB reactors makes the application of the TFM difficult due to the various scaling elements, i.e. dense near wall and core clustering, and individual particles. Whilst dense flows are preferentially modelled using the kinetic theory of granular flow (KTGF), dilute flows require the application of a suitable turbulence model. Establishing a turbulence model capable of transitioning between dense and dilute systems will have a profound impact on the modelling of dense and dilute systems.

This project will introduce a novel multiphase dispersed model approach for modelling and simulating turbulent multiphase dense and dilute systems. Turbulence models that utilise various particle-particle interaction models are considered, including the TFM models solely using the KTGF, the two-equation  $k_s - k_{gs}$  model [Peirano and Leckner (1998)], a modified isotropic two-equation  $k_s - k_{gs}$  model, and the newly proposed multiphase dispersed  $v^2 - f$  model which is capable of transitioning between dense and dilute systems based on local particle densities. The models are validated using DNS and experimental data and simulated using a backward-step configuration using Ansys Fluent 14.5 and its UDF utility as well as Matlab 2014a.

Finally, to improve the reactor efficiency, a novel dimpled wall design, which is capable of minimising pressure drop, is implemented and chemical reactions are incorporated for the consideration of coal gasification processes and their impact on harmful emissions.



# Contents

<b>Declaration of Authorship</b>	<b>xi</b>
<b>Acknowledgements</b>	<b>xiv</b>
<b>Nomenclature</b>	<b>xiv</b>
<b>1 Introduction</b>	<b>1</b>
1.1 Motivation . . . . .	1
1.2 Aim of the project . . . . .	5
1.3 Thesis layout . . . . .	6
<b>2 Mathematical modelling of two-phase flow</b>	<b>9</b>
2.1 Overview . . . . .	9
2.2 Fluidisation . . . . .	10
2.3 Kinetic theory of granular flow . . . . .	13
2.3.1 The statistical description of the particulate phase . . . . .	14
2.4 Instantaneous local equations of two-phase flow . . . . .	16
2.4.1 Conservation of mass . . . . .	16
2.4.2 Conservation of momentum . . . . .	17
2.4.3 Conservation of energy . . . . .	22
2.5 Averaged equations of two-phase flow . . . . .	23
2.5.1 Conservation of mass equation . . . . .	23
2.5.2 Conservation of momentum equation . . . . .	24
2.6 Drag models . . . . .	24
2.6.1 Wen-Yu drag model . . . . .	25
2.6.2 Gidaspow drag model . . . . .	25
2.6.3 Syamlal-O'Brien drag model . . . . .	25
2.6.4 Energy minimisation multiscale drag model (EMMS) . . . . .	27
2.7 Wall boundary condition . . . . .	29
2.8 Summary . . . . .	29
<b>3 Turbulence</b>	<b>31</b>
3.1 Overview . . . . .	31
3.2 Fundamentals of turbulent motion . . . . .	32
3.2.1 Classification of gas-solid flows . . . . .	34
3.2.2 Turbulence modelling . . . . .	35
3.2.2.1 Characteristic time scales . . . . .	37
3.3 Two-equation $k_s$ - $k_{gs}$ model [Peirano and Leckner (1998)] . . . . .	39

<b>3.4 Decaying homogeneous isotropic turbulence two-equation <math>k_s - k_{gs}</math> model . . . . .</b>	<b>41</b>
<b>3.4.1 Results and discussion for homogeneous isotropic turbulence . . . . .</b>	<b>43</b>
3.4.1.1 Effect of particle relaxation time $\tau_{gs}^x$ . . . . .	43
3.4.1.2 Effect of the Stokes number . . . . .	45
3.4.1.3 Effect of source terms . . . . .	46
3.4.1.4 Effect of solid volume fraction . . . . .	47
3.4.1.5 Effect of $X_{gs}$ term . . . . .	48
3.4.1.6 Conclusion and summary . . . . .	48
<b>3.4.2 Modelling of 2D backward-facing step using the two-equation <math>k_s - k_{gs}</math> model . . . . .</b>	<b>50</b>
<b>3.4.3 Geometry and boundary conditions . . . . .</b>	<b>50</b>
<b>3.4.4 Results and discussion . . . . .</b>	<b>51</b>
3.4.4.1 Solid volume fraction . . . . .	52
3.4.4.2 Gas velocity profiles . . . . .	53
3.4.4.3 Solid velocity profiles . . . . .	54
3.4.4.4 Turbulent intensities . . . . .	56
3.4.4.5 Conclusion and summary . . . . .	59
<b>4 Dispersed <math>v^2 - f</math> model . . . . .</b>	<b>61</b>
<b>4.1 Introduction . . . . .</b>	<b>61</b>
<b>4.2 Model description . . . . .</b>	<b>61</b>
<b>4.3 Results and discussion . . . . .</b>	<b>66</b>
4.3.1 Geometry and boundary conditions . . . . .	66
4.3.2 Solid volume fraction . . . . .	66
4.3.3 Profiles of solid velocities . . . . .	67
4.3.4 Profiles of gas velocities . . . . .	68
4.3.5 Turbulent intensities . . . . .	69
4.3.6 Conclusion and summary . . . . .	72
<b>5 Hydrodynamic modelling of gas-solid flow in a dimpled wall CFB reactor . . . . .</b>	<b>73</b>
<b>5.1 Overview . . . . .</b>	<b>73</b>
<b>5.2 Geometry and boundary conditions . . . . .</b>	<b>74</b>
<b>5.3 Results and discussion . . . . .</b>	<b>75</b>
5.3.1 Solid volume fraction . . . . .	76
5.3.2 Solid velocity profiles . . . . .	83
5.3.3 Gas velocity profiles . . . . .	87
<b>5.4 Conclusion and summary . . . . .</b>	<b>90</b>
<b>6 Coal gasification modelling of a dimpled wall reactor . . . . .</b>	<b>93</b>
<b>6.1 Overview . . . . .</b>	<b>93</b>
<b>6.2 Reaction modelling . . . . .</b>	<b>94</b>
6.2.1 Species transport . . . . .	94
6.2.1.1 Heterogeneous reactions . . . . .	95
6.2.1.2 Homogeneous reactions . . . . .	97
<b>6.3 Bubbling fluidised bed reaction modelling with dimpled walls . . . . .</b>	<b>98</b>
6.3.1 Geometry and boundary conditions . . . . .	98
6.3.2 Results and discussion . . . . .	100

6.3.3	Volume fractions . . . . .	100
6.3.4	Temperature distribution . . . . .	103
6.3.5	Gasification products . . . . .	103
6.3.6	Conclusion and summary . . . . .	108
6.4	Circulating fluidised bed reaction modelling with dimpled walls . . . . .	110
6.4.1	Geometry and boundary conditions . . . . .	110
6.4.2	Results and discussion . . . . .	111
6.4.3	Volume fraction . . . . .	112
6.4.4	Velocity profiles . . . . .	117
6.4.5	Temperature distribution . . . . .	120
6.4.6	Heterogeneous reaction rates . . . . .	122
6.4.7	Gasification products . . . . .	124
6.4.8	Conclusion and summary . . . . .	130
<b>7</b>	<b>Conclusions</b>	<b>133</b>
7.1	Conclusions . . . . .	133
7.2	Contributions . . . . .	135
7.3	Future Work . . . . .	136
<b>A</b>	<b>General averaging techniques</b>	<b>139</b>
A.1	Averaging . . . . .	139
<b>B</b>	<b>RANS</b>	<b>143</b>
B.1	Reynolds averaged Navier-Stokes Equation (RANS) . . . . .	143
<b>References</b>		<b>147</b>



# List of Figures

1.1	A schematic figure of a CFB consisting of a riser and a cyclone. . . . .	2
1.2	Dispersed particles in a fully developed turbulent pipe flow (adapted from [Fessler et al. (1994)]) . . . . .	5
2.1	Geldart classification of particles for air at ambient conditions (adapted from [Geldart (1973)]). . . . .	12
2.2	Viscous dissipation due to kinetic, collision and friction within a granular flow . . . . .	18
2.3	Relationship of Mohr-Coulomb in the N-S plane. . . . .	20
2.4	Internal friction angle. . . . .	20
2.5	Cluster formation in CFB. . . . .	27
3.1	Scheme of various lengthscales and ranges for eddies at a very high Reynolds number . . . . .	32
3.2	Eddy effect on particle trajectory. The dashed line represents particle trajectory, whereas the solid line represents eddies [Benavides and van Wachem (2009)]. . . . .	34
3.3	Classification of flow regimes for gas-solid flows [Elghobashi (1994)]. . . . .	35
3.4	Effect of particle relaxation time, $\tau_{gs}^x$ , on turbulent kinetic energy normalised by the initial value of $k_g(0)$ , with respect to time and compared to DNS data [Elghobashi and Truesdell (1993)]. . . . .	44
3.5	Particle diameter effect on turbulent kinetic energy with respect to time, where $k_g$ is normalised by initial condition $k_g(0)$ . . . . .	44
3.6	Effect of the Stokes number ( $St = \frac{\tau_{gs}^x}{\tau_\eta}$ ) on time the development of primary phase turbulent kinetic energy, $k_g$ and dissipation rate, $\varepsilon_g$ . . . . .	45
3.7	Effect of the Stokes number on time the development of secondary phase turbulent kinetic energy, $k_s$ and fluid-particle velocity covariance, $k_{gs}$ . . . . .	46
3.8	Source terms $k_{sA}$ , $k_{sB}$ for $k_s$ from Eq. 3.36 and $k_{gsA}$ , $k_{gsB}$ and $k_{gsC}$ for $k_{gs}$ from Eq. 3.37 . . . . .	46
3.9	Source terms $k_{gA}$ , $k_{gB}$ , $k_{\varepsilon A}$ , $k_{\varepsilon B}$ and 'All' is the actual result in Eqs. 3.34 and 3.35 for $k_g$ and $\varepsilon_g$ , respectively. . . . .	47
3.10	Effect of solid volume fraction, $\alpha_s$ , in time development of primary phase turbulent kinetic energy, $k_g$ and dissipation rate, $\varepsilon_g$ . . . . .	47
3.11	Effect of solid volume fraction $\alpha_s$ in time development of secondary phase turbulent kinetic energy, $k_s$ and fluid-particle velocity covariance, $k_{gs}$ . . . . .	48
3.12	Geometry of a vertically oriented backward facing step with a width $h=40$ mm and step height $H=26.7$ mm. . . . .	51
3.13	<b>Case 1:</b> mean solid volume fraction for $k_s-k_{gs}$ model with 40% mass-loading. . . . .	52

3.14	Mean solid volume fraction for the $k_s-k_{gs}$ model with a 20% mass-loading for Case 1 (solid line) and Case 2 (dashed line). . . . .	52
3.15	<b>Case 1:</b> streamwise mean gas velocity for the $k_s-k_{gs}$ model with a 40% mass-loading. . . . .	53
3.16	<b>Case 3:</b> streamwise mean gas velocity for the $k_s-k_{gs}$ model (solid line), the standard dispersed $k_g-\varepsilon_g$ model (solid line with circle markers) and experimental data (squares) for a 40% mass-loading [Fessler and Eaton (1999)]. . . . .	53
3.17	<b>Case 4 and 5:</b> for the $k_s-k_{gs}$ model streamwise mean gas velocity profiles using $\alpha_s = 0.1$ (dashed line with full circle markers) and $\alpha_s = 0.2$ (dashed line with empty circle markers). . . . .	54
3.18	<b>Case 1:</b> streamwise particle mean velocity profile for the $k_s-k_{gs}$ model with a 40% mass-loading. . . . .	54
3.19	<b>Case 1:</b> streamwise mean particle velocity profiles for the $k_s-k_{gs}$ model (solid line), the standard dispersed $k_g-\varepsilon_g$ model (solid line with circle markers) and experimental data (squares) for a 40% mass-loading [Fessler and Eaton (1999)]. . . . .	55
3.20	<b>Case 2:</b> streamwise particle velocity profiles for the $k_s-k_{gs}$ model (solid line), the standard dispersed $k_g-\varepsilon_g$ model (solid line with circle markers) and experimental data (squares) for a 20% mass-loading [Fessler and Eaton (1999)]. . . . .	55
3.21	<b>Case 4 and 5:</b> for the $k_s-k_{gs}$ model streamwise mean gas velocity profiles using $\alpha_s = 0.1$ (dashed line with full circle markers) and $\alpha_s = 0.2$ (dashed line with empty circle markers). . . . .	56
3.22	<b>Case 3:</b> turbulence intensity gas phase profiles for the $k_s-k_{gs}$ model (solid line), the standard dispersed $k_g-\varepsilon_g$ model (solid line with circle markers) and experimental data (squares) for a 40% mass-loading [Fessler and Eaton (1999)]. . . . .	57
3.23	<b>Case 1:</b> Turbulence intensity gas phase profiles for the $k_s-k_{gs}$ model (solid line), the standard dispersed $k_g-\varepsilon_g$ model (solid line with circle markers) and experimental data (squares) for a 20% mass-loading [Fessler and Eaton (1999), Benavides and van Wachem (2009)]. . . . .	57
3.24	<b>Case 1:</b> turbulence intensity in particle phase profiles for the $k_s-k_{gs}$ model (solid line), granular temperature with the standard dispersed $k_g-\varepsilon_g$ model (dashed line) and experimental data (squares) represent the stream wise particle fluctuating velocity for a 40% mass-loading [Fessler and Eaton (1999)]. . . . .	58
3.25	<b>Case 4:</b> turbulence intensity in particle phase profiles for the $k_s-k_{gs}$ model (solid line with square markers) and granular temperature with the standard dispersed $k_g-\varepsilon_g$ model (solid line with circle markers). . . . .	58
3.26	<b>Case 5:</b> turbulence intensity in particle phase profiles for the $k_s-k_{gs}$ model (dashed line with square markers) and granular temperature with the standard dispersed $k_g-\varepsilon_g$ model (solid line with circle markers). . . . .	59
4.1	<b>Case 1:</b> mean solid volume fraction for the dispersed $v^2 - f$ model with a 40% mass-loading. . . . .	67
4.2	<b>Case 1:</b> mean solid volume fraction dispersed $v^2 - f$ model with a 20% mass-loading. . . . .	67

4.3	<b>Case 1:</b> streamwise mean particle velocity contours with a 20% high mass loading. . . . .	67
4.4	<b>Case 2:</b> streamwise particle velocity profiles for the dispersed $v^2 - f$ model (solid line), the standard dispersed $k - \varepsilon$ model (solid line with square markers) and experimental data (squares) for a 20% mass-loading [Fessler and Eaton (1999)]. . . . .	68
4.5	<b>Case 1:</b> streamwise particle mean velocity profiles for the dispersed $v^2 - f$ model (solid line), the standard dispersed $k_g - \varepsilon_g$ model (solid line with square markers) and experimental data (squares) with a 40% mass-loading. . . . .	68
4.6	<b>Case 1:</b> streamwise mean gas velocity for the dispersed $v^2 - f$ model with a 40% mass-loading. . . . .	69
4.7	<b>Case 3:</b> streamwise mean gas velocity for the dispersed $v^2 - f$ model (solid line), the standard dispersed $k - \varepsilon$ model (solid line with square markers) and experimental data (squares) for a 40% mass-loading [Fessler and Eaton (1999)]. . . . .	69
4.8	<b>Case 1:</b> turbulence intensity gas phase profiles for the dispersed $v^2 - f$ model (solid line), the standard dispersed $k_g - \varepsilon_g$ model (solid line with square markers) and experimental data (squares) for a 20% mass-loading [Fessler and Eaton (1995, 1999)]. . . . .	70
4.9	<b>Case 1:</b> turbulence intensity gas phase profiles of the dispersed $v^2 - f$ model (solid line), the standard dispersed $k_g - \varepsilon_g$ model (solid line with square markers) and experimental data (squares) for a 40% mass-loading [Fessler and Eaton (1995, 1999)]. . . . .	70
4.10	<b>Case 2:</b> turbulence intensity gas phase profiles of the dispersed $v^2 - f$ model (solid line), the standard dispersed $k_g - \varepsilon_g$ model (solid line with square markers) and experimental data (squares) for a 20% mass-loading[Fessler and Eaton (1995, 1999)]. . . . .	71
4.11	<b>Case 3:</b> turbulence intensity gas phase profiles of the dispersed $v^2 - f$ model (solid line), the standard dispersed $k - \varepsilon$ model (solid line with square markers) and experimental data (squares) for a 40% mass-loading[Fessler and Eaton (1995, 1999)]. . . . .	71
4.12	<b>Case 1:</b> mean turbulent kinetic energy contours with a 20% mass-loading. . . . .	72
4.13	<b>Case 1:</b> mean $v^2$ contours with a 20% mass-loading. . . . .	72
5.1	Geometry of flat and dimpled walls in a CFB reactor. . . . .	75
5.2	Dimensions of the shallow and deep dimples as well as the wide and narrow necks. . . . .	76
5.3	Grid independence study . . . . .	77
5.4	Instantaneous volume fraction, $\alpha_s$ , for flat (Case 1), shallow (Case 2) and deep (Case 3) dimpled wall at 15.0 s. . . . .	77
5.5	Time averaged horizontal solid volume fraction in the dense region for Cases 1-3. . . . .	78
5.6	Time averaged horizontal solid volume fraction in the dilute region for Cases 1-3. . . . .	79
5.7	Time averaged vertical solid volume fraction for Cases 1-3 and experimental data for a flat reactor. . . . .	79
5.8	Time averaged vertical solid volume fraction for Cases 4-7 and experimental data for a flat reactor. . . . .	80
5.9	Time averaged solid volume fraction in the dense region for Cases 4-7. . . . .	81

5.10 Time averaged solid volume fraction in the transition region for Cases 4-7.	81
5.11 Time averaged solid volume fraction in the transition region for Case 5 and 7.	82
5.12 Time averaged solid volume fraction in the dilute region for Cases 4-7.	82
5.13 Time averaged solid volume fraction in the dilute region for Cases 5 and 7.	83
5.14 Time averaged horizontal solid velocity at 0.37 m for Cases 1-3.	84
5.15 Time averaged horizontal solid velocity at 0.71 m for Cases 1-3 and experimental data for a flat reactor.	84
5.16 Instantaneous solid velocity at random time.	85
5.17 Time averaged horizontal solid velocity at 0.79 m for Cases 4-7.	85
5.18 Time averaged horizontal solid velocity at height of 0.37 m for Cases 4-7.	86
5.19 Time averaged horizontal solid velocity at 1.07 m height for Cases 4-7.	87
5.20 Time averaged horizontal gas velocity at 0.37 m for Cases 1-3.	88
5.21 Instantaneous velocity vector plot at 15 s at 0.37 m.	88
5.22 Time averaged horizontal gas velocity at 1.07 m for Cases 1-3.	89
5.23 Time averaged horizontal gas velocity at 0.71 m for Cases 4-7.	89
5.24 Time averaged horizontal gas velocity at 1.07 m for Cases 4-7.	90
 6.1 Geometry of the BFB reactor.	99
6.2 Gas volume fraction between 9.5 s and 10 s in a flat wall BFB reactor.	100
6.3 Volume fractions of (a) gas, (b) sand and (c) char at 10 s.	101
6.4 Gas volume fraction between 9.5 s and 10 s in a shallow dimpled wall BFB reactor.	102
6.5 Gas volume fraction between 9.5 s and 10 s in a deep dimpled wall BFB reactor.	103
6.6 Mean mole fraction of exiting products calculated using Gerber's model [Gerber et al. (2010)].	104
6.7 Mean mole fraction of exiting products calculated using Yu's model [Yu et al. (2007)].	104
6.8 Mean mole fraction of the exiting gaseous products CO <sub>2</sub> , CO, H <sub>2</sub> , N <sub>2</sub> and CH <sub>4</sub> in flat, shallow and deep BFB reactors.	105
6.9 The mean mole fractions of CO, CO <sub>2</sub> and H <sub>2</sub> in a deep dimpled BFB reactor.	106
6.10 The mean mole fractions of CH <sub>4</sub> , N <sub>2</sub> and H <sub>2</sub> O in a deep dimpled BFB reactor.	107
6.11 Mean mole fractions of CO, CO <sub>2</sub> and H <sub>2</sub> in a shallow dimpled BFB reactor.	107
6.12 The mean mole fractions of CH <sub>4</sub> , N <sub>2</sub> and H <sub>2</sub> O in a shallow dimpled BFB reactor.	108
6.13 Geometry of the CFB reactor.	110
6.14 Mean mole fraction of the exiting gaseous products CO <sub>2</sub> and O <sub>2</sub> in experimental [Zhou et al. (2011)] and flat, shallow and deep dimple CFB reactors.	112
6.15 Mean solid volume fraction profile in flat, shallow and deep dimpled wall CFB reactors.	113
6.16 Solid volume fraction between 10.5 s and 10.8 s in a flat wall CFB reactor.	114
6.17 Vertical mean char volume fraction profiles for flat, shallow and deep dimpled reactors.	114

---

6.18 Solid volume fraction between 10.5 s and 10.8 s in a shallow dimpled wall CFB reactor . . . . .	115
6.19 Horizontal mean char vertical volume fraction profiles for flat, shallow and deep dimpled wall cases at the top of the reactor. . . . .	115
6.20 Solid volume fraction between 10.5 s and 10.8 s in a deep dimpled wall CFB reactor. . . . .	116
6.21 Horizontal mean char vertical volume fraction profiles for flat, shallow and deep dimpled wall cases at the middle of the reactor. . . . .	116
6.22 Horizontal mean char vertical volume fraction profiles for flat, shallow and deep dimpled reactors at the bottom of the reactor. . . . .	117
6.23 Mean velocity profile in a streamwise direction for the gas phase in flat, shallow and deep dimpled wall CFB reactors. . . . .	118
6.24 Horizontal mean char velocity profiles for flat, shallow and deep dimpled wall cases at the middle of the reactor. . . . .	118
6.25 Mean velocity profile in a streamwise direction for the particle phase in flat, shallow and deep dimpled wall CFB reactors. . . . .	119
6.26 Horizontal mean char velocity profiles for flat, shallow and deep dimpled wall cases at the top of the reactor. . . . .	119
6.27 Mean velocity vector profile in a streamwise direction for the gas phase in flat, shallow and deep dimpled wall CFB reactors. . . . .	120
6.28 Mean temperature distribution in an experimental [Zhou et al. (2011)] and flat wall CFB reactor. . . . .	121
6.29 Mean temperature distribution in flat, shallow and deep dimpled wall CFB reactors. . . . .	121
6.30 Heterogeneous reaction rates for a flat wall reactor. . . . .	122
6.31 Heterogeneous reaction rates for a shallow dimpled wall reactor. . . . .	123
6.32 Heterogeneous reaction rates for a deep dimpled wall reactor. . . . .	123
6.33 Mean mole fractions of CO, CO <sub>2</sub> and H <sub>2</sub> in a flat wall reactor. . . . .	125
6.34 Mean mole fractions of CH <sub>4</sub> , H <sub>2</sub> O and O <sub>2</sub> in a flat wall reactor. . . . .	125
6.35 Mean mole fractions of CO, CO <sub>2</sub> and H <sub>2</sub> in a shallow dimpled reactor. . . . .	126
6.36 Mean mole fractions of CH <sub>4</sub> , H <sub>2</sub> O and O <sub>2</sub> in a shallow dimpled reactor. . . . .	126
6.37 Mean mole fractions of CO, CO <sub>2</sub> and H <sub>2</sub> in a deep dimpled reactor. . . . .	127
6.38 Mean mole fractions of CH <sub>4</sub> , H <sub>2</sub> O and O <sub>2</sub> in a deep dimpled reactor. . . . .	127
6.39 Vertical mean mole fraction of CO <sub>2</sub> in flat, shallow and deep dimpled wall CFB reactors. . . . .	128
6.40 Vertical mean mole fraction profile of CO in flat, shallow and deep dimpled wall CFB reactors. . . . .	129
6.41 Outlet mean mole fraction profile of CO <sub>2</sub> in flat, shallow and deep dimpled wall CFB reactors. . . . .	129
6.42 Outlet mean mole fraction profile of CO in flat, shallow and deep dimpled wall CFB reactors. . . . .	129
6.43 Outlet mean mole fraction profile of H <sub>2</sub> O in flat, shallow and deep dimpled wall CFB reactors. . . . .	130
6.44 Outlet mean mole fraction profile of H <sub>2</sub> in flat, shallow and deep dimpled wall CFB reactors. . . . .	130



# List of Tables

3.1	Dilute mass loadings and particle properties for cases A to F in isotropic turbulence. . . . .	43
3.2	Dense mass loadings and particle properties for different cases in isotropic turbulence. . . . .	43
3.3	Mass loadings and particle properties in different cases. . . . .	51
5.1	Dimple type, neck type and particle diameters in the CFB reactor. . . . .	74
6.1	Operating conditions of the BFB reactor. . . . .	98
6.2	Coal properties used in the simulations. . . . .	99
6.3	Operating conditions of the CFB reactor. . . . .	111



## **Declaration of Authorship**

I, Recep Kahraman, declare that the thesis entitled *CFD Modelling of Turbulent Gas-Solid Flows* and the work presented in the thesis are both my own, and have been generated by me as the result of my own original research. I confirm that:

- this work was done wholly or mainly while in candidature for a research degree at this University;
- where any part of this thesis has previously been submitted for a degree or any other qualification at this University or any other institution, this has been clearly stated;
- where I have consulted the published work of others, this is always clearly attributed;
- where I have quoted from the work of others, the source is always given. With the exception of such quotations, this thesis is entirely my own work;
- I have acknowledged all main sources of help;
- where the thesis is based on work done by myself jointly with others, I have made clear exactly what was done by others and what I have contributed myself;
- parts of this work have been published as given in the list of publications

Signed: Recep Kahraman

Date: 18.08.2015



## List of Publications

- Kahraman, R., Shrimpton, J., Luo, K., Gu, S. and Armstrong, L.-M. (2014) Novel wall design for circulating fluidised bed reactors, *International Conferences on Circulating Fluidized Beds*, Beijing, China.
- Kahraman, R., Armstrong, L.M. and Shrimpton, J. (2015). Prediction of turbulent gas-solid flow by using  $k_s - k_{gs}$  model in a backward-facing step. *Int. J. Multiphase Flow* (in preparation)
- Kahraman, R., Armstrong, L.M. and Shrimpton, J. (2015). Dispersed  $v^2 - f$  model implementation in turbulent gas-solid flow in a backward-facing step. *Int. J. Multiphase Flow* (in preparation)
- Kahraman R., Shrimpton J. and Armstrong L.M. and (2015). Novel wall design to improve fluidisation in a CFB gasifier with parametric study. *Chem. Eng. J.* (in preparation)
- Kahraman R., Shrimpton J. and Armstrong L.M. and (2015). Coal combustion simulation in dimpled wall fluidised bed reactors. *Chem. Eng. J.* (in preparation)



## **Acknowledgements**

First and foremost I would like to thank my supervisor Dr. Lindsay-Marie Armstrong. It has been an honour to be her first PhD student. I appreciate all her contributions and motivation during weekly meetings which helped make my PhD experience more productive and stimulating. I would also like to thank my second supervisor Prof. John Shrimpton for his invaluable advice, ideas, knowledge and help during my last stage of the work. Moreover, I would like to thank Prof. Sai Gu and Prof. Kai Luo for providing the funding and giving me the opportunity to complete my PhD study at the University of Southampton.

I would like to thank all my friends and colleagues who supported me and motivated me to strive towards my goal. I would especially like to thank my Victoria's Wolves team mates and my best friends Ruben Porras, Giorgos Ragkousis and Wali Sayed with whom I had the chance to win two times in a row the veterans football league of University of Southampton.

A special thanks goes to my family. It is very difficult to express with words how grateful I am to my mother, my father, my brother and to my mother-in law for their support and encouragement over the years. At the end, I would like to give a huge thank you and express my appreciation to my gorgeous daughter Sena and my love Dr Ekaterina Gongadze with whom we shared the lots of sleepless nights. She always supported me when I needed support. The words are not enough to express how much I love them...



# Nomenclature

## *Greek letters*

$\alpha_g$	gas volume fraction	[ $\cdot$ ]
$\alpha_s$	solid volume fraction	[ $\cdot$ ]
$\varepsilon$	dissipation rate	[ $\text{m}^2 \text{s}^{-3}$ ]
$\eta$	Kolmogorov length scale	[m]
$\gamma_\Theta$	collisional dissipation	[ $\text{kg s}^{-3} \text{m}^{-1}$ ]
$\lambda$	thermal conductivity	[ $\text{W m}^{-1} \text{K}^{-1}$ ]
$\mu$	fluid viscosity	[ $\text{kg m}^{-1} \text{s}$ ]
$\mu_g$	gas viscosity	[ $\text{kg m}^{-1} \text{s}$ ]
$\mu_{gl}$	gas laminar viscosity	[ $\text{kg m}^{-1} \text{s}$ ]
$\mu_{gt}$	gas phase turbulent viscosity	[ $\text{kg m}^{-1} \text{s}$ ]
$\mu_s$	solid shear viscosity	[ $\text{kg m}^{-1} \text{s}$ ]
$\mu_{s,col}$	collisional viscosity	[ $\text{kg m}^{-1} \text{s}$ ]
$\mu_{s,fr}$	frictional viscosity	[ $\text{kg m}^{-1} \text{s}$ ]
$\mu_{s,kin}$	kinetic viscosity	[ $\text{kg m}^{-1} \text{s}$ ]
$\nu$	kinematic viscosity	[ $\text{m}^2 \text{s}^{-1}$ ]
$\omega_i$	species molar weight	[ $\text{kg kmol}^{-1}$ ]
$\phi_i$	angle of internal friction	[ $^\circ$ ]
$\phi_s$	particle sphericity	[ $\cdot$ ]
$\psi$	transported properties	[ $\cdot$ ]
$\Pi$	fluid particle interaction term	[ $\text{m}^2 \text{s}^{-3}$ ]
$\rho$	density	[ $\text{kg m}^{-3}$ ]
$\rho_g$	gas density	[ $\text{kg m}^{-3}$ ]
$\rho_s$	particle density	[ $\text{kg m}^{-3}$ ]
$\sigma$	turbulent Prandtl number	[ $\cdot$ ]
$\bar{\tau}_g$	gas viscous stress tensor	[Pa]
$\bar{\tau}_s$	solid viscous stress tensor	[Pa]
$\tau_0$	time scale of the largest eddies	[s]
$\tau_\eta$	Kolmogorov time scale	[s]
$\tau_g^t$	large eddy characteristic time scale	[s]
$\tau_{gs}^x$	particle relaxation time	[s]
$\tau_s^c$	particle collision time	[s]

$\Theta$	granular temperature	$\text{m}^2 \text{s}^{-2}$
$v_{r,s}$	terminal velocity correlation of the particles	$\text{m s}^{-1}$
$\xi_s$	solid bulk phase viscosity	$\text{kg m}^{-1} \text{s}$

### Roman letters

$Ar$	Archimedes number	[ $\cdot$ ]
$C(\psi)$	source term for collisional rate of change of $\psi$	[ $\cdot$ ]
$C_D$	drag coefficient	[ $\cdot$ ]
$C_p$	specific heat capacity	$\text{J kg}^{-1} \text{K}^{-1}$
$d_s$	particle diameter	[m]
$D_{gs}$	diffusion coefficient	$\text{m}^2 \text{s}^{-1}$
$D_{m,i}$	mixture diffusion coefficient	[ $\cdot$ ]
$e$	restitution coefficient	[ $\cdot$ ]
$g$	gravity	$\text{m s}^{-2}$
$g_0$	radial distribution function	[ $\cdot$ ]
$F$	external force acting on particle per mass unit	$\text{N kg}^{-1}$
$G_k$	turbulent kinetic energy	$\text{m}^2 \text{s}^{-2}$
$h_{sg}$	heat transfer coefficient	$\text{W m}^{-2} \text{K}^{-1}$
$H_i$	enthalpy for each species	$\text{J kg}^{-1}$
$\bar{I}_g$	identity tensor	[ $\cdot$ ]
$i$	phase	[ $\cdot$ ]
$J_i$	diffusion flux	$\text{kg m}^{-2} \text{s}^{-1}$
$k$	turbulent kinetic energy	$\text{m}^2 \text{s}^{-2}$
$k_{gs}$	fluid particle covariance	$\text{m}^2 \text{s}^{-2}$
$k_i$	kinetic reaction rate	$\text{s}^{-1}$
$k_\Theta$	diffusion coefficient	$\text{kg m}^{-2} \text{s}$
$K_{gs}$	interphase drag constant	[ $\cdot$ ]
$Me_x$	metal	[ $\cdot$ ]
$Nu$	Nusselt number	[ $\cdot$ ]
$p$	pressure	[Pa]
$p_s$	solid pressure	[Pa]
$Pr$	Prandtl number	[ $\cdot$ ]
$Q_{gs}$	heat exchange between phases	$\text{W m}^{-2} \text{K}^{-1}$
$R$	universal gas constant	$\text{J mol}^{-1} \text{K}^{-1}$
$R_i$	net production rate	$\text{kg m}^{-3} \text{s}$
$Re$	Reynolds number	[ $\cdot$ ]
$S_{ct}$	Schmidt number	[ $\cdot$ ]
$S_i$	unreacted char	$\text{kg m}^{-3} \text{s}^{-1}$
$S_{sg}$	source term which describes the specific rate of production of mass	[ $\cdot$ ]
$Sh$	Sherwood number	[ $\cdot$ ]
$St$	Stoke number	[ $\cdot$ ]

$T_p$	particle temperature	[K]
$u_0$	largest eddy velocity	[m s <sup>-1</sup> ]
$u_\eta$	Kolmogorov velocity	[m s <sup>-1</sup> ]
$u_l$	largest eddy length scale	[m]
$U$	average velocity	[m s <sup>-1</sup> ]
$U_c$	critical superficial velocity	[m s <sup>-1</sup> ]
$U_{di}$	drift velocity	[m s <sup>-1</sup> ]
$U_{mf}$	minimum fluidisation velocity	[m s <sup>-1</sup> ]
$U_{ri}$	relative velocity	[m s <sup>-1</sup> ]
$U_t$	terminal or settling velocity	[m s <sup>-1</sup> ]
$V_i$	produced volatile	[ $\cdot$ ]
$x_{gs}$	mass loading	[ $\cdot$ ]
$X_i$	mole fraction of each species	[ $\cdot$ ]
$Y_i$	mass fraction of species	[ $\cdot$ ]
$Z_i$	yield factor	[ $\cdot$ ]
$Z_1$	volatile production at low temperature	[ $\cdot$ ]
$Z_2$	volatile production at high temperature	[ $\cdot$ ]

### *Subscripts*

$g$	gas
$mf$	minimum fluidisation
$p$	particle
$s$	solid
$t$	terminal

### *Superscripts*

$c$	collision
$t$	fluid particle interaction
$x$	particle

### *Acronyms*

<i>BFB</i>	bubbling fluidised bed
<i>CFB</i>	circulating fluidised bed
<i>CFD</i>	computational fluid dynamics
<i>DNS</i>	direct numerical simulation
<i>RANS</i>	Reynolds averaged Navier-Stokes



# Chapter 1

## Introduction

### 1.1 Motivation

Global warming is a challenge for the humanity to cope with. One of the sources of global warming are the high emissions of CO, CO<sub>2</sub>, NO<sub>x</sub> and SO<sub>x</sub> which are byproducts of the combustion process in power plants. Fossil fuels, like oil (37%), natural gas (21%) and coal (25%) are the major constituents in the production of energy [[Armstrong \(2011\)](#)]. In the next 120 years, coal will be still used as it offers competitive prices and simple technology despite the higher amount of harmful emissions. In order to overcome this problem, research is under way to study and analyse the fuel properties and gas-solid flow applications like circulating (CFB) and bubbling fluidised beds (BFB). For the first time, the term CFB was mentioned by Reh [[Reh \(1971\)](#)], who applied it to alumina calciners. It is also commonly met in literature as fast fluidised bed, circulating solid riser, entrained bed, riser reactor, etc. The first commercial application of the CFB system was designed by Standard Oil Development Company for the fluid catalytic cracking (FCC) system at the Baton Rouge refinery in 1942 [[Squires \(1986\)](#)]. In fluidised beds, the combustion process is a result of the turbulent mixing of gas and solids which provides a more effective mixing by enhancing chemical reactions and heat transfer. BFB and CFB technologies are able to burn various solid fuels and biofuels, but BFB operates in a low velocity regime. The CFB ends having higher efficiency due to its higher mixing effect and better contact between air and solid fuel. It offers combustion efficiency, operational flexibility and overall profitability.

The fluid carries particles to the outlet from where they continue to the cyclone and separate there from the air. The feedback pushes them through the screwer to the riser and the cycle is repeated (see Fig. 1.1). The typical operational ranges are: superficial gas velocity: 2–12 m s<sup>-1</sup>, net solid flux range of the riser: 10–1000 kg m<sup>-2</sup> s, temperatures are varying depending on the application: 20–950 °C, pressure: 50–2000 kPa, used mean particle diameter: 100–2000 µm and overall riser height: 15–40 m [[Yang \(2003\)](#)]. The

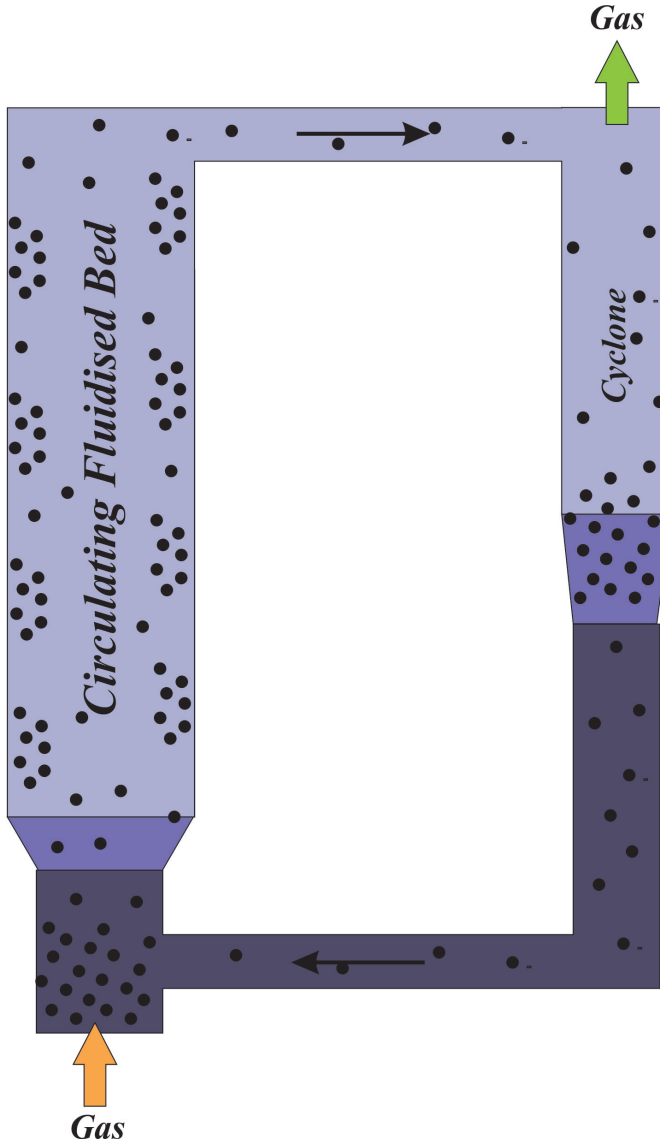


Figure 1.1: A schematic figure of a CFB consisting of a riser and a cyclone.

advantages of the technology start with the limited backmixing of gas and long and controllable residence time of the particles. Moreover, temperature are uniform and there is no hot spots in the entire bed. The technology allows handling particles of different size, density and shapes. Last but not least, high velocity facilitates effective mixing, resulting in a more accurate contact between gas and particles [Yang (2003)]. Some of the disadvantages are: need of long beds, clusters near the wall, significant lateral gradients and loss of particles due to entrainment.

The phenomenon of cluster formation is a complicated mechanism which depends on the interplay between hydrodynamic and surface forces. The cluster formation takes place in the middle of the reactor or near the wall. After the clusters become larger and denser, they start to fall down near the wall (i.e. this results in a negative velocity and higher solid concentration) as the gravity force becomes dominant. The developed

velocity profile has roughly a parabolic shape with the maximum velocity located in the middle. These velocity gradients push the particles to the wall region which causes clusters formation. The clustering effect has been also extensively observed experimentally [[Yousfi and Gau \(1974\)](#); [Yarushalmi and Squires \(1977\)](#); [Luo \(1987\)](#); [Horio et al. \(1988\)](#)]. It is vital to understand that the clustering effect is the key factor in designing new efficient reactors. Clusters influence the system hydrodynamics by forming and disrupting it dynamically. This effect is not desired for coal combustion as it decreases the contact surface between particles and oxygen attenuating the combustion efficiency.

The hydrodynamical transition from BFB to CFB in two and three dimensions was carried out [[Armstrong et al. \(2010\)](#)]. Sammuelsberg and Hjertager [[Sammuelsberg and Hjertager \(1996\)](#)] provided a numerical study accompanied with experiments for radial profiles of axial velocity components in a cold hydrodynamics model in a lab scale CFB reactor. Gungor created a 2D-dimensional model by dividing the reactor in two zones [[Gungor and Eskin \(2008\)](#)]. The bottom zone was treated like a bubbling bed and the upper zone like a high velocity model. However, a transition zone was not described. Moreover, Jiradilok and Gidaspow [[Jiradilok et al. \(2006\)](#)] contributed to a corrected drag model where the cluster model was taken into account. It has been shown that particle oscillations are a result of clusters and not of the oscillations of individual particles like in the B type particles in the turbulent regimes. There is the so-called energy minimisation multi-scale (EMMS) model developed specially for CFB reactors which are operating in a high-velocity regime.

From an operational point of view, the flexibility of the CFB reactor is one of the major features making it attractive for industrial applications. Moreover, its good mixing properties and good gas-solid contact are vital for the combustion technology and the excellent heat and mass transfer capabilities turn to be their basic advantage. On the other hand, there is a need for a better understanding of its hydrodynamic behaviour in order to use it more efficiently. The fluidised beds operate as a two-phase system presenting the interaction between the gas and the solid in the flow. An analysis of such multiphase flows is crucial to understand the complex hydrodynamical behaviour of CFBs. The term "multiphase" includes a huge range of flow patterns and regimes, as they need to be classified by either their physical states or topologically –liquid-gas, liquid-liquid, etc. and separated, dispersed.

For industrial applications it is challenging to get experimental data during their processes, because of their high operational temperatures and pressures or hazardous substances. The design of the systems depends on experimental pilot scale or empirical correlations [[Harnby et al. \(1992\)](#)]. The pilot scale experiments are designed in smaller scales in ambient temperature and pressure, but they are time consuming and very expensive. Moreover, the pilot scale design needs an extensive study of the scaling parameters of the commercial application which is not an easy task for such a complex system. The empirical correlations also suffer because of their non-universality. The

reasons mentioned above show that it is necessary to develop a methodology, which is able to predict the flow properties in details and with high accuracy - namely the computational fluid dynamics (CFD). CFD is capable of analyzing turbulent multiphase flows, heat transfer, chemical reactions and related phenomena by computer based modelling. It is developed to avoid experimental studies and empirical correlations, in order to create more general and applicable mathematical models for engineering applications. CFD is still under development in many ways, although it is able to predict a wide range of applications. Simultaneously, experimental and empirical methods are also improving. Indeed, these methods are interconnected and their development co-dependent.

As CFB - type applications are operating in a turbulent regime, turbulence prediction becomes one of the biggest challenges in gas-solid systems. The gas phase turbulence and the small dense particle interaction are extremely complex. Even though turbulence modification due to gas-solid interaction is of great interest to wide industrial and natural gas-solid flows, it is poorly understood. Analytically, only the simplest cases, e.g, particle dispersion in homogeneous gas-solid flows can be solved. Unfortunately, in reality gas-solid flows are very inhomogeneous and anisotropic, which makes them very difficult to model. The dilute gas-solid flow can be predicted successfully by two-way coupling where particle-particle interactions are neglected. For a dilute phase, the particle volume fraction range lies between  $10^{-3}$ – $10^{-6}$  [Elghobashi (1994)]. The dispersion of the particles in the fully developed channel can be seen in Fig.1.2 [Fessler et al. (1994)]. But in case of dense solid-gas flow, particle-particle interaction is also vital to understand and improve the process. The four-way coupling turbulence modelling is studied in several works [Reeks (1991); Peirano and Leckner (1998); Zhang and Reese (2001); Fevrier et al. (2005); Fede et al. (2006); Ozel et al. (2013)]. The turbulence in multiphase flows is derived by using the Langevin model in order to ensure particle-fluid velocity correlation. Large eddy simulations (LES) and direct numerical simulations (DNS) are coupled by taking into account the effect of particles on a subgrid-scale fluid and particle turbulence [Fede et al. (2006)]. The algebraic particle-fluid velocity correlation model is introduced and a new gas turbulence model is derived which shows that the microscopic effect of gas turbulence modulation on particles cannot be neglected even for a dilute suspension [Zhang and Reese (2001)]. For a thorough understanding of particle velocity spatial distribution in dilute gas-particle flows, statistical methods were employed [Fevrier et al. (2005)]. Here, the instantaneous particle velocity contribution is divided into a continuous turbulent velocity field shared by all the particles and the quasi-Brownian velocity distribution. In a two-fluid multiphase model, simulations are performed with larger mesh size than the smallest structure due to the limitations of computational resources. Yet, vital phenomena, like segregation of the particles, cannot be captured. In order to take into account this unresolved structures, mesh independent results filtered by volume averaging and a filtered balance equation are used with the proposed sub-grid drift velocity and particle sub-grid stresses [Ozel et al. (2013)]. In the  $k_s$ - $k_{gs}$  model [Peirano and Leckner (1998)] particle-particle interaction is taken

into account by calculating particle turbulent kinetic energy  $k_s$ , whereas the velocity covariance transport equation  $k_{gs}$  is still neglected.



Figure 1.2: Dispersed particles in a fully developed turbulent pipe flow (adapted from [Fessler et al. (1994)])

One of the main problems in a CFB reactor, affecting their efficiency, is the accumulation of particles near the wall. In order to increase it, several issues may be taken into account like mixing between fuel and oxygen and residence time of the fuel. The accumulation of particles near the wall leads to the formation of clusters. The clusters decrease the contact area between oxygen and fuel leading to a reduced mixing in the reactor. Besides, the clusters are causing stability problems and pressure losses in the reactor. To overcome these problems, a novel geometrical modification is introduced in this work –a dimpled wall. Dimples are widely used in aerodynamics and heat transfer applications, but for the first time applied in CFB. The dimples are enhancing the breaking down of the clusters and creating circulation and thus increasing the fuel residence time. In heat exchangers they are used to avoid the fouling effect and here the agglomeration of the particles on the wall which can increase the life of the reactors. Cold flow simulations are studied here for CFB type reactors with a dimpled wall. Also, the dimpled wall is applied to BFB and CFB reactors together with coal gasification chemical reactions.

## 1.2 Aim of the project

CFD is a very powerful and cheaper tool for modelling multiphase flows. As multiphase flows, like the turbulent gas-solid flow are very complex, a development and an improvement of the model is needed. Moreover, the applications of the multiphase flow as circulating fluidised bed are widely used but still demands investigations in the hydrodynamical and chemical reaction (like coal gasification) aspect. The aim of the project

is to understand the complex hydrodynamic structure of the fluidised bed reactors and to increase their efficiency. In order to do this, turbulence modulation of the gas-solid flow is investigated. The proposed decaying homogeneous isotropic turbulence model will help to understand the contribution of particle - particle and particle- fluid interaction to the turbulence modulation and full  $k_s-k_{gs}$  model model will also provide deeper understanding of the four-way coupling. Moreover, widely used  $v^2-f$  turbulence model is modified for multiphase flow and first time introduced here as a dispersed  $v^2-f$  model which will use the elliptic transport equation instead of wall and damping functions to describe the near-wall effect of turbulence. This is more realistic because the pressure field is elliptic in nature, single point closure models are not able to describe it. Furthermore, novel CFB reactor design is introduced with a dimple wall structure, to help increase the residential time, the mixing effect, to avoid pressure losses due to near-wall clusters and possible downscaling of the reactior. Finally, the novel CFB reactor with dimpled wall will be introduced to a chemically reacting coal gasification system.

- As the CFB reactor has a complex inhomogeneous hydrodynamics structure, the classical drag models overestimate the solid fraction in the top region of the CFB reactor. Therefore, to handle this flow inhomogeneity, the EMMS model is applied using ANSYS Fluent 14.5. Also, an UDF code is developed to capture the solid outflow and to apply it on the inlet in order to keep the solid flux constant. In this way, the design of additional cyclone and feedback structure are avoided, which optimises the computational time.
- A geometrical modification has been done by applying two types of the wall dimpled structure in order to facilitate the mixing effect, to increase the resident time of the particles in the reactor and most importantly, to break down the clusters near the wall.
- The multiphase turbulence model, based on the  $k_s-k_{gs}$  model [Peirano and Leckner (1998)], is applied to the Fluent 14.5. The model is simplified also to the isotropic case in order to understand the source terms effect on two phase turbulence modelling. The whole model is implemented in ANSYS Fluent 14.5 using UDF utility. The isotropic turbulence calculations are performed by using MATLAB R2014b code. Moreover, an entirely new model for gas-solid flow applications dispersed  $v^2-f$  model is introduced and applied to the ANSYS Fluent 14.5 by using UDF.
- The dimpled wall design is also applied to a hot reactor design and a coal gasification model is applied in ANSYS Fluent 14.5 by using UDF utility.

### 1.3 Thesis layout

The thesis is organised as follows:

- Chapter 2 provides the fundamental physical understanding of the fluidisation process and its applications in CFB and BFB. The governing equations of the multiphase solid-gas flow and introduces the kinetic theory of granular flow are theoretically described here. Also, a wide literature review is included about the Eulerian-Eulerian model.
- Chapter 3 explains turbulent flow fundamentals which take place in the gas-solid flow and a literature review is presented about turbulence modelling. Also, two-equation turbulence  $k_s-k_{gs}$  model [Peirano and Leckner (1998)] is used and simplified to consider isotropic gas-solid turbulence. Moreover, the modification of a single phase  $v^2-f$  model to a two phase dispersed  $v^2-f$  model is presented and a literature review about  $v^2-f$  model is also included. At the end of the chapter, the results from all the models are presented and validated by using data from the literature.
- Chapter 5 introduces briefly the dimples and reactor walls which are modified. Cold flow simulations are performed and validated from the data literature. The results of the dimpled wall calculations are presented at end of the chapter.
- Chapter 6 is dedicated to the literature review and results of the chemical reaction modelling in BFB and CFB reactors with and without dimpled walls.
- Chapter 7 rounds off the work by drawing final inferences and pointing to future work and possible applications.



# Chapter 2

## Mathematical modelling of two-phase flow

### 2.1 Overview

Computational fluid dynamics has become a very important tool to simulate and predict fluid dynamic processes prevailing in fluidised bed technology. The flow behaviour can be described by the conservation equations of mass, momentum and energy. Eulerian-Eulerian and Lagrangian models can be used to model the flow behaviour in the fluidised bed.

The Lagrangian model treats particles individually using Newton's law of motion giving an asset to determine easily particle properties, like velocity, temperature, mass and/or diameter of the particle [Radjai and Dubois (2011)]. Therefore, the segregation effect, a result of different velocity combinations and particle-particle interactions, was determined [Gera et al. (2004); Kawaguchi et al. (1998); van Wachem et al. (2001a); Helland et al. (2000)]. Another advantage is the simple implementation; however, the empirical adjustments need further elaboration and huge computational time and storage space are required.

Also, the Eulerian-Eulerian model is widely used to model multiphase flows. In scope of the Eulerian model, the solid phase is treated as a continuum and its properties are calculated using the kinetic theory of granular flow (KTGF) [Gidaspow (1994)] which is analogous to the kinetic theory of gas. The model has a lower computational cost in comparison to the Lagrangian model and has shown high accuracy for flow description of the fluidised bed [Pain et al. (2001)]. Each solid particle is assumed to have the same diameter and density in one phase. The general idea of the model is modelling of the particulate phase as a continuum with additional Navier-Stokes equations to the carrier (gas) phases and thus to implement the integral balances of continuity, momentum

and energy equations for each phase. There is still a need for additional variables, like solid pressure and viscosity, to describe solid phase averaging momentum balance. Importantly, gas-particle and particle-particle interactions must be taken into account to complete the Eulerian multiphase model by including drag models into the momentum balance. The momentum balance consists of interphase momentum transfer between gas and solid phase with dominant drag forces. The Eulerian approach is used during this work in order to describe the hydrodynamics and the reaction processes in gas-solid flows

The chapter is structured as following:

- Fundamentals of fluidisation, particle properties and behaviour in a particular regime;
- Theory and background of kinetic theory of granular flow is presented;
- Instantaneous conservation equations of the Eulerian-Eulerian model are presented together with a wide literature review;
- Existing drag models are presented and discussed. The EMMS model is chosen in order to capture the inhomogeneity of the system. The EMMS model is implemented in ANSYS Fluent 14.5 using UDF. Moreover, solid phase boundary conditions are introduced to take into account wall-particle interaction [[Johnson and Jackson \(1987\)](#)];

## 2.2 Fluidisation

In a fluidised bed, solid particles are located over a porous plate through which gas is flowing and the process of fluidisation starts. The gas is searching for a suitable path through the particles. Two physical phenomena—gravitational and drag (a frictional force between solid particles and gas) forces have effect on the process. When the velocity of the gas flow is low, the acting drag forces on each particle are low as well. Thus, the insignificant effect of drag forces and low velocities result in stationary particles (i.e. a fixed bed). By increasing the inlet velocity, drag forces increase counteracting the gravitational force. When lift forces overtake the gravitational force, the bed expansion process begins and particles start to separate from each other. Eventually, the velocity will reach the level, where the gravitational downward and upward forces will be equal. This critical velocity is called minimum fluidisation velocity ( $U_{mf}$ ) and it is determined by equations Eq. 2.1-2.2, which depend on the particle size [[Gidaspow \(1994\)](#); [Yang \(2003\)](#)]:

$$U_{mf} = \frac{d_s^2(\rho_s - \rho_g)g}{1650\mu}, \quad Re_{mf} < 20 \quad (2.1)$$

$$U_{mf}^2 = \frac{d_s^2(\rho_s - \rho_g)g}{24.5\rho_g}, \quad Re_{mf} > 1000 \quad (2.2)$$

where  $d_s$  is the particle diameter,  $\rho_s$  and  $\rho_g$  are the particle and gas density, respectively,  $g$  is the gravity and  $\mu$  is the fluid viscosity. The above equations are derived using buoyancy-equals-drag balance (Stoke's law) by assuming that there is no gas-wall friction and solid stress is not transmitted by the particles. To determine the minimum fluidisation velocity Reynolds number,  $Re_{mf}$ , we use an approximation, determined from the data of porosity versus sphericity and utilising Reynolds ( $Re_{mf}$ ) and Archimedes ( $Ar$ ) numbers [Wen and Yu (1966)] :

$$Re_{mf} = \sqrt{[33.7^2 + 0.0408Ar]} - 33.7, \quad (2.3)$$

where  $Ar$  is described as:

$$Ar = \frac{d_s^3(\rho_s - \rho_g)\rho_g g}{\mu^2}. \quad (2.4)$$

In this stage, the bed pressure drop becomes constant and equals the bed weight [Gidaspow (1994)]. A further increase in inlet gas velocity will reduce the bulk viscosity (i.e. fluidisation becomes dominant) allowing particles to move upward obeying the gas flow. At this level, particles start to behave fluid like. Generally, significant instabilities occur when upward-moving bubbles start to form inside the bed as gas flow is reaching the bubbling velocity. This phenomenon is called heterogeneous, aggregative or bubbling fluidisation. As a result of the further increase in the mass flow rate or velocity of carrier phase, several coalesce bubbles will occupy the whole cross-section (i.e. slugging effect). Higher Reynolds numbers lead to a turbulent regime where particle clusters are formed and particles are reaching the top (dilute part) of the reactor. Moreover, fluctuations caused by pressure reach the highest deviation at a turbulent level and dense and dilute regions are changing rapidly [Grace and Bi (1997)]. The final stage is the fast fluidisation regime where dilute and dense regions coexist [Li and Kwaik (1980)] and downward moving clusters take place near the wall. The operating range of the velocities is categorised by the minimum fluidisation velocity (as lower bound Eq. 2.1-2.2) and terminal or settling velocity,  $U_t$  (as upper bound) [Gidaspow (1994)]:

$$U_t = \frac{d_s^2(\rho_s - \rho_g)g}{18\mu}, \quad Re_p \leq 2.0 \quad (2.5)$$

$$U_t = \frac{0.153d_s^{1.14}g^{0.71}(\rho_s - \rho_g)^{0.71}}{\mu^{0.43}\rho_g^{0.29}}, \quad 2.0 < Re_p < 1000 \quad (2.6)$$

$$U_t = \frac{\sqrt{g d_s(\rho_s - \rho_g)}}{\rho_g}, \quad 1000 < Re_p < 250000 \quad (2.7)$$

where the particle Reynolds number is  $Re_p = \frac{d_s U_t \rho_g}{\mu}$ . Gas velocities larger than terminal ones will cause the particles to leave the reactor.

The particles (see Fig. 3.3) can be classified as [Geldart (1973)]:

- Geldart Type A –the particles from this type have a size of  $30 \mu\text{m} < d_s < 100 \mu\text{m}$  and a density below  $1400 \text{ kg m}^{-3}$ . Bubbling has not yet started, particles exhibit dense phase expansion after reaching the minimum fluidisation velocity.
- Geldart Type B –here the bubbles appear at a minimum fluidisation velocity and the size of the particles ranges between  $100 \mu\text{m} < d_s < 1000 \mu\text{m}$ , while the density falls in the interval  $1400 \text{ kg m}^{-3} < \rho_s < 4000 \text{ kg m}^{-3}$ .
- Geldart Type C –the particles falling in this group can be described as cohesive and difficult to fluidise (size:  $20 \mu\text{m} < d_s < 30 \mu\text{m}$ ).
- Geldart Type D –as the particles here are either too large or too dense, spouted bed can be easily formed (size:  $d_s > 1000 \mu\text{m}$ ).

In the initial simulations (see chapter 6), particles of type B and D have been used in order to make a consistent comparison with the existing literature results.

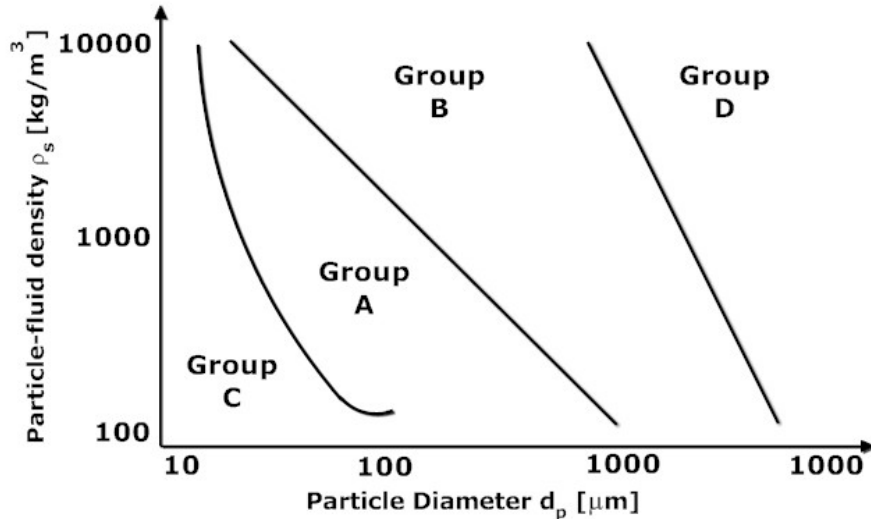


Figure 2.1: Geldart classification of particles for air at ambient conditions (adapted from [Geldart (1973)]).

The multiphase flow can be fluid-fluid or fluid-solid. If it is a fluid-solid mixture, the fluid is called a carrier phase and the solid a dispersed phase. A monodispersed phase includes only one particle type in contrast to the polydispersed phase which has more particle types with different properties. Also, the dense gas-solid flows can be categorised by their operating and minimum fluidised velocities.

- The fixed bed regime takes place when  $0 < U < U_{mf}$  – particles stay static at the bottom and pressure drop depends on the initial bed height and fluidisation velocity.
- The bubbling regime takes place when  $U_{mf} < U < U_{ms}$  – bubbles start to form near the distributor and then rise and coalesce. There is a clear upper surface and bubbles collapse at the top of the reactor which leads to large pressure fluctuations.
- The slugging regime takes place when  $U_{ms} < U < U_c$  – solid fraction occupies most of the reactor, large bubbles rise and collapse regularly at the top leading to large pressure fluctuations.
- The turbulent regime takes place when  $U_c < U < U_{se}$  – near the wall small clusters are forming and moving downwards causing pressure fluctuations.
- The fast regime takes place when  $U_{se} < U$  – the middle of the reactor is very dilute, there is no upper surface and the dense near-wall region moves downwards.

At the critical superficial velocity,  $U_c$ , a transition to turbulence fluidisation takes place and the standard deviation of pressure fluctuations reaches a maximum [Bi and Grace (1995); Bi et al. (1995)].  $U_{se}$  is the velocity at which the entrainment process begins and transition from turbulent to fast fluidisation occurs.

## 2.3 Kinetic theory of granular flow

To define the behaviour of many particles as a continuum, granular kinetic theory can be applied. The theory is built upon an analogy of dense gas phase molecules assumed to be nearly elastic [Gidaspow (1994)]. The kinetic theory model has different approaches to define the solid shear viscosity which represents the resistance of the mixture (gas-solid) against the compression. In contrast to solid shear viscosity being tangential forces, these are normal forces. Gidaspow [Gidaspow (1994)] does not take into account the inelastic behaviour of particle kinetic contribution to the total stress as Lun [Lun et al. (1984)]. Sinclair and Hrenya [Sinclair and Jackson (1989); Hrenya and Sinclair (1997)] followed Lun's model, but confine the mean path of the particle by the actual dimension characteristic of the physical system. Syamlal [Syamlal et al. (1993)] neglects the kinetic contribution which dominates the dilute region.

Similar to solid shear viscosity, solid thermal conductivity can be described by kinetic and collisional contributions. Physically, kinetic contributions are achieved by momentum, transferred by moving particles through the system. Collisional contributions are a result of momentum transfer due to direct particle-particle collision. Unlike Lun [Lun et al. (1984)], Gidaspow derived the dependency of solid thermal conductivity on the restitution coefficient [Gidaspow (1994)]. Syamlal [Syamlal et al. (1993)] has neglected

the kinetic contribution on solid thermal conductivity. As in the solid viscosity case, Sinclair and Hrenya [Sinclair and Jackson (1989); Hrenya and Sinclair (1997)] confine the particle mean path by the actual dimension characteristic of the physical system to define the solid thermal conductivity.

The radial distribution function is derived from statistical mechanics and it measures the probability of a particle-particle contact. Several radial distribution functions are provided in the literature to explain the solid phase stress which depends on the radial distribution function at contact. One of them is the Carnahan and Starling model [Carnahan and Starling (1967)] which does not reach the correct limit at the closest solid packing. Because particles at maximum solid volume fraction are in constant contact, the radial distribution function at contact becomes infinite. Thus, an alternative radial distribution function [Gidaspow (1994); Sinclair and Jackson (1989)] has been developed to correct the packing limit at closest packing stage. However, Gidaspow's radial distribution function has certain limitations to predict the correct limit when solid volume fraction approaches zero.

The frictional stress resulting from continuous contact between particles occurs at high solid volume fractions. Since the collision of particles is not instantaneous [Zhang and Rauenzahn (1997)], as assumed by the kinetic theory, a new model based on empirical data is used [Schaeffer (1987)].

Particle elasticity is a vital characteristic of granular flow behaviour though not included in the classical kinetic theory. The restitution coefficient [Jenkins and Savage (1983)] ranges between 0 and 1, where 0 explains a fully inelastic collision and 1 a fully elastic one. The energy dissipation is caused by inelastic collisions of particles [Lun et al. (1984)]. According to Goldschmidt [Goldschmidt et al. (2001)], more inelastic collisions lead to more energy dissipation, in other words, when the restitution coefficient is decreasing, collisions produce lower fluctuating kinetic energy. Besides that, the bubbling behaviour strongly depends on energy dissipation from particle-particle interaction. In the dense case, particle interaction time is high, so interaction takes place with more than one particle. Thus, the assumption that interaction between two particles should finish before another particle can interact with another one is not applicable in this regime [Zhang and Rauenzahn (2000)]. Particle roughness and rotation in the BFB model were also included later [Sun and Battaglia (2006)].

### 2.3.1 The statistical description of the particulate phase

The idea of granular flow originated from the similar behaviour observed in gas molecules. The granular flow transport equations (e.g, mass, momentum and energy) and quantities (e.g, fluxes and rate of dissipation) are expressed via classical gas kinetics [Chapman and Cowling (1970)]. Therefore, the thermodynamic temperature of the gas is replaced

by the granular flow temperature. The solid stress and viscosity are a function of the granular temperature, which changes with respect to time and space. The work about the granular flow was completed by deriving classical gas dense theory and combining it with Grad's theory. This approach needs to be modelled (by averaging and approximations) to obtain mean values of the granular flow properties due to system complexity. The theory is based on the Maxwell-Boltzmann equation. The probability function consists of  $x$ , which defines the position of the particle and  $u_s$  – the particle velocity in the volume element  $dx$ . By applying external force,  $F_i$ , these variables will be changed with time  $t+dt$ , so the probability function of finding a particle at a position  $x$  with a velocity  $u$  in the volume element  $dx$ , can be written as:

$$f = f(u_s; x, t) \quad (2.8)$$

The mean value of any particle property is given by  $\psi(u)$

$$\bar{\psi}(u) = \frac{1}{n} \int \psi(u_s; x, t) f(u_s; x, t) du \quad (2.9)$$

where the number of particles per unit volume is obtained when  $\psi = 1$

$$n(x, t) = \int f(u_s; x, t) du \quad (2.10)$$

The number density can be related to particle volume fraction, when the particles are assumed to be spherical [Benavides (2009)],

$$nm_p = \alpha_s \rho_s \quad (2.11)$$

where

$$m_p = \frac{\pi}{6} d_s^3 \rho_s. \quad (2.12)$$

Mean particle velocity can be calculated as

$$U_{si} = \frac{1}{n} \int u_{si} f(u_s; x, t) du \quad (2.13)$$

and the Maxwell-Boltzmann equation can be written as:

$$\frac{\partial}{\partial t} (n\bar{\psi}) + \frac{\partial}{\partial x_j} (n\bar{u}_{si}\bar{\psi}) + \frac{\partial}{\partial u_i} (F_i f) = \frac{\partial f}{\partial t}|_{coll}, \quad (2.14)$$

where  $F_i$  is the rate of change of particle velocity which can be obtained along the particle paths and is a result of particle interaction with the fluid flow. The collision effect must be a defined source term (r.h.s) by which the rate of change of distribution due to particle collision is expressed. The equation of motion can be simplified for heavy particles  $\frac{\rho_s}{\rho_g} \sim 10^3$  as

$$F_i = g - \frac{1}{\rho_s} \frac{\partial p}{\partial x_j} + f_d, \quad (2.15)$$

where the first term on the right hand side is gravity, the second one is Archimedes force and the last one is drag. In Eulerian modelling, trajectory information of every particle is lost due to the averaging procedure [Benavides (2009)].

The Enskog's equation is a general transport equation for any particle property which can be obtained by multiplying Eq. 2.14 with  $\psi$  and integrating over the particle velocity space

$$\frac{\partial f}{\partial t} + \frac{\partial}{\partial x_i} (u_i f) = n \overline{F_i \frac{\partial \psi}{\partial u_i}} + n C(\psi), \quad (2.16)$$

where  $C(\psi)$  represents particle-particle interaction.

Yet, severe average constraints exist here as equilibrium distributions of velocities and continuum particle phase are applied. Moreover, particles are treated as perfectly smooth and their rotation is ignored. Yet, the kinetic theory takes into account particle loading, collision and friction effects typical for BFB and CFBs.

## 2.4 Instantaneous local equations of two-phase flow

A formal mathematical formulation of the local mean variables is used to convert the point Navier-Stokes equations for the fluid and Newton's equation of motion of a single particle to continuum equations [Anderson and Jackson (1967)]. The point variables are averaged over the regions that are larger than the particle diameter and at the same time smaller than the characteristic dimensions of the complete system.

### 2.4.1 Conservation of mass

The continuity equation for gas and solid phases, respectively, shows that the rate of mass accumulation per unit volume together with the net rate of convective mass flux must be equal to the interphase mass transfer due to chemical reactions:

$$\frac{\partial}{\partial t} (\alpha_g \rho_g) + \frac{\partial}{\partial x_j} (\alpha_g \rho_g u_{g,j}) = S_{sg} \quad (2.17)$$

$$\frac{\partial}{\partial t} (\alpha_s \rho_s) + \frac{\partial}{\partial x_j} (\alpha_s \rho_s u_{s,j}) = S_{sg} \quad (2.18)$$

where

$$\alpha_g + \alpha_s = 1 \quad (2.19)$$

$$S_{sg} = -S_{gs} = \omega_i \Sigma Y_i R_i . \quad (2.20)$$

The subscripts  $g$  and  $s$  represent the gas and solid phases, respectively. The  $u$  is the instantaneous velocity,  $\rho$  is the density and  $\alpha$  the volume fraction.  $S_{sg}$  is the source term which describes the specific rate of production of mass of phase  $i$  due to chemical reactions.  $Y_i$  is the mass fraction of species,  $R_i$  is the net production rate and  $\omega_i$  is the species molar weight. When there is no mass exchange, the source term becomes zero. In the control volume, the sum of all phases must equal 1.

## 2.4.2 Conservation of momentum

The momentum equation for each phase, with the left hand side representing the net rate of momentum increase and of momentum transfer by convection, is given respectively as:

$$\begin{aligned} \frac{\partial (\alpha_g \rho_g u_{g,i})}{\partial t} + \frac{\partial}{\partial x_j} (\alpha_g \rho_g u_{g,i} u_{g,j}) = \\ - \alpha_g \frac{\partial p}{\partial x_i} + \nabla \cdot \alpha_g \tau_{g,ij} + \alpha_g \rho_g g + K_{gs} (u_g - u_s) + S_{gs} u_g \end{aligned} \quad (2.21)$$

$$\begin{aligned} \frac{\partial (\alpha_s \rho_s u_{s,i})}{\partial t} + \frac{\partial}{\partial x_j} (\alpha_s \rho_s u_{s,i} u_{s,j}) = \\ - \alpha_s \frac{\partial p}{\partial x_i} - \frac{\partial p_s}{\partial x_i} + \nabla \cdot \alpha_s \tau_{s,ij} + \alpha_s \rho_s g + K_{gs} (u_g - u_s) + S_{sg} u_s \end{aligned} \quad (2.22)$$

where on the right hand side the first term shows the pressure gradient, to which, in the solid case, the solid pressure  $p_s$  must be added. The second term is the viscous stress tensor,  $\tau_s$  (i.e. the traction exerted on the gas phase by the particle surfaces), whereas the third term takes into account external forces due to gravity. The fourth term,  $K_{gs}$ , describes the interphase momentum transfer between solid/gas phases and the last source term is the rate of production due to chemical reactions. The stress-strain tensor for gas and solid phases can be written as:

$$\bar{\tau}_g = \alpha_g \mu_g (\nabla u_g + \nabla u_g^T) - \frac{2}{3} \alpha_g \mu_g (\nabla \cdot u_g) \bar{I}_g \quad (2.23)$$

$$\bar{\tau}_s = \alpha_s \mu_s (\nabla u_s + \nabla u_s^T) - \alpha_s \left( \xi_s - \frac{2}{3} \mu_s \right) \nabla \cdot u_s \quad (2.24)$$

where  $\bar{I}$  is the identity tensor,  $\mu$  is the viscosity and  $\xi_s$  is the solid bulk phase viscosity which defines the particle suspension resistance against compression [van Wachem et al. (2001b)]. Bulk viscosity strongly depends on velocity gradients and it is in the same order of magnitude with shear viscosity in fluidised bed systems. Therefore, bulk viscosity should not be neglected as in Newtonian fluids. The equation for bulk viscosity is [Lun et al. (1984)]:

$$\xi_s = \frac{4}{3} \alpha_s d_s \rho_s g_0 (1 + e) \left( \frac{\Theta_s}{\pi} \right)^{\frac{1}{2}}, \quad (2.25)$$

where  $\Theta_s$  is the granular temperature,  $g_0$  is the radial distribution function,  $e$  is the restitution coefficient and  $d_s$  is the particle diameter. In our model, the gas viscosity,  $\mu_g$ , is a function of the gas phase turbulent viscosity,  $\mu_{gt}$ , and gas laminar viscosity,  $\mu_{gl}$ :

$$\mu_g = \mu_{gt} + \mu_{gl}. \quad (2.26)$$

In particle phase, the flow can be described depending on its concentration as dilute, transition or dense flow (see Fig. 2.2). In the dilute region particles randomly translate and fluctuate leading to the so-called kinetic dissipation. In the transition region, particles collide shortly causing additional dissipation and stress. This denser than the dilute regime is called collisional dissipation. At very high concentrations, particles begin to endure long, sliding and rubbing contacts which results into frictional dissipation. The solid shear viscosity,  $\mu_s$ , includes collisional ( $\mu_{s_{col}}$ ), kinetic ( $\mu_{s_{kin}}$ ) and frictional ( $\mu_{s_{fr}}$ ) effects. For the collisional and kinetic parts, the most important parameter is the restitution coefficient,  $e$ , which ranges between 0 and 1. When  $e$  is equal to 0, the particle is fully inelastic, and when  $e = 1$ , it is the opposite. The bulk viscosity and particle pressure describe the normal forces mentioned above, whereas the shear viscosity accounts for tangential forces. Finally, our shear viscosity model depends on the particle kinetic, collisional and frictional viscosities [Gidaspow (1994)]:

$$\mu_s = \mu_{s_{col}} + \mu_{s_{kin}} + \mu_{s_{fr}}. \quad (2.27)$$

When the flow becomes more dense, the collision probability also increases, leading to viscosity change. The collisional viscosity has been presented by Ding and Gidaspow [Ding and Gidaspow (1990)] as:

$$\mu_{s_{col}} = \frac{4}{5} \alpha_s d_s \rho_s g_0 (1 + e) \left( \frac{\Theta_s}{\pi} \right)^{\frac{1}{2}}. \quad (2.28)$$

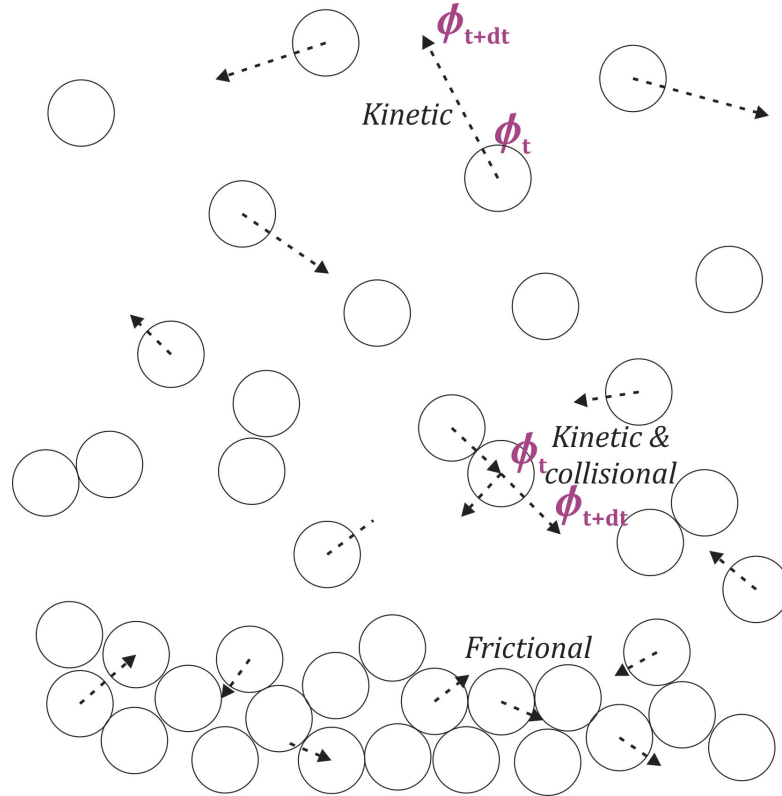


Figure 2.2: Viscous dissipation due to kinetic, collision and friction within a granular flow

The kinetic viscous term developed by Gidaspow [Gidaspow et al. (1992)] is:

$$\mu_{s_{kin}} = \frac{10d_s \rho_s \sqrt{\Theta_s \pi}}{96\alpha_s (1 + e) g_0} \left[ 1 + \frac{4}{5} \alpha_s g_0 (1 + e) \right]^2. \quad (2.29)$$

When particles endure long and permanent contacts by rubbing and/or rolling on each other, Boltzmanns equation based kinetic-collisional stress model becomes inappropriate as it assumes binary collisions instantaneous. At very high concentrations (above 50 % in volume) collisions are not instantaneous anymore. Therefore, frictional stress must be taken into account by using the plasticity theory (or similar) where the material behavior is assumed to be independent of the velocity gradient or the rate-of-strain. Under a normal stress, a well-compacted particles will shear only when the shear stress attains a critical magnitude. This is described by Mohr-Coulomb law based on the laws of sliding friction. It is a linear law between the shear ( $S$ ) and normal ( $N$ ) stresses (see Fig . 2.3) and  $k$  is a material property which captures cohesive state of particles. The exponential line is a yielding condition for shearing.

Schaeffer [Schaeffer (1987)] provided an expression for a very dense case to take into account friction forces between the particles (very close to the maximum packing limit

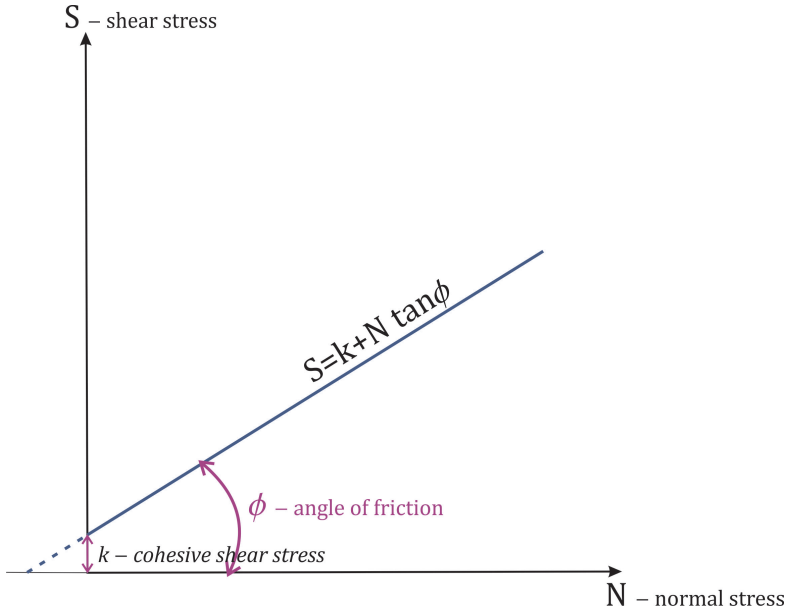


Figure 2.3: Relationship of Mohr-Coulomb in the N-S plane.

$\alpha_s \approx \alpha_{s_{max}}$  ):

$$\mu_{s_{fr}} = \frac{p_s \sin \phi}{2\sqrt{I_{2D}}} , \quad (2.30)$$

where the internal particle friction angle is taken to be  $28^\circ$  [van Wachem et al. (2001b); Ocone et al. (1993)]. This angle represents the angle of repose or internal friction angle of the material (see Fig. 2.4). When particles are smooth, coarse and round, the angle of repose becomes low. Yet, it is high for sticky and fine particles. Typically, internal particle friction angle is between  $15^\circ$ - $45^\circ$ .  $I_{2D}$  is the second invariant of the deviatoric stress tensor. The solid pressure,  $p_s$ , describes the solid phase normal forces

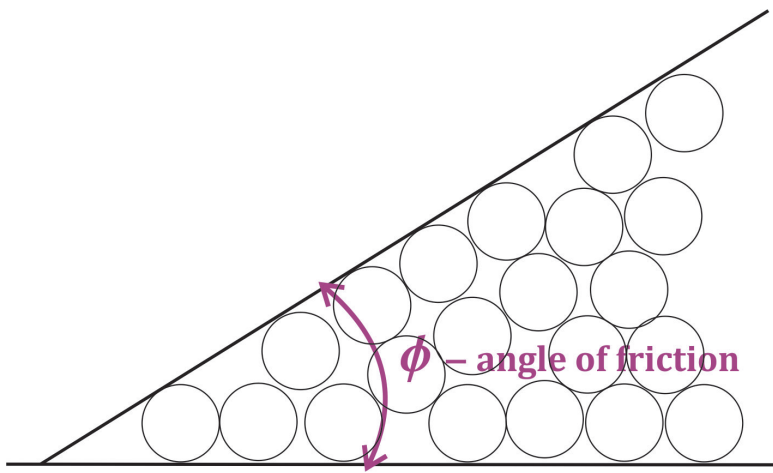


Figure 2.4: Internal friction angle.

due to particle-particle interaction and it is developed based on the kinetic theory of granular flow. The description of the solid pressure includes both kinetic and collisional effects. The collisional influence captures the momentum transfer due to direct collisions, whereas the kinetic part explains the particle translation:

$$p_s = \alpha_s \rho_s \Theta_s + 2\rho_s (1 + e) \alpha_s^2 g_0 \Theta_s , \quad (2.31)$$

where the radial distribution function,  $g_0$ , gives the probability of particle collisions and it is derived from statistical mechanics:

$$g_0 = \left[ 1 - \left( \frac{\alpha_s}{\alpha_{s_{max}}} \right)^{\frac{1}{3}} \right]^{-1} , \quad (2.32)$$

where  $\alpha_{s_{max}}$  is the maximum packing limit. Usually, the packing limit is accepted to range between 0.6 – 0.7.

The granular temperature,  $\Theta_s$ , defines particle velocity fluctuations due to random kinetic energy of individual particles and particle velocity fluctuations resulting from collisions between particles. The granular temperature particle equation considers fluctuations caused by shear forces and dissipation due to kinetic and collisional heat flow, inelastic collision and fluid interaction [Gidaspow (1994)]:

$$\Theta_s = \frac{1}{3}(u_x^2 + u_y^2 + u_z^2), \quad (2.33)$$

and

$$\begin{aligned} \frac{3}{2} \left[ \frac{\partial}{\partial t} (\alpha_s \rho_s \Theta_s) + \frac{\partial}{\partial x_i} (\alpha_s \rho_s u_s \Theta_s) \right] = \\ \frac{\partial}{\partial x_i} \left( \alpha_s k_{\Theta_s} \frac{\partial \Theta_s}{\partial x_i} \right) + \tau_{s_{ij}} \frac{\partial \Theta_s}{\partial x_j} - \gamma_{\Theta_s} - 3K_{gs} \Theta_s. \end{aligned} \quad (2.34)$$

The first term is the energy flux due to a random motion of particles and a particle-particle interaction. The second term on the right hand side represents the production of fluctuating energy due to particle phase shear and pressure. The third term represents the rate of dissipation due to collision and the last term the dissipation of fluctuating energy caused by the interaction of the particles with the surrounding fluid. The particle shear stress tensor,  $\tau_{s_{ij}}$ , can be calculated as follows

$$\tau_{s_{ij}} = \left( -P_s + \eta \mu_b \frac{\partial U_{si}}{\partial x_i} \right) \delta_{ij} + 2\mu_s S_{s_{ij}}, \quad (2.35)$$

where  $\eta = \frac{1+e}{2}$  and  $\mu_b = \frac{256}{5\pi} \mu_s \alpha_s^2 g_0$  [Pannala et al. (2011)]. The strain rate tensor can be written as

$$S_{s_{ij}} = \frac{1}{2} \left( \frac{\partial U_{si}}{\partial x_j} + \frac{\partial U_{sj}}{\partial x_i} \right) - \frac{1}{3} \frac{\partial U_{si}}{\partial x_i}. \quad (2.36)$$

The diffusion coefficient,  $k_{\Theta_s}$ , is:

$$k_{\Theta_s} = \frac{150\rho_s d_s \sqrt{\Theta_s \pi}}{384(1+e)g_0} \left[ 1 + \frac{6}{5}\alpha_s g_0 (1+e) \right]^2 + 2\alpha_s^2 \rho_s d_s (1+e) g_0 \sqrt{\frac{\Theta_s}{\pi}} \quad (2.37)$$

where the first term represents the kinetic component produced by particle velocity fluctuations and the second term includes particle collision components.  $\gamma_{\Theta_s}$  is the collisional dissipation:

$$\gamma_{\Theta_s} = \frac{12(1-e)^2 g_0}{d_s \sqrt{\pi}} \alpha_s^2 \rho_s \Theta_s^{3/2}. \quad (2.38)$$

### 2.4.3 Conservation of energy

The conservation of energy can be written for both phases in terms of enthalpy:

$$\frac{\partial(\alpha_g \rho_g H_g)}{\partial t} + \nabla \cdot (\alpha_g \rho_g u_g H_g) = \nabla(\lambda_g \nabla T_g) + Q_{gs} + S_{gs} H_g \quad (2.39)$$

$$\frac{\partial(\alpha_s \rho_s H_s)}{\partial t} + \nabla \cdot (\alpha_s \rho_s u_s H_s) = \nabla(\lambda_s \nabla T_s) + Q_{sg} + S_{sg} H_s \quad (2.40)$$

where  $H_i$  is the enthalpy for each species and  $\lambda$  represents the thermal conductivity. The enthalpy,  $H_i$ , can be defined for individual species in a mixture as follows:

$$H_i = \int C_{p,i} dT + \Delta H_{f,i}, \quad (2.41)$$

where  $C_p$  is the specific heat capacity and  $\Delta H_{f,i}$  shows the change of enthalpy required to form 1 mole of substance. The thermal conductivity,  $\lambda$ , can be written as:

$$\lambda_g = \sum \frac{X_j \lambda_j}{\Sigma_j X_j \phi_{ij}}, \quad (2.42)$$

where  $X_i$  describes the mole fraction of each species and  $\phi_{ij}$  are dimensionless quantities for mixtures of light and heavy gases [Warnatz et al. (1996); Bird (1976)]:

$$\phi_{ij} = \left[ 1 + \left( \frac{\mu_i}{\mu_j} \right)^{1/2} \left( \frac{\omega_i}{\omega_j} \right)^{1/4} \right] / \left[ 8 \left( 1 + \frac{\omega_i}{\omega_j} \right) \right]^{1/2} \quad (2.43)$$

$Q_{gs}$  is the heat exchange between the phases given by:

$$Q_{gs} = -Q_{sg} = h_{sg} (T_g - T_s), \quad (2.44)$$

where  $h_{sg}$  is the heat transfer coefficient. For multiphase applications, it can be calculated using the following equation:

$$h_{sg} = \frac{6\lambda_g \alpha_g \alpha_s N u_s}{d_s^2}, \quad (2.45)$$

where  $N u_s$  is the Nusselt number,  $d_s$  is the particle diameter and  $\lambda_g$  is the thermal conductivity of gases. The empirical correlation between  $N u_s$ , Prandtl number  $Pr$  and particle Reynolds  $R e_s$  was proposed as following [Gunn (1978)]:

$$N u_s = (7 - 10\alpha_g + 5\alpha_g^2)[1 + 0.7(R e_s)^{0.2}(Pr)^{1/3}] + \\ + (1.33 + 2.40\alpha_g + 1.20\alpha_g^2)(R e_p)^{0.2}(Pr)^{1/3} \quad (2.46)$$

where

$$Pr = \frac{C_{p,g}\mu_g}{\lambda_g} \quad (2.47)$$

and  $C_{p,g}$  is the gas specific heat capacity.

## 2.5 Averaged equations of two-phase flow

Reynolds averaging (see Appendix B) is applied to the above described conservation equations. To decrease the number of terms which appear due to Reynolds averaging, Favre or weighted averaging is applied to Eq. 2.48 [Benavides and van Wachem (2008)]:

$$\alpha_s = \bar{\alpha}_s + \alpha'_s; \quad (2.48)$$

where  $\bar{\alpha}_s$  and  $\alpha'_s$  are the mean and the fluctuating part, respectively. As the volume fraction is a volume-averaged quantity,  $\alpha'_s$  defines larger scale fluctuations than those presented here. Particle clusters can be an example of such fluctuations. Favre averaging values obtained from LDA measurements (laser Doppler anemometry) when the flow quantities like velocity, volume fraction are sampled. As soon as a phase is detected, the flow quantities start sampling [Benavides and van Wachem (2008)]. Favre averaged velocity takes the following form [Benavides and van Wachem (2008)]:

$$U_{si} = \overline{\frac{\alpha_s u_{si}}{\bar{\alpha}_s}} = \overline{U_{si}} + \overline{\frac{\alpha'_s u'_{si}}{\bar{\alpha}_s}} \quad (2.49)$$

### 2.5.1 Conservation of mass equation

After averaging Eq. 2.17 for gas phase:

$$\frac{\partial}{\partial t} (\overline{\alpha_g \rho_g}) + \frac{\partial}{\partial x_i} (\overline{\alpha_g \rho_g} U_g) = S_{sg} \quad (2.50)$$

Analogically to gas phase, the solid phase can be written as

$$\frac{\partial}{\partial t} (\overline{\alpha_s \rho_s}) + \frac{\partial}{\partial x_i} (\overline{\alpha_s \rho_s} U_s) = S_{sg} \quad (2.51)$$

It must be highlighted here that if a time-averaging procedure was used, an extra source term would appear in Eqs. 2.50-2.51 due to the correlation between volume fraction and velocity fluctuation components [Elghobashi and Abou-Arab (1983)]. An additional term appears in the momentum conservation equation  $\overline{\alpha'_s u'_s}$  which is also neglected [Elghobashi and Abou-Arab (1983); Benavides and van Wachem (2008)].

### 2.5.2 Conservation of momentum equation

Similarly to Eqs. 2.50-2.51, the momentum equation is derived as

$$\begin{aligned} \frac{\partial (\overline{\alpha_g \rho_g} U_g)}{\partial t} + \frac{\partial}{\partial x_j} (\overline{\alpha_g \rho_g} U_g U_g) &= -\overline{\alpha_g} \frac{\partial \overline{P}}{\partial x_i} + \frac{\partial}{\partial x_j} \left[ \overline{\alpha_g} (\overline{\tau}_{g_{ij}} + \overline{R}_{g_{ij}}) - \overline{\rho_g} \overline{\alpha_g u'_i u'_j} \right] + \\ &\quad + \overline{\alpha_g} \overline{\rho_g} g + K_{gs} (U_g - U_s) + S_{gs} U_g \end{aligned} \quad (2.52)$$

where  $\overline{R}_{g_{ij}} = -\overline{\rho_g} \overline{u'_i u'_j}$  is the Reynolds stress tensor (see Appendix B), together with the triple correlation between the components of velocity and volume fraction  $\overline{\alpha_g u'_i u'_j}$ . This term appears due to Favre averaging. In the current models, this term is neglected because it requires an additional transport equation or closure model due to the gradients of  $\overline{\alpha_g u'_i}$  [Elghobashi and Abou-Arab (1983)]. The term  $\overline{\tau}_{g_{ij}}$  is the viscous stress tensor for the gas phase. The drag coefficient,  $K_{gs}$ , can be calculated by one of the models from Section 2.6.

The momentum equation for the solid phase becomes

$$\begin{aligned} \frac{\partial (\overline{\alpha_s \rho_s} U_s)}{\partial t} + \frac{\partial}{\partial x_j} (\overline{\alpha_s \rho_s} U_s U_s) &= -\overline{\alpha_s} \frac{\partial \overline{P}}{\partial x_i} + \frac{\partial}{\partial x_j} [\overline{\alpha_s} \overline{\tau}_{s_{ij}} + \overline{R}_{s_{ij}}] + \\ &\quad + \overline{\alpha_s} \overline{\rho_s} g + K_{gs} (U_g - U_s) + S_{gs} U_s \end{aligned} \quad (2.53)$$

where the first term on the right hand side is the collisional stress tensor and  $\overline{\tau}_{s_{ij}}$  is derived from the kinetic theory of granular flow [Gidaspow (1994)]. The second term is the kinetic stress tensor  $R_{s_{ij}}$ . As it can be seen, the correlation term between the volume fraction and the velocity fluctuation is neglected here as well.

## 2.6 Drag models

Drag interaction between solid and gas acts as a driving force in gas-solid flows and plays a vital role in the dissipation of energy due to drag losses. Such behaviour makes the system even more complex as drag forces, due to the variations in solid spatio-temporal distributions, are highly non-linear and multiscaled in nature [Pannala et al. (2011)]. Drag models are vital to both phases, otherwise the two phases would move independently. The drag force is always a dominant component of interaction between gas and solid phases and the quantification of the drag force is very critical for the predictability of the simulations.

The first model of momentum interphase transfer between phases captured only a particle dense area and the pressure drop was calculated in a packed bed [Ergun (1952)]. By using the Ergun equation, the frictional pressure drop can be calculated for dense packed beds:

$$K_{gs} = 150 \frac{\alpha_s^2 \mu_g}{\alpha_g (\phi_s d_s)^2} + 1.75 \frac{\alpha_s \rho_g (U_g - U_s)}{\alpha_g^3 \phi_s d_s}, \quad (2.54)$$

where  $\phi_s$  describes the particle sphericity. However, this model neglected the top (dilute) part and areas where particle concentration was low.

### 2.6.1 Wen-Yu drag model

In 1966 Wen and Yu overcame the above mentioned deficiencies by creating a new drag model, which took into account a wide range of volume fractions [Wen and Yu (1966)]. Yet, in the Wen-Yu drag model, particle rich and very dilute zones are considered [Wen and Yu (1966)]:

$$K_{gs} = \frac{3}{4} C_D \frac{\alpha_s \alpha_g \rho_g |U_s - U_g|}{d_s} \alpha_g^{-2.65}, \quad (2.55)$$

where the drag coefficient  $C_D$  is defined as:

$$C_D = \frac{24}{\alpha_g Re_s} \left[ 1 + 0.15 (\alpha_g Re_s)^{0.687} \right]. \quad (2.56)$$

The Reynolds number is calculated as follows:

$$Re_s = \frac{\alpha_g \rho_g d_s |U_g - U_s|}{\mu_g}. \quad (2.57)$$

### 2.6.2 Gidaspow drag model

The most commonly used model [Gidaspow (1994)] is a combination of these drag models: the dense phase is based on the Ergun's model, where  $\varepsilon_g \leq 0.8$  and the dilute phase is described by Wen's model  $\varepsilon_g > 0.8$ . Yet, there was still a lack of explanation of the transition period (e.g., dense to dilute regime) of the process. To simulate the interphase momentum transfer, the Gidaspow's drag model [Gidaspow (1994)], consisting of Wen and Yu model for dilute phases [Wen and Yu (1966)] and the Ergun model for dense phases [Ergun (1952)] is used:

$$K_{gs} = \begin{cases} 150 \frac{\alpha_s^2 \mu_g}{\alpha_g d_s^2} + 1.75 \frac{\alpha_s \rho_g |U_s - U_g|}{d_s}, & \alpha_g \leq 0.8 \\ \frac{3}{4} C_D \frac{\alpha_s \alpha_g \rho_g |U_s - U_g|}{d_s} \alpha_g^{-2.65}, & \alpha_g > 0.8 \end{cases} \quad (2.58)$$

Here the same  $C_D$  is used as in Wen-Yu model:

$$C_D = \frac{24}{\alpha_g Re_s} \left[ 1 + 0.15 (\alpha_g Re_s)^{0.687} \right] \quad (2.59)$$

### 2.6.3 Syamlal-O'Brien drag model

Model development was continued by the Syamlal-O'Brien drag model [Syamlal and O'Brien (1989)], in which the empirical correlations of Richardson and Zaki [Richardson and Zaki (1954)] and Garside and Al-Duboni [Garside and Al-Duboni (1977)] were used to calculate the terminal velocity (a function of the volume fraction and particle Reynolds number). The Syamlal-O'Brien drag model [Syamlal and O'Brien (1987)] was built upon the effect of terminal velocity of a single particle:

$$K_{gs} = \frac{3}{4} \frac{\alpha_s \alpha_g \rho_g}{u_{r,s}^2 d_s} C_D \frac{Re_s}{u_{r,s}} |U_s - U_g|, \quad (2.60)$$

where

$$C_D = \left( 0.63 + \frac{4.8}{\sqrt{Re_s} u_{r,s}} \right)^2 \quad (2.61)$$

and terminal velocity correlation of the particles,  $u_{r,s}$ , [Garside and Al-Duboni (1977)] is:

$$u_{r,s} = 0.5 \left( A - 0.06 Re_s + \sqrt{(0.06 Re_s)^2 + 0.12 Re_s (2B - A) + A^2} \right) \quad (2.62)$$

with

$$A = \alpha_g^{4.14}, \quad B = \alpha_g^{2.65} \quad \text{for } \alpha_g > 0.85 \quad (2.63)$$

or

$$A = \alpha_g^{4.14}, \quad B = 0.8\alpha_g^{1.28} \quad \text{for } \alpha_g \leq 0.85 . \quad (2.64)$$

The Reynolds number is calculated here as follows:

$$Re_s = \frac{\alpha_g \rho_g d_s |U_g - U_s|}{\mu_g} . \quad (2.65)$$

In case of more than one solid phase simulation, the particle-particle interaction must be described as well. The model was derived by Syamlal [[Syamlal and O'Brien \(1987\)](#)] who took into account a different diameter of particles, an appropriate distribution function and particle-particle friction factors.

$$K_{s1,s2} = \frac{3(1+e) \left( \frac{\pi}{2} + C_{fr,s1,s2} \frac{\pi^2}{8} \right) \alpha_s 1 \alpha_s 2 \rho_s 1 \rho_s 2 (d_s 1 + d_s 2)^2 g_{0,s1,s2}}{2\pi(\rho_{s1} d_{s1}^3 + \rho_{s2} d_{s2}^3)} |U_{s,i} - U_{s,j}| \quad (2.66)$$

A detailed overview and comparison of the existing drag models has been previously published [[van Wachem et al. \(2001b\)](#)]. The authors showed that some drag models may predict a lower bed expansion or even produce discontinuity in the drag coefficient. In the thesis Wen-Yu drag model is used for BFB simulations and EMMS model, which is an extension of the Gidaspow drag model, is applied to the CFB simulations. The EMMS model has been chosen here because it is a filter model able to identify multiple scales present in the heterogeneous flow. Thus, it considers micro-scale particles, meso-scale clustering and axial and radial heterogeneity due to macro-scale boundaries. Several authors have used successfully the EMMS model for CFB reactors [[Armstrong et al. \(2010\)](#); [Li et al. \(1998\)](#); [Yang et al. \(2004\)](#); [Wang and Li \(2007\)](#); [Pannala et al. \(2011\)](#)].

#### 2.6.4 Energy minimisation multiscale drag model (EMMS)

Nevertheless different drag models [[Gibilaro et al. \(1985\)](#); [Arastoopour et al. \(1990\)](#)] have been proposed over the years, they are mostly applicable to the bubbling fluidised bed. Fast fluidisation regimes require different capabilities to be able to take into account downward moving particle clusters near the wall. This property was included in the energy minimisation multiscale model (EMMS) [[Li et al. \(1993\)](#)]. In a gas-solid flow, particles have a tendency to form clusters resulting into a particle dominating regime, whilst in the dilute regime the gas carries the particles giving gas dominating regime. If none of the participating phases (gas or solid) prevail, the regime becomes particle-gas-compromising regime. These regimes are characterised by a minimum energy per unit mass of the particles, and the mechanisms of gas-particle interactions are analysed for different scales. Hence, the EMMS model is used in this work to capture inhomogeneous structures present in the dimpled reactors. The EMMS model facilitates to define the different scales caused by the dimpled wall which breaks down the large clusters into

smaller or meso-scale clusters. The micro-scale represents the smallest space being

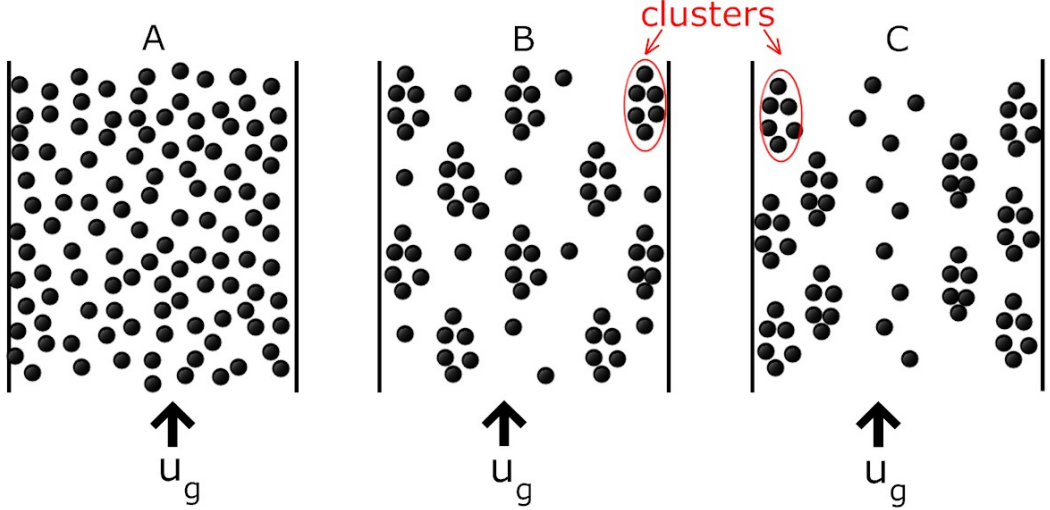


Figure 2.5: Cluster formation in CFB.

captured such as a particle or one grid point. The macro-scale is the averaging over the whole domain consisting of microstates which share the same properties. Meso-scales are located between the macro- and micro-scales. The meso structures can be unstable due to a gas-solid slip or inelastic collisions between particles [Agrawal et al. (2001)]. These structures are mostly shapeless, a few particle diameters big. The EMMS approach considers the micro-, meso- and macro-scales to be able to describe, more realistically, the heterogeneous gas-solid flow in CFBs [Li et al. (1993)]. It resolves the structure into a gas-rich dilute phase and particle-rich dense phase. Besides that it includes an interaction between meso-scale structures (clusters) (Fig. 2.5) and the surrounding particles or fluid. The formation of clusters tends to decrease the effective drag coefficient. If the inhomogeneity of these structures increases, it further decreases the drag effective coefficient. In Fig. 2.5, C, in contrast to A, has the lowest effective drag coefficient favouring the cluster formation. Therefore, we can conclude that the drag coefficient is not only a function of the Reynolds number, but that it also depends on the cluster formation [Li et al. (1993)].

To include this approach into the two-fluid model, the EMMS model has been simplified by assuming that in the dense phase the solid fraction is constant [Yang et al. (2004)]:

$$K_{gs} = \begin{cases} 150 \frac{\alpha_s^2 \mu_g}{\alpha_g d_s^2} + 1.75 \frac{\alpha_s \rho_g |\mathbf{u}_g - \mathbf{u}_s|}{d_s} , & \alpha_g \leq 0.74 \\ \frac{3}{4} C_D \frac{\alpha_s \rho_g |\mathbf{u}_g - \mathbf{u}_s|}{d_s} \omega(\varepsilon) , & \alpha_g > 0.8 \end{cases} \quad (2.67)$$

where

$$C_D = \begin{cases} \frac{24}{Re_s} [1 + 0.15 Re_s^{0.687}] , & Re_s \leq 1000 \\ 0.44 , & Re_s > 1000 \end{cases} \quad (2.68)$$

and

$$\omega(\alpha_g) = \begin{cases} -0.5760 + \frac{0.0214}{4(\alpha_g - 0.7463)^2 + 0.0044}, & 0.74 < \alpha_g \leq 0.82 \\ -0.0101 + \frac{0.0038}{4(\alpha_g - 0.7789)^2 + 0.0040}, & 0.82 < \alpha_g \leq 0.97 \\ -31.8295 + 32.8295\alpha_g, & \alpha_g > 0.97 \end{cases} \quad (2.69)$$

where  $\omega$  is the correction factor for the drag coefficient in each local control volume.

Furthermore, the EMMS model provides a physical explanation about the so-called "choking" which is a crucial parameter to describe CFB hydrodynamics in a gas-solid system. The choking point expresses the transition regime between dilute and dense fluidisation. The top of the reactor is characterised as a dilute region where transport takes place and the bottom of the reactor is the dense region, where collisional and frictional behaviour of particles is dominant. The choking transition represents a jump between the dilute and dense flow, while the global stability condition is satisfied. The global stability condition can be obtained by compromising between the gas or the particle dominance. The gas dominance is achieved by the minimisation of energy consumption used for particle transportation and suspension in unit volume. Whereas by particle dominance the potential energy of the particles is minimised to reach a minimal solid fraction. The choking phenomenon was observed by keeping the superficial velocity constant and imposing two solid masses (achieved by two bed heights). Then, the solid flux was dynamically measured at the outlet. It was observed that the flux was almost constant when the solid inventory was increased and the cross-sectional solid volume fraction between the dilute and dense region was coincident. The saturation was reached by EMMS although the solid inventory was increased [Li et al. (1998); Yang et al. (2004)].

## 2.7 Wall boundary condition

The wall boundary condition (BC) is critical for the solid phase, whereas the gas phase can be treated with no slip wall BC. In order to capture the particle behaviour, their granular properties should be taken into account. As the normal component of the solid phase at the wall velocity is zero, the parallel velocity of the particles to the wall is set to be slip.

In order to obtain the BC for granular flows, Johnson and Jackson [Johnson and Jackson (1987)] assumed that the tangential force resulting from the flowing particles near the wall is equal to the corresponding stress within this cluster. This force applied on the boundary by the particles considers the collision and friction during collisions. The BC

for granular energy, with  $\mathbf{n}$  being the unit normal vector of the wall, is derived as:

$$-\mathbf{n} \cdot \mathbf{q}_s = D + \mathbf{u}_{sl} \cdot \mathbf{S}_s^b \quad (2.70)$$

where  $\mathbf{u}_{sl}$  is the slip velocity of the particles and the flux of the fluctuation energy is  $\mathbf{q}_s$ . The rate of dissipation of the fluctuation energy ( $D$ ), due to inelastic particle-wall collisions, is:

$$D = \frac{1}{4} \pi \rho_s d_s^3 \theta (1 - e_w^2) \frac{\sqrt{3\theta}}{d_s \left[ (\alpha_{s,max}/\alpha_s)^{1/3} - 1 \right]} \frac{1}{d_s^2 (\alpha_{s,max}/\alpha_s)^{2/3}} \quad (2.71)$$

where  $e_w$  is the normal restitution coefficient of particle-wall collisions and  $S_c^b$  is the shear stress on the wall due to them:

$$S_c^b = \frac{\phi \sqrt{3\theta} \pi \rho_s \alpha_s \mathbf{u}_{sl}}{6 \alpha_{s,max} \left[ 1 - (\alpha_{s,max}/\alpha_s)^{1/3} \right]} \quad (2.72)$$

Moreover, the collision between the wall and particles is also taken into account through the specularity coefficient ( $\phi$ ), which depends on the wall large-scaled roughness and varies between 0 (i.e. perfectly reflective collision) and 1 (i.e. diffusive collision).

## 2.8 Summary

The governing equations for the Eulerian-Eulerian model are described. Moreover, the kinetic theory of granular flow is explained and discussed. The interphase momentum interchange models are discussed and the EMMS model which can predict the inhomogeneous particle distribution as seen in dense clusters. Also, it can resolve the structures in between the clusters as well as the dilute zone in the CFB reactor [Yang et al. (2003)]. Besides that specific particle boundary conditions, which take into account particle-wall interaction, are highlighted.

# Chapter 3

## Turbulence

### 3.1 Overview

Single phase turbulence remains one of the greatest challenges in fluid mechanics. In addition, the existence of particles makes the problem even more complex. Because of that, the development of theoretical and mathematical models is crucial to understand and predict the turbulence modulation. The first part of this chapter provides the fundamental understanding of a single turbulent flow. The second part includes particle properties and their impact on turbulence structures in a two-phase turbulent flow. Also, the  $k_s-k_{gs}$  model [Peirano and Leckner (1998)] is presented and simplified in an isotropic turbulence case in order to better understand the particle-particle interaction contribution to a particulate phase turbulence modification. The particulate phase turbulence and particle-particle interaction (four-way coupling) is vital to understand the hydrodynamics of dense systems such as CFB and BFB reactors. The implementation of a dispersed  $v^2-f$  model is introduced here. The chapter contains:

- The Kolmogorov's hypothesis and scales to comprehend the primary phase turbulence modulation;
- The classification of flow regimes which are vital for turbulence modulation in gas-solid flows;
- Time scales which describe particle-fluid and particle-particle interactions and a wide literature review about the two-phase turbulence modelling;
- The  $k_s-k_{gs}$  model [Peirano and Leckner (1998)] and a derivation for a stationary homogeneous isotropic turbulence case investigated to understand the source term effect on the two-phase turbulence modelling;
- The computation of a two-phase flow by deriving a multiphase  $v^2-f$  model in order to avoid wall and damping functions to capture the near-wall effect;

- The calculations performed for a 2D backward facing step flow using UDF utility in ANSYS Fluent 14.5 and a validation [Fessler and Eaton (1999)]. The stationary homogeneous isotropic turbulence case is calculated using the Runge-Kutta method in Matlab 2014a and validated [Elghobashi and Truesdell (1993)].

## 3.2 Fundamentals of turbulent motion

Turbulence is a chaotic and random motion leading to a constant change of velocity and pressure of the flow in space and time. Turbulent flows are very common in engineering applications –for example mixing of coal and oxygen in a CFB system (described in detail in Ch. 6). This phenomenon has two vital characteristics –a more efficient transport and a better mixing effect than a laminar flow. Through the energy cascade [Richardson (1922)] perspective, turbulence consists of small and large scale motions. The large scale formation is dependant on geometry, whereas the small scales are affected by the rate of receiving energy from them and by the viscosity. The concept of energy cascade lies in the generation (at large eddies) of energy and its transfer from large to small scales followed by its dissipation (at small eddies). This process continues until sufficiently small eddies are reached so that the kinetic energy can be dissipated by molecular viscosity. These eddies were discovered by Kolmogorov who introduced the relation between velocity ( $u$ ), timescale ( $\tau$ ), size ( $\eta$ ) and their characteristic length ( $l$ ) in his three hypotheses [Kolmogorov (1941)]:

**Kolmogorov's hypothesis of local isotropy:** *At sufficiently high Reynolds number, the small-scale turbulent motions ( $l \ll l_0$ ) are statistically isotropic.*

**Kolmogorov's first similarity hypothesis:** *In every turbulent flow at sufficiently high Reynolds number, the statistics of the small-scale motions ( $l < l_{EI}$ ) have a universal form that is uniquely determined by  $\varepsilon$  and  $\nu$ .*

**Kolmogorov's second similarity hypothesis:** *In every turbulent flow at sufficiently high Reynolds number, the statistics of motions of scale  $l$  in the range  $l_0 \gg l \gg \eta$  have a universal form that is uniquely determined by  $\varepsilon$ , independent of  $\nu$ .*

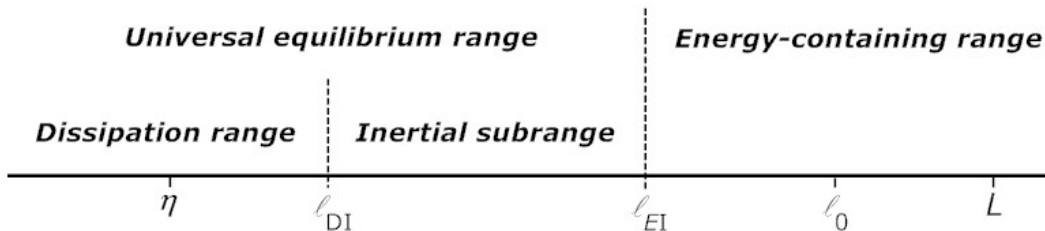


Figure 3.1: Scheme of various lengthscales and ranges for eddies at a very high Reynolds number

According to the Kolmogorov's hypothesis of local isotropy, eddies with the largest size have the length scale  $l_0$ , they are anisotropic and affected by the boundary conditions. During the above described energy transfer, their information is lost, making the small eddies in a way universal (locally isotropic). In the Kolmogorov's first similarity hypothesis, the size range  $l < l_{EI}$  ( $l_{EI} \approx \frac{1}{6}l_0$ ) is described as the universal equilibrium range where a rapid adaptation of small-scale eddies takes place to preserve the dynamic equilibrium with energy transfer hierarchy from large- to small-scale eddies (see Fig. 3.1). The Kolmogorov scales are determined by two parameters –kinematic viscosity ( $\nu$ ) and dissipation rate ( $\varepsilon$ ) [Pope (2010)]:

$$\eta \equiv (\nu^3/\varepsilon)^{1/4}, \quad (3.1)$$

where  $\eta$  is the scale of the smallest dissipative eddies. The velocity of Kolmogorov eddies is

$$u_\eta \equiv (\nu\varepsilon)^{1/4}, \quad (3.2)$$

and the time of the turn over the smallest eddies is

$$\tau_\eta \equiv (\nu/\varepsilon)^{1/2}. \quad (3.3)$$

The proof that the smallest dissipative eddies are characterised by the Kolmogorov scales lies in the unity of the Reynolds number based on these scales:

$$\eta u_\eta / \nu = 1. \quad (3.4)$$

and the dissipation rate:

$$\varepsilon = \nu(\eta u_\eta / \eta)^2 = \nu / (\tau_\eta)^2. \quad (3.5)$$

Another useful ratio is the smallest to the largest scale calculated from Kolmogorov scales and  $\varepsilon \sim u_0^3/l_0$  ( $u_0$  is the large-scale eddies turning velocity):

$$\eta/l_0 \sim Re^{-3/4}, \quad (3.6)$$

$$u_\eta/u_0 \sim Re^{-1/4}, \quad (3.7)$$

$$u_\tau/\tau_0 \sim Re^{-1/2}, \quad (3.8)$$

where  $\tau_0$  is the large-scale eddies turning time. The second similarity hypothesis states that viscous forces are small enough to be negligible. Here, an additional length scale ( $l_{DI}$ ) is introduced, and which divides the universal equilibrium range into inertial ( $l_{EI} >$

$l > l_{DI}$ ) and dissipation range ( $l > l_{DI}$ ) (Fig.3.1)

### 3.2.1 Classification of gas-solid flows

Turbulence is an unpredictable problem whose complexity increases with adding particles to the system. These particles cause changes in the turbulent structure and flow behaviour [Sproull (1961); Popper et al. (1961)]. As interaction between primary (gas) and secondary (solid) phases is inevitable, we need to have a closer look how this flow can be categorised. The gas-solid flow can be classified as a dilute one where particle motion is affected by the fluid body and surface forces and a dense one where particle-particle interaction and collision is dominant. The most useful parameter here is the Stokes number which describes the relation between particle response time  $\tau_p$  and fluid characteristic time  $\tau_f$ :

$$St = \frac{\tau_{gs}^x}{\tau_\eta}, \quad (3.9)$$

A small Stokes number ( $St \ll 1$ ) means that particles intend to obey the fluid path and to react as a single-phase flow [Crowe et al. (1996)]. Stokes numbers ( $1 \ll St$ ) are acting independent from the fluid phase. In case of turbulence, a larger Stokes number will unleash extra mechanisms which will affect the production and dissipation of energy and dispersion of fluid particles. If the Stokes number is nearly 1 ( $St \sim 1$ ), particles are accumulating in between the eddies by leading to significant deviations in particle trajectories (Fig. 3.2).

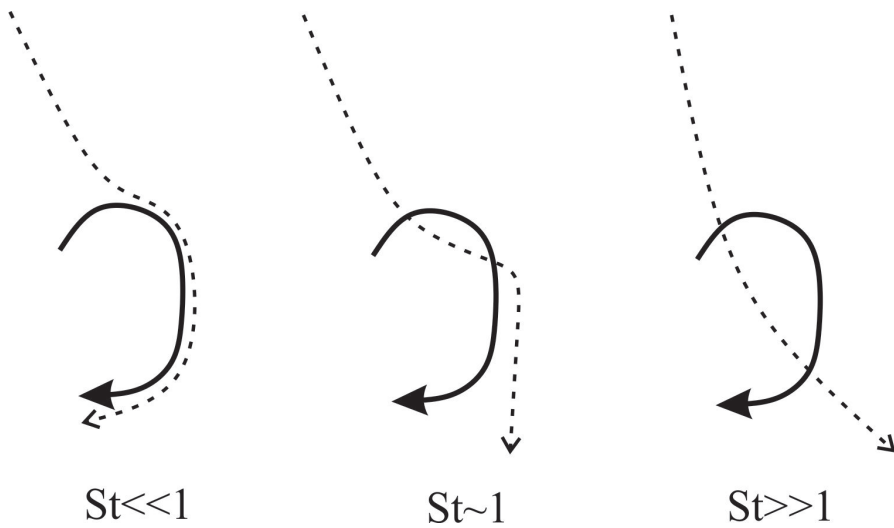


Figure 3.2: Eddy effect on particle trajectory. The dashed line represents particle trajectory, whereas the solid line represents eddies [Benavides and van Wachem (2009)].

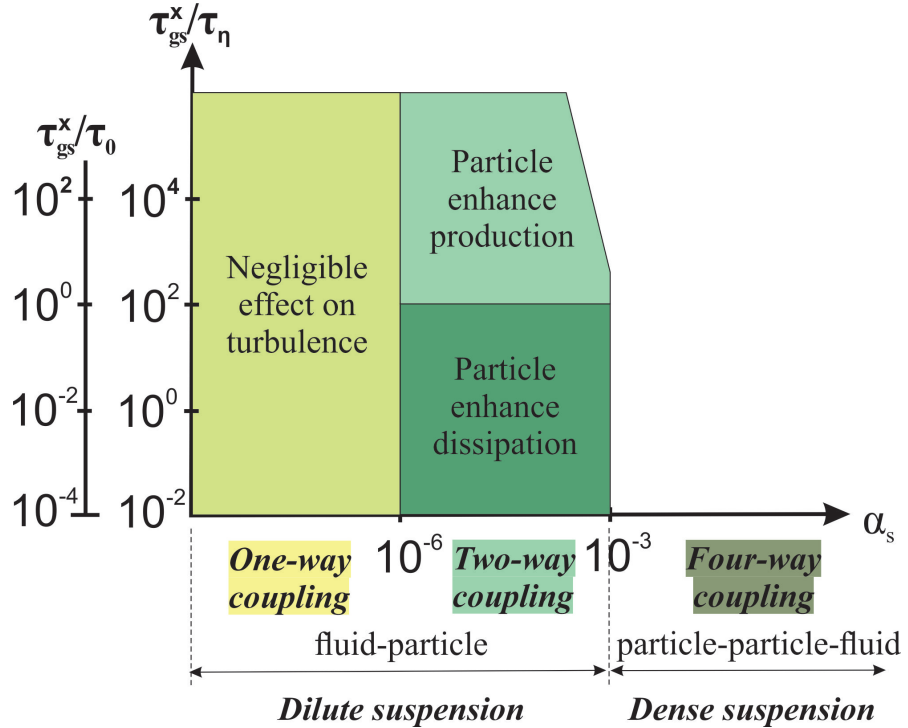


Figure 3.3: Classification of flow regimes for gas-solid flows [Elghobashi (1994)].

From Fig. 3.3 we can conclude that the gas-solid flow depends on the characteristic time ( $\tau_{gs}^x$ ), the relative distance between particles and Kolmogorov time scales,  $\tau_\eta$ . In case of a very dilute suspension (solid volume fraction less than  $10^{-6}$ ), particles have no effect on turbulence structures [Elghobashi (1994)]. If particle mass-loading is small enough, particles should observe a turbulent motion of the primary phase. It is the so-called "one-way coupling". The "two-way coupling" happens in higher solid volume fractions (about  $10^{-3}$ ) where particles start to change the behaviour of the turbulent motion. The presence of particles can lead to turbulence increasing or damping. The turbulence enhances when the particle diameter increases which means particle relaxation time is increasing too. Also, a higher Reynolds number causes the enhancing of turbulent kinetic energy because of vortex shedding effect. On the other hand, particles with a decreasing diameter (and decreasing relaxation time) damp the turbulence effect because the energy is used by the eddies to accelerate the particles and there is no vortex shedding effect any more. When the suspension is denser (solid volume fraction greater than  $10^{-3}$ ), the collisional effect between particles plays an important role in the flow - "four-way coupling".

### 3.2.2 Turbulence modelling

After the dispersion of solid particles in the primary gas phase, not only a significant reduction of the shear stress takes place in the flow [Sproull (1961)], but also the turbulence intensity is decreased [Popper et al. (1961); Hetsroni and Sokolov (1971)]. Due to gravitational forces, particles (with a higher Stokes number) start to lag behind the turbulent fluctuations creating a relative velocity between the phases and leading to a reduction of the turbulence energy. In fact, vortex shedding from particles with high Reynolds number enhances turbulence, whereas particles with a low Reynolds number damps it [Hetsroni (1989)]. The nature of this complex particle-gas interaction is not yet completely understood.

Although a two-phase turbulent pipe flow was of great interest for several applications, until late 1960s almost no experimental data was available. Owen made an excellent discussion about turbulence conveying but not validating it with experimental data [Owen (1969)]. The first profound experimental analysis was performed for a very dilute flow with small size particles (e.g., 200  $\mu\text{m}$ , 500  $\mu\text{m}$ , 1 mm) [Tsuji and Morikawa (1982, 1984)]. It was discovered that the velocity of particle size  $< 200 \mu\text{m}$  is higher than the mean gas velocity. Even though the bottom region was assumed to be isotropic, it remained to be critical, which can not be said for the wall region. Particles with a diameter of 1 mm enhanced the turbulence, whereas those with 200  $\mu\text{m}$  damped it. Particles with 500  $\mu\text{m}$  also increased the turbulence but still near the wall turbulence damping behaviour was observed.

An important computation was performed with and without gravity forces concluding that particles-fluid coupling led to a small eddies increase [Elghobashi and Truesdell (1993)]. For zero gravity, it was observed that the time dependent dissipation rate was increasing, whereas the kinetic energy had an opposite tendency. In terms of kinetic energy, the destruction of large eddies was dominant over the production in small eddies. The reverse effect occurred in terms of dissipation. The same behaviour was recorded in the case of non-zero gravity, but particle energy was transformed from small to large eddies (in fact reverse cascade phenomenon). Notably, gravity induced an anisotropic behaviour at small eddies [Peirano and Leckner (1998)].

Recently, turbulence in multiphase flows is derived by using the Langevin model in order to ensure particle-fluid velocity correlation. Large eddy simulations (LES) and direct numerical simulations (DNS) are coupled by taking into account the effect of particles on a subgrid-scale fluid and particle turbulence [Fede et al. (2006)]. The algebraic particle-fluid velocity correlation model is introduced and a new gas turbulence model is derived which shows that the microscopic effect of gas turbulence modulation on particles cannot be neglected even for a dilute suspension [Zhang and Reese (2001)]. For a thorough understanding of particle velocity spatial distribution in dilute gas-particle flows, statistical methods were employed [Fevrier et al. (2005)]. Here, the instantaneous particle velocity

contribution is divided into a continuous turbulent velocity field shared by all the particles and the quasi-Brownian velocity distribution. In a two-fluid multiphase model, simulations are performed with larger mesh size than the smallest structure due to the limitations of computational resources. Yet, vital phenomena, like segregation of the particles, cannot be captured. In order to take into account this unresolved structures, mesh independent results filtered by volume averaging and a filtered balance equation are used with the proposed sub-grid drift velocity and particle sub-grid stresses [Ozel et al. (2013)].

To sum up, increasing the resistance of particles in the flow enhances the dissipation due to particle drag and the effective viscosity increase can decrease the turbulence. On the other hand, the increase in turbulence can result from flow instabilities caused by the buoyancy effect and vortex shedding which enhances velocity fluctuations [Balachandar and Eaton (2010)]. A detailed review of experimental and computational strategies in turbulence multiphase flow has been done by [Balachandar and Eaton (2010)].

The beginning of a two-phase modelling was given by simple one-dimensional models which assumed a vanishing slip between gas and solid phases and were valid only for high or low Stokes numbers [Saffman (1962); Owen (1969)]. In recent years, large eddy simulations (LES) for homogeneous turbulent flow with particles were introduced [Deutsch and Simonin (1991)]. In LES, large eddies can be straightforwardly calculated, whereas small eddies need to be modelled. It is worth to apply it to two-phase flows. Yet, the method has difficulties handling the near-wall region where anisotropic small structures are dominant. Thus, this region requires a very fine grid in order to obtain reasonable results. Another type of simulations are direct numerical simulations (DNS), which are an exact solution of Navier-Stokes equations, but applicable only for simple geometries and low Reynolds numbers. The dispersion of a limited number of particles was modelled here for the decaying isotropic and homogeneous turbulence [Riley and Patterson (1974); Elghobashi and Truesdell (1992, 1993); Elghobashi (1994); Squires and Eaton (1990, 1991)].

The above described models are computationally very expensive, especially, for chemical reaction modelling and capturing the particle effect. Therefore, to model larger and sophisticated systems with high Reynolds numbers, time averaged two-equation turbulence models will be employed. Although they are derived for single-phase turbulence applications, after adding an extra term in the transport equations, they are able to capture the particle-fluid interaction in good agreement with experimental data [Elghobashi and Abou-Arab (1983); Shih et al. (1995)].

### 3.2.2.1 Characteristic time scales

Several time scales which are needed to explain the dominant mechanism in the gas-solid flows are presented here. The large eddies characteristic time scale is described as follows [Peirano and Leckner (1998)]:

$$\tau_0 = C_\mu \frac{k_1}{\varepsilon_1}, \quad (3.10)$$

where  $C_\mu = 0.09$ . Time scales for gas phase fluctuations and solid phase motion interactions are defined as following:

$$\tau_{gs}^t = \tau_0 (1 + C_\beta \xi_r)^{-1/2}, \quad (3.11)$$

where  $\xi_r = 3|U_r|^2/2k_1$  and  $C_\beta$  is a constant which depends on the direction of the velocities.  $\tau_0$  is the characteristic time scale for large eddies.  $\tau_{gs}^t$  is Lagrangian integral time scale which is experienced by the particles. It explains the loss of correlation because of the mean movements of particles, also known as the trajectory effect. In other words, virtual fluid and solid particles do not spend the same time in an eddy because of the mean relative velocities between the two phases. Particle relaxation time,  $\tau_{gs}^x$ , or actually how long the particles entrain in the primary phase, is defined as:

$$\tau_{gs}^x = \frac{4d_s \rho_s}{3\rho_g \langle C_D \rangle_s \langle |U_r| \rangle_s}, \quad (3.12)$$

where  $C_D$  is the drag coefficient which is calculated as:

$$C_D = 18\alpha_g^{-1.7}(1 + 0.15Re_s^{0.687})/Re_s, \alpha_s < 0.2 \quad (3.13)$$

$$C_D = [150\alpha_s/(\alpha_g Re_s)] + 1.75, \alpha_s > 0.2 \quad (3.14)$$

and  $U_r$  is the relative velocity,  $\rho_g$  and  $\rho_s$  are the densities for gas and solid phase, respectively, and  $d_s$  is the particle diameter. The drag coefficient is a function of the particle Reynolds number,  $Re_s = |U_r|d_s/\nu_g$ . Particle collision time,  $\tau_s^c$ , is expressed as:

$$\tau_s^c = \frac{d_s}{24\alpha_s g_0} \left( \frac{\pi}{\Theta_s} \right)^{1/2}, \quad (3.15)$$

where  $\Theta_s$  is the granular temperature which is  $\Theta_s = \frac{2}{3}k_2$ .

### 3.3 Two-equation $k_s$ - $k_{gs}$ model [Peirano and Leckner (1998)]

The primary phase turbulent kinetic energy,  $k_g$ , is calculated by

$$\begin{aligned} \frac{\partial}{\partial t} (\rho_g \alpha_g k_g) + \frac{\partial}{\partial x_j} (\rho_g \alpha_g k_g U_{gi}) = \\ \frac{\partial}{\partial x_i} \left( D_{k_g} \frac{\partial k_g}{\partial x_j} \right) - \alpha_g \rho_g \tau_{g,ij} \frac{\partial U_{gi}}{\partial x_j} + \alpha_g \rho_g \Pi_g k_g - \alpha_g \rho_g \varepsilon_g \end{aligned} \quad (3.16)$$

The interaction term for turbulence modification in presence of particles is

$$\Pi_{gk_g} = \frac{X_{gs}}{\tau_{gs}^x} (-2k_g + k_{gs} + U_{ri} U_{di}) \quad (3.17)$$

The term,  $\Pi_{gk_g}$  may lead to the attenuation of the primary phase turbulence by increasing particle loading. Between the parentheses, the dissipation due to drag and the second term represent the energy transfer to the particle phase fluctuations. Although the contribution of the last term is expected not to be very significant, it modulates turbulent kinetic energy as a result of turbulent particle transport.  $U_{ri}$  is the relative velocity and  $U_{di}$  is the drift velocity, which describes the correlation between the larger primary phase turbulent structures and particle size and velocity distributions. A good approximation can be shown by a gradient diffusion model as follows

$$U_{di} = -D_{gs} \left( \frac{1}{\sigma_{sg} \alpha_s} \frac{\partial \alpha_s}{\partial x_i} - \frac{1}{\sigma_{sg} \alpha_g} \frac{\partial \alpha_s}{\partial x_i} \right). \quad (3.18)$$

where  $D_{gs}$  is the turbulent dispersion coefficient.  $D_{gs}$  describes the product of a turbulent time scale characteristic seen by particles and a velocity scale determined along the particle trajectories. The dissipation of turbulent kinetic energy  $\varepsilon_g$  is given by

$$\begin{aligned} \frac{\partial}{\partial t} (\rho_g \alpha_g \varepsilon_g) + \frac{\partial}{\partial x_i} (\rho_g \alpha_g \varepsilon_g U_{gi}) = \\ \frac{\partial}{\partial x_i} \left( D_{\varepsilon_g} \frac{\partial \varepsilon_g}{\partial x_i} \right) - \alpha_g \rho_g \frac{\varepsilon_g}{k_g} \left( C_{\varepsilon_g} M_{gij} \frac{\partial U_{gi}}{\partial x_j} + C_{\varepsilon_g} \varepsilon_g \right) + \alpha_g \rho_g \Pi_{g\varepsilon_g} \end{aligned} \quad (3.19)$$

The term on the left hand side shows the rate of change and the transport of  $k_g$  or  $\varepsilon_g$  by convection. On the right hand side, the first term describes the transport of  $k_g$  or  $\varepsilon_g$  by diffusion, the second term is the production rate of  $k_g$  or  $\varepsilon_g$ . The third term is the fluid-particle interaction and the last term represents the destruction rate of  $k_g$ . The interaction term is

$$\Pi_{g\varepsilon_g} = C_{\varepsilon_3} \frac{\varepsilon_g}{k_g} \Pi_{gk_g} \quad (3.20)$$

The second order velocity moment is

$$M_{gij} = \frac{2}{3} k_g \delta_{ij} - 2 \nu_g^t S_{gij} \quad (3.21)$$

Turbulent viscosity is

$$\nu_g^t = \frac{C_\mu k_g^2}{\varepsilon_g} \quad (3.22)$$

The particle based two-equation  $k_s - k_{gs}$  model [Peirano and Leckner (1998)] is used in order to understand the source terms which play an important role in collision dominant systems.

$$\begin{aligned} \frac{\partial}{\partial t} (\rho_s \alpha_s k_s) + \frac{\partial}{\partial x_j} (\rho_s \alpha_s k_s U_{si}) = \\ \frac{\partial}{\partial x_i} \left( D_{k_s} \frac{\partial k_s}{\partial x_i} \right) - \Sigma_{ij} \frac{\partial U_{si}}{\partial x_j} - \frac{\alpha_s \rho_s}{\tau_{gs}^x} (2k_s - k_{gs}) + \alpha_s \rho_s \frac{e^2 - 1}{3\tau_s^c} k_s \end{aligned} \quad (3.23)$$

where  $D_{k_s}$  is the diffusion coefficient. The terms on the right hand side of Eq. 3.23 are diffusion, the production term due to solid velocity gradients, the effective stress tensor  $\Sigma_{ij} = \theta_{ij} + \alpha_s \rho_s M_{sij}$ , and the solid-fluid interaction term, which can represent either production or dissipation and depends on the velocity covariance  $k_{gs}$ . The last one is the dissipation term due to particle-particle collision, where the collisional stress tensor,  $\theta_{ij}$ , is:

$$\begin{aligned} \theta_{ij} = 2\alpha_s^2 \rho_s g_0 (1+e) \Theta_s \delta_{ij} - \frac{4}{5} 2\alpha_s^2 \rho_s d_s g_0 (1+e) \sqrt{\frac{\Theta_s}{\pi}} (2S_{ij} + S_{mm} \delta_{ij}) + \\ \frac{4}{5} 2\alpha_s^2 \rho_s g_0 (1+e) (-2\nu_s^t) \end{aligned} \quad (3.24)$$

where turbulent viscosity  $\nu_s^t$  is

$$\nu_s^t = \left( \frac{2}{3} \frac{\tau_{gs}^t}{\tau_{gs}^x} k_{gs} + \Theta_s (1 + \alpha_s g_0 A) \right) / \left( \frac{2}{\tau_{gs}^x \tau_s^c} B \right) \quad (3.25)$$

The constants A and B are dependant on the restitution coefficient,  $e$ , and can be calculated as  $A = \frac{2}{5}(1+e)(3e+1)$  and  $B = \frac{1}{5}(1+e)(3-e)$ . The collisional viscosity is calculated as:

$$\nu_s^c = \frac{4}{5} 2\alpha_s^2 \rho_s g_0 (1+e) \left( \nu_s^t + d_s \sqrt{\frac{\Theta_s}{\pi}} \right) \quad (3.26)$$

where  $\Theta_s = \frac{2}{3} k_s$ .

The velocity covariance,  $k_{gs}$ , represents the correlation between the particle and gas phase fluctuations and is calculated by the following transport equation:

$$\begin{aligned} \frac{\partial}{\partial t} (\rho_s \alpha_s k_{gs}) + \frac{\partial}{\partial x_j} (\rho_s \alpha_s k_{gs} U_{si}) = \\ \frac{\partial}{\partial x_j} \left( D_{k_{gs}} \frac{\partial k_{gs}}{\partial x_j} \right) - \alpha_s \rho_s \langle u''_{gi} u'_{sj} \rangle_s \frac{\partial U_{si}}{\partial x_j} - \alpha_s \rho_s \langle u''_{gi} u'_{sj} \rangle_s \frac{\partial U_{gi}}{\partial x_j} + \Pi_{gs} - \alpha_s \rho_s \varepsilon_{gs} \end{aligned} \quad (3.27)$$

The first term on the right-hand side is the diffusion term, followed by the production terms due to fluid velocity correlation tensors and fluid and particle mean shear. The

fourth term is the phase interaction term, which is largely determined by the mass ratio between particle and gas and particle inertia. The last one is the dissipation term due to viscous and crossing trajectories effects, where

$$\varepsilon_{gs} = \frac{k_{gs}}{\tau_{gs}^t} \quad (3.28)$$

and  $D_{k_{gs}}$  is the diffusion coefficient. The phase interaction term is:

$$\Pi_{gs} = -\frac{\alpha_s \rho_s}{\tau_{gs}^x} ((1 + X_{gs}) k_{gs} - 2X_{gs} k_s - 2k_g) \quad (3.29)$$

where  $X_{gs} = \alpha_s \rho_s / \alpha_g \rho_g$  and  $k_s$  is the primary phase turbulent kinetic energy.

### 3.4 Decaying homogeneous isotropic turbulence two-equation $k_s - k_{gs}$ model

By assuming zero shear, equations Eq. 3.16, 3.19, 3.23, 3.27 can be simplified to show the decaying stationary homogeneous isotropic turbulence. Calculations are performed using the same conditions as  $\tau_{gs}^x$  from the literature [Elghobashi and Truesdell (1993)]. Relative velocity and crossing trajectory effects are neglected here. The following assumptions are applied studying particle diameter,  $X_{gs}$ , dissipation due to collision and particle relaxation time. In the future, the model can be improved by editing the effect of relative velocities and drift velocity as well. By following the assumption that relative velocity between phases can be ignored:

$$\tau_{gs}^x = \frac{d_s^2 \rho_s}{18\mu}, \quad (3.30)$$

when  $Re \ll 1$ , then the drag coefficient becomes  $C_D = \frac{24}{Re}$ . By ignoring crossing trajectory effects, further simplifications of Eq. 3.11 are made as follows:

$$\tau_{gs}^t = \tau_0 (1 + C_\beta \xi_r)^{-1/2} = \frac{C_\mu \frac{k_g}{\varepsilon_g}}{\left(1 + C_\beta \frac{3}{2} \left(\frac{U_g^2}{k_g}\right)\right)^{1/2}} \quad (3.31)$$

Similarly, Eq. 3.31 becomes

$$\tau_{gs}^t \approx C_\mu \frac{k_g}{\varepsilon_g} \quad (3.32)$$

when the collision interval  $\alpha_s \rightarrow 0$  and  $\tau_s^c \rightarrow \infty$ :

$$\tau_s^c = \frac{d_s}{24\alpha_s g_0} \left(\frac{\pi}{\Theta_s}\right)^{1/2} = C_4 \frac{d_s}{\alpha_s g_0} k_s^{-\frac{1}{2}} \quad (3.33)$$

Further assumptions and initial conditions are described in section 3.4.1. Primary phase turbulent kinetic energy for isotropic turbulence is:

$$\frac{\partial}{\partial t} k_g = \underbrace{-\varepsilon_g}_{k_{gA}} + \underbrace{\Pi_{gk_g}}_{k_{gB}} \quad (3.34)$$

Dissipation of the turbulent kinetic energy is:

$$\frac{\partial}{\partial t} \epsilon_g = -C_{\epsilon_2} \underbrace{\frac{\epsilon_g^2}{k_g}}_{\varepsilon_{gA}} + \underbrace{\Pi_{g\varepsilon_g}}_{\varepsilon_{gB}} \quad (3.35)$$

Discrete phase turbulent kinetic energy is:

$$\frac{\partial}{\partial t} k_s = -\underbrace{\frac{1}{\tau_{gs}^x} (2k_s - k_{gs})}_{k_{sA}} + \underbrace{\frac{e^2 - 1}{3\tau_s^c} k_s}_{k_{sB}} \quad (3.36)$$

Fluid-particle velocity covariance equation is defined as:

$$\frac{\partial}{\partial t} k_{gs} = -\frac{1}{\tau_{gs}^x} \left( \underbrace{(1 + X_{gs}) k_{gs}}_{k_{gsA}} - \underbrace{2X_{gs} k_s - 2k_g}_{k_{gsB}} \right) - \underbrace{\varepsilon_{gs}}_{k_{gsC}} \quad (3.37)$$

In Eqs. 3.34 – 3.35, source term B describes the interaction between gas and solid turbulent kinetic energy and the dissipation rate of turbulent kinetic energy for the primary phase. These two terms have a significant effect when the system is dense as it can be seen in Section 3.4.1.3. When  $\alpha_s \rightarrow 0$ , Eqs. 3.34 – 3.35 turn into the standard  $k-\varepsilon$  model and the system is one-way coupled. As the system is getting denser,  $\tau_s^c$  is getting smaller which means that particle collision is dominant in the system. The B term in Eq. 3.36 considers particle-particle interaction as well. In addition, when  $\alpha_s \rightarrow 0$ , the collision effect disappears and  $k_s$  and  $k_g$  are weakly coupled.  $X_{gs}$  describes the mass loading to the system when  $X_{gs}$  is getting higher or the system is getting denser. Eq. 3.37 shows that the velocity covariance term is highly dependent on mass-loading.

Each equation plays a different role in the different zones of the CFB. At the bottom of the reactor, particle-particle effect is essential, which means  $\tau_s^c \ll \tau_{gs}^x$  and therefore Eqs. 3.34 – 3.37 are strongly coupled ("four-way coupling"). In the middle part of the reactor, i.e. the transitional region, collision and gas phase turbulence have the same effect, which means the full four equations must be solved. The top of the reactor is very dilute (which means  $\tau_s^c \gg \tau_{gs}^x$ ) and particle-particle interaction is not taking part, due to which Eqs. 3.36–3.37 are negligible. The transport equation (Eq. 3.37) correlating particle and gas fluctuating velocity is very dependent on  $X_{gs}$  and on particle inertia.

### 3.4.1 Results and discussion for homogeneous isotropic turbulence

For a very dilute suspension, calculations are performed using DNS simulation [Elghobashi and Truesdell (1993)] dimensionless parameters  $U_0 = 0.0508$ ,  $\lambda_0 = 0.0348$ ,  $\varepsilon_0 = 0.00162$ ,  $\nu = 5.05 * 10^{-5}$ . To normalise these quantities, the reference length scale  $L_{ref} = 0.1859$  and time scale  $T_{ref} = 0.1068$  are used. To calculate isotropic turbulence (Eqs. 3.34 –3.37), the Runge-Kutta fourth order method is used and both phases are accepted as a continuum. In addition to different range solid volume fraction, mass loading and Stokes numbers are chosen to analyse the model thoroughly. The aim is to understand the contribution of particle-particle and particle-fluid interaction to the turbulence modification. The dilute cases used during the calculations are shown in Table 3.1 and the dense cases in Table 3.2, respectively.

Table 3.1: Dilute mass loadings and particle properties for cases A to F in isotropic turbulence.

Case	$\tau_{gs}^x$	$\rho_s/\rho_g$	$\alpha_s$	$X_{12}$
A	...	...	0.0	0.0
B	0.25	909	$2.5 \times 10^{-4}$	0.23
C	0.50	1818	$2.5 \times 10^{-4}$	0.45
D	1.00	3636	$2.5 \times 10^{-4}$	0.91
E	0.50	808	$2.5 \times 10^{-4}$	0.20
F	0.50	455	$2.5 \times 10^{-4}$	0.11

Table 3.2: Dense mass loadings and particle properties for different cases in isotropic turbulence.

Case	$St$	$\rho_s/\rho_g$	$\alpha_s$	$X_{12}$
A	...	...	0.0	0.0
G	0.10	1818	0.1	181.8
H	1.00	1818	0.1	181.8
I	1.00	1818	0.1	181.8
J	1.00	1818	0.01	18.18

#### 3.4.1.1 Effect of particle relaxation time $\tau_{gs}^x$

Fig. 3.4 compares the particle relaxation time,  $\tau_{gs}^x$  for our model and DNS data. At the beginning of the calculations particle properties do not have any effect on the turbulent kinetic energy. The model shows reaction after  $0.75T$  and the DNS data curves coincide until  $1T$  after which two-way coupling effects become noticeable. It takes a shorter amount of time to see the effect of four-way coupling by our model. The possible reason for this can be the particle-particle interaction is accounted for. Initial decay is higher in the model, because the solid volume fraction is very low. Moreover, dissipation may still exist due to particle-particle and particle-fluid interaction and errors due to approximations in the model. In the model,  $k_g$  differs significantly from DNS cases for

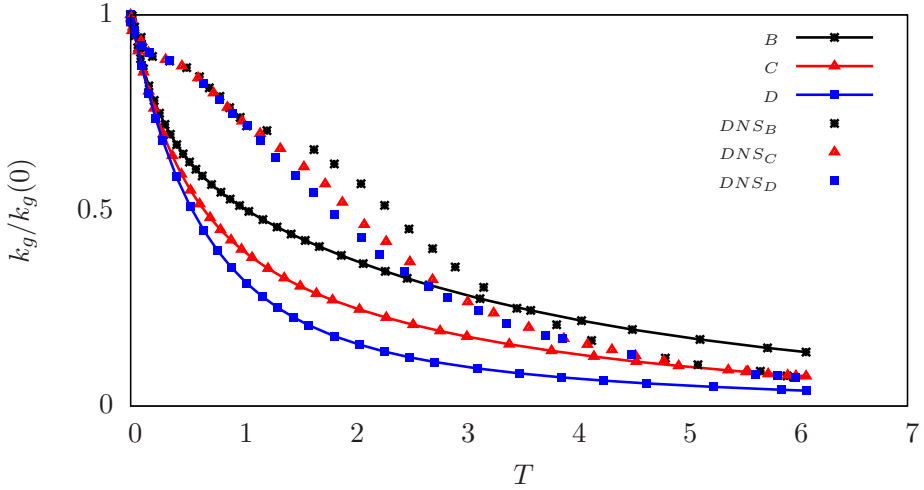


Figure 3.4: Effect of particle relaxation time,  $\tau_{gs}^x$ , on turbulent kinetic energy normalised by the initial value of  $k_g(0)$ , with respect to time and compared to DNS data [Elghobashi and Truesdell (1993)].

different particle relaxation times. It means that the model is very sensitive to  $X_{gs}$  as well. The four-way coupling model is also more suitable for denser suspensions, although it gives acceptable prediction even for dilute cases.

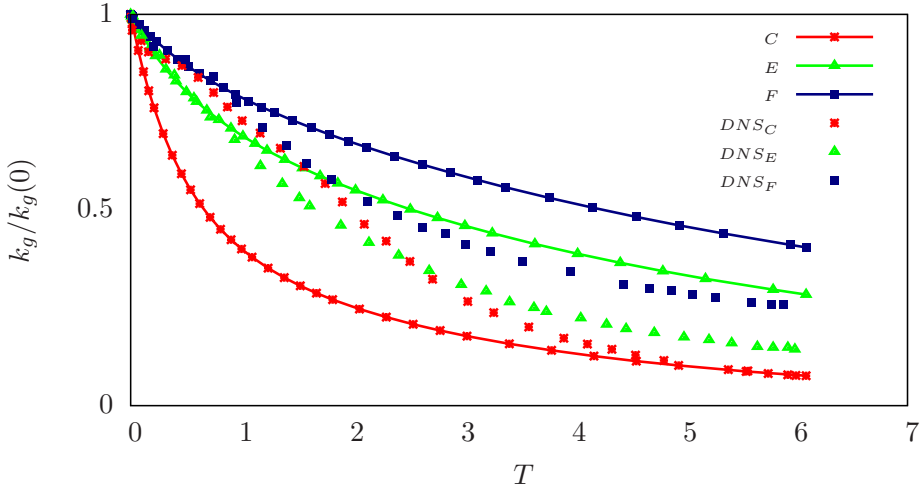


Figure 3.5: Particle diameter effect on turbulent kinetic energy with respect to time, where  $k_g$  is normalised by initial condition  $k_g(0)$ .

Fig. 3.5 shows the effect of particle diameter on turbulent kinetic energy. The model is more sensitive to particle relaxation time  $\tau_{gs}^x$ . The model and DNS data agreed that by increasing  $\tau_{gs}^x$ , the dissipation rate decreases. This is due to a lower particle relaxation time and overpredicted higher velocity covariance  $k_{gs}$  values. The model overpredicts the turbulent kinetic energy for higher particle diameters (case D). For case C, the results

agree until  $1.5T$ , after which there is a decrease in decay in comparison to DNS data. The case C gives the closest agreement with DNS, although at the beginning the decay is high in comparison to DNS data.

### 3.4.1.2 Effect of the Stokes number

Two-way coupling has so far been considered with a very low  $\alpha_s = 2.5e - 4$  (Table I). Four-way coupling is taking place in the following calculations, where the suspension is denser ( $\alpha_s = 0.1$  and  $0.01$ ) and particle-particle interaction is dominant. Moreover, three different Stokes numbers ( $St = 0.1, 1, 10$ ) are used in order to observe the effect on gas, particle turbulent kinetic energy ( $k_g, k_s$ ), dissipation rate ( $\varepsilon_g$ ), and velocity covariance ( $k_{gs}$ ) (see Table 3.2). During the calculation, time is normalised with particle relaxation time,  $\tau_{gs}^x$ , and turbulent quantities are normalised by their initial values.

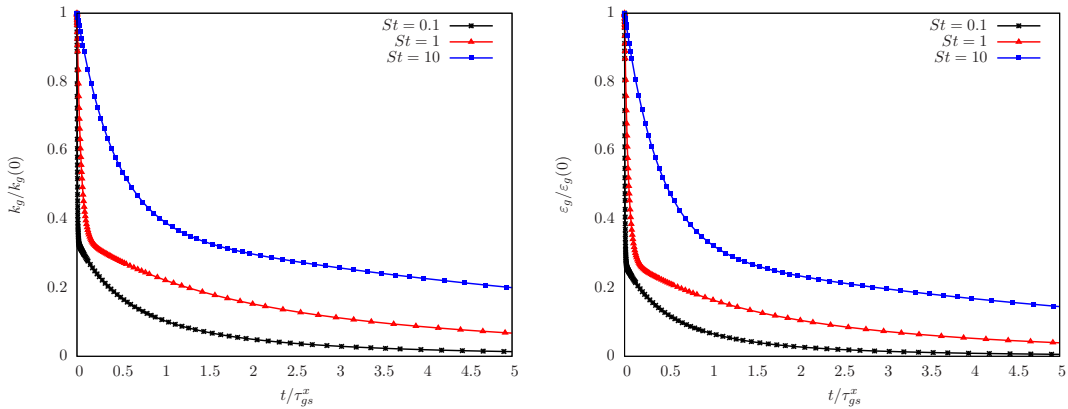


Figure 3.6: Effect of the Stokes number ( $St = \frac{\tau_{gs}^x}{\tau_\eta}$ ) on time the development of primary phase turbulent kinetic energy,  $k_g$  and dissipation rate,  $\varepsilon_g$

Fig. 3.6 shows the Stokes number effect on the primary phase turbulent kinetic energy  $k_g$  and the dissipation rate  $\varepsilon_g$ . Lower Stokes numbers lead to higher decay in turbulent kinetic energy as well as dissipation rate. Yet, for single phase flow both terms would have a significantly lower decay rate. This illustrates the B terms dominance in Eqs. 3.34 – 3.35 and their limiting effect on the primary phase viscous dissipation (see Fig. 3.9). Fig. 3.7 shows that higher Stokes numbers decrease the decay of particle turbulent kinetic energy and increase particle relaxation time,  $\tau_{gs}^x$ . Higher  $\tau_{gs}^x$  decreases the term A in Eq. 3.36 and reduces the decay. Moreover,  $\tau_{gs}^x$  decreases the proportion of term A in Eq. 3.37 and reduces the decay rate of  $k_{gs}$ .

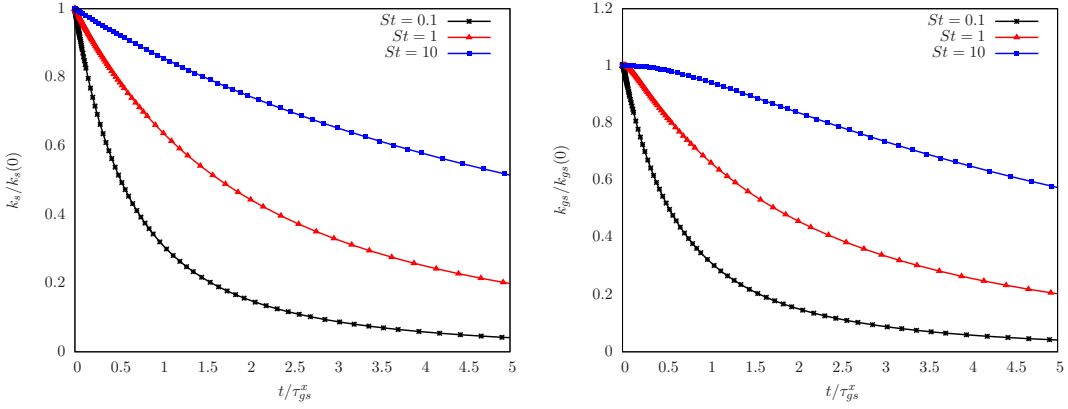


Figure 3.7: Effect of the Stokes number on time the development of secondary phase turbulent kinetic energy,  $k_s$  and fluid-particle velocity covariance,  $k_{gs}$

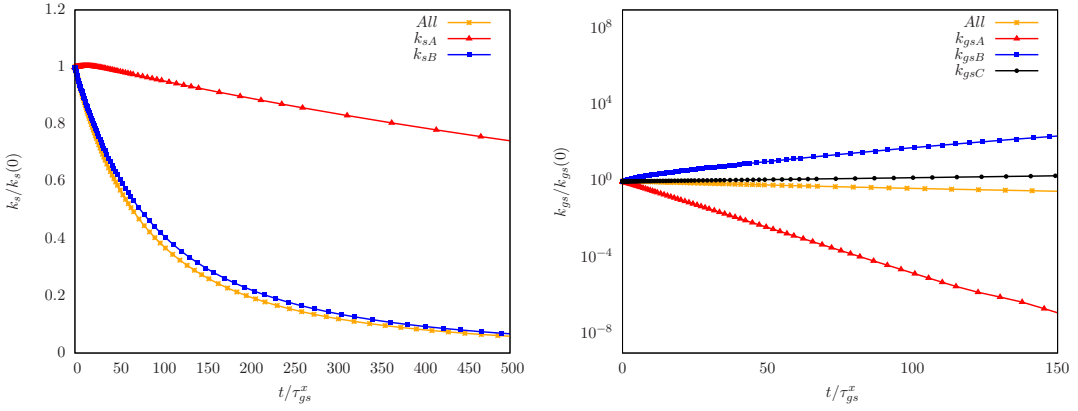


Figure 3.8: Source terms  $k_{sA}$ ,  $k_{sB}$  for  $k_s$  from Eq. 3.36 and  $k_{gsA}$ ,  $k_{gsB}$  and  $k_{gsC}$  for  $k_{gs}$  from Eq. 3.37

### 3.4.1.3 Effect of source terms

The source terms  $k_{sA}$  and  $k_{sB}$  for particle turbulent kinetic energy,  $k_s$ , and the source terms  $k_{gsA}$ ,  $k_{gsB}$  and  $k_{gsC}$  for velocity covariance,  $k_{gs}$ , are shown in Fig. 3.8. It can be seen that the collisional mechanism (term B) is dominant and is causing a significant part of the decay in Eq. 3.36. On the other hand, the fluid-particle velocity covariance  $k_{gs}$ , term A is several magnitude higher than terms B and C, which explains the higher decay rate in the higher volume fraction in Fig. 3.11. Fig. 3.9 shows the dominance of the fluid-solid interaction terms A and B on the result (All). The primary phase has a very weak effect on both  $k_g$  and  $\varepsilon_g$ . This is possibly due to the high solid volume fraction  $\alpha_s = 0.1$ , so that  $k_g$  and  $k_s$  are strongly coupled and particle-particle interaction plays an important role in the system.

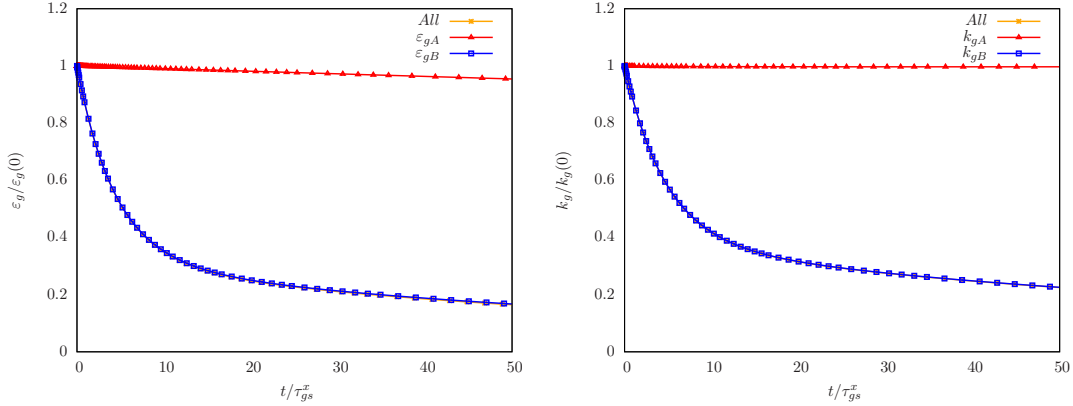


Figure 3.9: Source terms  $k_{gA}$ ,  $k_{gB}$ ,  $k_{\varepsilon A}$ ,  $k_{\varepsilon B}$  and 'All' is the actual result in Eqs. 3.34 and 3.35 for  $k_g$  and  $\varepsilon_g$ , respectively.

### 3.4.1.4 Effect of solid volume fraction

It is evidenced in Fig. 3.10 that the flow without particles ( $\alpha_s = 0$ ) has a very slow decay rate. Yet, the introduction of particles into the system leads to a faster decay of the turbulent kinetic energy due to term  $(-2k_g)$  in the particle interaction term (see Eq. 4.22). As expected, increased solid volume fraction causes higher decay rates because the term,  $X_{gs}$ , increases too. When the solid volume fraction gets higher,  $k_g$  and  $k_s$  equations become strongly coupled. This means that the collisional dissipation also has an impact on this sharp decay (for solid volume fraction  $\alpha_s = 0.1$ ). Particle

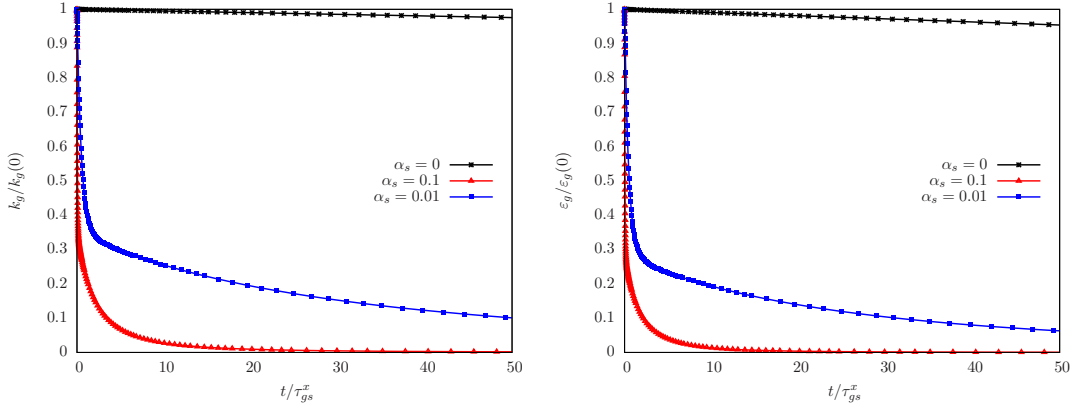


Figure 3.10: Effect of solid volume fraction,  $\alpha_s$ , in time development of primary phase turbulent kinetic energy,  $k_g$  and dissipation rate,  $\varepsilon_g$ .

turbulent kinetic energy and fluid-particle velocity covariance show different behaviour with different solid fractions, as can be seen from Fig. 3.11. The higher volume fractions lead to higher decay in  $k_g$  and  $k_{gs}$ . It is clear that higher volume fractions lead to lower particle collisional time (see Eq. 3.15). This means that collisional dissipation is increasing in higher solid volume fractions. The reason for the higher rate of decay

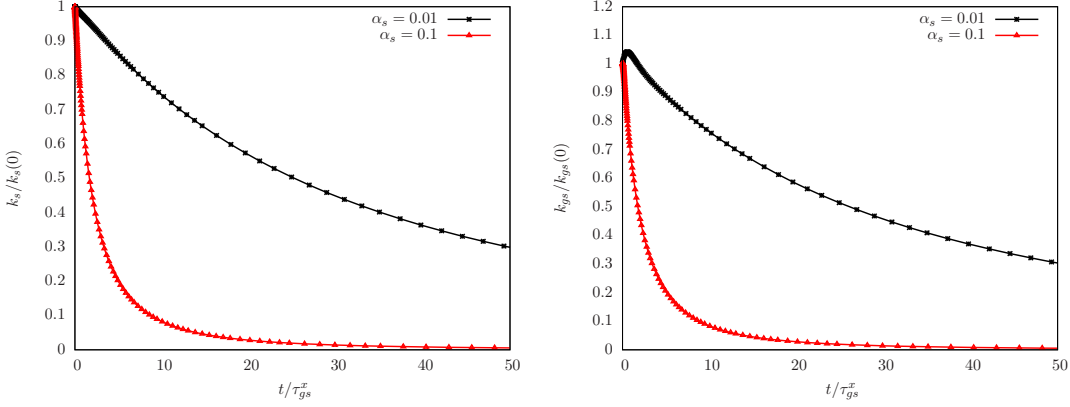


Figure 3.11: Effect of solid volume fraction  $\alpha_s$  in time development of secondary phase turbulent kinetic energy,  $k_s$  and fluid-particle velocity covariance,  $k_{gs}$ .

stems from term  $-(1 + X_{gs})$  in Eq. 3.37. It is clear that by increasing  $\alpha_s$ ,  $X_{gs}$  also increases which means a higher rate of decay of  $k_{12}$ .

#### 3.4.1.5 Effect of $X_{gs}$ term

The  $X_{gs}$  term is one of the most important parameters in gas-solid turbulence modulation. For moderately small particles, the  $X_{gs}$  term attenuates gas primary phase velocity fluctuations in the channel flow [Kulick et al. (1994)]. As can be seen from Fig. 3.10, the  $X_{gs}$  term also shows vital influence on turbulence modulation. In Fig. 3.10, case A is a single flow and the decay is very slow. Introducing particles into the system makes the decay more rapid (Case J) and increasing the  $X_{gs}$  term tenfold, makes turbulence attenuation faster (Case I).

#### 3.4.1.6 Conclusion and summary

Decaying isotropic turbulence calculations are performed. The two-equation  $k_s-k_{gs}$  model [Peirano and Leckner (1998)] is simplified by neglecting shear production terms. The equations present a four-way coupling. Primary phase turbulent kinetic energy and the turbulent dissipation rate are calculated using the dispersed  $k_g-\varepsilon_g$  model. Moreover, two additional transport equations are used to calculate turbulent kinetic energy of the particulate phase and the correlation between gas-particle velocity fluctuation. Particle turbulent kinetic energy takes into account the particle-particle interaction, although the velocity covariance transport equation does not consider the collision. In order to validate the model, DNS data is used [Elghobashi and Truesdell (1993)]. Although, at the beginning of the calculation turbulent kinetic energy shows a faster decay rate than the DNS calculation, in general, calculations showed reasonable agreement with DNS data. Moreover, in the calculations the higher volume fractions and mass loading are

found to have a significant impact on the turbulent kinetic energy and the dissipation rate. In addition, fluid-particle interaction terms in dispersed  $k_g - \varepsilon_g$  become dominant with particle existence.

### 3.4.2 Modelling of 2D backward-facing step using the two-equation $k_s - k_{gs}$ model

Moderate particle existence in turbulent flows may modify turbulence structures. They can either augment or attenuate turbulence [Hetsroni (1989); Gore and Crowe (1991)]. Thus, moderate mass loading of small and dense particles decreases the intensity of gas velocity fluctuations [Kulick et al. (1994)]. Mass loading has an influence on the particle-gas interaction terms in the model. The particle Reynolds number and Stokes number have direct correlation with turbulent modulation. Increasing the particle Reynolds number also increases the attenuation turbulence modulation of the primary phase. The Stokes number also plays an important role in the turbulence modulation. Therefore, higher Stokes numbers increase the turbulence intensity of the primary phase [Fessler and Eaton (1999)]. Particles with large Stokes numbers cannot respond to the fluid behaviour, which means that these kind of particles have a higher particle relaxation time,  $\tau_{gs}^x$ . Moreover, recent research shows that particle shape also has an effect on turbulence intensity [Zhao et al. (2015)]. However, the shape of the particles is not considered in this model. By applying LES and the Lagrangian approach, the effects of different Stokes numbers on dispersion are investigated. However, the work neglected the effect of particles on the primary phase (one-way coupling) [Yu et al. (2004)]. As a parameter, the ratio between particle diameter and the characteristic eddy length scale can be used to explain particle influence on the turbulence modulation [Gore and Crowe (1991)]. Furthermore, the Reynolds number is the key parameter to describe particle impact on turbulence structures [Hetsroni (1989)]. In a fully developed channel flow, it is reported that turbulence attenuation increases with both mass loading and the Stokes number [Kulick et al. (1994)]. However, later works contradicted this by stating that 'extra dissipation due to particles' is inversely proportional to the particle relaxation time constant [Fessler and Eaton (1995); Elghobashi and Truesdell (1993)]. Hence, the problem is not yet fully understood. For a 50% mass loading and 45  $\mu\text{m}$  glass particles, a slight modification is observed after the reattachment point and an attenuation of turbulence is found along the dividing streamline [Maeda et al. (1980, 1982)].

### 3.4.3 Geometry and boundary conditions

The following study compares dilute experimental results [Fessler and Eaton (1995, 1999); Benavides and van Wachem (2009)] and the  $k_s - k_{gs}$  model within a backward-facing step flow. Eqs. 3.16, 3.19, 3.23, 3.27 are implemented in Ansys Fluent 14.5 using UDF subroutines. The backward-facing step flow helps to understand how the  $k_s - k_{gs}$  model will suit the separation. Separation and circulation also takes place in the reactor with dimpled walls (explained in Ch. 5). The two-dimensional computational backward-facing step domain starts with 65H upstream from the step and continues up to 34H downstream as shown in Fig. 3.12. Air is used in the standard conditions for

the primary phase, while different particle properties are used for the solid phase (see Table 3.3).

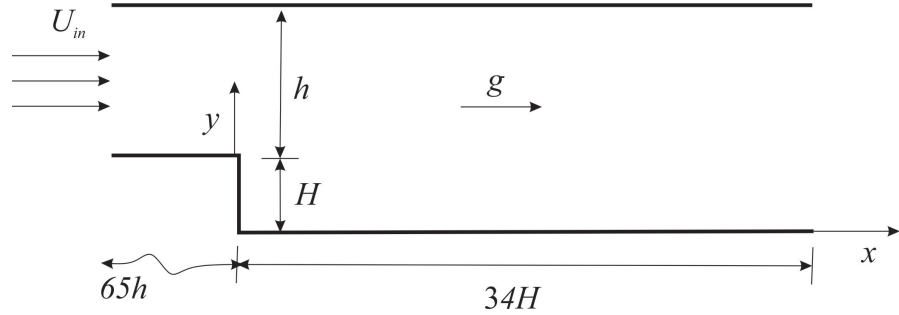


Figure 3.12: Geometry of a vertically oriented backward facing step with a width  $h=40$  mm and step height  $H=26.7$  mm.

Table 3.3: Mass loadings and particle properties in different cases.

Case	$d_s[\mu\text{m}]$	$\rho_s[\text{kg}/\text{m}^3]$	Loading	$\tau_{gs}^x[\text{ms}]$	$St$	$Re_p$
Case1	150	2500	20% and 40%	101	7.9	10.1
Case2	90	2500	20%	48	3.8	2.9
Case3	70	8800	40%	94.5	7.4	4.4
Case4	150	2500	$\alpha_s = 0.1$	101	7.9	10.1
Case5	150	2500	$\alpha_s = 0.2$	101	7.9	10.1

All equations are solved sequentially at each iteration using a two-fluid model where both phases are accepted as a continuum. The second-order central difference scheme is used and the time step is set to  $10^{-4}$  s. Calculations are run until a converged solution is obtained and a grid independence study is performed.

The inlet velocity boundary condition for the primary phase is set to 9.3 m/s in order to attain the center-line velocity  $U_{cl}$  of about 10.5 m/s at the step. By assuming the gas-to-particle-velocity ratio to be constant and using the uniform solid volume fraction  $\alpha_s$ , specific mass-loading at the inlet is obtained. A standard wall function is used for the gas phase and particle effect near the wall is neglected. For the particulate phase wall boundary condition, wall-particle interaction is considered [Johnson and Jackson (1987)]. The  $k_s$  and  $k_{gs}$  are set to zero at the wall. Derivatives of the solid volume fraction, velocity and turbulent components are set to zero at the outlet as the flow is assumed to be fully developed.

### 3.4.4 Results and discussion

The main aim is to compare the mean quantities of both the gas and the solid phase. The simulated cases from the two-fluid model using the  $k_s-k_{gs}$  model [Peirano and Leckner (1998)] are compared with the experimental data [Fessler and Eaton (1999)]. Critical positions are chosen, like recirculation ( $x/H=2$ ), reattachment ( $x/H=7$ ) and

redevelopment ( $x/H=14$ ) in order to show the velocities and turbulent intensities for both phases. The current simulations consider three different classes of particles, as can be seen from Table 3.3. Glass is used for Case 1 and Case 3, whereas mass loading and particle diameters are changing. The third case uses copper particles with a higher density. The Stokes number is calculated as follows:

$$St = \frac{\tau_{gs}^x U_{cl}}{5H} \quad (3.38)$$

#### 3.4.4.1 Solid volume fraction

Fig. 3.13 shows that the mean solid volume fraction is very low at the bottom of the downstream region. Very few particles are found in the recirculation region as well [Fessler and Eaton (1999); Benavides and van Wachem (2009)]. Previous studies [Hardalupas et al. (1992)] showed that particles can be dispersed into the recirculation zone only when their large-eddy Stokes numbers are less than one. The mean flow is expected to be affected by particle existence. However, the recirculation region has much higher pressure gradient in comparison to the fully developed channel [Fessler and Eaton (1999)]. Therefore, higher pressure may overwhelm particles in the recirculation region.

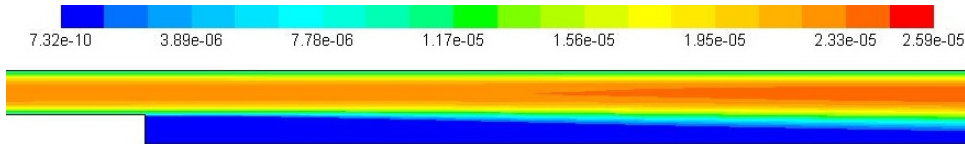


Figure 3.13: **Case 1:** mean solid volume fraction for  $k_s-k_{gs}$  model with 40% mass-loading.

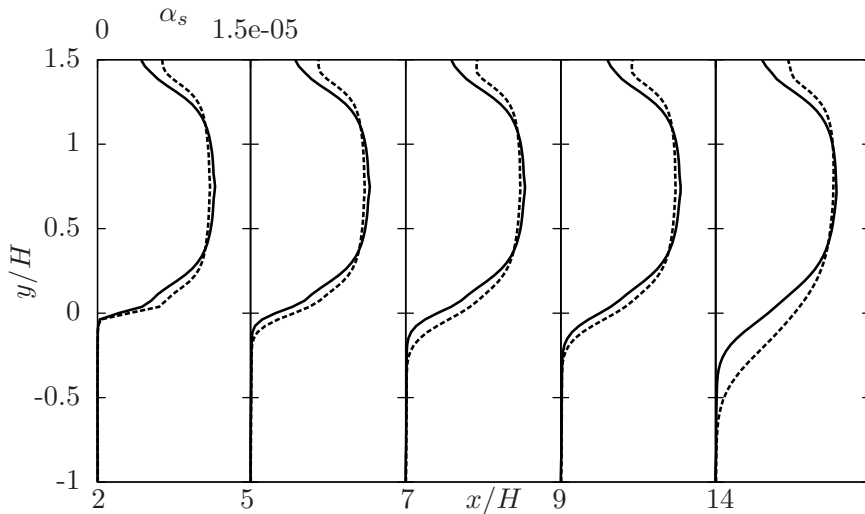


Figure 3.14: Mean solid volume fraction for the  $k_s-k_{gs}$  model with a 20% mass-loading for Case 1 (solid line) and Case 2 (dashed line).

As can be seen, at lower Stokes numbers (Case 2), particles spread more because they tend to obey the primary phase. At higher Stokes numbers (Case 1), however, particles tend to follow gravity, have higher Reynolds number and move more independently (see Fig. 3.14.).

#### 3.4.4.2 Gas velocity profiles

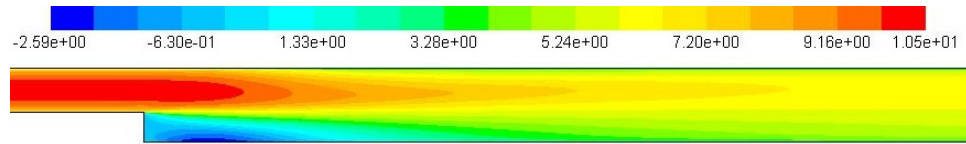


Figure 3.15: **Case 1:** streamwise mean gas velocity for the  $k_s-k_{gs}$  model with a 40% mass-loading.

Fig. 3.15 presents a 2D mean streamwise gas phase velocity profile where recirculation and reattachment are clearly visible. After circulation, the flow starts to redevelop but cannot reach the same stage as before the step point. After the step, the flow starts to circulate and develop a shear layer between the main and the circulating flow. This shear layer leads to energy loss. The mean carrier phase velocity shows almost the same behaviour as a single phase backward-facing step flow. Similar profiles were found for all types of particles. As can be seen from Fig. 3.16, the mean gas velocity profiles for Case 3 is in a fair agreement with the experimental data. It is not surprising that the  $k_s-k_{gs}$  and the standard dispersed  $k_g-\varepsilon_g$  models are giving very close predictions for the gas phase, since the system is dilute, which means that four-way coupling is weak for the the  $k_s-k_{gs}$  model.

There is no significant change in the gas velocity when doubling the solid volume fraction (Fig. 3.17). In the denser case, the velocity is slightly lower in some regions than expected.

#### 3.4.4.3 Solid velocity profiles

Fig. 3.18 shows that after the recirculation stage, the redevelopment of velocity takes a longer time. Presumably, it can be due to the gravitational force because of higher Stokes number, which also proceeds in a streamwise direction, does not allow the particles to spread too much. The same effect can be seen in the experiment as well. Also, the reason can be turbulence dispersion which is a random process. In contrast to turbulent diffusion which is depend only characteristics of turbulence, while turbulent dispersion is depend on turbulence characteristics and particle properties. The particles with smaller Stokes number will follow their aasociate fluid element but here Stokes number are large enough so that particles are not following and dispersing in the recirculation zone.

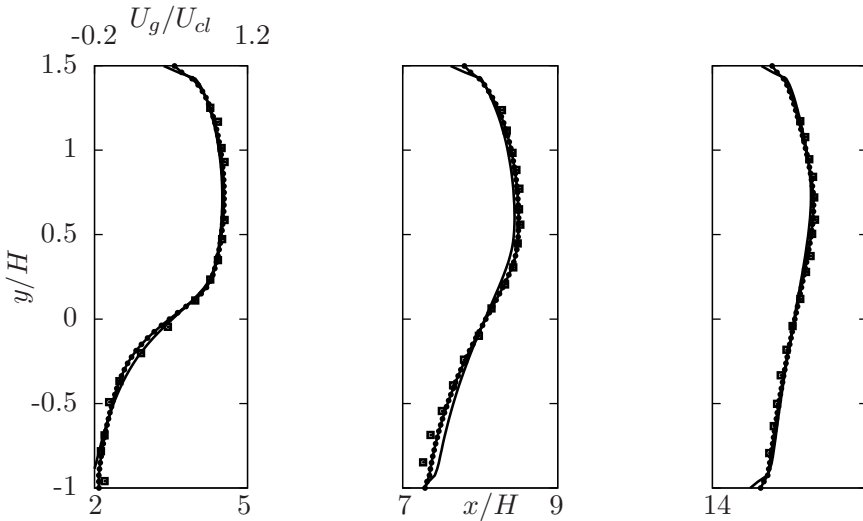


Figure 3.16: **Case 3:** streamwise mean gas velocity for the  $k_s-k_{gs}$  model (solid line), the standard dispersed  $k_g-\varepsilon_g$  model (solid line with circle markers) and experimental data (squares) for a 40% mass-loading [Fessler and Eaton (1999)].

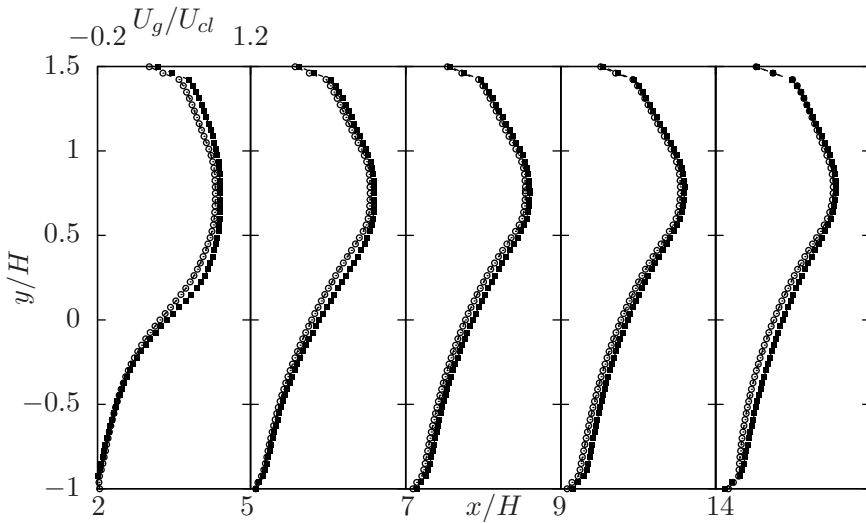


Figure 3.17: **Case 4 and 5:** for the  $k_s-k_{gs}$  model streamwise mean gas velocity profiles using  $\alpha_s = 0.1$  (dashed line with full circle markers) and  $\alpha_s = 0.2$  (dashed line with empty circle markers).

Because of that, particle existence is too low in the region after the step. All particle

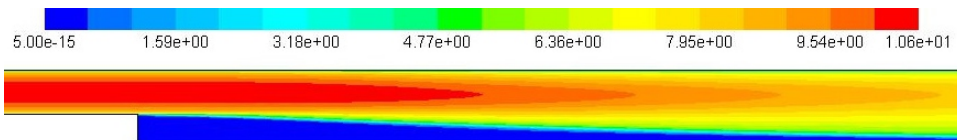


Figure 3.18: **Case 1:** streamwise particle mean velocity profile for the  $k_s-k_{gs}$  model with a 40% mass-loading.

velocities are validated by experimental data [Fessler and Eaton (1999); Benavides and van Wachem (2009)]. In Figs. 3.19 and 3.20, dispersed phase mean velocities show a fairly good agreement with experimental data. The kinetic theory of granular flow transport equation is used in the dispersed  $k_g-\varepsilon_g$  model. The model slightly disagrees with the particulate phase mean velocities in the reattachment zone. Yet, the  $k_s-k_{gs}$  model predicts it relatively well.

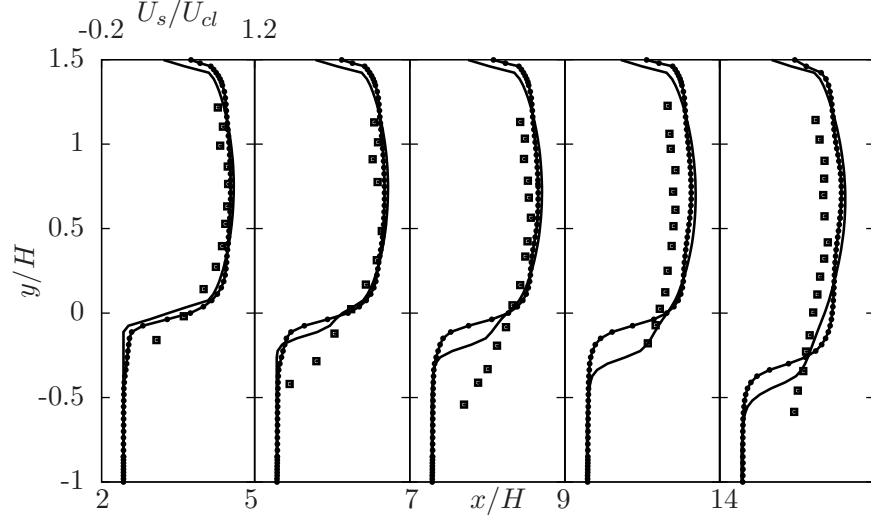


Figure 3.19: **Case 1:** streamwise mean particle velocity profiles for the  $k_s-k_{gs}$  model (solid line), the standard dispersed  $k_g-\varepsilon_g$  model (solid line with circle markers) and experimental data (squares) for a 40% mass-loading [Fessler and Eaton (1999)].

Case 1 with a higher Stokes number is presented in Fig. 3.19. The models give slightly higher values of  $U_s$  in the redevelopment region, probably due to a higher relative velocity and independent phases. Yet, it is in better agreement with experimental data in the recirculation and reattachment regions. The  $k_s-k_{gs}$  model (solid line) gives better predictions in the shear layer.

In general, the  $k_s-k_{gs}$  model could predict better the mean solid velocity, unlike the dispersed  $k_g-\varepsilon_g$  model, where KTGF and special viscosity models are used. Even better predictions could be expected for denser systems, where four-way coupling is strongly coupled. The dense cases 4 and 5 give slightly different solid velocity profiles for different mass loadings. Fig. 3.21 shows that the recirculation region does not change by varying the mass loading. In this way, particles are pushed outside of the region by circulation [Fessler and Eaton (1999)]. A slight decrease in solid velocity in the higher volume fraction may occur due to collisional dissipation (particle-particle interaction).

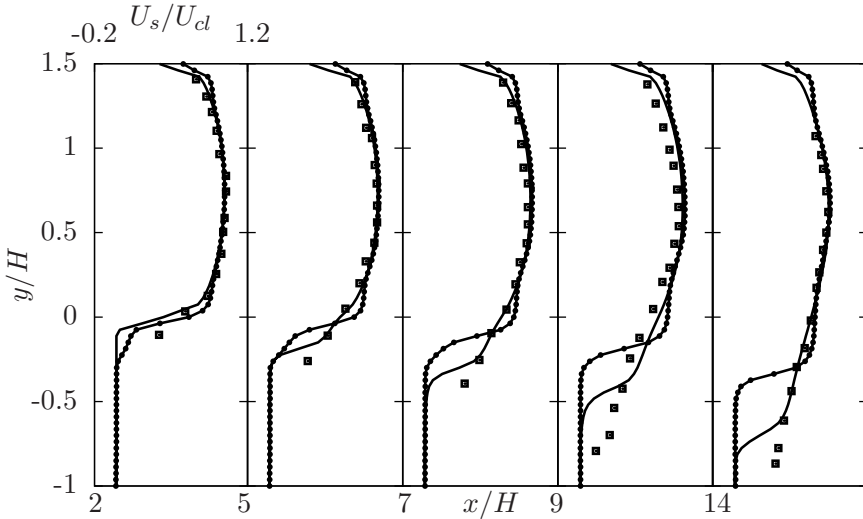


Figure 3.20: **Case 2:** streamwise particle velocity profiles for the  $k_s-k_{gs}$  model (solid line), the standard dispersed  $k_g-\varepsilon_g$  model (solid line with circle markers) and experimental data (squares) for a 20% mass-loading [Fessler and Eaton (1999)]

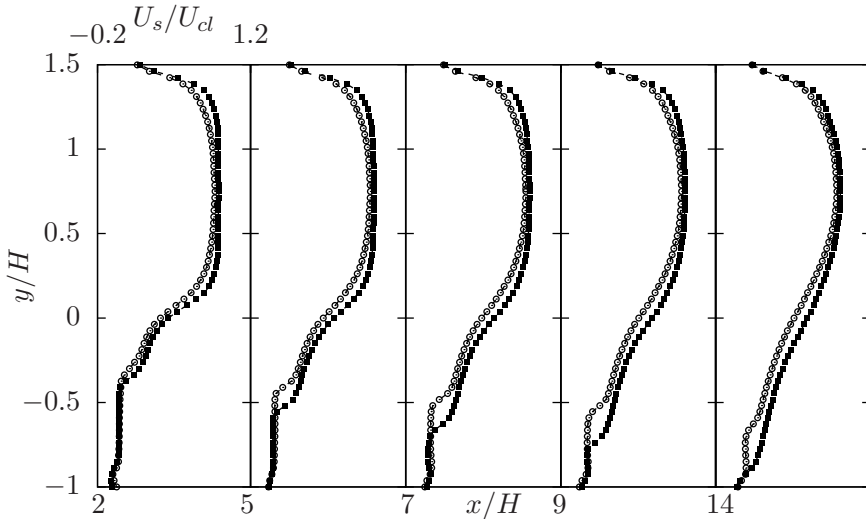


Figure 3.21: **Case 4 and 5:** for the  $k_s-k_{gs}$  model streamwise mean gas velocity profiles using  $\alpha_s = 0.1$  (dashed line with full circle markers) and  $\alpha_s = 0.2$  (dashed line with empty circle markers).

#### 3.4.4.4 Turbulent intensities

As can be seen from Fig. 3.22 and 3.23, the results are in good agreement with the experimental data for gas phase turbulence intensities for the  $k_s-k_{gs}$  and the  $k_g-\varepsilon_g$  models. It is expected that it gives good results for such a dilute case [Benavides and van Wachem (2009)]. Here,  $k_2$  and  $k_g$  are weakly coupled. The mass loading is low and the particle-particle interaction term has a weaker influence leading to less dissipation

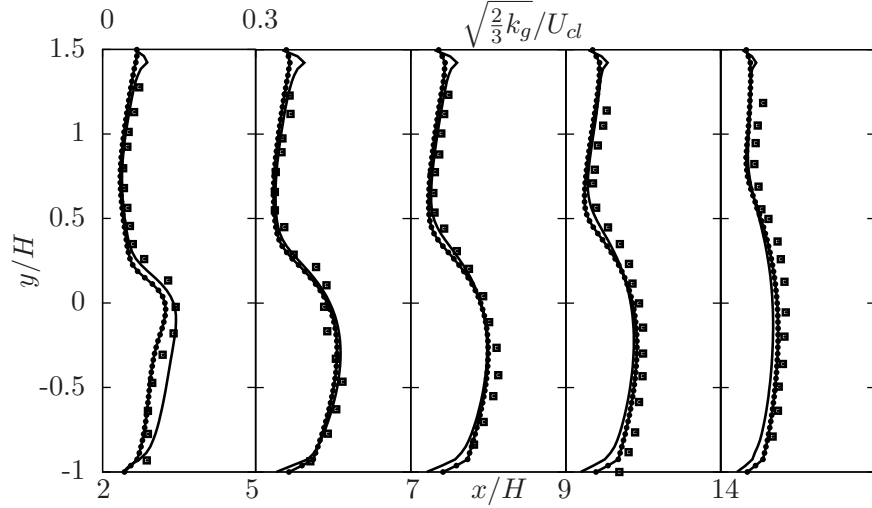


Figure 3.22: **Case 3:** turbulence intensity gas phase profiles for the  $k_s-k_{gs}$  model (solid line), the standard dispersed  $k_g-\varepsilon_g$  model (solid line with circle markers) and experimental data (squares) for a 40% mass-loading [Fessler and Eaton (1999)].

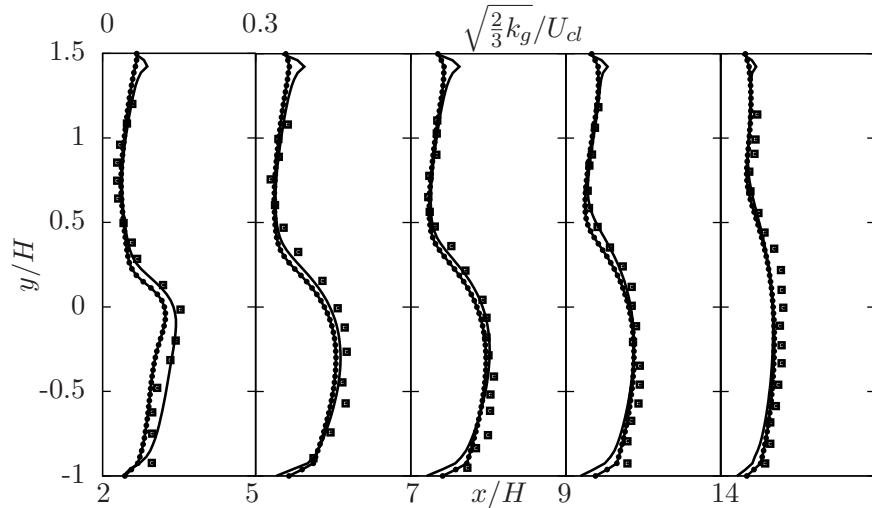


Figure 3.23: **Case 1:** Turbulence intensity gas phase profiles for the  $k_s-k_{gs}$  model (solid line), the standard dispersed  $k-\varepsilon$  model (solid line with circle markers) and experimental data (squares) for a 20% mass-loading [Fessler and Eaton (1999), Benavides and van Wachem (2009)].

of turbulent kinetic energy. Furthermore, the  $k_{gs}$  equation is derived for dilute systems because it neglects particle-particle interaction. Further improvement is needed for the velocity covariance equation in order to capture particle-particle interaction. The latter may explain the underestimation of particle phase turbulent intensities.

The results presented in Fig. 3.24 confirmed the underestimation of solid phase turbulence intensities in most of the areas, since  $k_{gs}$  is overestimated in the  $k_s-k_{gs}$  model.

Later, alternative models were developed for the particle-gas fluctuating velocity correlation [Reeks (1991); Zhang and Reese (2001); Fevrier et al. (2005); Fede et al. (2006); Ozel et al. (2013)]. Still, the  $k_s-k_{gs}$  model gives comparable results to the granular temperature model, which is widely used in gas-solid flow. In the most critical region 2, the  $k_s-k_{gs}$  model provides a better estimation than granular temperature equation. In the middle, both models give relatively similar results, but far from the step,  $k_s-k_{gs}$  model is underestimating the intensity. The probable reason for the lower turbulence intensities in region 14 is that particles start to slow down due to geometric expansion. Additionally, although this model is derived for dense systems, there is a lack of available data for such turbulence properties. Previous works [Benavides and van Wachem (2009); Peirano and Leckner (1998)] have shown that particle phase turbulence modelling still needs further improvement.

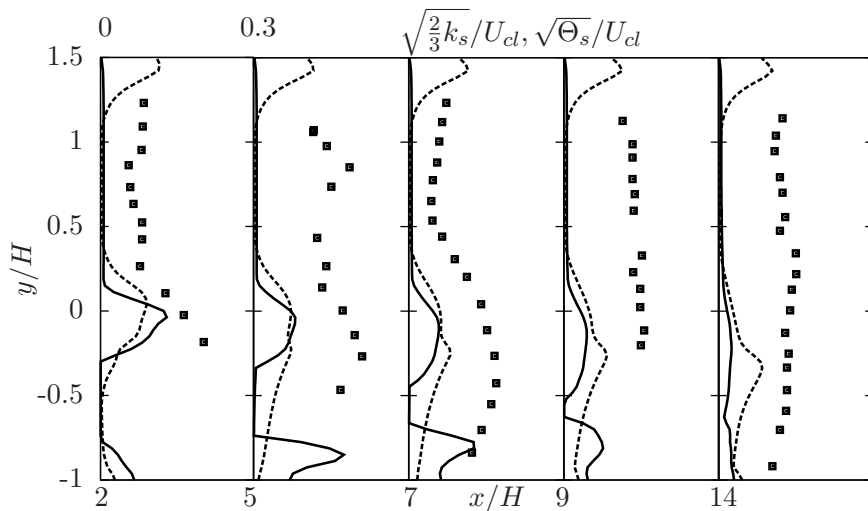


Figure 3.24: **Case 1:** turbulence intensity in particle phase profiles for the  $k_s-k_{gs}$  model (solid line), granular temperature with the standard dispersed  $k_g-\varepsilon_g$  model (dashed line) and experimental data (squares) represent the stream wise particle fluctuating velocity for a 40% mass-loading [Fessler and Eaton (1999)].

Furthermore, two dense cases Case 4 and 5 are simulated here in order to observe the performance of the model for solid volume fractions  $\alpha_s$  0.1 and 0.2 and compared it with the widely used granular temperature model  $\Theta_s$ . Fig. 3.25 and Fig. 3.26 confirm that for solid volume fraction  $\alpha_s = 0.1$  both models give similar predictions for particle turbulent intensities.

The  $k_s-k_{gs}$  model gives approximately twice the intensity in the recirculation region where the main flow and the recirculating flow create a shear layer. In the near-wall region, both models give similar results in the recirculation zone where the solid fraction is almost zero. In the further regions however, the  $k_s-k_{gs}$  model gives higher intensities

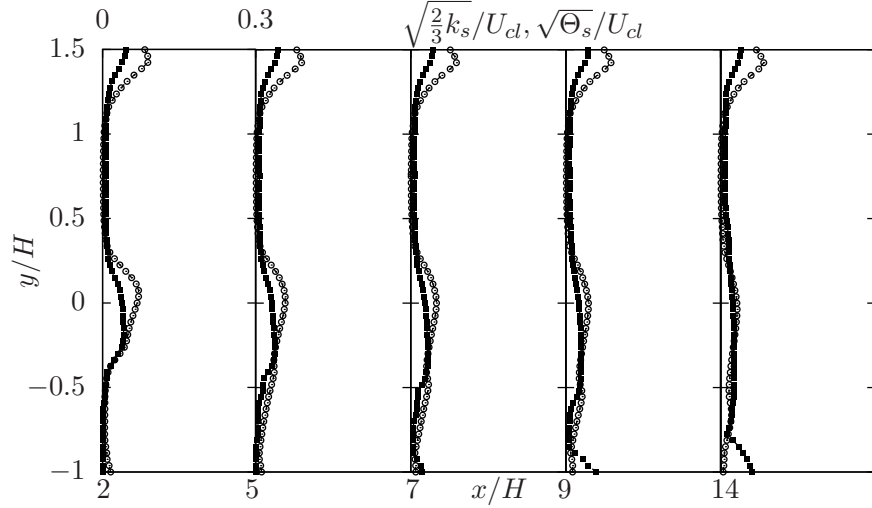


Figure 3.25: **Case 4:** turbulence intensity in particle phase profiles for the  $k_s - k_{gs}$  model (solid line with square markers) and granular temperature with the standard dispersed  $k_g - \varepsilon_g$  model (solid line with circle markers).

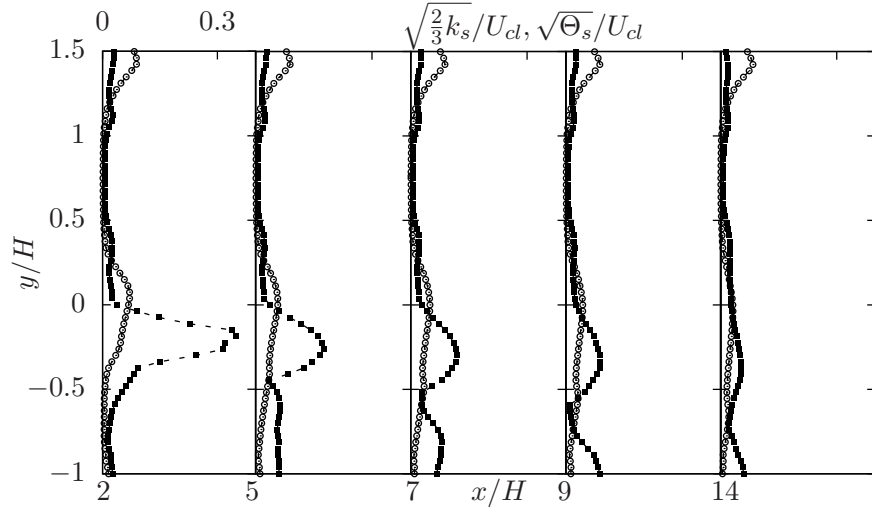


Figure 3.26: **Case 5:** turbulence intensity in particle phase profiles for the  $k_s - k_{gs}$  model (dashed line with square markers) and granular temperature with the standard dispersed  $k_g - \varepsilon_g$  model (solid line with circle markers).

near the bottom wall, where solid volume fraction starts to increase after the reattachment zone. As expected, the particle turbulent intensities gradually decrease after the recirculation zone.

#### 3.4.4.5 Conclusion and summary

The four-way coupled  $k_s - k_{gs}$  model is applied to a vertically oriented backward-facing step in the Eulerian framework. Four transport equations are applied to ANSYS Fluent

14.5 by using the UDF utility. In addition to the dispersed  $k_g-\varepsilon_g$  model, two additional transport equations are included [[Peirano and Leckner \(1998\)](#)]. The first equation is the particle turbulent kinetic energy,  $k_s$ , which takes into account particle-particle interaction and the second one is the transport equation for particle-gas velocity covariance equation,  $k_{gs}$ , which ignores particle-particle interaction.

The calculated results are compared with the experimental data [[Fessler and Eaton \(1999\)](#)]. The model gives fairly good predictions, but it underestimates particle turbulent intensity, probably because the model is designed for much denser systems. The calculation also shows that in the recirculation region the particle volume fraction is very low, which is the case in the experiment as well. Actually, the particles are not able to affect turbulence modulation after the recirculating point. Turbulence modifies mostly by lasting effect from the free shear layer, which is formed in the separation zone [[Fessler and Eaton \(1999\)](#)]. Overall, the  $k_s-k_{gs}$  model provides satisfying results, although further investigations and improvements are needed. For instance, particle-gas velocity covariance,  $k_{gs}$ , is also affected by particle-particle interaction, but is neglected here. Furthermore, experiments with denser systems need to be conducted in order to achieve a clearer understanding of particle-particle interaction. Also, the near wall treatment is needed in order to describe efficiently wall effect on the turbulent gas-solid flow. Currently, wall and damping functions are used in order to describe the wall effect in the gas-solid flow. These wall and damping functions are only based on gas phase properties, therefore, this is questionable and needs further investigations [[Peirano and Leckner \(1998\)](#)]. In the next chapter, an elliptic equation is introduced for the first time in gas-solid flows.

# Chapter 4

## Dispersed $v^2 - f$ model

### 4.1 Introduction

The models previously described require a wall function to capture the near wall effect on turbulence. As the pressure field is elliptic in nature, single point closure models are not able to describe it. Another problem is that when sudden changes or higher gradients occur, far away they are neglected. For instance, sudden changes occur very often in CFB reactors like the near-wall closing effect. The dispersed  $v^2 - f$  model includes the particle effect and four-way coupling (particle-particle interaction) in the near wall region. Additionally, the elliptic transport equation is used instead of wall and damping functions to describe the near-wall effect of turbulence. In addition, dimpled structured walls lead to circulation near the wall. Circulation can be captured with the  $v^2 - f$  model much better than with the  $k_g - \varepsilon_g$  model [Sveningsson and Davidsson (2005)] which facilitates improved efficiency of the predictions.

### 4.2 Model description

All  $v^2 - f$  models [Durbin (1991, 1993)] are based on the standard  $k - \varepsilon$  model. In the standard  $k - \varepsilon$  model, a logarithmic wall or damping functions are used for low Reynolds numbers to capture near wall physics. As opposed to the two equation models, the  $v^2 - f$  model solves an additional transport equation  $v^2$ , which provides an additional velocity scale. The latter one is used as a turbulent velocity scale  $V = (v^2)^{\frac{1}{2}}$  instead of the usual  $k^{\frac{1}{2}}$ . The  $v^2$  is a scalar, which represents the fluctuating energy normal to the streamlines. The  $v^2 - f$  model requires two additional transport equations which increase the computational expenses by 30% in comparison to the classical  $k - \varepsilon$  models. Nine partial differential equations must be solved instead of seven, even though it is still cheaper than second order moment closures (they require twelve PDEs).

After examining the mean flow momentum equation, it can be seen that only the Reynolds stress component, affected by the mean flow, is the shear stress  $\overline{u_i u_j}$ . Therefore, for the mean flow, a good model for predicting the stress component is required. From the  $v^2$  transport equation, the production term,  $P_{u_i u_j}$ , can be calculated as

$$P_{u_i u_j} = -\overline{v^2} \frac{\partial U_{gi}}{\partial x_j} \quad (4.1)$$

For eddy viscosity modelling, it can be assumed that the shear stress divided by the turbulent time scale,  $T$ , is proportional to  $P_{u_i u_j}$  in:

$$\frac{\overline{u_i u_j}}{T} \sim P_{u_i u_j} \quad (4.2)$$

Hence,

$$\overline{u_i u_j} \sim T P_{u_i u_j} = -\overline{v^2} T \frac{\partial U_{gi}}{\partial x_j} \quad (4.3)$$

where

$$T = \frac{L}{k_g^{1/2}} \quad (4.4)$$

and the turbulent length scale for standard  $k - \varepsilon$  model is

$$L = \frac{k_g^{3/2}}{\varepsilon} \quad (4.5)$$

By using classical eddy viscosity approach, the stress components can be calculated by

$$-\overline{u_i u_j} = C_\mu V^2 T \frac{\partial U_{gi}}{\partial x_j} \quad (4.6)$$

which is similar to Eq.4.3 when the proportionality coefficient ( $C_\mu$ ) and velocity scale are chosen to be  $(v^2)^{\frac{1}{2}}$ . The importance of the fluctuating velocity components was shown in a eddy-viscosity based Reynolds stress generation mechanism [Phillips (1969)]. He performed an analytical analysis of homogeneous shear flow and found that Reynolds stresses as well as eddy viscosity are not local but can be considered as a local property. Furthermore, the eddy viscosity is proportional to the kinetic energy of vertical fluctuations and convected by their time scale.

It is well known that the standard estimation of the velocity scale is done by the turbulent kinetic energy,  $(k)^{\frac{1}{2}}$ . In the vicinity of the solid walls ( $k \sim y^2$  and  $\overline{v^2} \sim k^4$ ), velocity scale  $v^2$  damping is much stronger than the damping of turbulent kinetic energy,  $k$ , because of the kinematic blocking of the wall. In order to deal with this physical phenomenon near the wall, velocity scales with  $(k)^{\frac{1}{2}}$  require an additional model. The model is used for describing the dependence of  $\overline{u_i u_j}$  on the distance to the wall during near wall damping. In standard  $k_g - \varepsilon_g$  models, a wall damping function is used for low Reynolds number in order to deal with the near-wall damping effect. The damping function is the ratio between  $C_\mu$  and  $\nu_t$ . Durbin [Durbin (1991)] showed that standard  $k_g - \varepsilon_g$  models are

not able to reproduce the correct eddy viscosity because  $y$  dependence of  $\frac{k_g^2}{\varepsilon_g}$  is simply not correct.

The reasons described in short above led to the derivation of the  $v^2$  model [Durbin (1991, 1993)]. The new transport equation introduces the imaginary stress component  $v^2$ , which is always normal to the closest wall, so the case can be applied to more complex geometries than channel flow. The whole idea of  $v^2$  equations is to apply the dependence of kinematic wall damping to the nearest wall. The normal wall component can be modelled by using the exact Reynolds transport equation:

$$\frac{\partial \bar{v}^2}{\partial t} + U_{gi} \frac{\partial \bar{v}^2}{\partial x_j} = \underbrace{-\frac{2}{\rho} \bar{p} \frac{\partial u_j}{\partial x_j}}_{\phi_{22}} - \underbrace{2\bar{u}_j u_j \frac{\partial U_{gj}}{\partial x_j}}_{P_{22}} - \underbrace{2\nu \frac{\partial u_j}{\partial x_j} \frac{\partial u_j}{\partial x_j}}_{\varepsilon_{22}} + \underbrace{\frac{\partial}{\partial x_j} \left[ -2\frac{2}{\rho} \bar{p} \bar{u}_j \delta_{ij} - \bar{v}^2 u_j + \nu \frac{\partial \bar{v}^2}{\partial x_j} \right]}_{D_{22}} \quad (4.7)$$

where  $\phi_{22}$  is the pressure strain,  $P_{22}$  is the production,  $\varepsilon_{22}$  is the dissipation term and  $D_{22}$  is the divergence term. The above equation must be simplified independent from the coordinate system. The mean kinetic energy transforms to turbulent kinetic energy via the shear stress component,  $u_i u_j$ , affecting the mean flow gradient  $\frac{\partial U_{gj}}{\partial x_j}$ . It is well known that turbulence is a three dimensional problem. Therefore, all produced turbulent kinetic energy is included in streamwise Reynolds stress components. The other two Reynolds stress components must obtain energy from the streamwise component. This kind of redistribution of the turbulent energy is generally due to the pressure strain term. Thus, in the turbulent boundary layer, wall normal components are not able to produce any turbulent energy. They will receive the turbulent energy from the pressure strain term, which is only modelled below.

Divergence term is modelled by using classical eddy diffusivity approximation

$$\frac{\partial}{\partial x_j} \left[ -2\frac{2}{\rho} \bar{p} \bar{u}_j \delta_{ij} - \bar{v}^2 u_j \right] \approx \frac{\partial}{\partial x_j} \left[ \frac{\nu_t}{\sigma_k} \frac{\partial \bar{v}^2}{\partial x_j} \right] \quad (4.8)$$

After that the pressure strain and dissipation terms are included in the  $v^2$  equation source term:

$$k f = \phi_{22} - \varepsilon_{22} + \frac{\bar{v}^2}{k} \varepsilon, \quad (4.9)$$

where the last term cancels out the sink term in the  $v^2$  equation.

For a multiphase flow the  $v^2$  equation [Durbin (1991, 1993)] can be written as follows:

$$\frac{\partial (\rho_g \alpha_g \bar{v}^2)}{\partial t} + \frac{\partial (\rho_g \alpha_g \bar{v}^2 U_{gi})}{\partial x_j} = \frac{\partial}{\partial x_j} \left( \left( \nu + \frac{\nu_t}{\sigma_k} \right) \frac{\partial \bar{v}^2}{\partial x_j} \right) + \rho_g \alpha_g k f - \frac{\rho_g \alpha_g \bar{v}^2}{k} \varepsilon \quad (4.10)$$

Eq. 4.9 describes wall normal Reynolds stress components but it still needs an additional flow variable to obtain the near wall properties. The elliptic Helmholtz modified equations  $f$  is derived as follows

$$\rho_g \alpha_g L_j \frac{\partial^2 f}{\partial f^2} + \rho_g \alpha_g f = \underbrace{\rho_g \alpha_g \frac{C_1}{T} \left( \frac{\bar{v^2}}{k_g} - \rho_g \alpha_g \frac{2}{3} \right)}_{\phi_{22,S}} - \underbrace{\rho_g \alpha_g C_2 \frac{P_k}{k_g}}_{\phi_{22,R}} - \rho_g \alpha_g \frac{1}{T} \left( \frac{\bar{v^2}}{k_g} - \frac{2}{3} \right) \quad (4.11)$$

The  $kf$  term describes the pressure strain effect,  $\phi_{22}$ , and the  $f$  term can be presented in the  $v^2$  equation as  $\frac{\phi_{22}}{k}$ . The terms  $\phi_{22,S}$  and  $\phi_{22,R}$  represent slow and rapid pressure strain terms, respectively. The last term on the right hand side describes the correct farfield behaviour.

The modelling of pressure strain with  $kf$  in the  $v^2$  equation takes into account nonlocal kinematic blocking of the normal stress component at the nearest wall. It is a vital feature for wall bounded turbulent flows as single point closure models generally are not able to capture it without wall functions. Moreover, pressure has an elliptic nature in the fluid flow as well as in pressure fluctuations and the velocity fluctuation gradient correlation [Manceau et al. (2001)].

The turbulent kinetic energy is calculated with the following equation for dispersed phase:

$$\begin{aligned} \frac{\partial}{\partial t} (\rho_g \alpha_g k_g) + \frac{\partial}{\partial t} (\rho_g \alpha_g k_g U_{gi}) &= \frac{\partial}{\partial x_i} \left( D_{k_g} \frac{\partial k_g}{\partial x_j} \right) - \\ &\quad - \alpha_g \rho_g \langle u'_{gi} u'_{gj} \rangle_s \frac{\partial U_{gi}}{\partial x_j} + \alpha_g \rho_g \Pi_{gk_{v2g}} - \alpha_g \rho_g \varepsilon_g \end{aligned} \quad (4.12)$$

The dissipation rate is calculated by the following equation

$$\begin{aligned} \frac{\partial}{\partial t} (\rho_g \alpha_g \varepsilon_g) + \frac{\partial}{\partial t} (\rho_g \alpha_g \varepsilon_g U_{gi}) &= \frac{\partial}{\partial x_i} \left( D_{\varepsilon_g} \frac{\partial \varepsilon_g}{\partial x_i} \right) - \\ &\quad - \alpha_g \rho_g \frac{\varepsilon_g}{k_g} \left( C_{\varepsilon_g} M_{gij} \frac{\partial U_{gi}}{\partial x_j} + C_{\varepsilon_g} \varepsilon_g \right) + \alpha_g \rho_g \Pi_{g\varepsilon_{v2g}} \end{aligned} \quad (4.13)$$

Eddy viscosity is

$$\nu_t = C_\mu \bar{v^2} T \quad (4.14)$$

The turbulent time scale,  $T$ , is obtained as

$$T = \max \left( \frac{k_g}{\varepsilon_g}, 6 \sqrt{\frac{\nu}{\varepsilon_g}} \right) \quad (4.15)$$

and the turbulent length scale as

$$L = C_L \max \left( \frac{k_g^{\frac{3}{2}}}{\varepsilon_g}, C_\nu \frac{\nu^{\frac{3}{4}}}{\varepsilon_g^{\frac{1}{4}}} \right) \quad (4.16)$$

The limits are used to avoid singularity effects in the governing equations near the wall.  $C_\mu$  is modelled as follows

$$C_\mu = 1.4 \left( 1 + C_{\mu d} \sqrt{\frac{\bar{v}^2}{k}} \right) \quad (4.17)$$

The wall boundary conditions for the dispersed  $v^2 - f$  model are  $U_g = k_g = v^2 = 0$  and for  $\varepsilon_g$  as  $y$  approaches zero  $\frac{\varepsilon_g}{\nu}$  becomes  $\frac{2k}{y^2}$ , where  $y$  is the normal distance to the nearest wall. The boundary conditions for  $f$  and  $\varepsilon_g$  can be written as

$$\varepsilon_g = 2\nu \left( \frac{k}{y^2} \right) \quad (4.18)$$

$$f = \frac{-20\bar{v}^2}{\varepsilon_g} \left( \frac{\bar{v}^2}{y^4} \right) \quad (4.19)$$

Finally, the constants of the model are  $C_\mu = 0.22$ ,  $C_{\varepsilon d} = 0.045$ ,  $C_{\varepsilon 2} = 1.9$ ,  $C_1 = 1.4$ ,  $C_2 = 0.3$ ,  $C_L = 0.25$ ,  $C_\eta = 85$ ,  $\sigma_k = 1.0$  and  $\sigma_\varepsilon = 1.3$ .

In order to avoid complexity and solving the whole transport equation, the gas-solid velocity covariance term,  $k_{gs_{v2}}$ , is modelled using mass loading,  $X_{gs}$ . The particle-fluid velocity covariance term is calculated using particle turbulent kinetic energy instead of granular temperature:

$$k_{gs_{v2}} = \frac{\eta}{1 + \eta(1 + X_{gs})} (2kgs + 2X_{gs}k_s) \quad (4.20)$$

where particle turbulent kinetic energy,  $k_s$ , is calculated as in Eq. 3.23 and the mass loading as  $X_{gs} = \alpha_s \rho_s / \alpha_g \rho_g$ . And  $\eta$  is

$$\eta = \frac{\tau_{gs}^t}{\tau_{gs}^x} \quad (4.21)$$

where  $\tau_{gs}^t$  is calculated in Eq. 3.11 and  $\tau_{gs}^x$  is calculated in Eq. 3.12.

The fluid-particle interaction term for  $k_g$  becomes as following

$$\Pi_{gk_g v^2} = \frac{X_{gs}}{\tau_{gs}^x} (-2k_g + k_{gs_{v2}} + U_{ri} U_{di}) \quad (4.22)$$

where the last term in the parenthesis is the drift velocity,  $U_{di}$  (Eq. 3.18).

Fluid-particle interaction term for dissipation rate is

$$\Pi_{g\varepsilon_g} = C_{\varepsilon_3} \frac{\varepsilon_g}{k_g} \Pi_{gk_g v2}. \quad (4.23)$$

Importantly, when  $\eta$  is much bigger than 1, particle motion is dictated by gas phase turbulence. Whereas when  $\eta$  is much smaller than 1, particle motion is slightly affected by gas phase turbulence.

## 4.3 Results and discussion

For the first time, the dispersed  $v^2 - f$  model is presented here for multiphase flows and preliminary results are shown in the following sections.

### 4.3.1 Geometry and boundary conditions

Experimental results [Fessler and Eaton (1995, 1999)] from the literature are used to validate the model. Cases 1 and 2 shown in table 3.3 are applied in the simulation, as well as the same geometry (see Fig. 3.12). The second order difference scheme is used for all values and a time step of  $10^{-4}$  is chosen. Simulations are performed until convergence is reached and a grid independence study is performed.

The inlet velocity boundary condition for the primary phase is set at 9.3 m/s in order to obtain a centre-line velocity  $U_{cl}$  of about 10.5 m/s at the step. By assuming gas-to-particle-velocity ratio to be constant and using a uniform solid volume fraction,  $\alpha_s$ , a specific mass-loading at the inlet is obtained. A standard wall function is used for the gas phase and particle effect near the wall is neglected. For the particulate phase wall boundary condition, wall-particle interaction is considered [Johnson and Jackson (1987)]. The normal gradient of  $k_g$  and  $v^2$  is set to zero at the wall and for  $\varepsilon_g$  and  $f$ , boundary conditions Eq. refepsv2 and Eq. 4.19 are applied at the wall, respectively. Derivatives of the solid volume fraction, velocity and turbulent components are set to zero at the outlet as the flow is assumed to be fully-developed.

### 4.3.2 Solid volume fraction

In the recirculation zone, similarly to the  $k_{gs} - k_s$  model, particle concentration is very low (see Fig. 4.1-4.2). It can be concluded that particles can be dispersed only to the recirculation region until their large eddy Stokes number is smaller than one [Fessler and Eaton (1999)]. The particles are accelerating due to gravity and tend to stay in the main flow region.

As it is a vertically oriented backward-facing step, gravity has a vital impact on the system. When the geometry is expanded, gas velocity slows down faster than the particles.

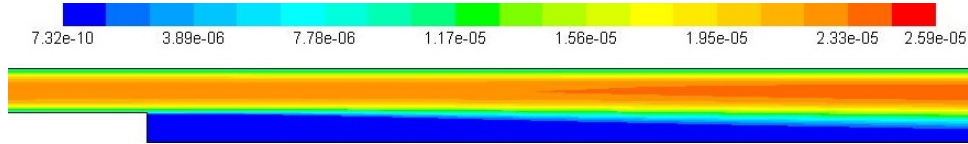


Figure 4.1: **Case 1:** mean solid volume fraction for the dispersed  $v^2 - f$  model with a 40% mass-loading.

This can be explained with the gravitational acceleration effect, which does not allow particles to go out from the mean flow (see Fig. 4.1-4.2). Thus, the particle volume fraction is very low in the recirculation zone as it can be seen in Figs. 4.1 and 4.2. Particles cannot be simply dispersed into the recirculation zone because their large-eddy Stokes numbers are not less than one. The dispersed  $v^2 - f$  model gives similar results to classical models pertaining to solid volume fraction.

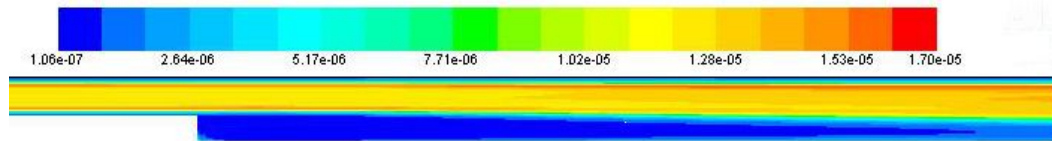


Figure 4.2: **Case 1:** mean solid volume fraction dispersed  $v^2 - f$  model with a 20% mass-loading.

### 4.3.3 Profiles of solid velocities

As can be seen from Fig. 4.3, the dispersed  $v^2 - f$  model is in good agreement with the experimental data. Discrepancies can be observed only at the bottom part after the step. These are due to the very low solid volume fractions (see Fig. 4.1) which are neglected because of machine precision. For smaller Stokes numbers, the results coincide with the

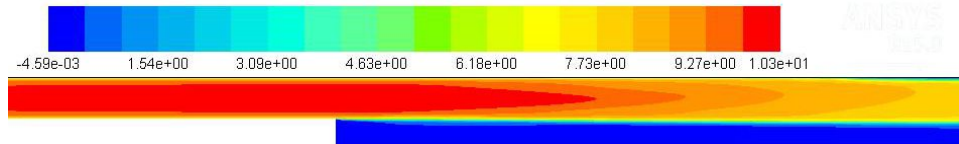


Figure 4.3: **Case 1:** streamwise mean particle velocity contours with a 20% high mass loading.

experimental data (Fig. 4.4). In the developed region, both the dispersed  $v^2 - f$  and the standard dispersed  $k_g - \varepsilon_g$  model give reasonable predictions. However, in the shear layer, the standard dispersed  $k_g - \varepsilon_g$  model has a slightly better degree of accuracy.

Fig. 4.5 shows the mean solid velocity profiles for both models with the experimental data. Indeed, in the lower part after the step, the velocity of the particles is very slow

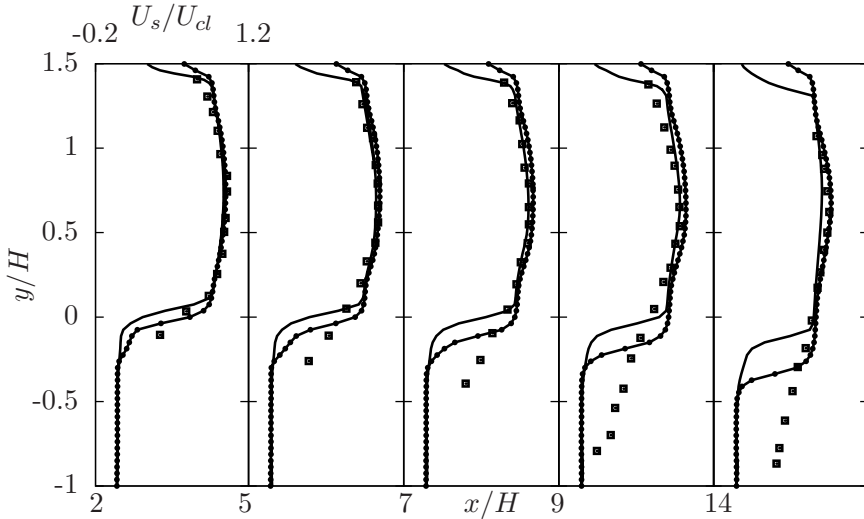


Figure 4.4: **Case 2:** streamwise particle velocity profiles for the dispersed  $v^2 - f$  model (solid line), the standard dispersed  $k - \varepsilon$  model (solid line with square markers) and experimental data (squares) for a 20% mass-loading [Fessler and Eaton (1999)].

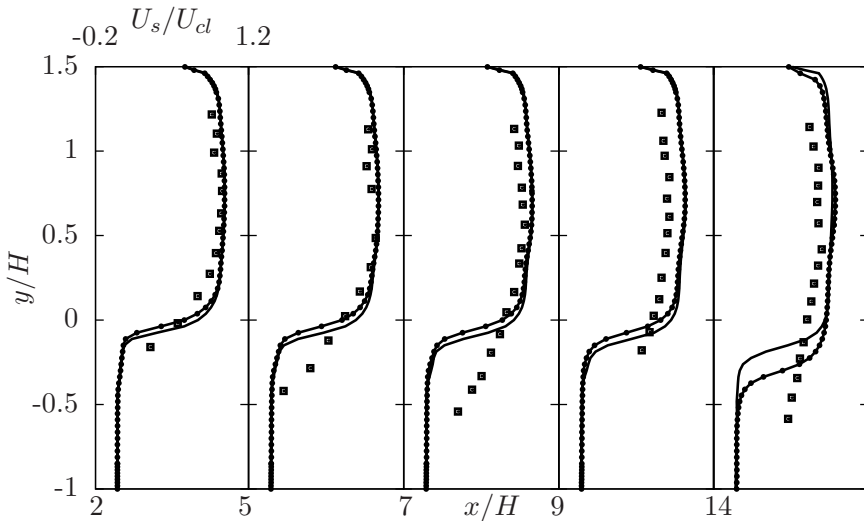


Figure 4.5: **Case 1:** streamwise particle mean velocity profiles for the dispersed  $v^2 - f$  model (solid line), the standard dispersed  $k_g - \varepsilon_g$  model (solid line with square markers) and experimental data (squares) with a 40% mass-loading.

or nearly zero due to the lack of particles in this region. Particle velocities are at a maximum before entering the expanded zone. After the step, particle velocities start to decelerate as expected.

#### 4.3.4 Profiles of gas velocities

The mean gas velocity profile, as shown in Fig. 4.6, presents a classical backward facing step behaviour. There is a recirculation zone after the step and the reattachment can be clearly seen as well. Gas phase velocity reaches its highest value before entering the expanded zone and then deceleration begins. The recirculation starts where the shear layer is produced, due to the interaction between the recirculating and main flows.

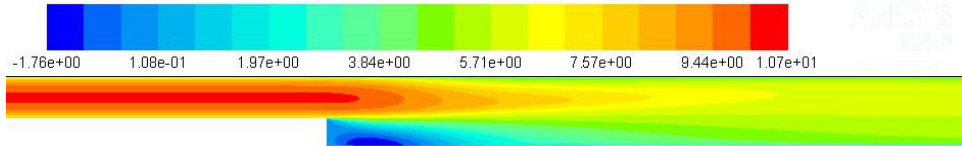


Figure 4.6: **Case 1:** streamwise mean gas velocity for the dispersed  $v^2 - f$  model with a 40% mass-loading.

Mean gas velocity profiles for the dispersed  $v^2 - f$  and the standard dispersed  $k_g - \varepsilon_g$  model are presented for Case 3 in Fig. 4.7. Both models are in good agreement with the experimental data.

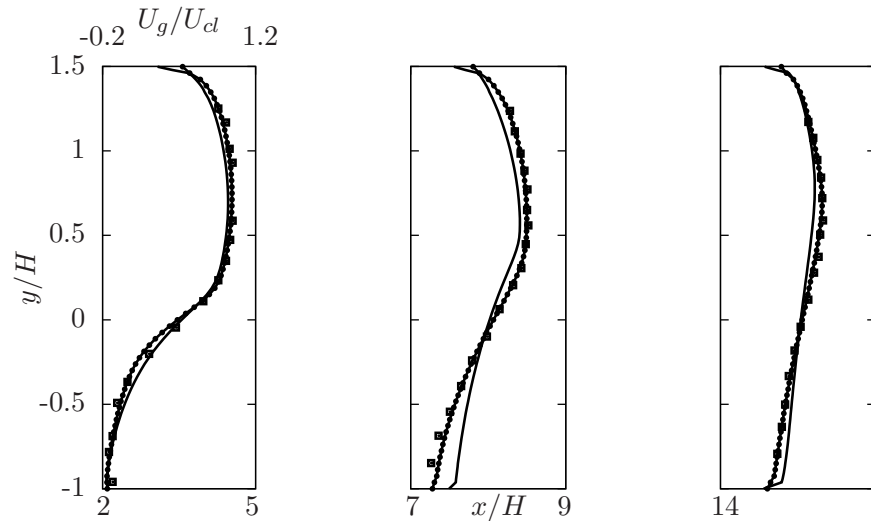


Figure 4.7: **Case 3:** streamwise mean gas velocity for the dispersed  $v^2 - f$  model (solid line), the standard dispersed  $k - \varepsilon$  model (solid line with square markers) and experimental data (squares) for a 40% mass-loading [Fessler and Eaton (1999)].

#### 4.3.5 Turbulent intensities

Turbulent intensities for dispersed  $v^2 - f$  and standard dispersed  $k_g - \varepsilon_g$  models are shown in Figs. 4.8 - 4.10 for four cases and compared with the experimental data. On

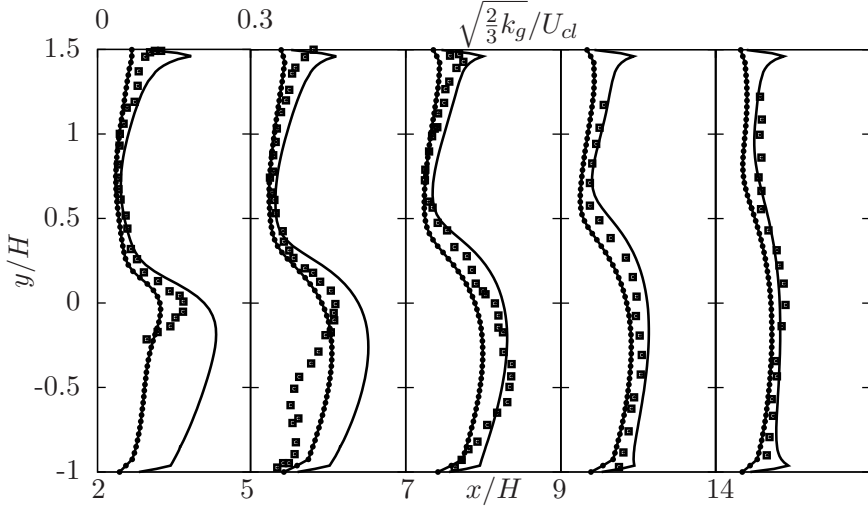


Figure 4.8: **Case 1:** turbulence intensity gas phase profiles for the dispersed  $v^2 - f$  model (solid line), the standard dispersed  $k_g - \varepsilon_g$  model (solid line with square markers) and experimental data (squares) for a 20% mass-loading [Fessler and Eaton (1995, 1999)].

Fig. 4.8 shows the gas phase turbulent intensities for Case 1. In the recirculating regions 2 and 5, the dispersed  $v^2 - f$  model slightly overestimates the intensity at the lower part. In regions 7, 9 and 10, the model is in good agreement with the measurements. On the other hand, the standard dispersed  $k_g - \varepsilon_g$  model underestimates the intensity in almost all of the regions.

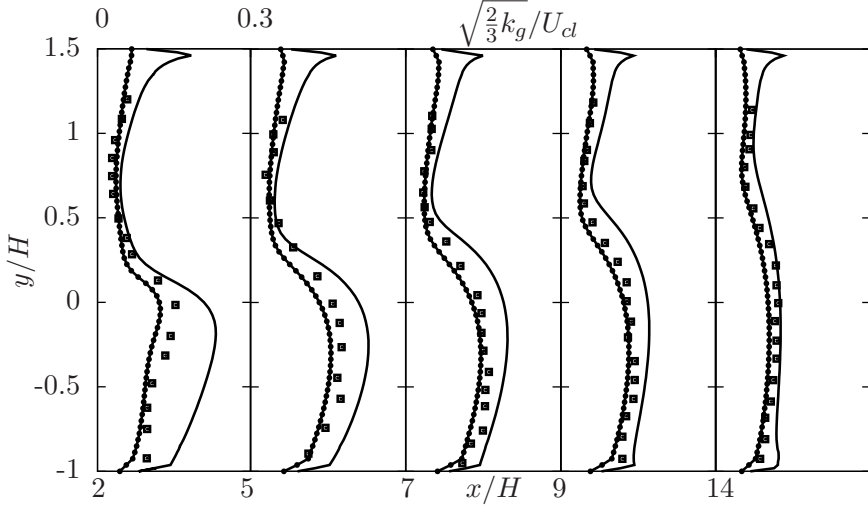


Figure 4.9: **Case 1:** turbulence intensity gas phase profiles of the dispersed  $v^2 - f$  model (solid line), the standard dispersed  $k_g - \varepsilon_g$  model (solid line with square markers) and experimental data (squares) for a 40% mass-loading [Fessler and Eaton (1995, 1999)].

For double mass loading (Fig. 4.9), the dispersed  $v^2 - f$  model is still able to predict

the turbulent intensities but again overestimates the lower part of zones 2 and 5. In the further zones, intensity prediction matches with the experimental data very well. The standard dispersed  $k_g - \varepsilon_g$  model shows the same behaviour as in Case 1.

Further calculations are performed by changing the Stokes number. In Fig. 4.10, the Stokes number is twice smaller than in Fig. 4.8, whereas mass loading is the same. Hence, the predictions of the model are similar. The model is able to predict gas phase turbulence intensities with fairly good accuracy. The standard dispersed  $k_g - \varepsilon_g$  model once again underestimates the intensity in most of the regions. In Case 3 (Fig. 4.11), more heavier are used to examine both models and the models show similar predictions as in previous cases.

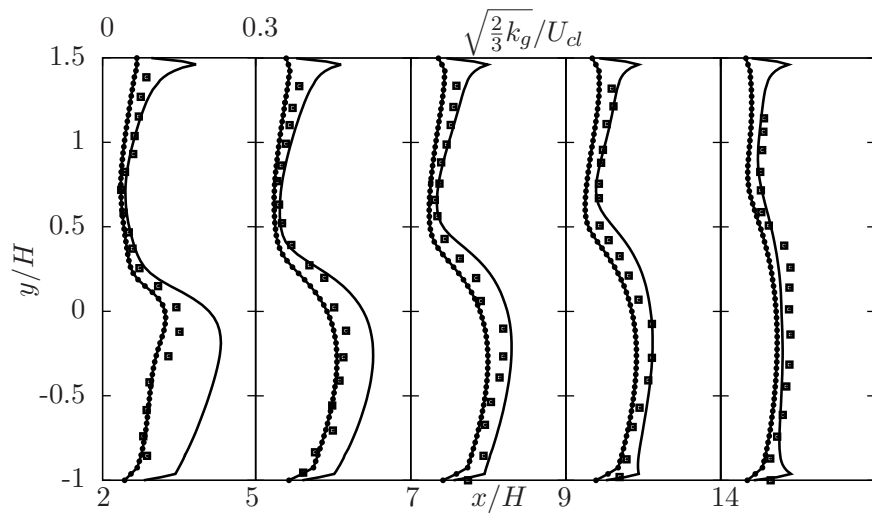


Figure 4.10: **Case 2:** turbulence intensity gas phase profiles of the dispersed  $v^2 - f$  model (solid line), the standard dispersed  $k_g - \varepsilon_g$  model (solid line with square markers) and experimental data (squares) for a 20% mass-loading [Fessler and Eaton (1995, 1999)].

Figs. 4.12 and 4.13 show turbulent kinetic energy and fluctuating energy normal to the streamlines, respectively. It can be clearly seen that the highest turbulent kinetic energy and fluctuating energy normal to the streamlines appear in the intersection zone between the recirculating and main flows. The main and recirculating flows in this area have opposite directions and thus a shear layer, which produces the turbulent kinetic energy and fluctuating energy normal to the streamlines, is created.

#### 4.3.6 Conclusion and summary

The dispersed  $v^2 - f$  model, presented here for the first time yields promising results for gas-solid flows. Hence, it has considerable potential to improve near wall treatment for multiphase flows. Although in the present study it is derived only for dilute gas-solid flows, it can be coupled easily with the  $k_s - k_{gs}$  model in order to consider dense

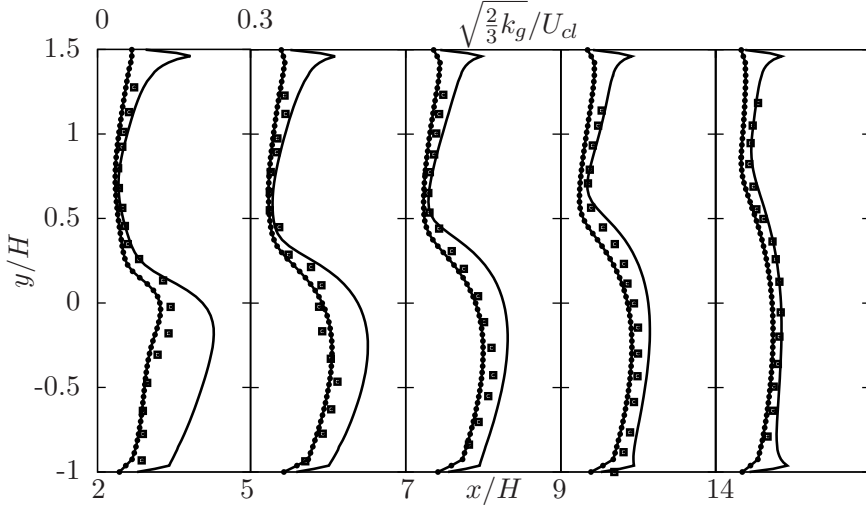


Figure 4.11: **Case 3:** turbulence intensity gas phase profiles of the dispersed  $v^2 - f$  model (solid line), the standard dispersed  $k - \varepsilon$  model (solid line with square markers) and experimental data (squares) for a 40% mass-loading [Fessler and Eaton (1995, 1999)].

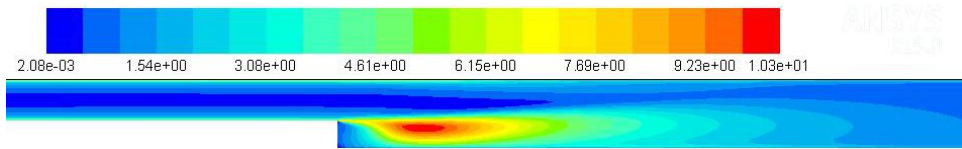


Figure 4.12: **Case 1:** mean turbulent kinetic energy contours with a 20% mass-loading.

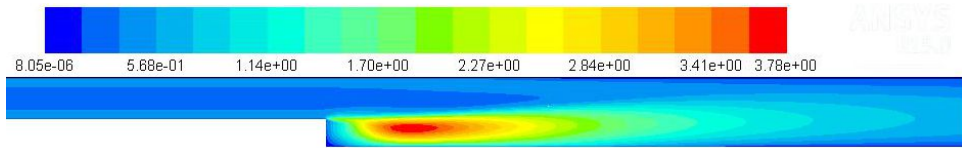


Figure 4.13: **Case 1:** mean  $v^2$  contours with a 20% mass-loading.

cases as well. The  $k_{gs}$  model used here neglects particle-particle interaction which is very questionable for dense systems. Moreover, the  $v^2$  equation may need an additional source term in order to consider particle-fluid interaction. It would also be valuable to compare the near-wall behaviour of both models, since a significant difference can be seen between the wall function used in the standard dispersed  $k - \varepsilon$  model and the elliptic equation used in the dispersed  $v^2 - f$  model.

To conclude, the dispersed  $v^2 - f$  model is applied to gas-solid flows for the first time and compared with experimental data from the literature [Fessler and Eaton (1995, 1999)]. Overall, the model gives good results, despite the above mentioned required

improvements. In order to validate the model for dense case, experiments need to be performed.



# Chapter 5

## Hydrodynamic modelling of gas-solid flow in a dimpled wall CFB reactor

### 5.1 Overview

Efficiency improvement of fluidised bed reactors is still a challenging topic in fluidisation technology. One of the ways to improve the effectiveness of the reactors is geometrical modification. In the past, wall modification was implemented for a BFB reactor and the same fluidisation effect was achieved with lower velocity because of the higher drag in the neck region [Wardag and Larachi (2012b,a); Wardag (2013)]. For a CFB reactor, baffles were implemented and an increased mixing effect in radial direction and elimination of backflow near the wall were observed [Samruamphianskun et al. (2012)]. Moreover, two different designs for CFB reactors were created for CLC applications and improvement of the gas-solid contact was achieved. It was illustrated that a countercurrent effect can improve conversions in gasifications. In addition, the pressure drop increase, due to the modification of the reactor was reported as acceptable [Schmid et al. (2011, 2012)].

In the course of this study, dimpled structures have been used in order to enhance the reactor efficiency. Dimples are widely spread in heat-exchangers and aerodynamical applications due to their several advantages. For instance, they increase the surface area and avoid fouling in heat transfer applications. They are used in golf balls to delay separation and create smaller vortices and less drag. The dimpled structure facilitates the mixing effect vital for combustion in gasification processes. In CFB reactors, they reduce the backward solid flow, which causes instability in the reactor. Potentially, dimples may bring fewer losses in comparison to previous designs [Schmid et al. (2011); Samruamphianskun et al. (2012); Wardag (2013)] because of their rounded structure.

The aim of this work is to investigate two types of dimpled (shallow and deep) walls and compare them with a standard flat wall reactor from the literature [Ibsen et al. (2001)]. Different neck sizes of the reactors are used - the wide size neck is the same as the flat one and the small one is calculated by subtracting the dimple depth from the flat diameter. Moreover, two particle diameters are used to investigate their effect on the gas-solid flow.

A 2D CFB simulation is performed on a fluidised bed column made of a single block measuring  $0.17 \times 1.5$  m with two inlets (Fig. 5.1): one for solid recirculation and one for gas inlet [Ibsen et al. (2001)]. Different dimpled wall depths and neck diameters are considered as shown in Fig. 5.2. The reactor is discretised with 17408 quadrilateral cells. A time step of  $1.0 \times 10^{-5}$  s is used. A grid independence study was performed (see Fig. 5.3). In horizontal and vertical direction about 0.003 m cell sizes are used. The same size cells are kept for other simulations as well. Second-order discretisation schemes for the convection terms are used in order to avoid numerical diffusion. For the pressure velocity coupling, the SIMPLE algorithm is applied. A column of 0.15 m in height is filled with glass-bead particles with diameters of 45  $\mu\text{m}$  (small) and 100  $\mu\text{m}$  (large), a density of  $7800 \text{ kg m}^{-3}$ , while air is introduced with an inlet velocity of  $1 \text{ m s}^{-1}$ , corresponding to the literature [Ibsen et al. (2001)].

## 5.2 Geometry and boundary conditions

The solid volume fraction is initialized at 0.62 in height of 0.15 m, which is the recommended 10 % of the whole reactor [Gidaspow (1994)]. A pressure outlet is used (i.e. ambient pressure and temperature) and no-slip wall conditions are applied for the gas phase. The Johnson and Jackson boundary condition [Johnson and Jackson (1987)] takes into account wall particle collision and wall roughness is utilized in the model with a specularity coefficient of 0.5 [Armstrong et al. (2010)]. A UDF code is developed to recycle the solid outflow and maintain a constant solid flux, thus reducing computational time/expense by avoiding the cyclone and feedback section of the process. The model is implemented using the Ansys FLUENT 14.5.

Table 5.1: Dimple type, neck type and particle diameters in the CFB reactor.

Case	Dimple type	Neck type	Particle diameter
1	Flat	0.17 m	45 $\mu\text{m}$
2	Shallow	0.17 m	45 $\mu\text{m}$
3	Deep	0.17 m	45 $\mu\text{m}$
4	Deep	0.14 m	45 $\mu\text{m}$
5	Deep	0.14 m	100 $\mu\text{m}$
6	Shallow	0.155 m	45 $\mu\text{m}$
7	Shallow	0.155 m	100 $\mu\text{m}$

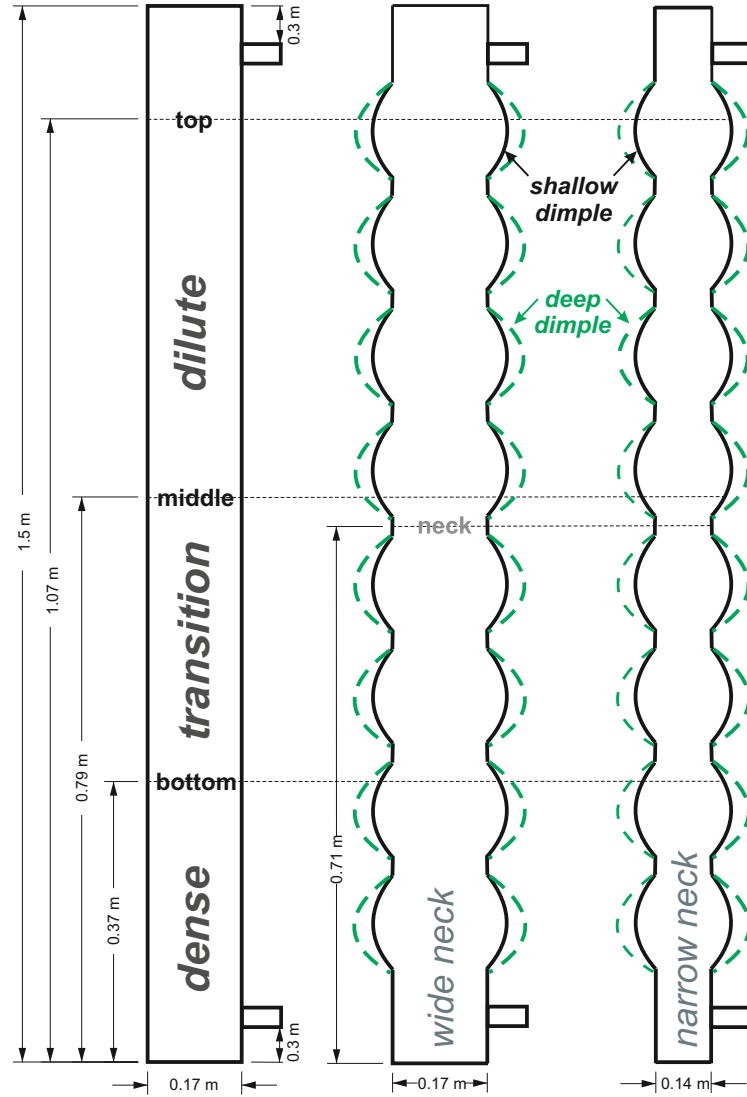


Figure 5.1: Geometry of flat and dimpled walls in a CFB reactor.

### 5.3 Results and discussion

Calculations are performed for two dimple depths (see Fig. 5.2) and two neck diameters. Also, two different particle diameters are used in order to investigate the effect of particle properties on the dimples. Based on the results, it can be concluded that particle diameter has a significant effect on the velocity and volume fraction profiles. In particular, large particles are affected by the backflow created by the dimples and gravitational force. A smaller neck diameter proved to be advantageous - with the same inlet velocity higher velocities are obtained in the reactor, confirming similarities to the BFB reactor [Wardag and Larachi (2012a,b); Wardag (2013)]. Thereby, a lower energy consumption is observed by achieving the same fluidisation regime with a narrower neck due to the dimple structure.

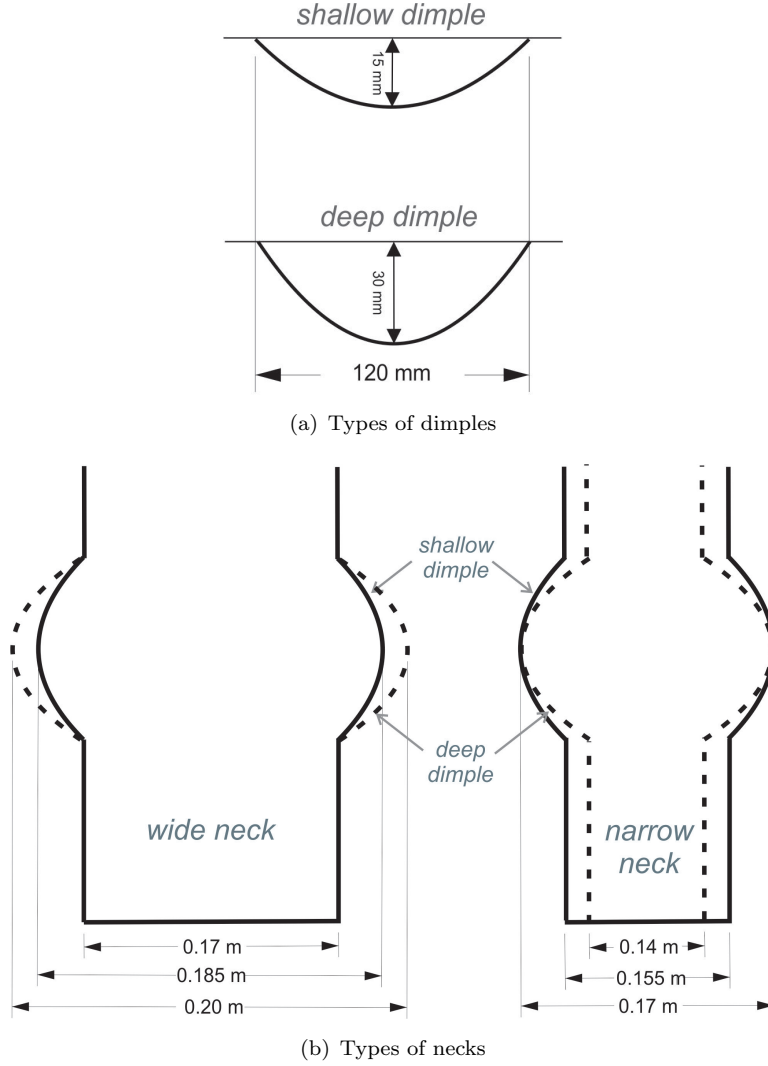


Figure 5.2: Dimensions of the shallow and deep dimples as well as the wide and narrow necks.

### 5.3.1 Solid volume fraction

An accurate prediction of particle distribution is crucial for the improvement of the hydrodynamic behaviour of the whole system. To achieve this, drag modelling is a key factor. Classical drag models overestimate the solid fraction in the dilute regions of the CFB reactor and are not able to deal with inhomogeneous distribution [Yang et al. (2003)]. Hence the EMMS drag model, developed to consider meso-scale structures [Li et al. (1993)], is used.

The instantaneous results, taken at 15.0 s in Fig. 5.4, display the volume fraction in the three types of CFB reactors. In the flat wall reactor, due to segregation, large particle clustering regions are observed. By contrast, the dimpled reactors (shallow and deep) reduce these to form thinner particle clusters, which becomes more apparent with the

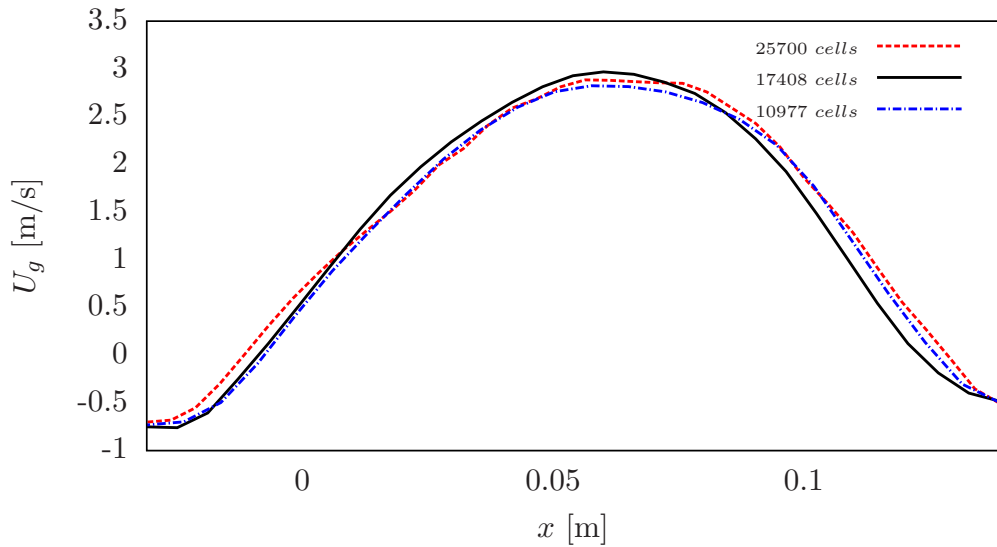
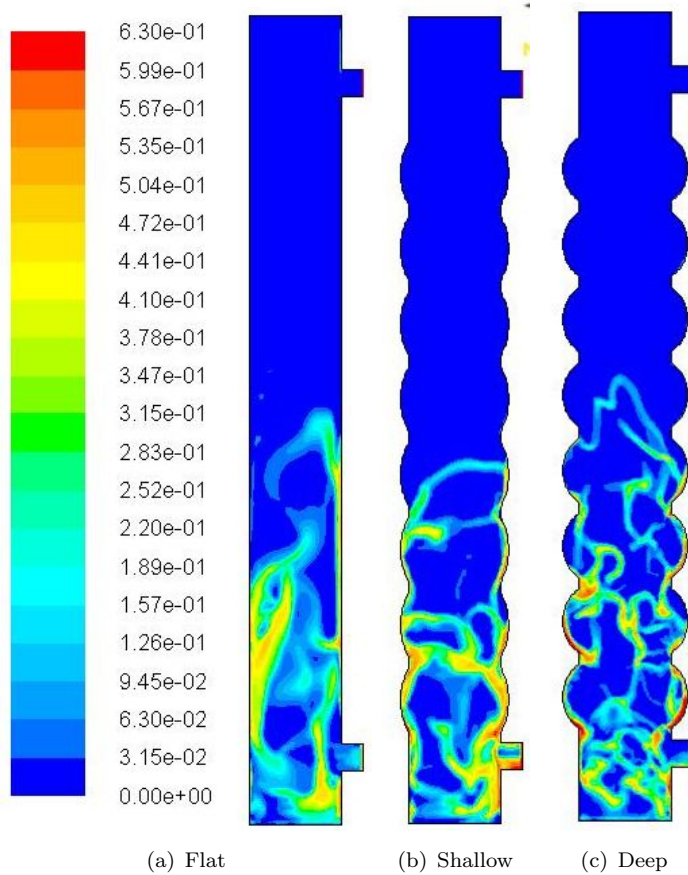


Figure 5.3: Grid independence study


 Figure 5.4: Instantaneous volume fraction,  $\alpha_s$ , for flat (Case 1), shallow (Case 2) and deep (Case 3) dimpled wall at 15.0 s.

dimple depth increase. This suggests that the curved design promotes particle migration back into the core of the reactor thus potentially increasing air/fuel contact, as well as the effective drag in the system. Moreover, it may reduce pressure losses due to the clusters. The shallow dimple facilitates a breaking down of the clusters near the wall and pushes the particles in the main flow (Fig. 5.4b). The deep dimples show a further reduction of the size of the clusters, which are yet denser near the wall as particles reside in the lower sections of the dimples (Fig. 5.4c).

The time averaged results below are taken for 20.0 s in the dense (0.37 m) and dilute (1.07 m) regions of the CFB reactor (see Fig. 5.1).

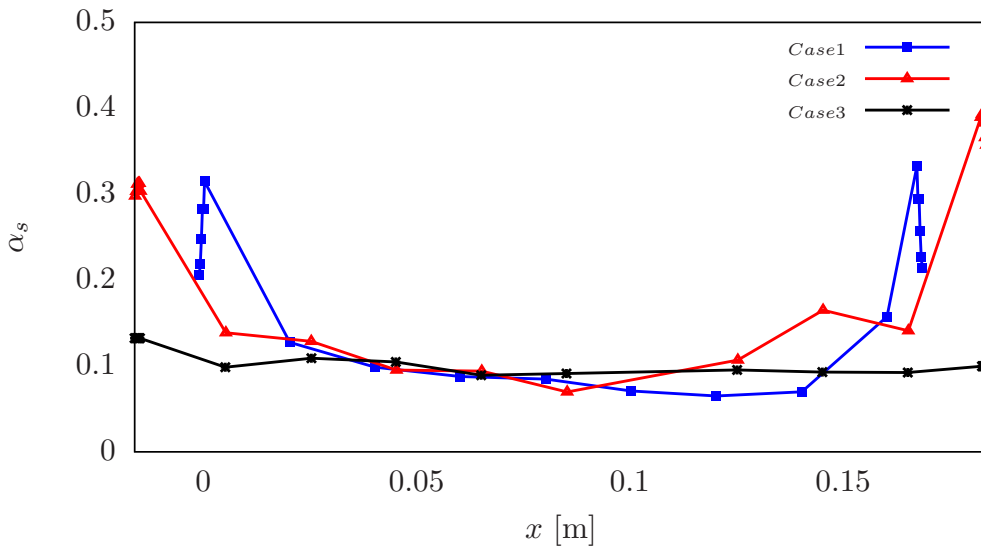


Figure 5.5: Time averaged horizontal solid volume fraction in the dense region for Cases 1-3.

In Fig. 5.5 and Fig. 5.6, Case 1 shows the classical wall behaviour of a CFB reactor - the near-wall region, due to velocity difference, is much denser than the middle one and the main flow pushes the particles towards the wall. The downward moving clusters cause hydrodynamic instability in the system and thus the inhomogeneous distribution of the particles reduces the effective drag of the system. Moreover, the contact between the fuel and oxygen is reduced. Indeed the above mentioned regions were predicted by the EMMS drag model [Tsuo (1989); Li et al. (1993); Gidaspow (1994); Pannala et al. (2011)]. At the base of the reactor, the solid volume fraction is much higher than in the dilute region as particles migrate and accumulate. The solid volume fraction in a vertical direction is displayed in Fig. 5.7. Although the solid volume fraction in the upper regions of the reactor is expectedly lower than at the base of the reactor, for each reactor the lower dense regions of both dimpled walls are still of about the same magnitude as in the flat walled reactor. This suggests that the dimpled walls promote particle residence in the lower regions. However, the dilute regions can suggest that deep

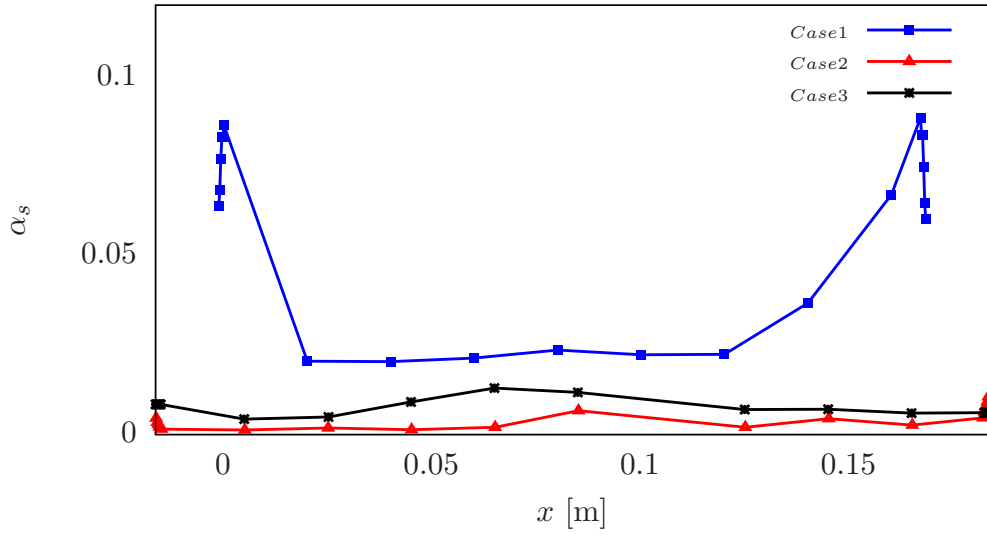


Figure 5.6: Time averaged horizontal solid volume fraction in the dilute region for Cases 1-3.

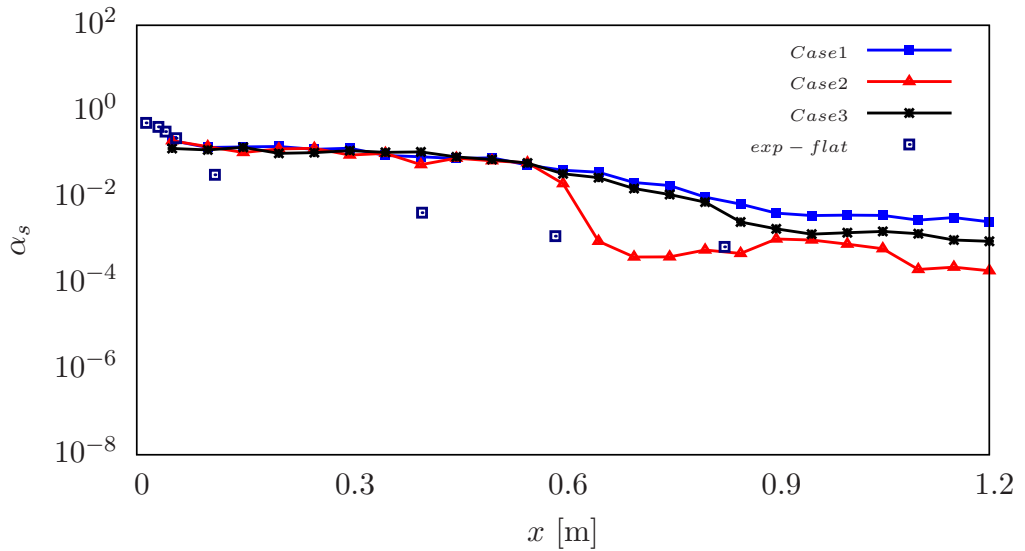


Figure 5.7: Time averaged vertical solid volume fraction for Cases 1-3 and experimental data for a flat reactor.

dimples behave similarly to flat walls, whereas shallow dimples display a lower volume fraction. This could be due to the circulation within the dimples which produces a shear layer between the core and the circulating region. The gas traverses along the reactor, prioritising the easiest route, i.e. through the core rather than attempting to bypass the shear layer. As such, this could potentially entrain more particles once within the core.

The distribution of the vertical solid fraction can be seen in Fig. 5.8. The results

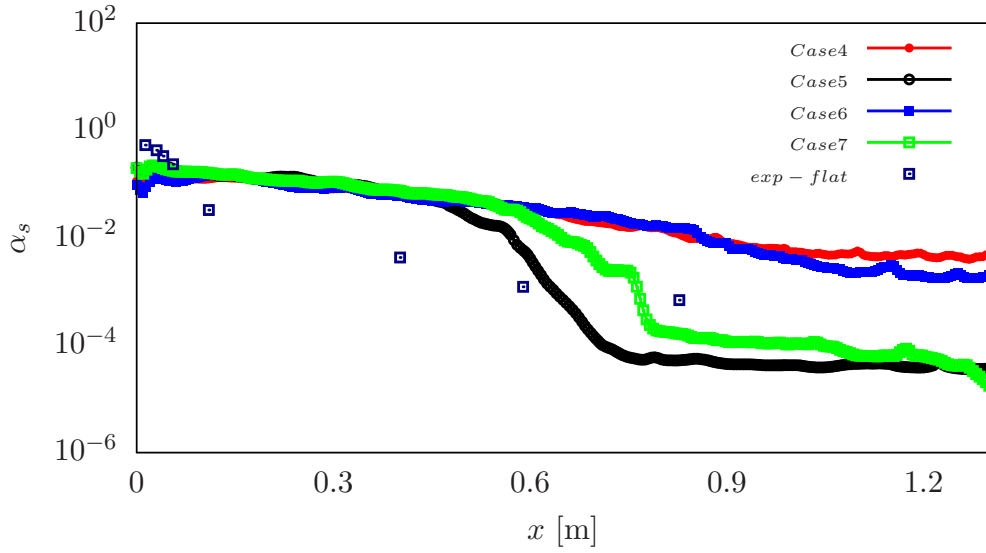


Figure 5.8: Time averaged vertical solid volume fraction for Cases 4-7 and experimental data for a flat reactor.

indicate that in the vertical direction the volume fractions for Cases 4 and 6 (narrow neck) are more homogeneously distributed due to the higher velocities. Comparing the vertical solid fraction for Cases 2, 3, 4 and 6 (Figs. 5.7 –5.8), which share the same particle diameter, it can be concluded that higher solid volume fractions are observed at the top of the deep dimple reactor due to stronger recirculation. The plots in Fig. 5.7 and Fig. 5.8 show higher volume fractions in the vertical direction due to the drag model. Different drag models could be implemented in dimpled wall geometries in order to examine whether better prediction of the vertical solid volume fraction distribution may be achieved.

In Case 2, a sudden decrease happens at about 0.6 m, yet the decrease is smoother in Case 6 (narrow neck with a shallow dimple structure). Due to the decrease of the reactor diameter, gas velocity heightens and therefore more particles can be held at the top of the reactor. For Cases 3 and 4, the change of the neck diameter does not show significant effect on the vertical distribution of the solid volume fraction. Different particle diameters are used only in the narrow neck reactor. Fig. 5.8 indicates that after 0.6 m, the solid volume fraction starts to decrease significantly. One of the reasons may be that the backflow produced by the dimples is highly affected by the larger diameter because of the larger surface area. But, the most significant reason is the gravitational force. Because of the higher mass of the particles, gravity starts to dominate earlier in comparison to smaller particles. Thus, as expected, most of the particles aim to remain below 0.6 m.

At the bottom, the narrow and wide neck reactors give similar results (see Figs. 5.5 and 5.9) except for the deep dimpled wall. The narrow neck reactors with deep dimples

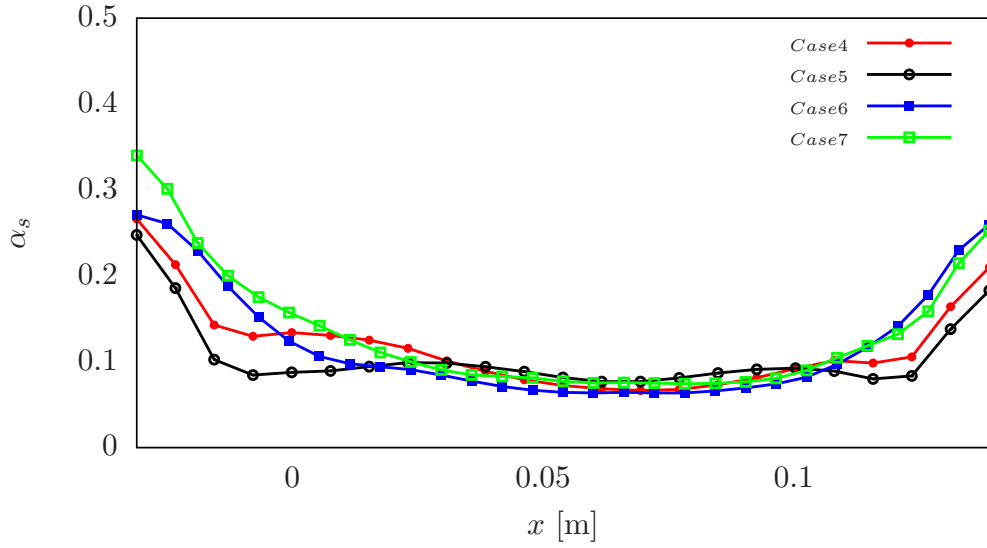


Figure 5.9: Time averaged solid volume fraction in the dense region for Cases 4-7.

(Cases 4 and 5) give the higher volume fraction near the wall. Presumably, the particles have limited space to entertain. Thus, the dense region of the reactor allows more collisions and limits the recirculation as the dimples push the particles towards the middle of the reactor. Yet, the size of the particles does not have any effect on the solid volume fraction distribution at the bottom of the reactor. However, as it can be seen from Fig. 5.9, particles with a large diameter have a slightly higher solid volume fraction near the wall.

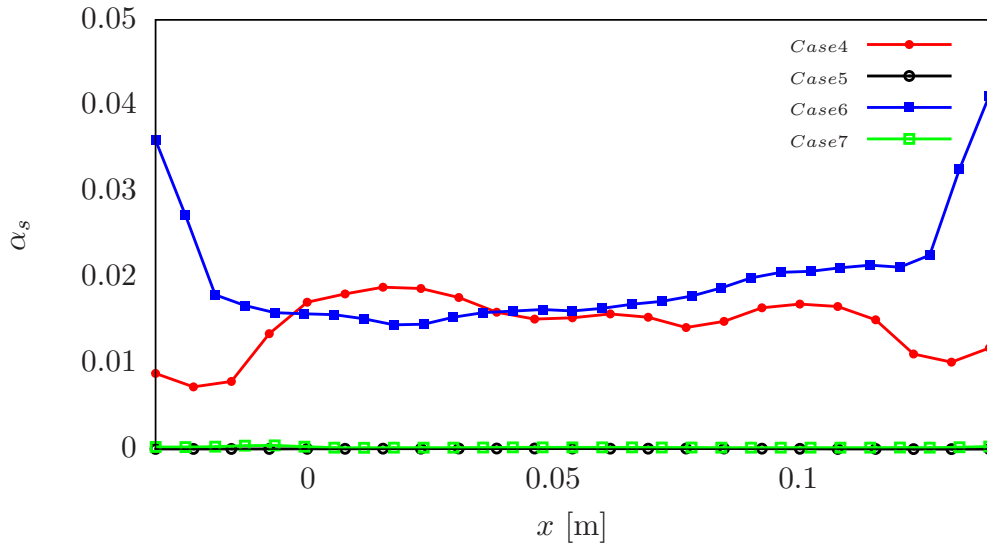


Figure 5.10: Time averaged solid volume fraction in the transition region for Cases 4-7.

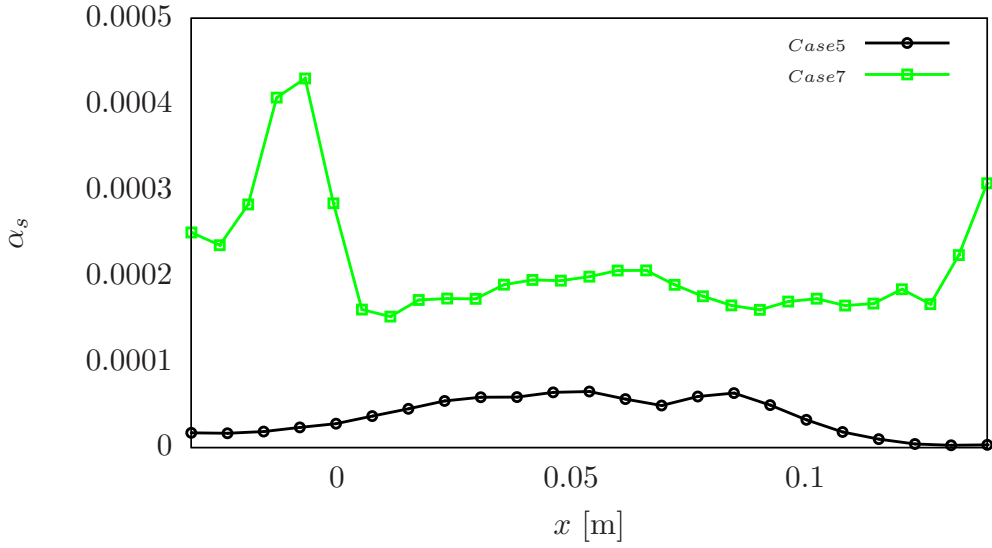


Figure 5.11: Time averaged solid volume fraction in the transition region for Case 5 and 7.

In the middle of the reactor, the distribution of the solid volume fraction in the narrow region becomes similar to the wide neck reactor as the deep dimple structure once again starts to push the particles to the main flow and to break down the clusters (Figs.5.10 and 5.11). Furthermore, the accumulation of the particles near the wall still occurs in the shallow dimples (Case 6,7). The deep dimples are able to push the particles to the main flow in the middle but not at the bottom of the reactor because this region is diluted enough, which allows recirculation to dominate over particle-particle interaction.

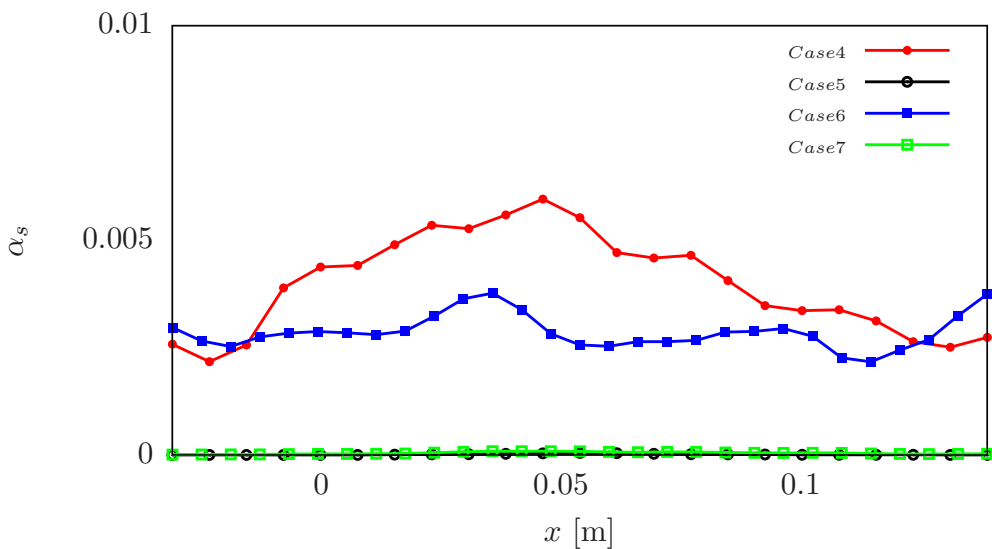


Figure 5.12: Time averaged solid volume fraction in the dilute region for Cases 4-7.

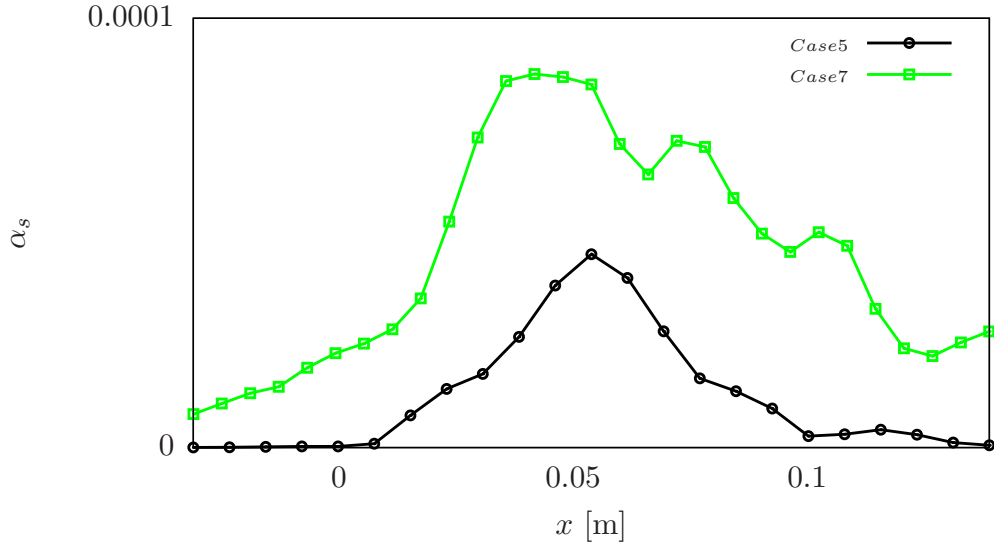


Figure 5.13: Time averaged solid volume fraction in the dilute region for Cases 5 and 7.

In Fig. 5.10 shows that the particle volume fraction is low in the middle part of the reactor, as explained before, larger particles are affected by the gravity to a higher degree. Hence, large particles tend to stay in the lower regions of the reactor. Fig. 5.11 shows that large particles behave similarly in both dimple types. Unlike shallow dimples, deep dimples manage to push the particles to the middle of the reactor.

At the top of the reactor near wall accumulation of particles is not visible anymore (see Fig. 5.12). Due to stronger recirculation in the deep dimple, the particle volume fraction is higher in the middle of the reactor (Cases 4 and 6) than the near wall. Fig. 5.13 shows the larger particle distribution at the top of the reactor. Large particles react similarly to small particles in both dimple structures (Cases 5 and 7).

### 5.3.2 Solid velocity profiles

Figs. 5.14 and 5.15 display the time averaged solid velocities across horizontal slices of different regions of the reactors. Fig. 5.14 refers to a height of 0.37 m, which is the widest point of the dimples and Fig. 5.15 is sliced at a height of 0.71 m, which is the narrowest diameter of the dimpled reactors. The results in the neck region (Fig. 5.15) are in good agreement with the flat wall simulations and experimental data [Ibsen et al. (2001)]. Negative velocities are observed indicating a downward motion of the particles due to segregation. The dimpled wall reactors offer a more homogeneous positive velocity distribution in the neck region despite having the same diameter. The velocities in both dimpled cores are lower than in the flat walled reactor due to the presence of circulation regions and their production of an opposing downward shear layer between the main

flow and the circulating regions. The circulatory flow would suggest negative velocities

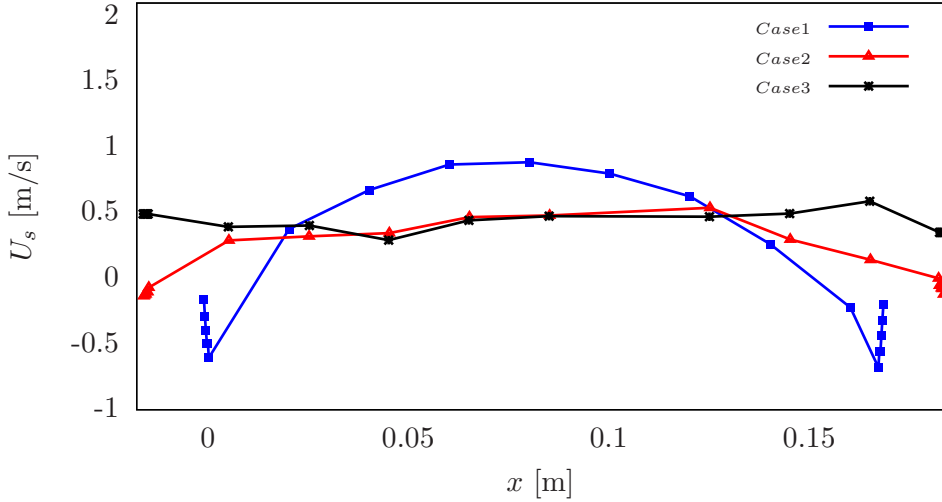


Figure 5.14: Time averaged horizontal solid velocity at 0.37 m for Cases 1-3.

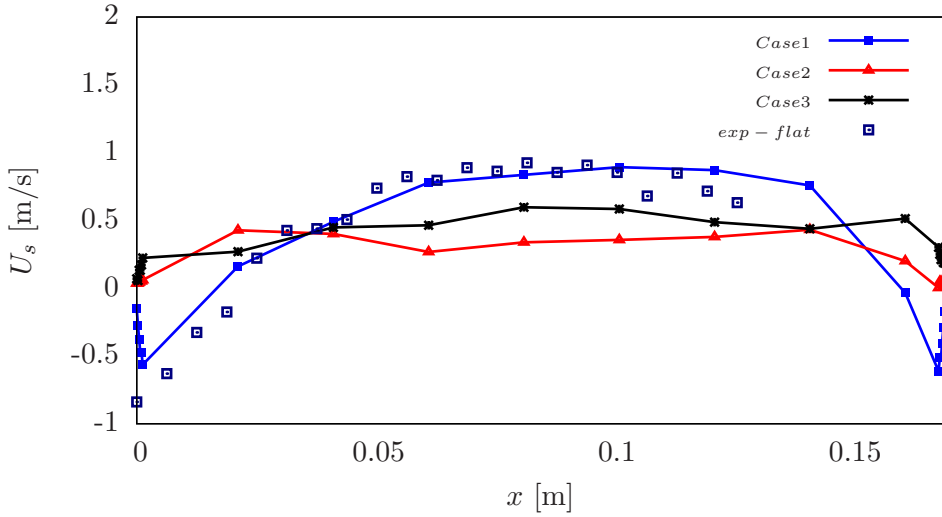


Figure 5.15: Time averaged horizontal solid velocity at 0.71 m for Cases 1-3 and experimental data for a flat reactor.

but the line graphs in Fig. 5.14 do not display this. However, this is explained further in Fig. 5.16 which displays velocity contours and selected velocity vectors within the lower right dimple at a height of 0.37 m at three time points. There is a significant difference in the flow after just 0.05 s. The main flow and circulatory shear layer varies in location, with upward moving particles dominating the upper region of the dimple at 10.1 s but lower regions at 10.1 s. The remaining regions contain stagnant or downward flowing particles. Further difference is observed at 13.1 s as the majority of the dimple experiences downward particle flows. These regions are crucial to the understanding of

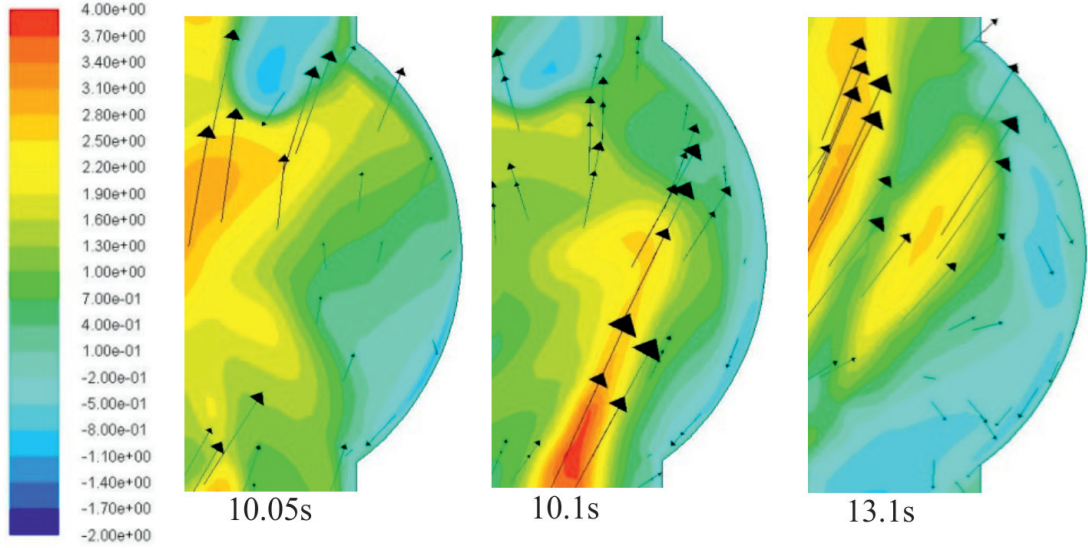


Figure 5.16: Instantaneous solid velocity at random time.

hydrodynamic behaviour of the structures. Whilst instantaneous results display regions of negative near wall velocities, they disappear during the time averaging procedure due to much higher positive velocities across the middle of the dimple. In each of the three plots negative velocities are observed in the bottom section of the dimple, which is due to friction, particle-particle and wall collisions, and gravity. Further investigations will explore the effects of these further, along with the effects of varying depths, as the shallow dimpled walls display slightly negative velocities near the wall although not to the magnitude of a flat wall reactor.

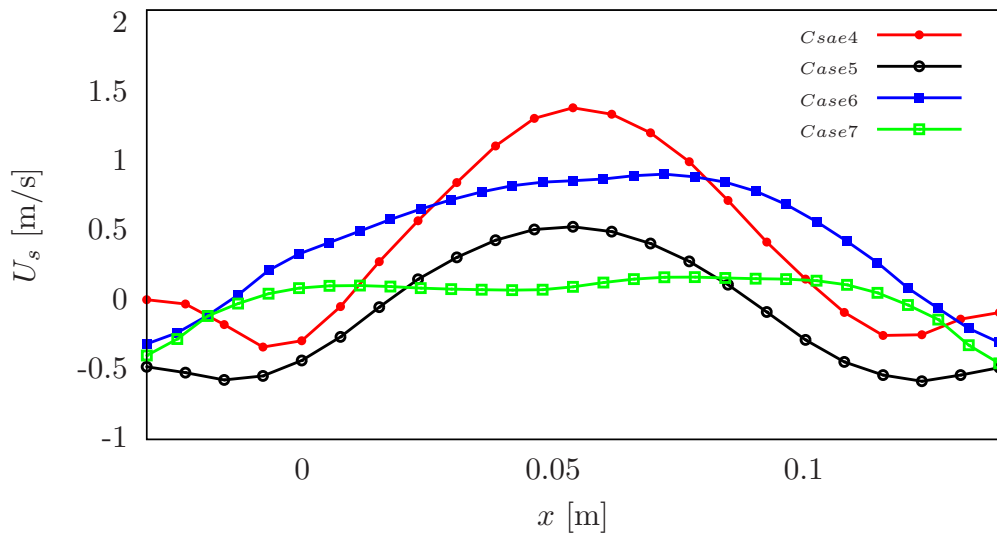


Figure 5.17: Time averaged horizontal solid velocity at 0.79 m for Cases 4-7.

As can be seen from Fig. 5.17, solid velocity is doubled in comparison to the wide neck reactor with small particles (Fig. 5.14). The necks cause a nozzle effect. As the neck diameter reduces, particles acceleration increase. This dimple phenomenon facilitates to obtain the same fluidisation properties with lower velocities. On the other hand, slightly negative velocities appear near the wall as the narrow channel may contribute to the interaction between particles. In particular, particles coming out of the dimple and particles going towards the dimples meet more often than particles in the wide neck. For Case 4, the solid velocity near the wall is almost zero, then it goes to the negative values, where the particle interaction is high and followed by solid velocity recovering to positive values via the deep dimples. This phenomenon is not observed in the wide neck for the same particle diameter (Fig. 5.14) because particles have enough place to entertain without interacting with each other. Double particle size is used for the narrow neck case (Fig. 5.17). Increasing particle size and while keeping the same density makes particles heavier and the gravity higher. As a result, lower particle velocities for Cases 5 and 7 are shown. This behaviour suggests that optimal dimple design can differ with different particle properties, so it makes it more challenging and may require optimisation techniques to find a global dimple design.

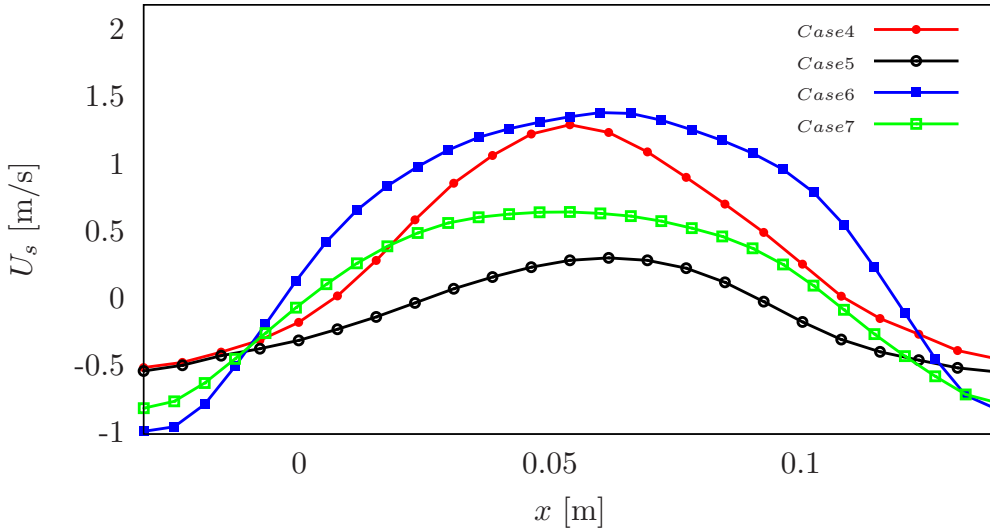


Figure 5.18: Time averaged horizontal solid velocity at height of 0.37 m for Cases 4-7.

Solid velocity profiles in the dense bottom zone, where the particle-particle interaction is dominant are shown in Fig. 5.18. Solid velocity distribution behaves differently in accordance with the different types of dimples. Transition and dilute regions give maximum velocities for deep dimples in the main flow (see Figs. 5.17 and 5.19) whereas in the bottom region, as it is shown in Fig. 5.18, there is an opposite tendency. Presumably, the existence of particles and their interaction with each other, together with a high recirculation rate, make velocities lower in the deep dimple case in this dense region.

Although, the deep dimple structure reduces negative velocities by half in comparison to shallow dimples, there are still negative values near the wall due to the particle-particle interaction.

Cases 5 and 7 with large particles again show lower velocities in the dense region, as expected due to the gravitational force (see Fig. 5.18). In this case, the deep dimple structure also gives lower velocities in comparison to the shallow dimple case.

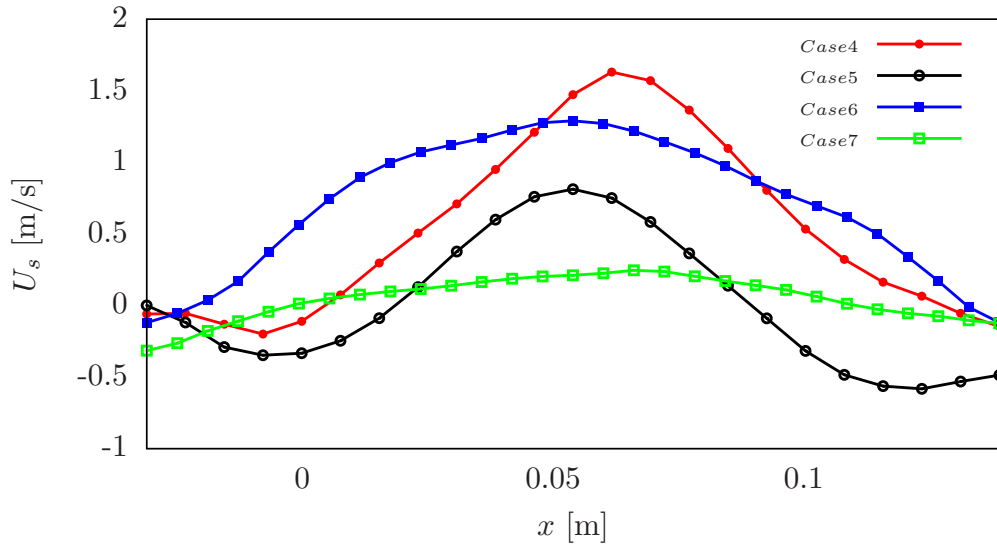


Figure 5.19: Time averaged horizontal solid velocity at 1.07 m height for Cases 4-7.

For the dilute region, solid velocities are presented in Fig. 5.19. They become positive for deep and shallow dimples with small particles. With the deep dimple structure, only 0.08 m away from the wall, negative values appear again. This is where two particle flows meet (one coming from the dimple and one from the main flow) and start to interact. For the large particle case, velocities are lower in all regions, as expected. As the fluidisation conditions are set up for small particle sizes [Ibsen et al. (2001)], it is normal to have such lower velocities for heavier particles.

### 5.3.3 Gas velocity profiles

Time-averaged gas velocities for wide and narrow necks are displayed here (Figs. 5.22 – 5.24). In the wide neck case (Cases 1 – 3), near wall velocities are lower than in the core, in fact, negative in flat walls, as clusters descend along with interstitial gases. There seems to be more asymmetry at lower heights (dense region) possibly due to particles collisions being more intensive (Fig. 5.20). As with solid velocities, the time averaged results show an overall positive order of magnitude, regardless of circulation regions (as seen in Fig. 5.21) as the swirling, tortuous flow within the core migrates to and from

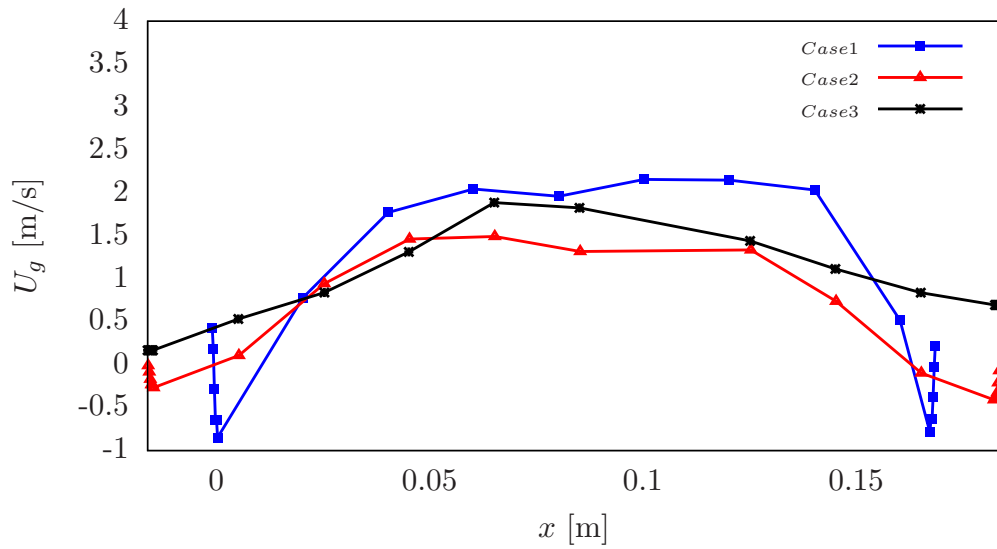


Figure 5.20: Time averaged horizontal gas velocity at 0.37 m for Cases 1-3.

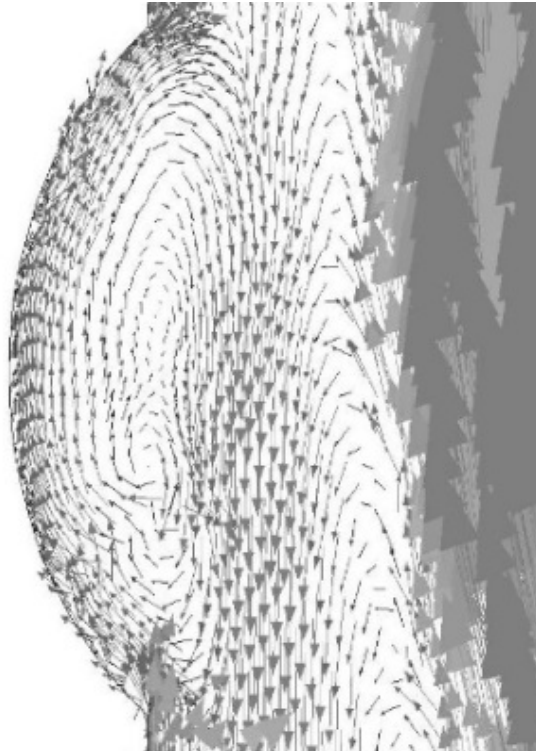


Figure 5.21: Instantaneous velocity vector plot at 15 s at 0.37 m.

the dimpled structure in a chaotic mixing fashion. This seems more pronounced when dimples become deeper. Further research will investigate the key regions such as the shear layer between the circulating and core to investigate its effect on cluster break up and the residence times of solids.

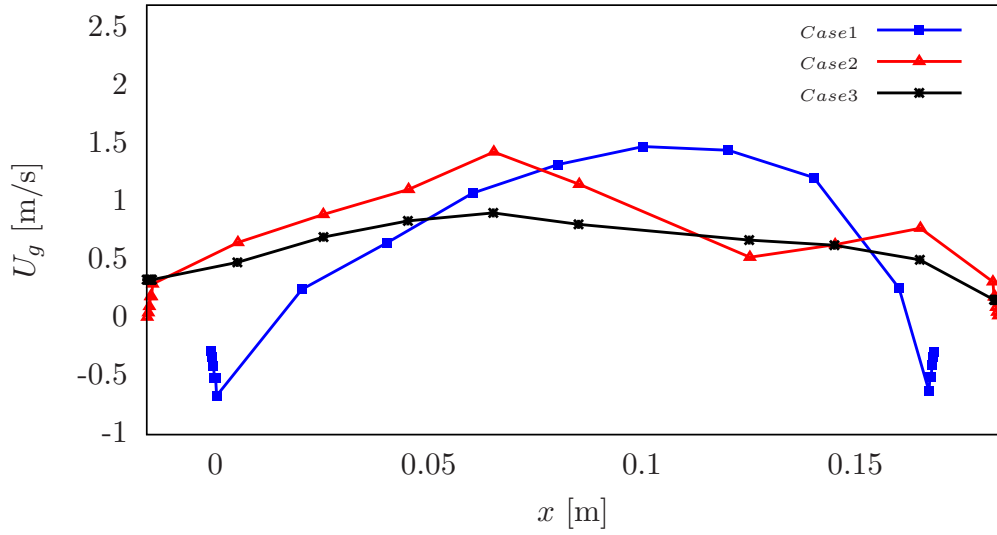


Figure 5.22: Time averaged horizontal gas velocity at 1.07 m for Cases 1-3.

Narrow wall reactors show higher velocities as expected in each region. Interestingly, the dimple structure, despite recirculation, can overtake the velocity of the standard flat wall reactor (see Figs. 5.22 – 5.24). Fig. 5.23 evidenced that the gas velocity in the narrow neck region reaches almost  $3.0 \text{ m s}^{-1}$  which is three times the inlet velocity. Such behaviour aims to reduce the velocity correspondingly the energy consumption. In the neck region, heavier particles give lower velocity as expected.

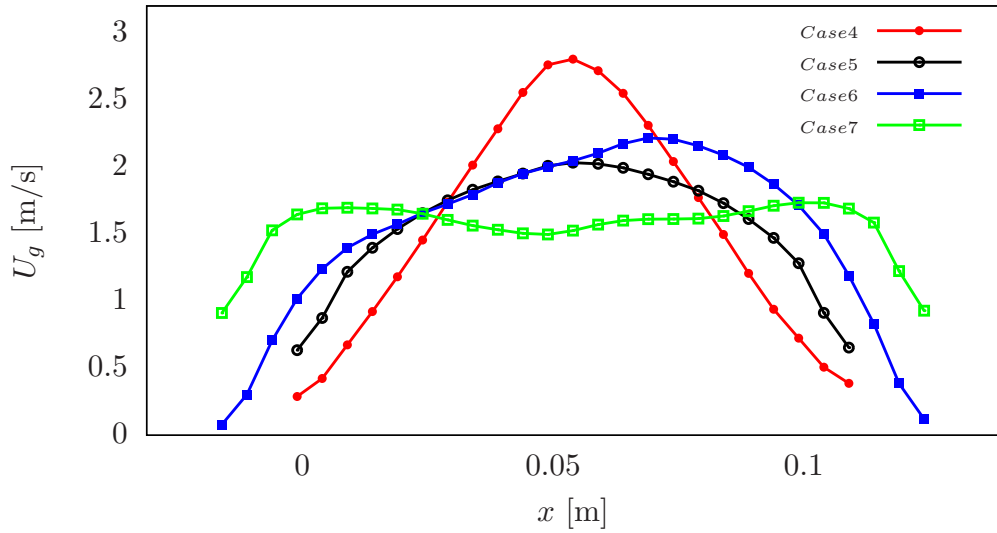


Figure 5.23: Time averaged horizontal gas velocity at 0.71 m for Cases 4-7.

At the top of the reactor, for Case 4 with deep dimple (see Fig. 5.24), the gas phase velocity reads slightly above  $2 \text{ m s}^{-1}$  and it is surprisingly similar to the heavy particle Case 5. It is obvious that in the height of 1.07 m, the heavy particles are very dilute.

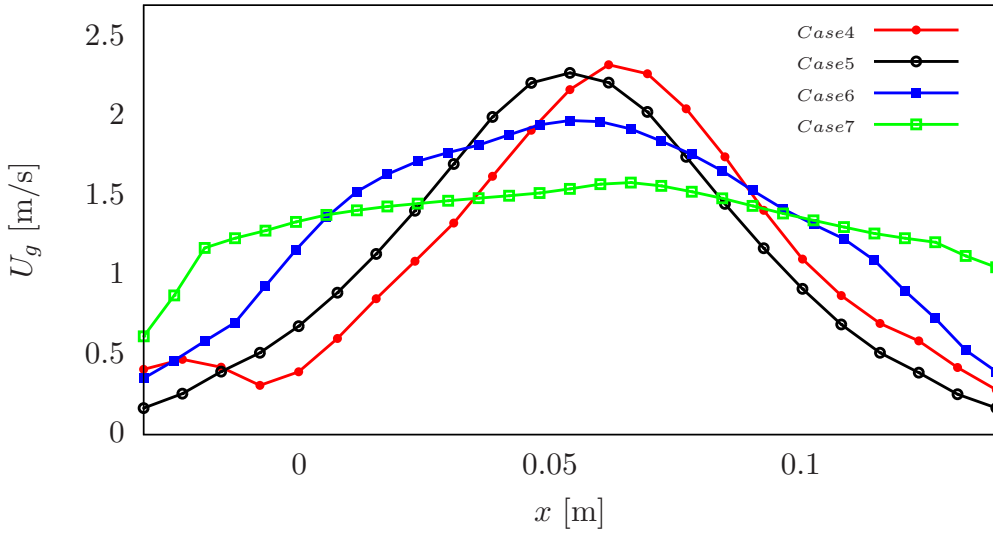


Figure 5.24: Time averaged horizontal gas velocity at 1.07 m for Cases 4-7.

Therefore, from Fig. 5.8 is also evident that particles cannot significantly affect the gas velocity profiles. In the shallow dimples, particle concentration is slightly high and it has an impact on the gas as seen in Figs. 5.8 and 5.24.

## 5.4 Conclusion and summary

The present work introduces a novel wall design which could potentially reduce particle segregation against CFB walls and potentially improve the overall efficiency. Initial findings suggest the wall structure can prevent the formation of large clusters, minimise pressure losses due to cluster presence and increase particle residence time within the reactor. Two necks, dimple depths and particle sizes are used in this work. The wide size neck is the same as the flat wall diameter, while the small size neck is calculated by subtracting the dimple depth from the flat diameter. The result shows that, the narrow neck gives higher velocities due to the nozzle effect. So, with significant lower velocities to reach the same fluidisation effect as in flat wall, is possible with dimpled wall. In the wide neck case the near wall negative velocities disappear with the deep dimple structure; therefore this means that recirculation is strong enough to push particles back to the main flow. On the other hand, shallow dimples do not manage to push the clusters to the main flow because dimples are not deep enough to create sufficient recirculating energy. Particle size also has a significant impact on the fluidisation behaviour of the reactor with dimples. The large particles are heavier and they need higher fluidisation velocities in order to cope with the gravity. That is why heavier particles give, in both deep and shallow dimple case, negative velocities near the wall. Larger particles give lower velocities overall in comparison to small particles. Therefore, the dimple structure

impact on fluidisation is very dependent on particle properties. In order to find an optimal dimple structure, optimisation study may be needed.

The dimpled structure promises a wide range of advantages to improve the CFB reactor efficiency. It may potentially increase the mixing between the gas and particles by breaking down the clusters and recirculating them. Also, during the breaking down of clusters, the contact area of particles and gas is increasing which is very vital in the combustion process of solid fuels. Moreover, due to recirculation, the residence time of the fuel in the reactor increases and it gives the fuel more time for contact with oxygen. Dimples may help to avoid fouling effect by using energetic recirculation which reduces the thermal efficiency near the wall. Vertical direction solid volume fraction is overestimated. It can be due to the choice of the drag model; therefore, it is recommendable to try different drag models. A further investigation is needed with different types of particles and optimised dimpled structures. Experimental work is required to comprehend in depth the dimpled wall phenomena and its impact on gas-solid flows.



# Chapter 6

## Coal gasification modelling of a dimpled wall reactor

### 6.1 Overview

Modelling of reaction kinetics plays a vital role in the development of combustion and gasification processes. Simplified mathematical models of chemical reactions and fluidised bed gasification process were developed by Smoot [[Smoot \(1984\)](#)]. Souza [[Souza-Santos \(1989\)](#)] provided a complete fluidisation model by including drying and devolatilisation processes. Furthermore, Huilin contributed to the combustion models of circulating fluidised bed [[Huilin et al. \(1998, 2000\)](#)] and Yan [[Yan et al. \(1999\)](#)] used several scales to simulate bubbling fluidised bed coal gasifiers. Nevertheless, until now none of the models have managed to avoid empirical correlations to describe the dynamical fluid properties. Also, the present devolatilisation models are based on different coal properties which make them non-universal models. Every model has its own specific data for its composition, like moisture, char, ash, hydrogen, oxygen and carbon. Several devolatilisation models have been implemented to predict the gasification process of coal, such as the constant model [[Baum and Street \(1971\); Pillai \(1981\)](#)], where the release of volatiles takes place in a constant rate; or the single rate model [[Badzioch and Hawksley \(1970\)](#)], where the volatile release was related to the volatile remaining of the coal in a first order dependence. In particular, the Kobayashi model [[Stickler et al. \(1974\); Kobayashi \(1976\)](#)] describes the process of coal devolatilisation and the volatile release with two equations. The first equation takes into account low temperatures, where less volatile yields take place and the second equation high temperatures, which cause much higher volatile yields. To describe the turbulence in such high solid volume fractions the  $k_s - k_{gs}$  model is used (see Ch. 3).

There are two types of reactions:

- homogeneous reactions used to describe gas-gas reactions, which are influenced by both the kinetic forces and the turbulent behaviour of gas. Therefore, it is important to decide whether the turbulent mixing behaviour or the kinetic rate is dominating local reactions [Yu et al. (2007); Wang et al. (2009)];
- heterogeneous reactions where gas-solid reactions take place. These kind of reactions can be captured by the Lagrangian model in which particle properties are treated individually. On the other hand, Eulerian models define the particulate phase as a fluid and the particle diameters remain constant restricting information of individual heterogeneous reactions. Successful works [Armstrong et al. (2011b)] include a coal reaction model with limestone to analyse gasification products of the coal. A three dimensional model of the coal gasification for fluidised bed was provided by Wang [Wang et al. (2009)] as well.

This chapter contains:

- theoretical background of chemical reactions;
- instantaneous conservation equations for a chemical reaction;
- modelling of the two-step devolatilisation of coal [Kobayashi et al. (1977)] and developing a code in the UDF utility of ANSYS Fluent 14.5;
- application of heterogeneous and homogeneous reactions [Yu et al. (2007); Gerber et al. (2010)] to predict gasification products from coal developed in a UDF code;
- simulation of a BFB type gasifier for the validation of the code [Yu et al. (2007); Gerber et al. (2010); Armstrong et al. (2011a)]; the code is applied also to a CFB reactor;
- novel wall modification with dimples and discussion;.

## 6.2 Reaction modelling

### 6.2.1 Species transport

The conservation equation for chemical species is the mass fraction for each species  $Y_i$  obtained through the solution of a convection-diffusion equation for the  $i$ th species:

$$\frac{\partial(\alpha_g \rho_g Y_i)}{\partial t} + \frac{\partial}{\partial x_j} (\alpha_g \rho_g \mathbf{u}_g Y_i) = - \frac{\partial}{\partial x_j} \alpha_g J_i + \varepsilon_g R_{g,i} + R_{s,i}, \quad (6.1)$$

where  $J_i$  is the diffusion flux of species  $i$ , which arises due to gradients of the concentration and temperature. The second term on the rhs represents the net rate of production

of species by homogeneous reactions and the third term the rate of production of species due to heterogeneous reactions. The diffusion flux of individual species  $J_i$  for turbulent flows is defined by using a dilute approximation procedure:

$$\mathbf{J}_i = - \left( \rho_g D_{i,m} + \frac{\mu_t}{Sc_t} \right) \nabla Y_i - D_{T,i} \frac{\nabla T}{T}, \quad (6.2)$$

where the turbulent Schmidt number,  $Sc_t$  is equal to 0.7,  $\mu_t$  is the turbulent viscosity,  $D_{T,i}$  is the thermal (Soret) diffusion coefficient and  $D_{m,i}$  is the mixture diffusion coefficient:

$$D_{m,i} = \frac{1 - X_i}{\sum_{j \neq i} \frac{X_j}{D_{i,j}}}. \quad (6.3)$$

As turbulent diffusivity is generally dominant in turbulent flows, laminar diffusivity is negligible.

$$k_i = A_i \exp \left( -\frac{E_i}{RT_s} \right), \quad (6.4)$$

Here  $k_1$  and  $k_2$  are determined by Eq.6.4 with  $A_1=2 \times 10^5 \text{ s}^{-1}$ ,  $A_2=1.3 \times 10^7 \text{ s}^{-1}$ ,  $E_1=1.046 \times 10^5 \text{ J mol}^{-1}$ ,  $E_2=1.67 \times 10^5 \text{ J mol}^{-1}$ ,  $R=8.314472 \text{ J mol}^{-1} \text{ K}$  is the universal gas constant and  $T_s$  is the particle temperature.

### 6.2.1.1 Heterogeneous reactions

Heterogenous reactions take place between solid and gas phase. In the coal combustion, they occur between the char and surrounding gaseous materials. There are different levels of reaction rates, for example, the reaction R1 between  $\text{O}_2$  and char happens very quickly, meaning they have a high reaction rate. In order to examine the impact of diffusion coefficient on  $\text{H}_2\text{O}$  and  $\text{CO}_2$ , while reacting with char, the following model is used [Yu et al. (2007)]:

$$R_C = \frac{6\alpha_s}{d_s} \left( (K_{Arr})^{-1} + (K_{Dif})^{-1} \right)^{-1} p X_i, \quad (6.5)$$

where  $R_C$  is the reaction rate and  $X_i$  is the mole fraction of the species in the mixture. Another parameter involved is the kinetic rate  $K_{Arr}$ :

$$K_{Arr} = AT_s^n \exp \left( -\frac{E}{RT_s} \right). \quad (6.6)$$

The diffusion rate of the gas is calculated as:

$$R_{Dif} = \frac{Sh D_{gs} \omega_C}{RT_s d_s}, \quad (6.7)$$

where  $Sh$  is the Sherwood number for gas,

$$Sh = 2.0 + 0.6Re^{1/2}Pr^{1/3}, \quad (6.8)$$

and  $D_{gs}$  is the diffusion coefficient:

$$D_{gs} = \frac{8.34 \cdot 10^{-6}T^{1.75}}{p}. \quad (6.9)$$

As mentioned already above, the reactions with oxygen are taking place very quickly, but heterogeneous reactions are much slower and thus the residence time in the bed is increased. The diffusion of the reactants ( $H_2O$ ,  $CO_2$  and  $H_2$ ) is not dominant in the char and therefore negligible [Gerber et al. (2010)]:

$$R_C = K_{Arr} [C_g] \quad (6.10)$$

where  $[C_g]$  is the concentration of the species.

The heterogeneous reactions with their corresponding kinetic rates can be calculated as:



$$K_{Arr_1} = 1.04 \cdot 10^5 \cdot T_c \cdot \exp\left(-\frac{11200}{T_c}\right) \quad [\text{kg m}^{-3} \text{s}]$$



$$K_{Arr_2} = 342 \cdot T_c \cdot \exp\left(-\frac{15600}{T_c}\right) \quad [\text{kg m}^{-3} \text{s}]$$



$$K_{Arr_3} = 342 \cdot T_c \cdot \exp\left(-\frac{15600}{T_c}\right) \quad [\text{kg m}^{-3} \text{s}]$$



$$K_{Arr_4} = 0.342 \cdot \exp\left(-\frac{15600}{T_c}\right) \quad [\text{kg m}^{-3} \text{s}]$$

The char-steam reaction R2 occurs slower than other reactions in the system. It is an endothermic reaction and together with the char-carbon-dioxide reaction (R3) they control the maximum temperature in the reactor. The reaction, R4, (between hydrogen and char) produces mainly methane and it is exothermic. When the temperature and the hydrogen partial pressure are low, R4 becomes very slow. If the hydrogen partial pressure increases and the temperature surpasses 700 °C, the reaction becomes significant. In this work, the reaction rate for reaction R4 is calculated using partial pressure of the species [Wen et al. (1982)], whilst for the reaction rates of reactions R1, R2 and R3, the species concentrations are used.

### 6.2.1.2 Homogeneous reactions

The chemical reaction rate and the turbulent flow have an important impact on homogeneous reactions. The finite rate/eddy-dissipation model has been used to determine the Arrhenius kinetic rate and the eddy-dissipation rate. The kinetic rate can be calculated depending on the dominating regime and it can be either a local reaction or turbulent mixing:

$$R_{i,r} = \min(R_{Arr}, R_{Edd}) \quad (6.11)$$

The kinetic rate constant is given as

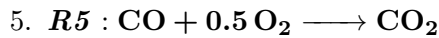
$$R_{Arr} = k_a T^z C_A^n C_B^m. \quad (6.12)$$

The turbulent mixing rate can be calculated by Eddy Break-up model as follows:

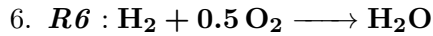
$$R_{Edd} = A \frac{\varepsilon}{k} \min \left[ \min \left( \frac{Y_{R,i}}{S_{R,i}} \right), B \frac{Y_{P,j}}{S_{P,j}} \right], \quad (6.13)$$

where  $A$  and  $B$  are constants and  $S_{P,j}$  and  $S_{R,i}$  are stoichiometric coefficients for reactants and products, respectively.

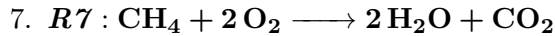
The homogeneous reactions with their corresponding kinetic rates are given as:



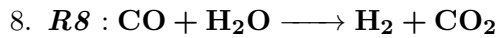
$$K_{Arr_5} = 1.0 \cdot 10^{15} \cdot \exp \left( -\frac{16000}{T_g} \right) [C_{CO}]^{0.5} [C_{O2}]^{1.5} \quad [\text{kg m}^{-3} \text{s}]$$



$$K_{Arr_6} = 5.159 \cdot 10^{15} \cdot \exp \left( -\frac{3430}{T_g} \right) T^{-1.5} [C_{H2}]^{1.5} [C_{O2}] \quad [\text{kg m}^{-3} \text{s}]$$



$$K_{Arr_7} = 3.552 \cdot 10^{14} \cdot \exp \left( -\frac{15700}{T_g} \right) T^{-1} [C_{H2}] [C_{O2}] \quad [\text{kg m}^{-3} \text{s}]$$



$$K_{Arr_8} = 2780 \cdot \exp \left( -\frac{15600}{T_g} \right) \left[ [C_{CO}] [C_{H2O}] - \frac{[C_{CO}] [C_{H2O}]}{0.0265 \cdot \exp(3968/T_g)} \right] \quad [\text{kg m}^{-3} \text{s}]$$

The water-gas shift reaction R5 is quick and dominant in the reactor. The reaction R6 hydrogen-oxygen is extremely fast. Therefore, an assumption can be made that hydrogen cannot exist in the presence of oxygen.

### 6.3 Bubbling fluidised bed reaction modelling with dimpled walls

Chemical reaction modelling has been implemented by developing a UDF code in ANSYS Fluent 14.5. The devolatilisation of coal, using the Kobayashi two-step model (accountable for high temperature and low temperature situations), a gas-gas homogeneous reaction and gas-char heterogeneous reactions are considered. The models are tested in a bubbling bed in order to validate the results with the available data from the literature [[Ocampo et al. \(2003\)](#); [Yu et al. \(2007\)](#); [Armstrong et al. \(2011a\)](#)]. Here, two cases are considered - for the first one the diffusion coefficient for the reaction between  $\text{H}_2\text{O}$  and  $\text{CO}_2$  and char is calculated [[Yu et al. \(2007\)](#)] and for the second one, the diffusion is considered only for the combustion of char as this reaction is very quick and others are calculated by concentrations [[Gerber et al. \(2010\)](#); [Armstrong et al. \(2011a\)](#)]. Moreover, the modification of the reactor walls is implemented to investigate the effect on the chemical reactions of coal gasification. The dimpled wall structure from Ch. 5 is used here and the results are compared with the flat wall BFB reactor.

Table 6.1: Operating conditions of the BFB reactor.

Operating conditions	Model
Air supply [ $\text{kg h}^{-1}$ ]	8.0
Steam supply [ $\text{kg h}^{-1}$ ]	21.9
Coal feed [ $\text{kg h}^{-1}$ ]	4.6
Air and steam temperature at entrance [°C]	420
Temperature of reactor [°C]	855
<i>Experimental result</i> [ <a href="#">Ocampo et al. (2003)</a> ]	
$\text{H}_2$ [%]	8.53
$\text{CO}_2$ [%]	19.31
$\text{N}_2$ [%]	60.37
$\text{CH}_4$ [%]	0.84
CO [%]	10.94

#### 6.3.1 Geometry and boundary conditions

The geometry (Fig. 6.1) and gas-solid phase parameters are taken from the literature [[Armstrong et al. \(2011a\)](#); [Yu et al. \(2007\)](#); [Gerber et al. \(2010\)](#)]. The reactor height is 2 m and the width is 0.22 m. The solid phases are coal, char and sand in the reactor. The fuel feeding inlet has a height of 0.3 m. A total of 1614 quadrilateral cells are used in near the coal inlet and the mesh is denser to capture the devolatilisation. Initially, the whole reactor is set to 1128 K and the initial volume fraction of sand and char is 0.24 at the height of 1 m. The gas mixture has 8 different species:  $\text{O}_2$ ,  $\text{H}_2\text{O}$ ,  $\text{CO}_2$ , CO,  $\text{CH}_4$ ,  $\text{H}_2$ ,  $\text{N}_2$  and tar ( $\text{C}_6\text{H}_6$ ). The coal properties can be seen in table 6.2. There are

Table 6.2: Coal properties used in the simulations.

<b><i>Coal properties</i></b>			
<i>Proximate analysis (wt %)</i>			
Moisture	2.6		
Volatile matter	41.8		
Fixed carbon	54.1		
Ash	1.5		
<i>Ultimate analysis (wt %)</i>			
Carbon	75.3		
Hydrogen	5.4		
Oxygen	15.6		
Nitrogen	1.8		
Sulphur	0.4		
Ash	1.5		
<i>Others</i>	<i>Sand</i>	<i>Coal</i>	<i>Char</i>
Mean particle size [m]	0.0006	0.0006	0.0006
Apparent density [ $\text{kg m}^{-3}$ ]	2700	1250	450

three solid phases - coal, char and sand, where sand is used to promote char fluidisation. Three different mesh sizes are used in order to have a grid independent solution.

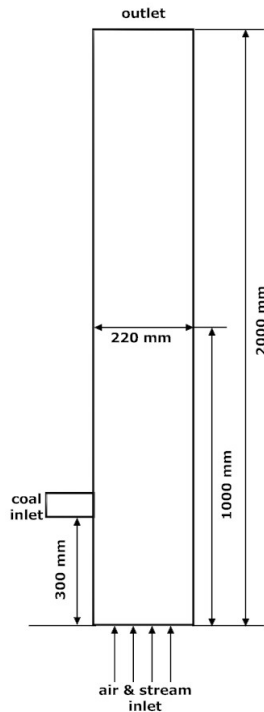


Figure 6.1: Geometry of the BFB reactor.

### 6.3.2 Results and discussion

Here, the novel dimpled wall design is applied to the BFB reactor. The reaction modelling is simulated in ANSYS Fluent 14.5 using UDF. Gerber [Gerber et al. (2010)] and Yu [Yu et al. (2007)] reaction models are used to describe coal gasification, while for coal devolatilisation the Kobayashi's two-step model is used. For the first step, low temperature reactions are considered and for the second step, high temperature ones. To validate the chemical reaction modelling, flat wall reaction products are compared with the experimental and computational data from the literature [Yu et al. (2007); Gerber et al. (2010); Armstrong et al. (2011a)]. It can be concluded that the results are in a fairly good agreement with the experimental data. Indeed, the dimpled wall has a vital impact on the fluidisation behaviour and gasification products.

### 6.3.3 Volume fractions

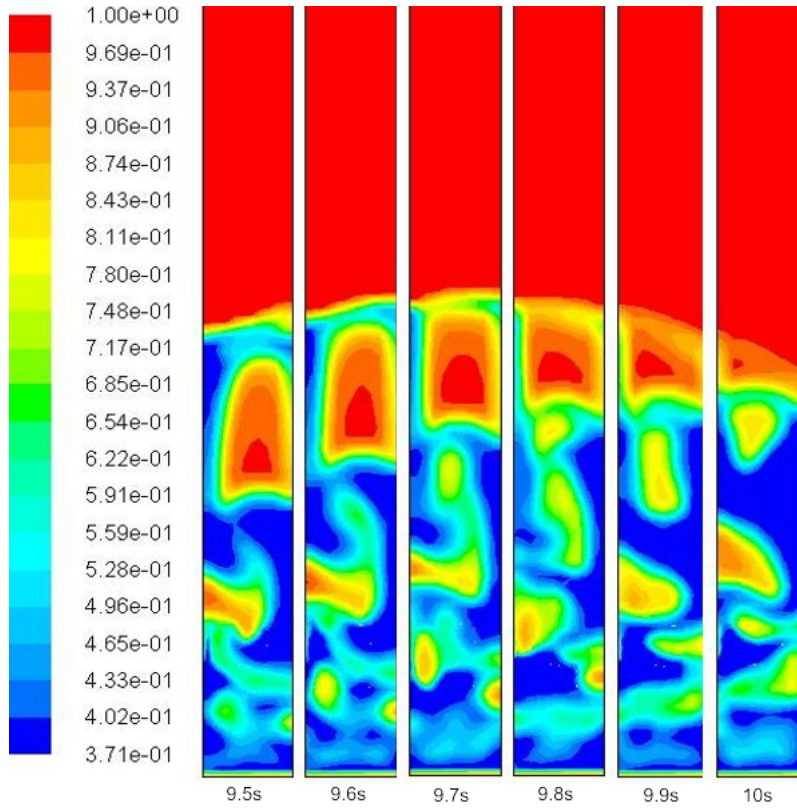


Figure 6.2: Gas volume fraction between 9.5 s and 10 s in a flat wall BFB reactor.

The fluidisation of the reactor is presented here in order to capture the four-phase (i.e. gas, coal, char and sand) interaction. Coal, char and sand have different densities  $1250 \text{ kg m}^{-3}$ ,  $450 \text{ kg m}^{-3}$  and  $2500 \text{ kg m}^{-3}$ , respectively, but they share the same particle diameter of  $0.0006 \text{ m}$ . After a steady state in the reactor is reached, the gas volume fraction is captured from 9.5 s to 10 s (Fig. 6.2). It can be seen that due to the coal

devolatilisation, the bubble formation starts at the bottom and the left side of the reactor. By increasing the height, the bubble size is grows as well. Small bubbles coalesce together and form large bubbles until reaching the top, where they break up. The reason for the bubble growth is the decreasing of the solid above the bubble, which due to the gravity pushes the bubbles together to coalescence. Bubble forming and breaking change the bed height too. Bubbles basically facilitate the mixing in the reactor. Yet, the bubbles, which carry gases inside that cannot come into contact with the fuel, affect the heterogeneous reactions.

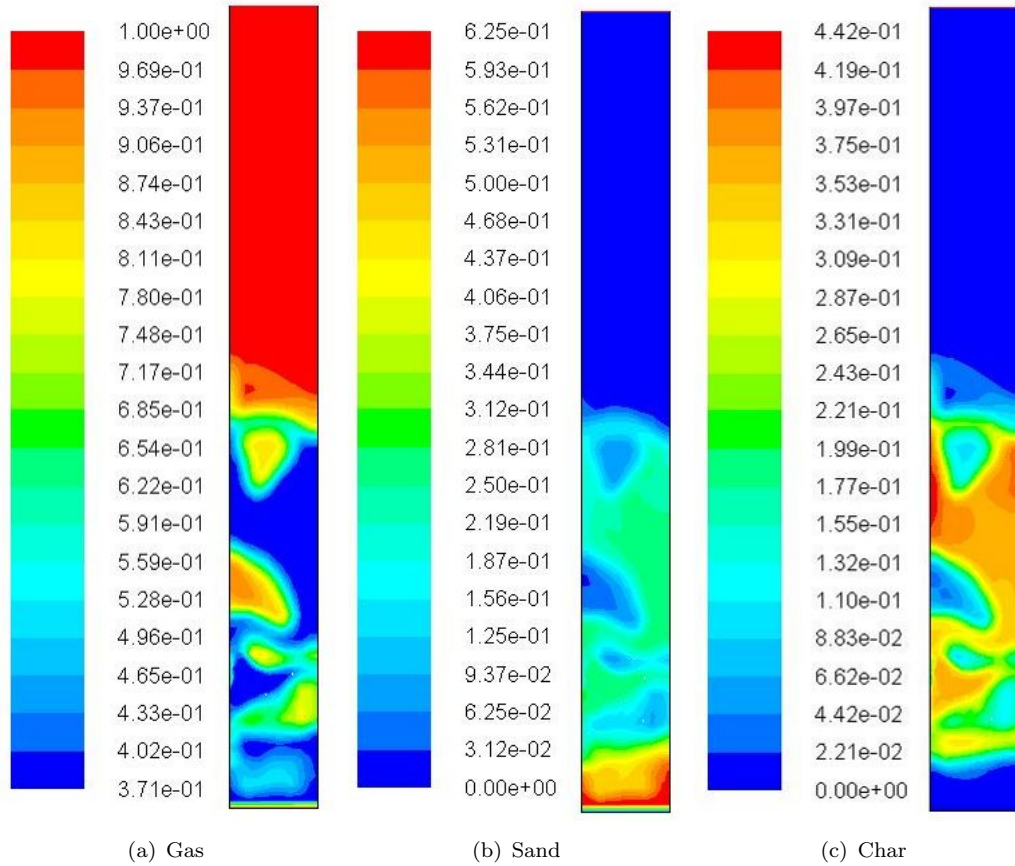


Figure 6.3: Volume fractions of (a) gas, (b) sand and (c) char at 10 s.

Fig. 6.3 displays the segregation effect due to density difference between char and sand. The sand has a higher density so it remains at the bottom of the reactor and pushes up the char, which has a lower density. This may delay the char-gas heterogeneous reactions due to the lack of char there. As can be seen in Fig. 6.3, the char phase bubbles are larger than the sand ones and the sand has a lower volume fraction in higher regions due to segregation.

After the validation of the reaction kinetics with the literature [Armstrong et al. (2011a); Yu et al. (2007); Gerber et al. (2010)], the same conditions are applied to the dimpled wall reactor. The dimpled structures used here are described in detail in Ch. 5 (see Fig.

5.2). Fig. 6.4 shows the gas volume fraction within the shallow dimpled wall reactor. The bubbles are formed at the bottom of the reactor after reaching the steady state. At the start, a similar behaviour of the bubbles is observed here and in the flat wall reactor (see Figs. 6.3 and 6.4). In Fig. 6.4 shows that once the dimpled structure occurs, bubble size starts to increase as well (see Fig. 6.3). The formed bubbles increase and coalescence with the bubbles following in the middle of the reactor at 9.7 s. Afterwards, both bubbles form a large bubble and keep rising together until they reach the top of the reactor. The break up in the shallow dimpled wall happens at 10 s in comparison to 9.8 s in the flat wall (see Figs. 6.3 and 6.4). When the bubble size increases, the hydrodynamics of the reactor changes as well. In particular, bed height increases with dimpled structure as the dimples cause higher velocities. In addition, larger bubble size promotes the homogeneous reaction in the bubble. It is possible to reach a similar bubble size and bed height with lower velocities which in return can reduce energy consumption.

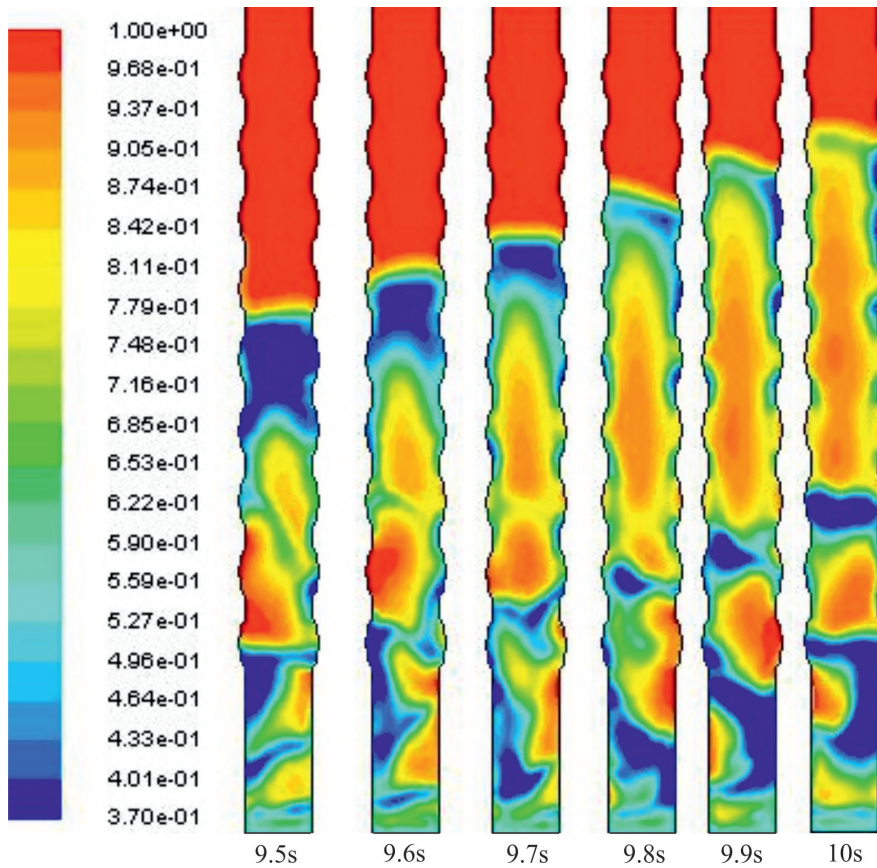


Figure 6.4: Gas volume fraction between 9.5 s and 10 s in a shallow dimpled wall BFB reactor.

The same conditions are reapplied to a deep dimpled wall as shown in Fig. 6.5. The most significant effect of the deeper dimpled wall is the reduction of the bubble size. The recirculation created by the deep dimples is much stronger. Stronger recirculations do not allow the bubbles to increase their size. While breaking the bubbles down, the deep dimples are increasing the mixing effect in the reactor. The break up of the bubbles at

the top of the reactor happens at the same time as the flat one. But the bed height is higher again, which means that with lower velocities the same fluidisation regime can be reached. Both dimple structures give a totally different fluidisation behaviour making them versatile for various applications.

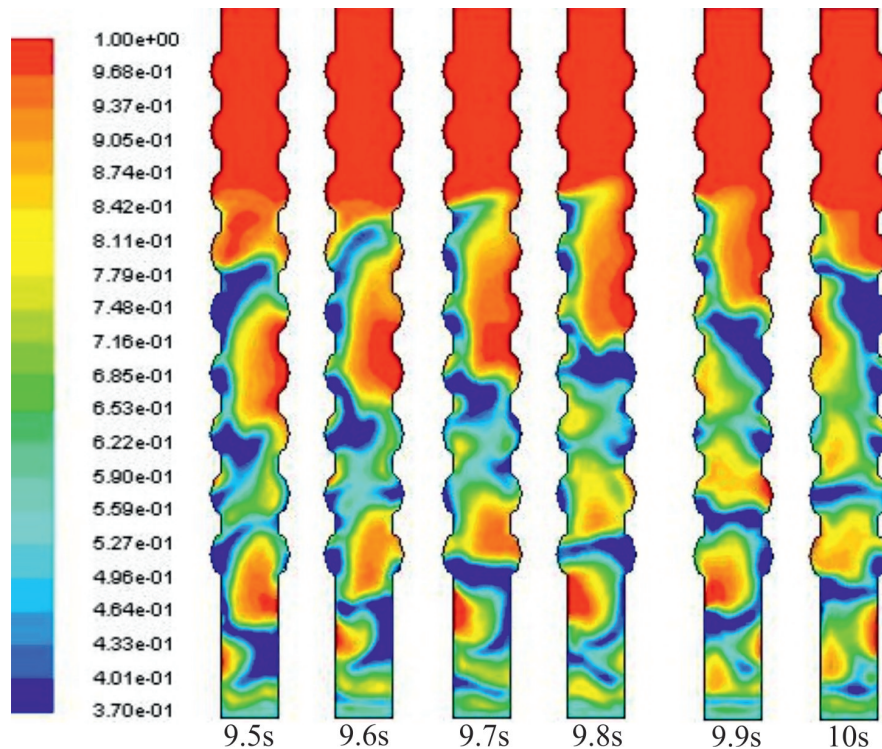


Figure 6.5: Gas volume fraction between 9.5 s and 10 s in a deep dimpled wall BFB reactor.

Dimples significantly change the hydrodynamical behaviour of the BFB reactor. As a result, this can have an impact on the gasification products and reaction kinetics in the reactor.

#### 6.3.4 Temperature distribution

#### 6.3.5 Gasification products

The gasification products, predicted with a diffusion coefficient from the heterogeneous reactions R2 and R3, are shown in Fig. 6.7 and without a diffusion coefficient in Fig. 6.6. The data was taken 0.3 m below the outlet. It can be seen that the products constantly increase until reaching the saturation point. The CH<sub>4</sub> production is quite low, because this endothermic reaction, R4, is strongly temperature dependent and is approachable above 1000 K. There is a difference between reactions R2 and R3 as the product CO from reaction R3 is slightly increased. But, in the case of reaction R2, we can see that

$H_2$  production has increased three times and the reduction of  $H_2O$  is 25% in comparison to the calculated concentration model (Fig. 6.6). It can be argued that  $H_2O$  is sensitive to the diffusion coefficient, whereas  $CO_2$  is not, while reacting with char.

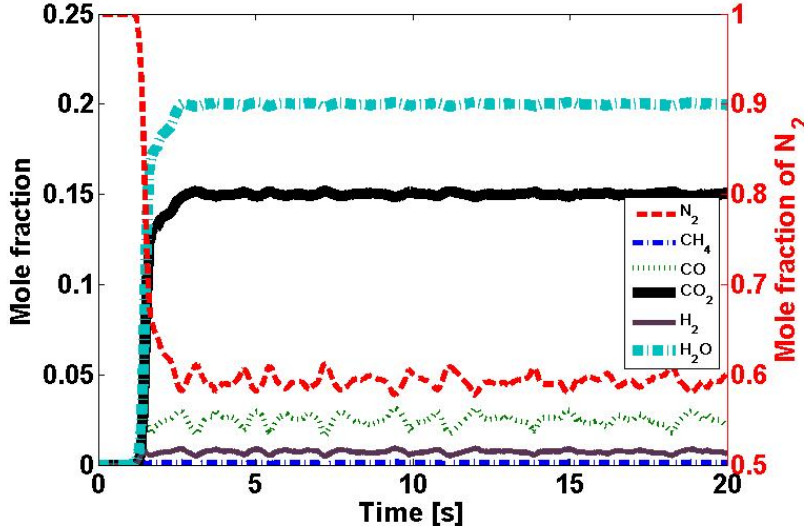


Figure 6.6: Mean mole fraction of exiting products calculated using Gerber's model [Gerber et al. (2010)].

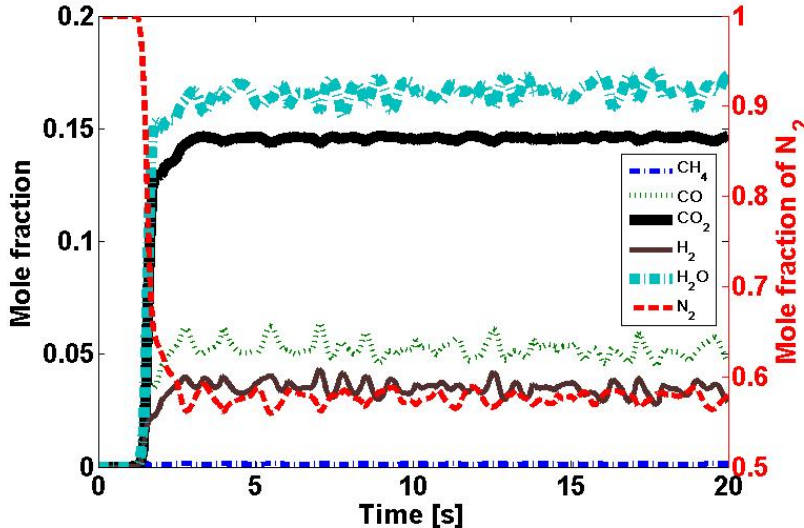


Figure 6.7: Mean mole fraction of exiting products calculated using Yu's model [Yu et al. (2007)].

The combustion reactions take place very quickly and they are dominant at the bottom of the reactor. But the segregation effect (see Fig. 6.3) of char and sand (at the bottom of the riser), due to their large difference in densities, postpones the reactions and develops after the sand dominant region. Therefore, char and oxygen react later. Thus, the segregation can be particularly a problem in higher velocity applications with oxygen

carriers like chemical looping combustion, where solid-solid interaction is also important for the combustion process.

At the top of the reactor, the dominant reaction is the water-gas shifting (R8). It has a significant effect on the mole fraction distribution of the species. It is a quick reaction and, as same as every reaction, it is very temperature dependent. In an ideal case, the reaction must reach equilibrium (usually in very high temperatures), but as we can see in the case with the diffusion coefficient in Fig. 6.7, fluctuations are higher due to a higher consumption of  $\text{H}_2\text{O}$ .

Finally, near the fuel inlet, a high production of species can be observed due to the coal devolatilisation. Most of the gasification products are created in this region; afterwards, they spread throughout the bed and react with the char and participate in homogeneous reactions and gas-water shifting. Although, the models with diffusion (Eq. 6.5) and without diffusion (Eq. 6.10) are slightly different, it can be concluded from Fig. 6.8 that the results from the flat wall geometry are in good agreement with the experimental data [Armstrong et al. (2011a); Yu et al. (2007); Gerber et al. (2010)]. The dimpled wall geometry behaves differently, which may confirm that dimples have effect on the gasification products. The main reason for the difference between the dimpled and the flat wall reactor is most probably the water-gas shifting reaction (R8). Dimples keep the products in the reactor longer and stimulate the backward reaction of reaction (R8).

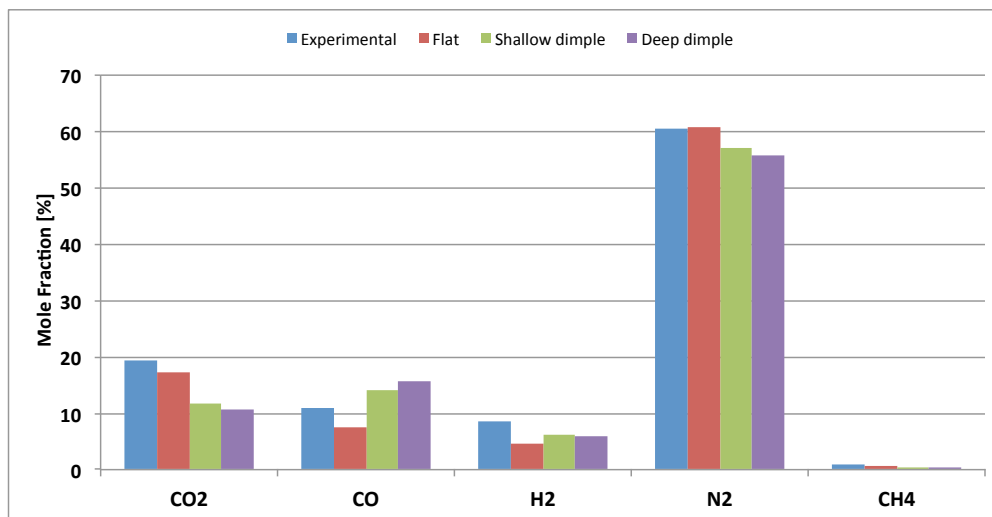


Figure 6.8: Mean mole fraction of the exiting gaseous products  $\text{CO}_2$ ,  $\text{CO}$ ,  $\text{H}_2$ ,  $\text{N}_2$  and  $\text{CH}_4$  in flat, shallow and deep BFB reactors.

Mean mole fractions of the gasification products of the coal combustion in the deep dimpled wall reactor are shown in Fig. 6.9 and 6.10. It can be clearly seen that the combustion products are concentrated at the bottom of the reactor as confirmed in the literature [Armstrong et al. (2011a)]. However, the other products are distributed

towards the top of the reactor. As the N<sub>2</sub> and H<sub>2</sub>O enter via the air/steam inlet, CO<sub>2</sub>, N<sub>2</sub> and H<sub>2</sub>O show higher mole fractions at the bottom of the reactor.

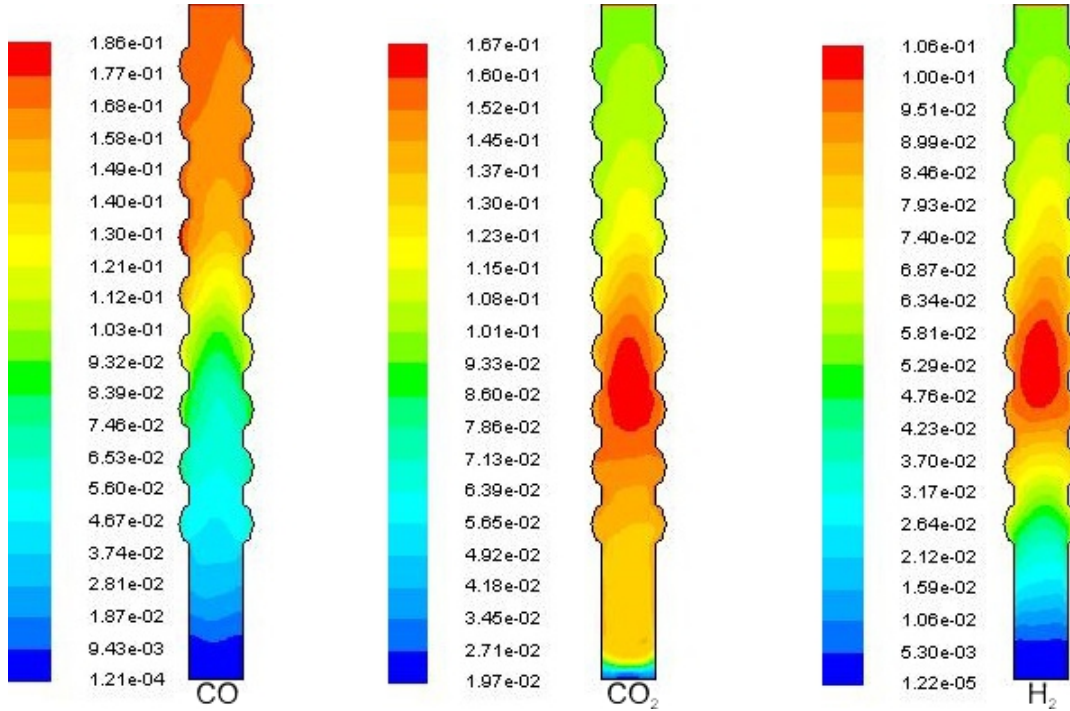


Figure 6.9: The mean mole fractions of CO, CO<sub>2</sub> and H<sub>2</sub> in a deep dimpled BFB reactor.

CO<sub>2</sub>, in particular, is dominates the bottom of the reactor as it is one of the basic products of heterogeneous combustion. The bottom dominating gases are decreasing with an increase in reactor height because they are being consumed by other reactions at the middle and top of the reactor. However, CH<sub>4</sub>, H<sub>2</sub> and CO molar fractions build up at the higher regions of the reactor as they are the outcome of heterogeneous reactions and they are accumulating at the top regions of the reactor in order to take part in further reactions. At the top of the reactor, a water-shift reaction takes place, but in the deep dimpled wall reactor the water shift takes place right above the middle of the reactor due to the recirculation of the products from coal combustion. Water has a very low mole fraction in this region as can be seen in Fig. 6.10. The dimple phenomenon does not allow gasification products to leave the reactor. Due to dimples, the recirculation leads to a longer entainment of the species in the reactor and it gives more time for the gasification products to react.

The segregation is decreased in comparison to the flat case, as can be seen from the CO<sub>2</sub> mole fraction in Fig. 6.11. The sand settled at the bottom of the reactor in lesser quantities. The CO<sub>2</sub> mole fraction indicates that the sand prevents the char to react with O<sub>2</sub> which means that CO<sub>2</sub> cannot be produced.

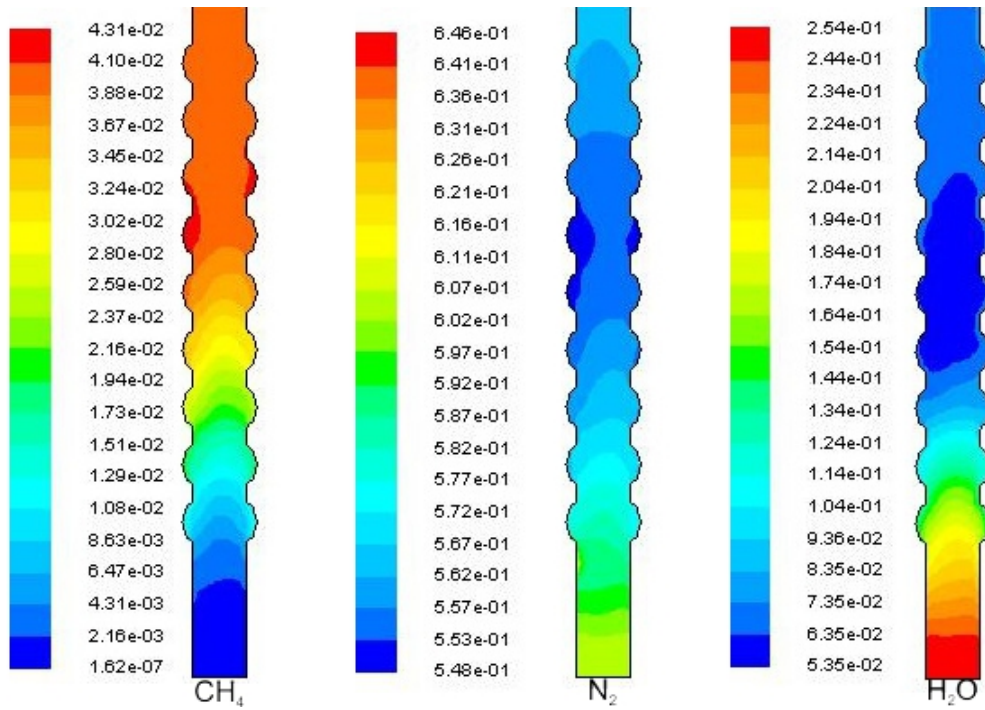


Figure 6.10: The mean mole fractions of  $\text{CH}_4$ ,  $\text{N}_2$  and  $\text{H}_2\text{O}$  in a deep dimpled BFB reactor.

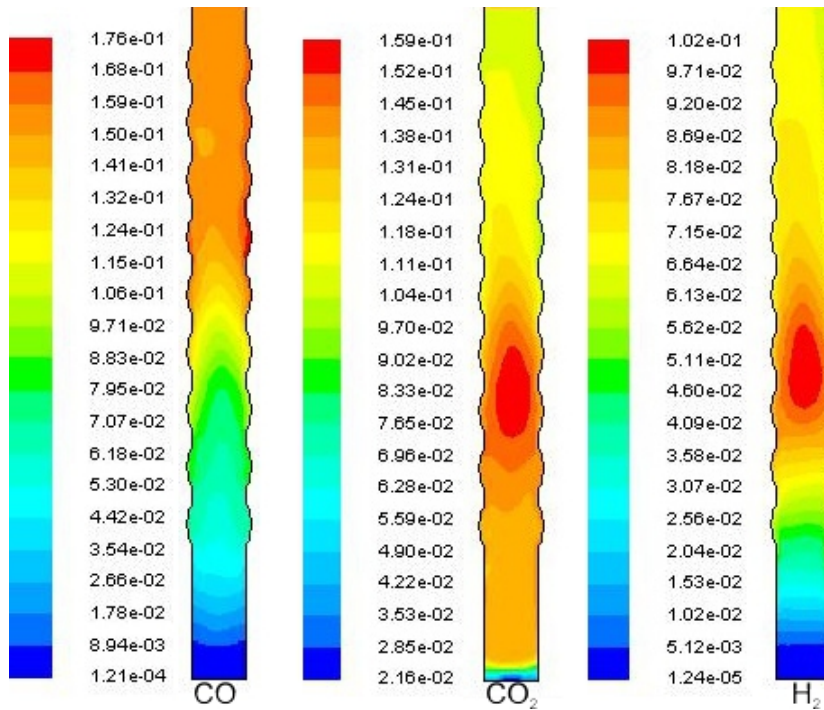


Figure 6.11: Mean mole fractions of  $\text{CO}$ ,  $\text{CO}_2$  and  $\text{H}_2$  in a shallow dimpled BFB reactor.

In terms of the gasification products, the shallow dimpled reactors give similar results to the deep dimpled one (see Figs. 6.9 and 6.10). Also, at the bottom of the reactor, near

the air/steam inlet,  $\text{H}_2\text{O}$ ,  $\text{CO}_2$  and  $\text{N}_2$  have the highest concentration.  $\text{CO}_2$  is produced by the heterogeneous reaction, R1, which is a char combustion. Afterwards,  $\text{CO}_2$  is consumed by the reactions at the top of the reactor. The  $\text{H}_2\text{O}$  concentration is very high at the bottom of the reactor because air contains water which is then needed in water-shift and other reactions.  $\text{O}_2$  is consumed immediately by the char at the bottom of the reactor, so almost nothing is left for the top of the reactor. One of the reasons to have a high mole fraction for  $\text{CO}$ ,  $\text{CH}_4$  and  $\text{H}_2$  at the top of the reactor is that there is not enough  $\text{O}_2$  concentration left for the homogeneous reactions R5, R6 and R7.

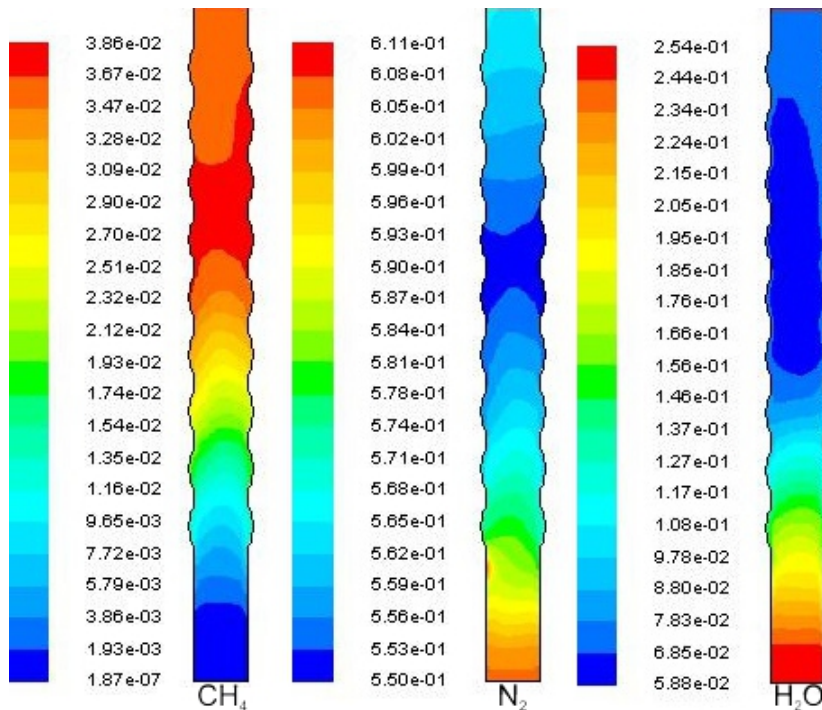


Figure 6.12: The mean mole fractions of  $\text{CH}_4$ ,  $\text{N}_2$  and  $\text{H}_2\text{O}$  in a shallow dimpled BFB reactor.

The segregation is again less than in the flat case but there is still some sand which settled at the bottom of the reactor, because the dimple structures do not start from at beginning of the reactor.

### 6.3.6 Conclusion and summary

The coal gasification model is presented here and computed in ANSYS Fluent 14.5 using its UDF utility. Simulations show good agreement with the experimental data [Armstrong et al. (2011a); Yu et al. (2007); Gerber et al. (2010)]. Therefore, this proves once again that CFD is a strong tool to predict such a complex system as coal gasification. Moreover, the results indicate that the modification of the walls can significantly influence the hydrodynamics of the system. Indeed, the bubble size can be altered by

varying the dimple depth. Dimples facilitate the increase of entertainment time of the gaseous products and the mixing in the reactor. Moreover, dimples may decrease the energy penalty by reaching the same fluidisation behaviour with lower velocities. Further parametric and geometrical modification studies are needed for BFB type reactors to uncover better dimple structure properties.

## 6.4 Circulating fluidised bed reaction modelling with dimpled walls

Despite being widely used and being an efficient reactor in coal combustion, modelling of a hot CFB reactor with chemical reactions has been underresearched. Hence, gasification products, the effect of wall modification on the gasification and fluidisation in a CFB reactor are studied here by applying CFD modelling and validating the results with experimental data from the literature [Zhou et al. (2011)].

### 6.4.1 Geometry and boundary conditions

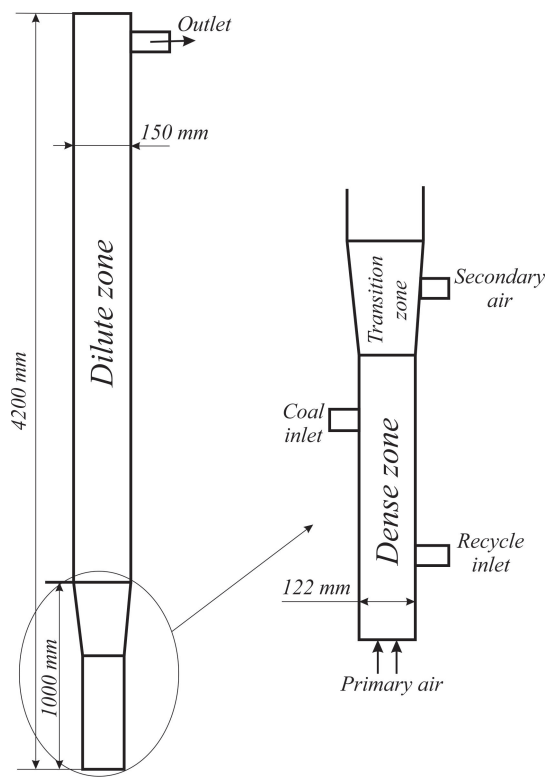


Figure 6.13: Geometry of the CFB reactor.

The geometry is taken from the literature [Zhou et al. (2011)]. The reason for choosing particularly this geometry is that it is a CFB type fluidisation application, although used for oxy-fuel combustion. The reactor has two inlets. The primary inlet is at the bottom of the reactor and the secondary inlet is at 0.9 m in the transition region of the reactor (see Fig. 6.13). Also, it has a fuel inlet on the left hand side above 0.7 m the primary inlet. Besides that, there is a recirculation inlet which is on the right hand side at a height of 0.2 m and connected to a cyclone, which is avoided in the simulations by developing additional boundary conditions in UDF to reintroduce entrained particles

rather than simulate the full feedback system. Furthermore, the EMMS drag model is applied to account for the inhomogeneity of the solid distribution in the reactor.

Table 6.3: Operating conditions of the CFB reactor.

Operating conditions	Model
Air supply primary inlet [ $\text{kg s}^{-1}$ ]	0.15
Air supply secondary inlet [ $\text{kg s}^{-1}$ ]	0.25
$\text{H}_2\text{O}$ supply in primary and secondary inlet [mass fraction]	0.1755
$\text{O}_2$ supply in primary and secondary inlet [mass fraction]	0.1731
Coal feed [ $\text{kg h}^{-1}$ ]	8
Air and steam temperature at entrance [ $^{\circ}\text{C}$ ]	450
Temperature of reactor [ $^{\circ}\text{C}$ ]	850

A totally of 1520 quadrilateral cells are used with a denser mesh near the coal inlet to capture the devolatilisation. Initially, the whole reactor is set to 1128 K and an initial volume fraction of sand and char is set to 0.24 at the height of 0.4 m. The gas mixture has 8 different species:  $\text{O}_2$ ,  $\text{H}_2\text{O}$ ,  $\text{CO}_2$ ,  $\text{CO}$ ,  $\text{CH}_4$ ,  $\text{H}_2$ ,  $\text{N}_2$  and tar ( $\text{C}_6\text{H}_6$ ). The coal properties can be seen in table 6.2. There are three solid phases - coal, char and sand, where sand is used to promote the char fluidisation. A grid independence study is performed with each simulation, which takes nearly two weeks.

In order to describe the momentum interchange between phases, the EMMS model is used. The EMMS model is able to capture the inhomogeneous distribution in the CFB reactors. A pressure outlet is used (i.e. ambient pressure and temperature) and no-slip wall conditions are applied the gas phase. The Johnson and Jackson boundary condition [Johnson and Jackson (1987)] takes into account wall particle collision and wall roughness; thus it was utilised in the model with a specularity coefficient of 0.95.

#### 6.4.2 Results and discussion

The novel dimpled wall design and reaction modelling are applied to the reacting CFB reactor via ANSYS Fluent 14.5 and its UDF utility. The Yu [Yu et al. (2007)] reaction model is used to describe coal gasification and the Kobayashi's two step model coal devolatilisation. In the first step, low temperature reactions are considered and in the second high temperature ones. Mean molar concentrations of  $\text{CO}_2$  and  $\text{O}_2$  are compared to the experimental data from the literature [Zhou et al. (2011)] (see Fig. 6.14). As can be seen the  $\text{CO}_2$  mole fraction is at its lowest in the deep dimpled reactor due to the higher mixing effect and longer residence time of the gasification products and char. Similarly, the  $\text{O}_2$  consumption is higher in the deep dimple as well.

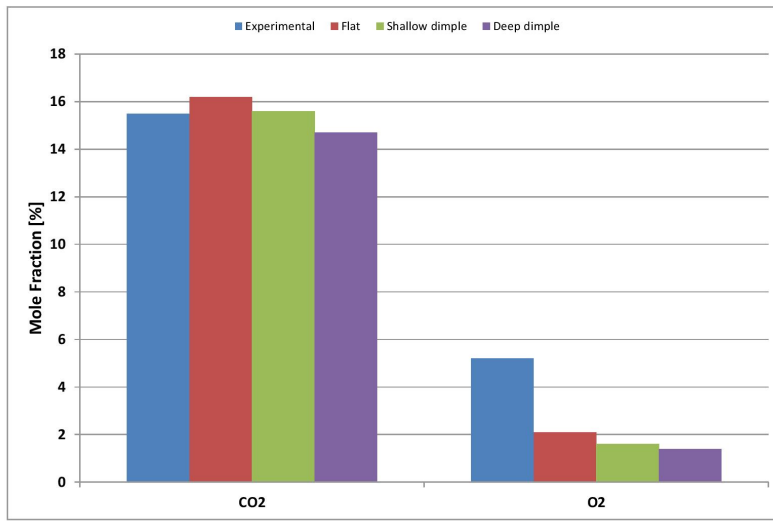


Figure 6.14: Mean mole fraction of the exiting gaseous products CO<sub>2</sub> and O<sub>2</sub> in experimental [Zhou et al. (2011)] and flat, shallow and deep dimple CFB reactors.

#### 6.4.3 Volume fraction

Mean volume fractions of the solid phase are shown in Fig. 6.15. In the hot dimpled CFB reactor, fuel accumulates at the lower part of the reactor. In the flat reactor, the fuel is distributed throughout the reactor, meaning it reaches the outlet much faster. Unlike the shallow one, in the deep dimpled case, the accumulation is reaching higher regions due to weaker circulation observed there. It is expected that the longer stay of fuel may increase the combustion efficiency of the CFB reactor. 3D calculations are probably necessary to understand and analyse the 3D nature of the dimples.

The instantaneous solid volume fractions are presented in Figs. 6.16 for flat, shallow and deep dimpled cases, respectively. The contours show the instantaneous solid volume fraction between 10.5 s and 10.8 s. Apparently, very high volume fraction clusters form in the flat wall case by reaching volume fractions of 0.35 in some regions (Fig. 6.16).

The mean char volume fraction is shown in Fig. 6.17. The bottom of the reactor has higher char volume fraction which is gradually decreasing with the height. At the top of the reactor char accumulation, which is much higher in the flat wall reactor, takes place. This suggests that dimples are helping to increase the residence time of the char in the reactor. Thus, shorter reactors with the same operational conditions may be built. Also, longer char residence time means longer char reactions with the oxygen and the rest of the gasification products which benefit the reactor efficiency.

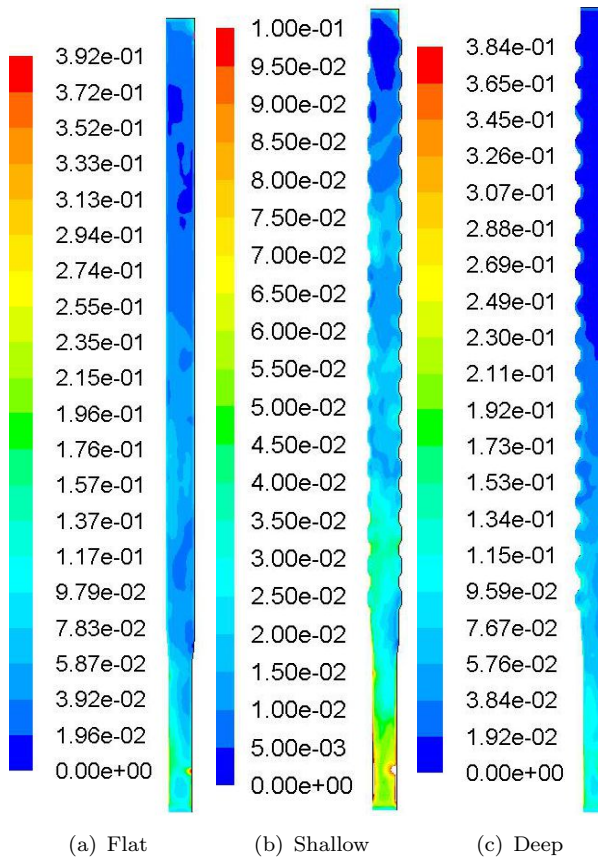


Figure 6.15: Mean solid volume fraction profile in flat, shallow and deep dimpled wall CFB reactors.

Clusters form at the middle of the reactor and then easily trailing by gaining, without any disturbance, more particles throughout the reactor. But in the shallow dimpled case (Fig. 6.18), a more homogeneous distribution is present and accumulation disappears. At 10.5 s, once the accumulation starts near the wall in the lower region, the cluster is pushed by the circulation via dimples to the centre of the reactor and the particles continue to the top of the reactor. There is an accumulation at the top of the reactor at 10.8 s due to the outlet positioning which can be optimised. Fig. 6.19 shows the char volume fraction at top of the reactor. A flat wall allows the particle to pass through the top quickly and due to that char volume fraction is high here. But this is opposite in the dimpled wall reactors. The dimpled wall recirculates the species involved and holds the coal and char longer in the reactor. That could be the reason for the lower char volume fraction at the top of the dimpled wall reactor.

In the deep dimpled wall (Fig. 6.20), accumulation takes place at the bottom of the reactor where walls are flat. But in the dilute region of the reactor, solid distribution is spread all over. Here, the strong circulation restricts the formation of dense and large clusters.

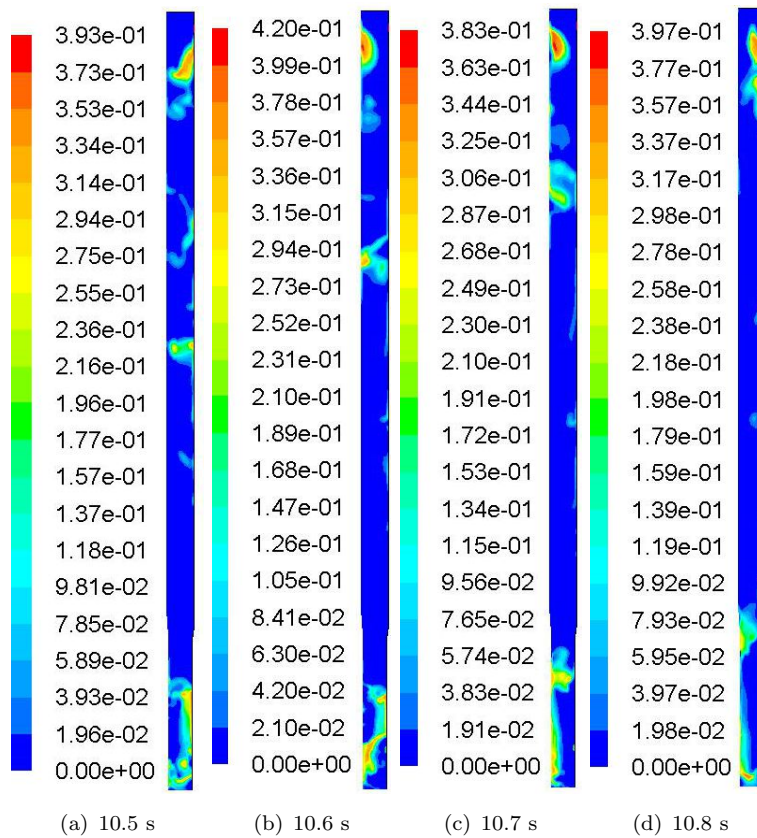


Figure 6.16: Solid volume fraction between 10.5 s and 10.8 s in a flat wall CFB reactor.

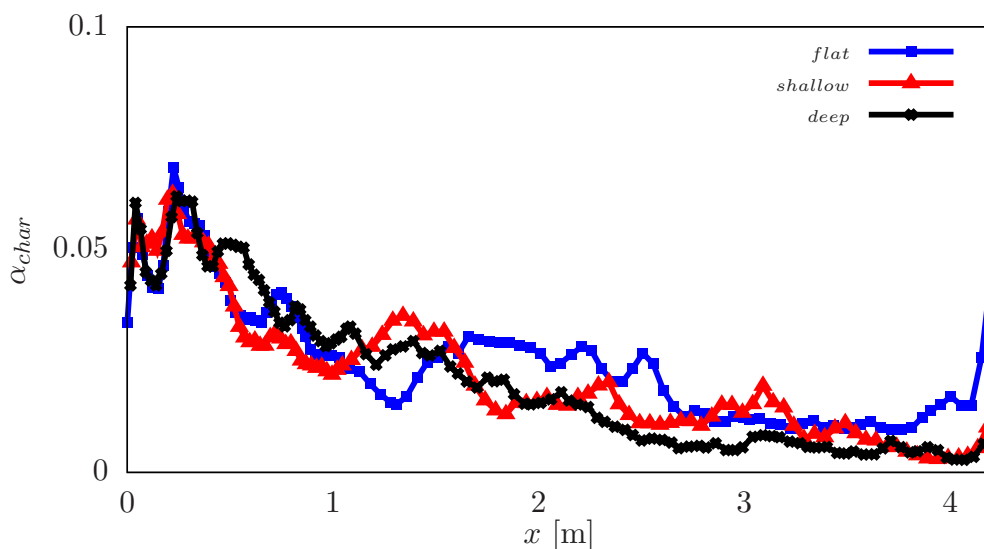


Figure 6.17: Vertical mean char volume fraction profiles for flat, shallow and deep dimpled reactors.

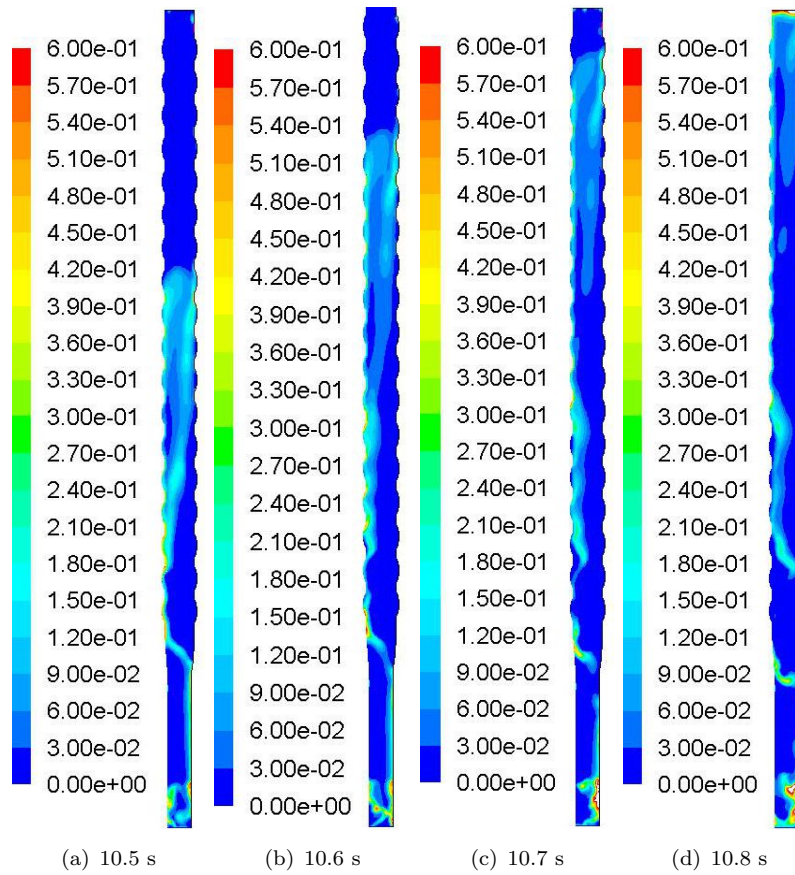


Figure 6.18: Solid volume fraction between 10.5 s and 10.8 s in a shallow dimpled wall CFB reactor.

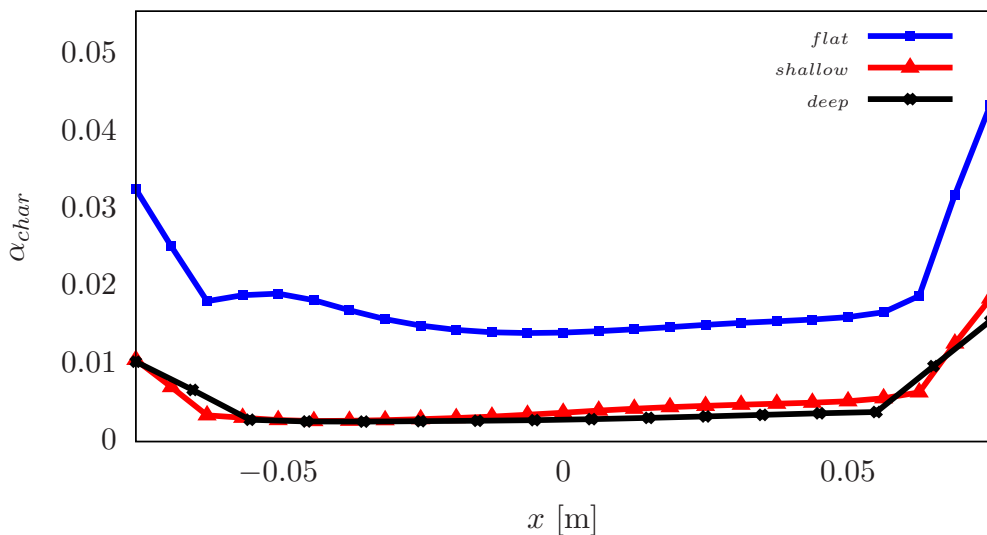


Figure 6.19: Horizontal mean char vertical volume fraction profiles for flat, shallow and deep dimpled wall cases at the top of the reactor.

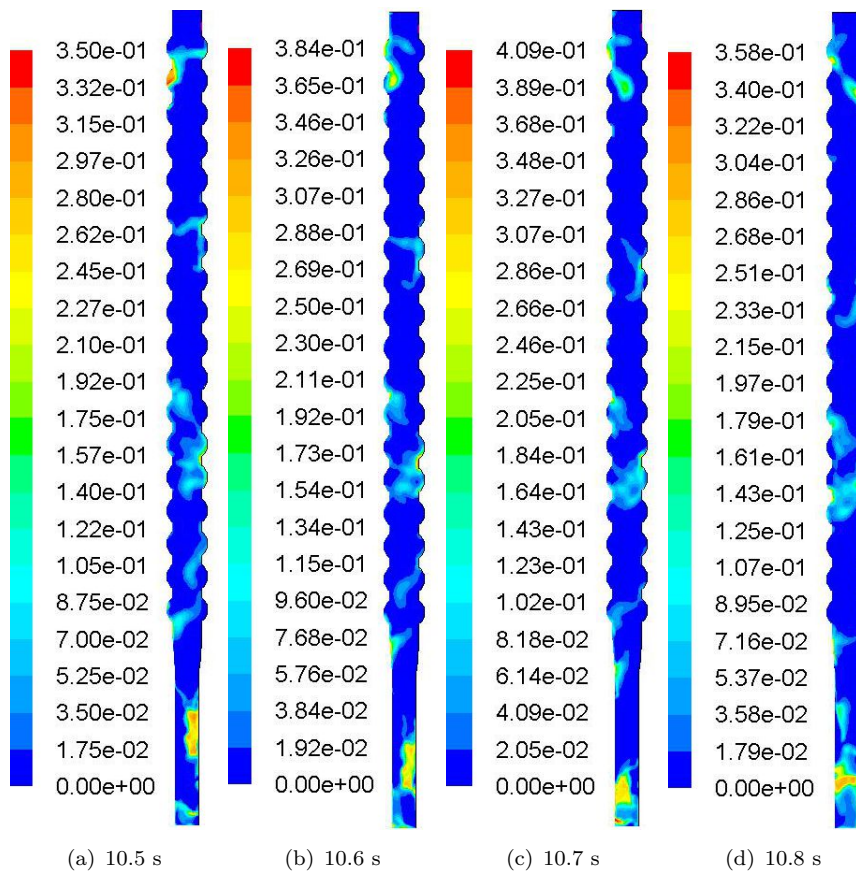


Figure 6.20: Solid volume fraction between 10.5 s and 10.8 s in a deep dimpled wall CFB reactor.

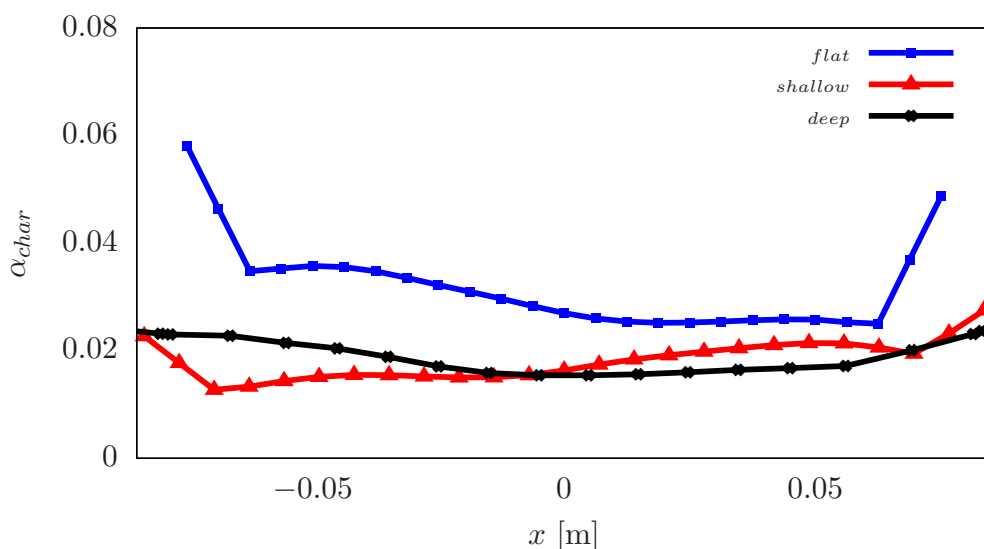


Figure 6.21: Horizontal mean char vertical volume fraction profiles for flat, shallow and deep dimpled wall cases at the middle of the reactor.

Fig. 6.21 presents a similar picture to Fig. 6.19. The flat wall reactor contains higher char volume fraction in the middle of the reactor. Also, clustering is observed near the wall. Dimpled wall reactors show lower char volume fraction near the wall because dimples create recirculation which facilitates the near wall accumulation break down.

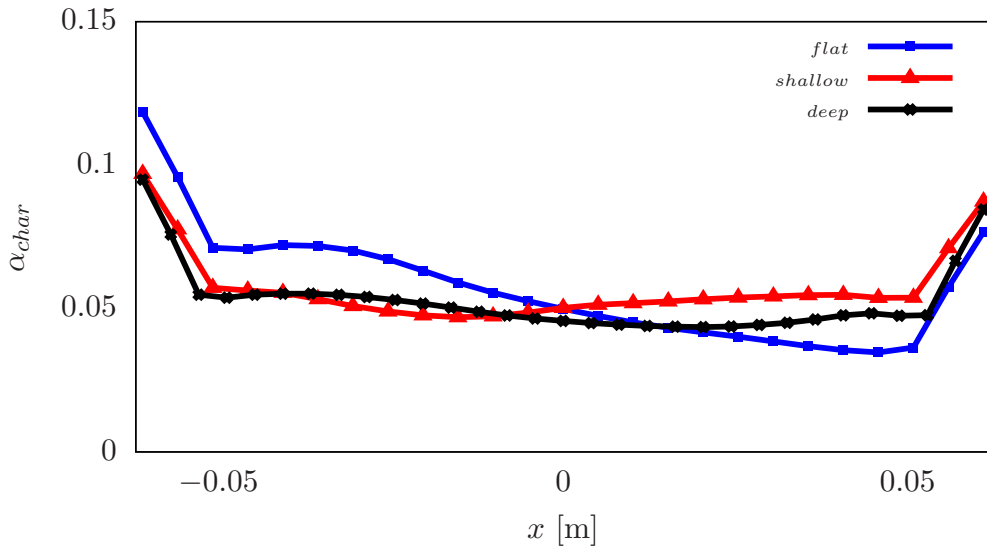


Figure 6.22: Horizontal mean char vertical volume fraction profiles for flat, shallow and deep dimpled reactors at the bottom of the reactor.

Fig. 6.22 shows that all the reactors have similar char volume fractions because all the reactors have flat walls at the bottom (see Fig. 6.13).

#### 6.4.4 Velocity profiles

Time averaged vertical velocities are presented in Fig. 6.23. Negative velocities appear mostly in the dense and second inlet region of the pipe. The reason for that is the high second inlet velocity, a result of gas and particles bouncing back from the walls and creating recirculation in this zone (see Fig. 6.25). As the second inlet velocity is much higher than the main inlet velocity, it causes recirculation leading to the downward movement of the fuel. The reason for using such high velocities in the second inlet is to increase the mixing in reactor [Zhou et al. (2011)]. But it seems that the higher velocity at the second inlet blocks the way of the fuel, coming from the dense region, to rise to the dilute region. A further improvement by decreasing the ratio between primary and secondary inlet velocity is probably needed to optimise the CFB reactor. Fig. 6.24 shows that deep dimpled walls have lower solid velocity due to strong recirculation in the middle of the reactor. Flat and shallow dimpled walls have similar higher velocity profiles as expected.

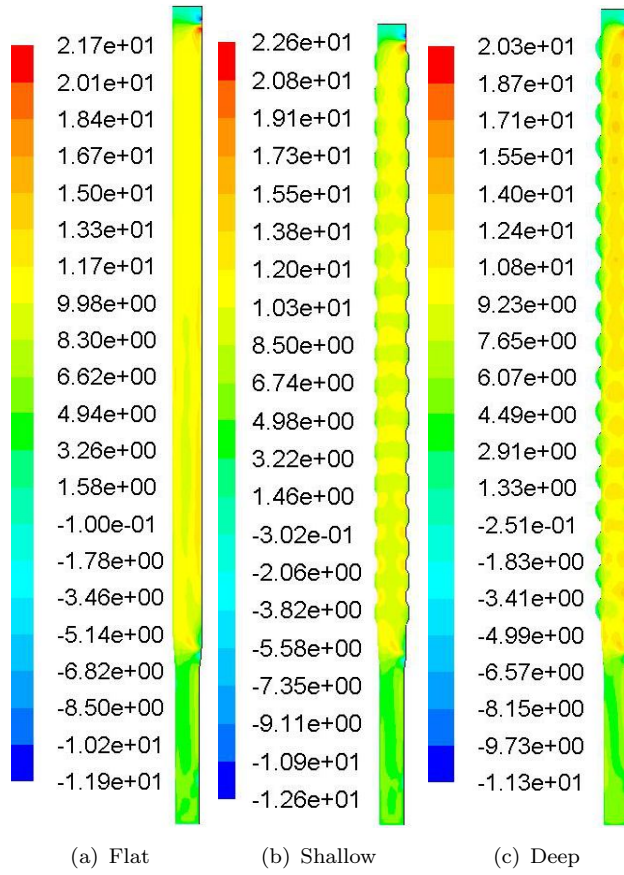


Figure 6.23: Mean velocity profile in a streamwise direction for the gas phase in flat, shallow and deep dimpled wall CFB reactors.

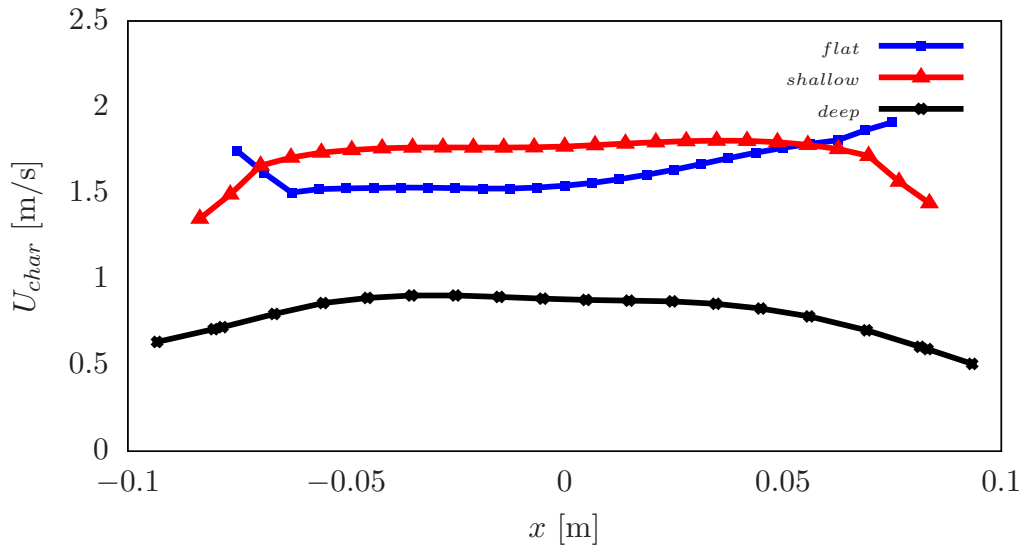


Figure 6.24: Horizontal mean char velocity profiles for flat, shallow and deep dimpled wall cases at the middle of the reactor.

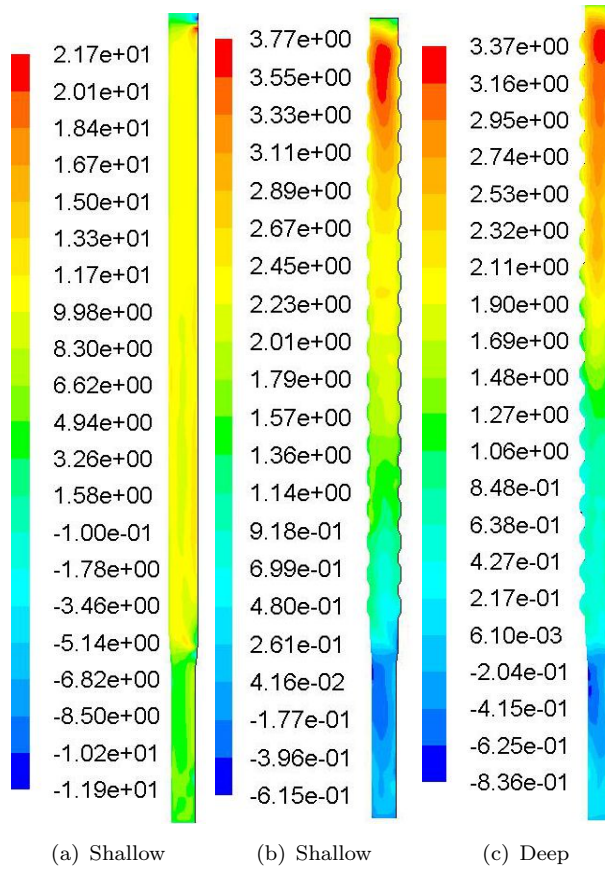


Figure 6.25: Mean velocity profile in a streamwise direction for the particle phase in flat, shallow and deep dimpled wall CFB reactors.

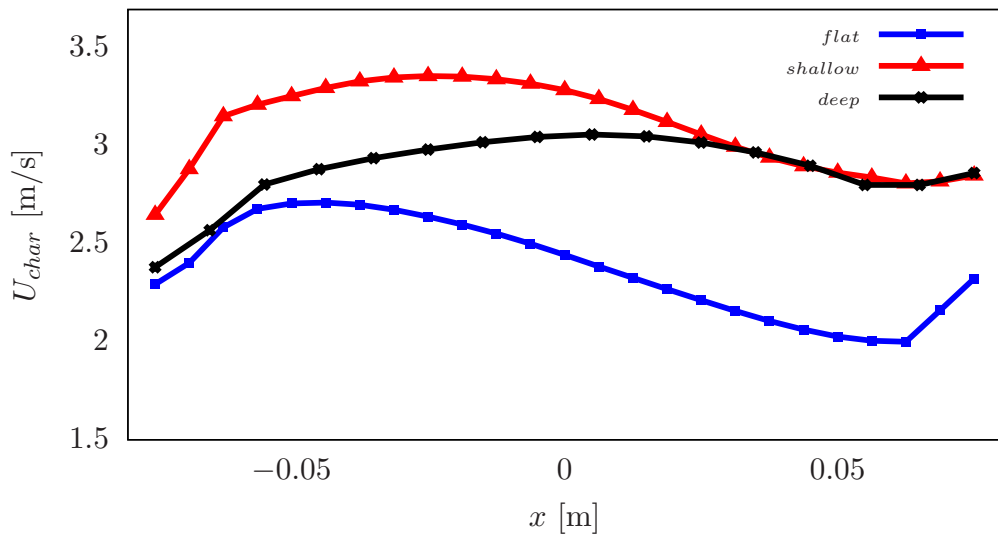


Figure 6.26: Horizontal mean char velocity profiles for flat, shallow and deep dimpled wall cases at the top of the reactor.

Fig. 6.26 shows higher velocity values for dimpled wall cases due to the much less particles concentration in comparison to the flat cases. Thus, a dilute mixture means particles can accelerate, yet there is much less particle-particle collision which means higher kinetic energy for the particles. At the top of the reactor particles accumulate and get blocked which leads to lower char velocity (Fig. 6.17).

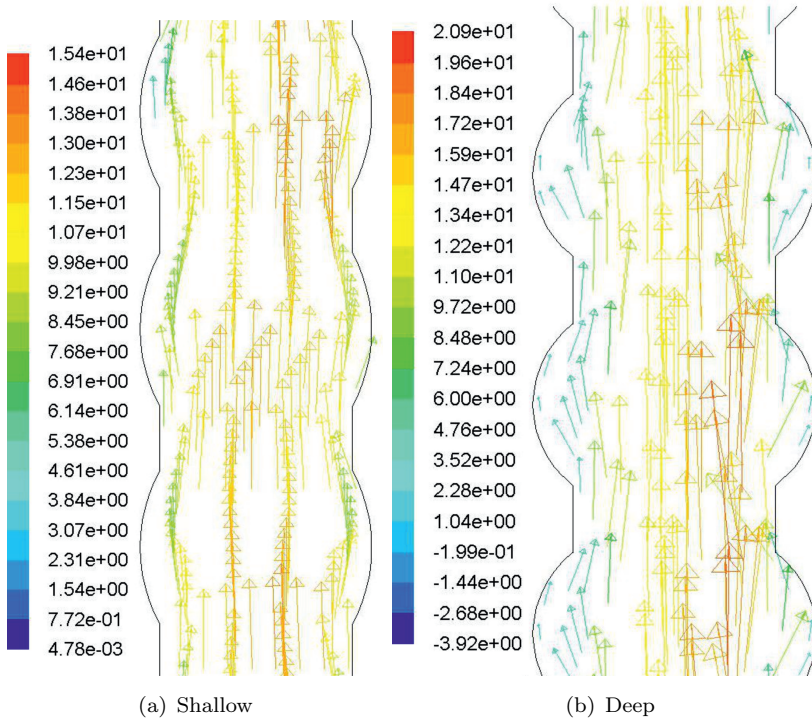


Figure 6.27: Mean velocity vector profile in a streamwise direction for the gas phase in flat, shallow and deep dimpled wall CFB reactors.

Fig. 6.27 displays the vector profiles of gas velocities for both dimple types. In the deep dimple, the gas, forced by the dimples, enters the main region of the reactor. Although in the shallow dimpled wall there is just a slight impact on the velocity vectors, the flow is still pushed inside the main flow. This behaviour is beneficial for mixing, residence time, etc.

#### 6.4.5 Temperature distribution

Experimental data is compared with the flat reactor temperature distribution. As it can be seen in Fig. 6.28, the highest temperature is at the fuel inlet at 1 m of height, because the temperature drop recirculation in the cyclone is not considered in the simulations.

The mean temperature distributions are shown in Fig. 6.29. The distributions are in good agreement with the experimental data from the literature [Zhou et al. (2011)]. Near the secondary inlet, the temperature decreases as colder air comes in and then

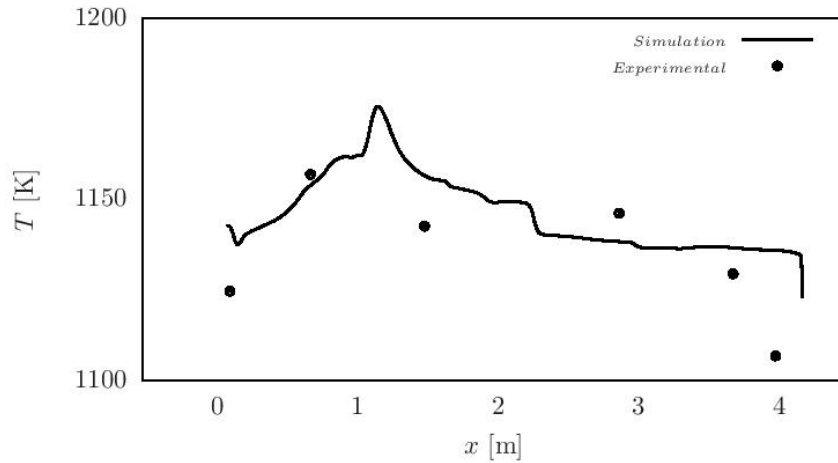


Figure 6.28: Mean temperature distribution in an experimental [Zhou et al. (2011)] and flat wall CFB reactor.

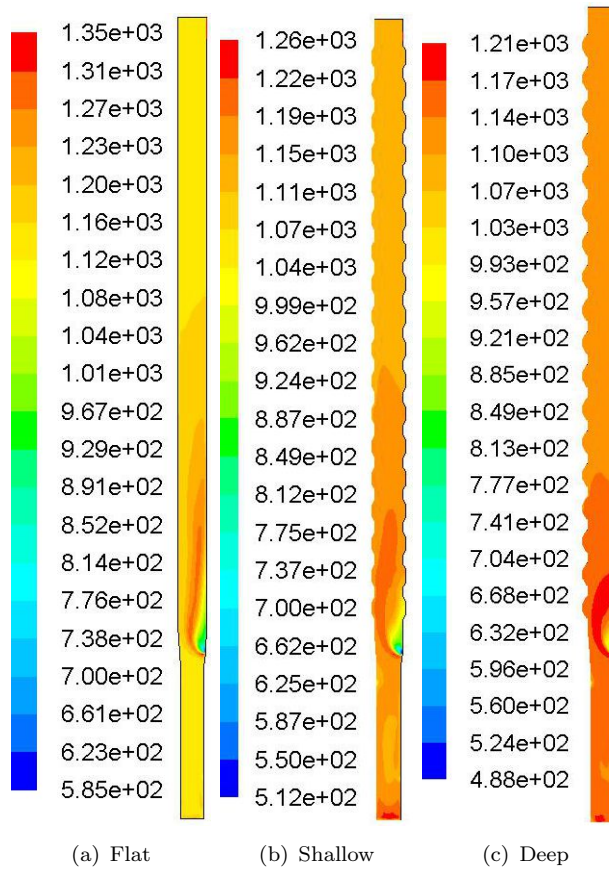


Figure 6.29: Mean temperature distribution in flat, shallow and deep dimpled wall CFB reactors.

suddenly increases due to the rich  $O_2$ , which causes the combustion in this zone. After some time, the top of the reactor starts getting slightly colder because of the reverse

flow from the outlet with a lower temperature.

#### 6.4.6 Heterogeneous reaction rates

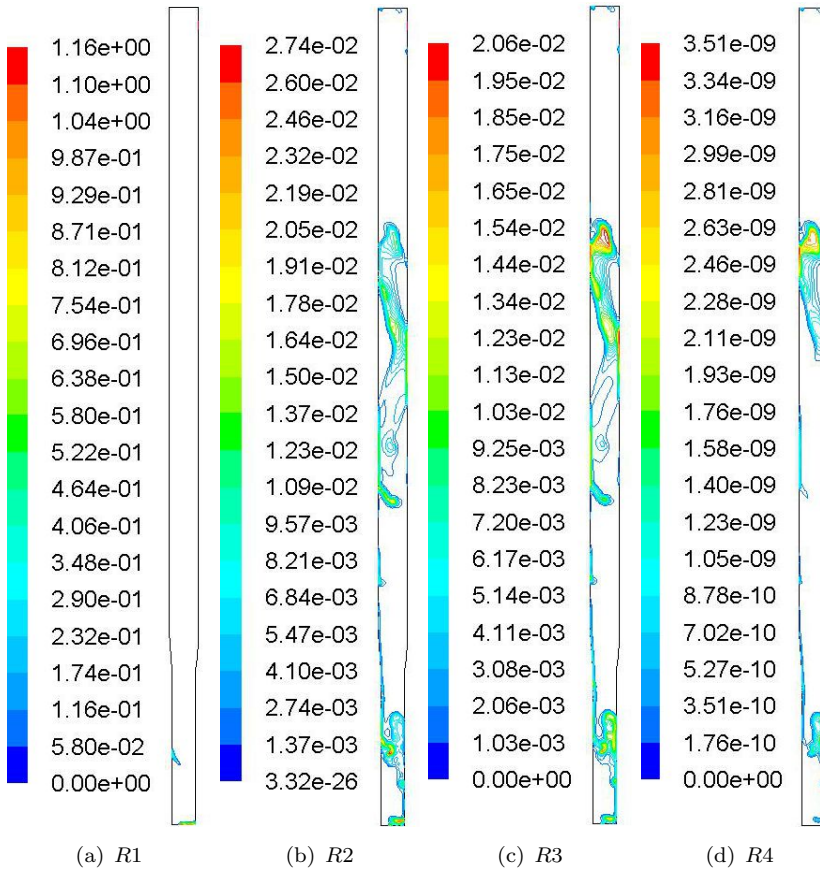


Figure 6.30: Heterogeneous reaction rates for a flat wall reactor.

The reaction rates of the heterogeneous reactions are presented as 2D contour plots in Figs. 6.30–6.32. In the flat wall CFB reactor, the rates are gathered together, whereas in both dimpled cases, they are scattered throughout. The reason for that is the circulating effect of the dimples. Therefore, even more patches are present in the deep dimpled wall reactor (see Fig. 6.32). As it can be seen from Figs. 6.30–6.32, reaction R1 is very fast near the inlets, i.e. the combustion starts when the oxygen enters the reactors. Reactions R3 and R4 behave similarly to reaction R1. Higher rates for reaction R2 occur at the bottom and middle of the flat wall reactor, but R2 reaction is active all over the reactor in the dimpled wall cases. Moreover, due to a higher circulation in the deep dimple case, the highest reaction rates are scattered around the reactor. This shows that wall modifications are affecting the reaction rate distribution in CFB reactors.

Interestingly, when fuel enters the reactor, devolatilisation takes place and produces char, CO, CO<sub>2</sub>, H<sub>2</sub>O, H<sub>2</sub> and CH<sub>4</sub>. Therefore, heterogeneous reactions occur at the fuel

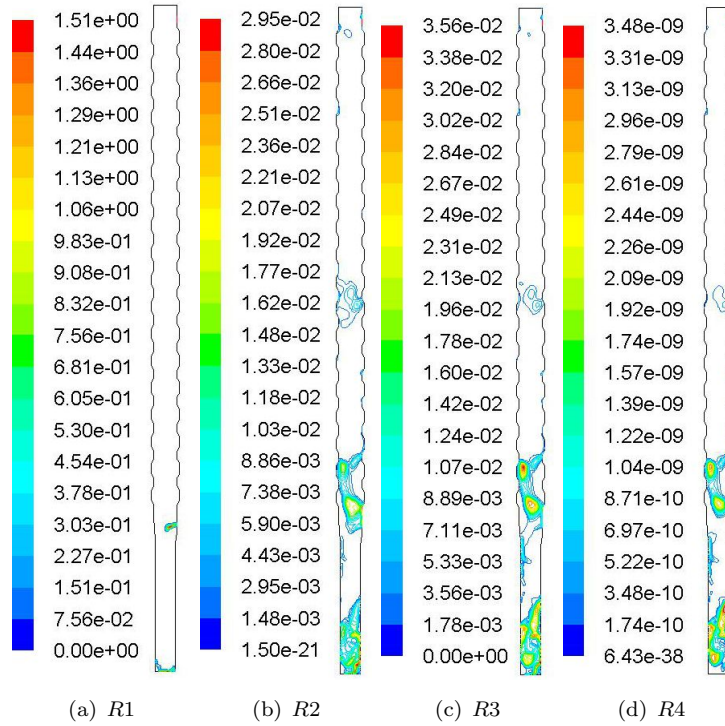


Figure 6.31: Heterogeneous reaction rates for a shallow dimpled wall reactor.

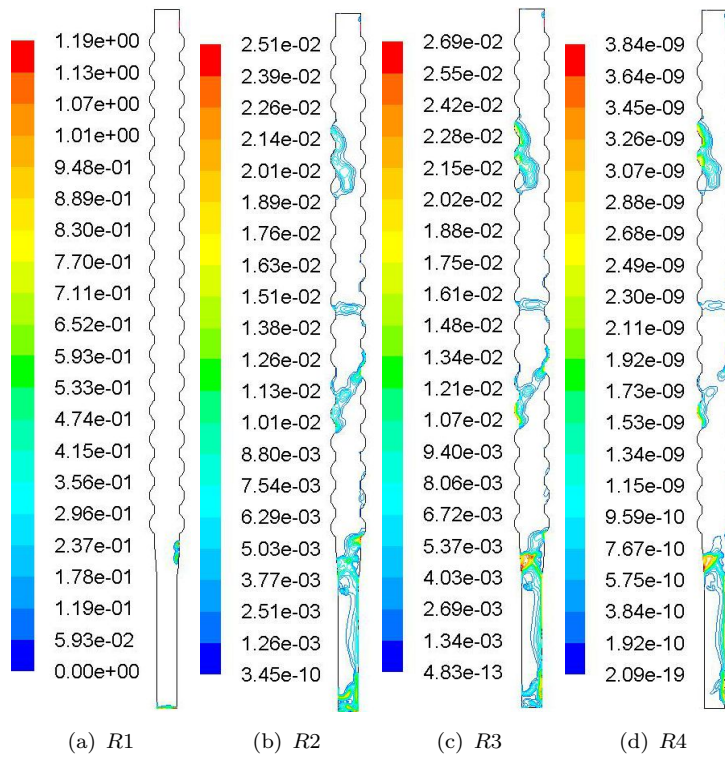


Figure 6.32: Heterogeneous reaction rates for a deep dimpled wall reactor.

inlet as clearly seen in the flat wall reactor (Fig. 6.30). Reactions begin from the coal entrance and continue upwards close to the wall. In contrast, the dimpled structures push devolatilisation products towards the middle and bottom of the reactor and thus change the behaviour of the reaction kinetics in the reactor (Fig. 6.31–6.32).

#### 6.4.7 Gasification products

The developed and validated UDF code in the previous sections for a BFB operating type reactor is applied here and compared with oxyfuel combustion results. Gasification products of coal combustion with air are presented in Figs. 6.33–6.38. The dominant products are  $\text{CO}_2$  and CO for all geometries involved. Comparison with the available literature results [Zhou et al. (2011)] shows that air combustion gives a high concentration of CO. This could be explained with the water-shift reaction R8 which plays a dominant role in the dilute region of the reactor during water existence. The  $\text{CO}_2$  concentration is almost the same as in the oxy-fuel reaction. Obviously, the  $\text{O}_2$  concentration is much lower at the outlet of the air combustion side due to the homogeneous reactions occur in the reactor. It can be seen in table 6.2.1.1 that the products from the water-shift reaction are consuming  $\text{O}_2$  very quickly in the system.

At the outlet of the reactors, the CO concentration is similar for all geometries (Figs. 6.33a, 6.35a and 6.37a). The CO concentration is mainly high at the top of the reactor due to the water-gas shift reaction (R8) and near the secondary inlet because of reactions R2 and R3. Reaction R2 is active near the secondary inlet due to steam entering the inlet and the produced  $\text{O}_2$  burning the available fuel there. As a result,  $\text{CO}_2$  is produced and reaction R3 becomes very dominant in this region. As illustrated in Figs. 6.33a, 6.35a and 6.37a, the CO production is much higher in the dense region of the dimpled wall meaning the wall structure recapitulates the fuel longer.

Similar behaviour is observed for the  $\text{CO}_2$  concentration at the outlet for all three cases (Figs. 6.33b, 6.35b and 6.37b). CO and  $\text{CO}_2$  productions are very dependent on each other. Therefore, the  $\text{CO}_2$  production, starting immediately at the bottom of the reactor in the dimpled cases, is caused by a higher amount of fuel and a higher mixing of the fuel and  $\text{O}_2$ . Again, due to the water-shift reaction R8 in the dilute part of the reactor, a significant amount of  $\text{CO}_2$  is produced there.

A slightly different amount of  $\text{H}_2$  comes out from each reactor outlet (Figs. 6.33c, 6.35c and 6.37c). The slight difference proves that the resistance time of the gaseous products affects the final product in the reactor. In the flat case, the  $\text{H}_2$  mole fraction is about 0.14, in the shallow one about 0.13 and in the deep one about 0.12. Hence, we can conclude that when the depth of the dimple increases,  $\text{H}_2$  is consumed more by reactions R4 and R8 due to the recirculation and a higher residence time of  $\text{H}_2$  in the reactor. A

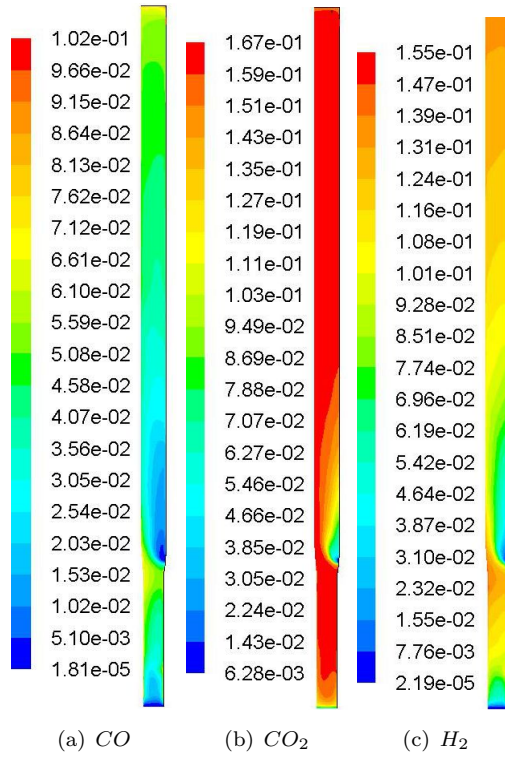


Figure 6.33: Mean mole fractions of  $\text{CO}$ ,  $\text{CO}_2$  and  $\text{H}_2$  in a flat wall reactor.

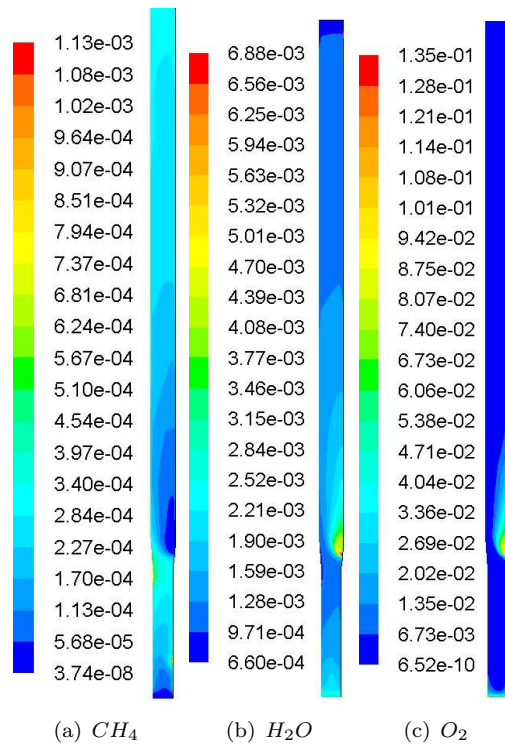


Figure 6.34: Mean mole fractions of  $\text{CH}_4$ ,  $\text{H}_2\text{O}$  and  $\text{O}_2$  in a flat wall reactor.

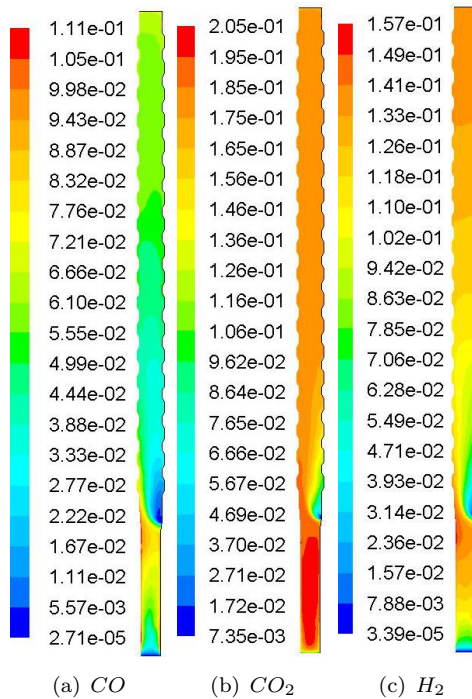


Figure 6.35: Mean mole fractions of  $CO$ ,  $CO_2$  and  $H_2$  in a shallow dimpled reactor.

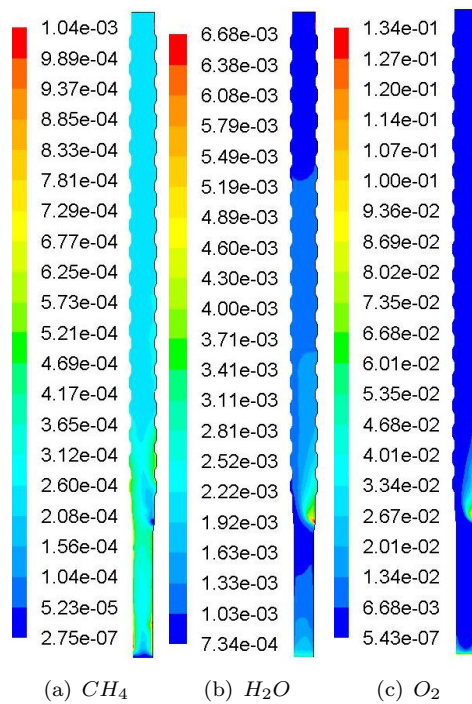
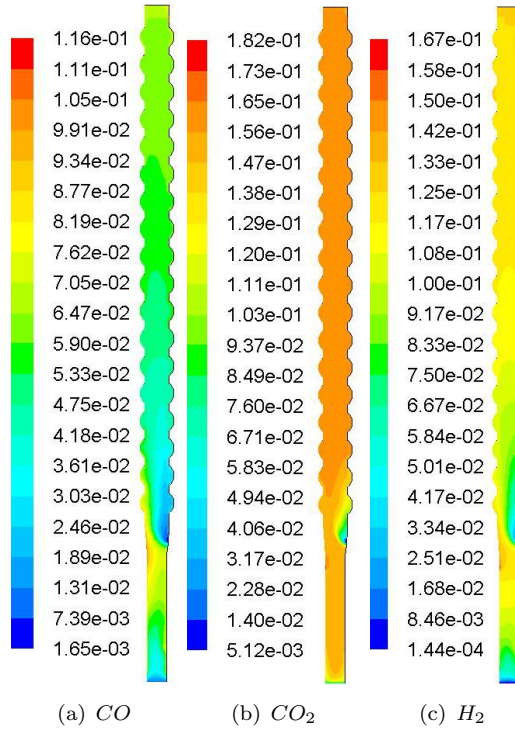
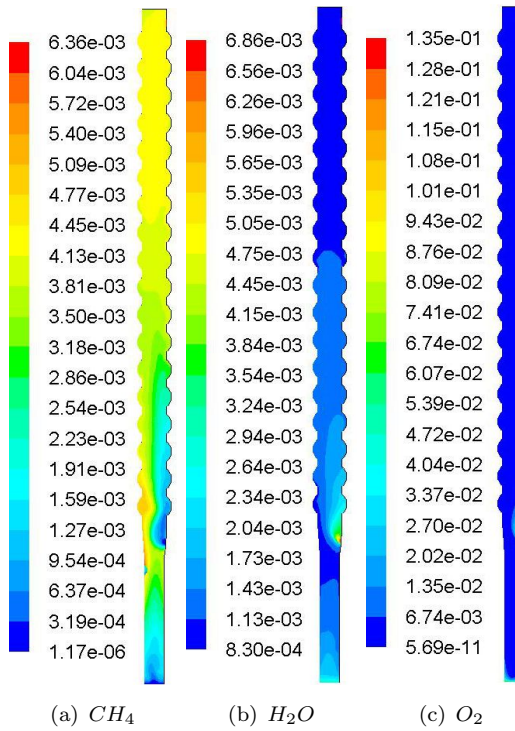


Figure 6.36: Mean mole fractions of  $CH_4$ ,  $H_2O$  and  $O_2$  in a shallow dimpled reactor.

Figure 6.37: Mean mole fractions of  $CO$ ,  $CO_2$  and  $H_2$  in a deep dimpled reactor.Figure 6.38: Mean mole fractions of  $CH_4$ ,  $H_2O$  and  $O_2$  in a deep dimpled reactor.

significant amount of H<sub>2</sub> can be noticed at the fuel entrance due to the devolatilisation of the coal.

The amount of CH<sub>4</sub> produced in the reactor is very low and most of CH<sub>4</sub> is produced by the coal devolatilisation because the reaction rate for reaction R4 is very low (Figs. 6.34a, 6.36a and 6.38a).

Water concentration differs in the reactors due to wall modification. As it can be seen in Figs. 6.34b, 6.36b and 6.38b, slightly higher water concentrations are reaching higher regions in the flat wall. Water is recirculated by the dimples and forced to react; thus cannot leave the reactor quickly. The same behaviour is observed for O<sub>2</sub>; in the shallow dimple it reaches the fourth dimple with a mole fraction of 0.0135 (see Fig. 6.36c). On the other hand, in the deep dimple case (Fig. 6.38c), where recirculation is much stronger, O<sub>2</sub> manages to reach only the second dimple with the same mole fraction. It shows that the dimple depth is an important parameter in defining the behaviour of chemical reactions. Also, O<sub>2</sub> coming from the main inlet is consumed very quickly in the char combustion reaction.

On Fig. 6.39 is presented the mean mole fraction of CO<sub>2</sub> in streamwise direction. The highest mole fraction is observed in the shallow dimple and lowest in the deep dimple one. The reason can be also increased residence time of the CO<sub>2</sub> and better mixing effect of the deep dimples. Breaking the clusters leads to increase of the contact surface which allows to increase reactivity of R3. Higher reactivity of the R3 leads to lower mole fraction of the CO<sub>2</sub> in the deep dimpled reactor.

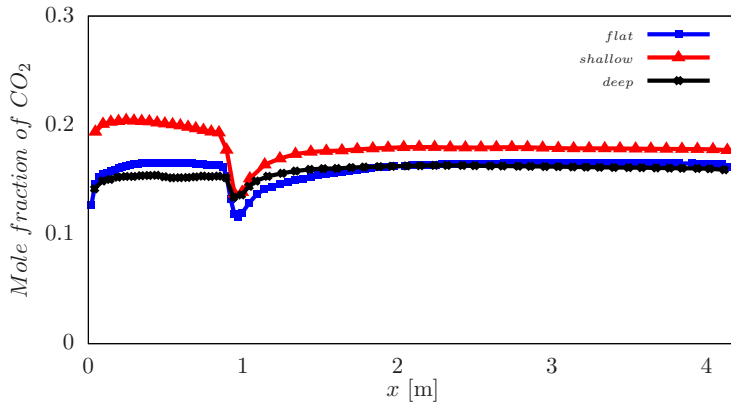


Figure 6.39: Vertical mean mole fraction of CO<sub>2</sub> in flat, shallow and deep dimpled wall CFB reactors.

Fig. 6.40 shows the mean mole fraction of CO in the streamwise direction. Higher mole fraction of CO is present in the dimpled wall reactor due to the better mixing, increased residence time and clusters breaking. Breaking of the clusters allows an increase of the reaction rates for R2 and R3 reactions due to increased contact surface area.

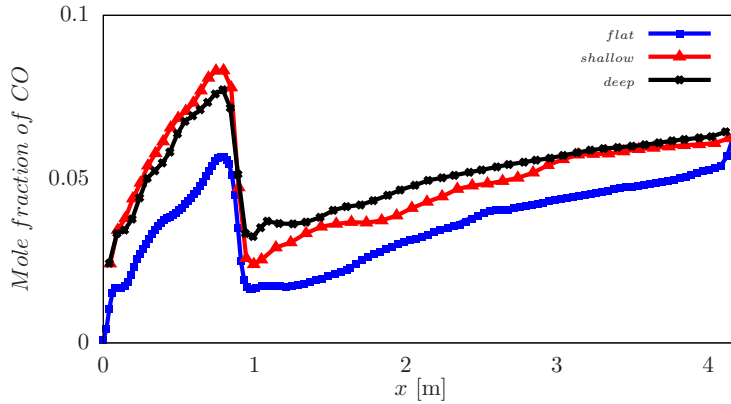


Figure 6.40: Vertical mean mole fraction profile of CO in flat, shallow and deep dimpled wall CFB reactors.

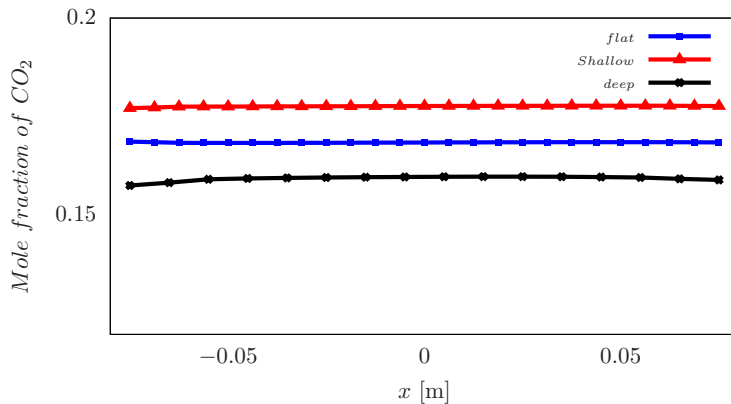


Figure 6.41: Outlet mean mole fraction profile of  $\text{CO}_2$  in flat, shallow and deep dimpled wall CFB reactors.

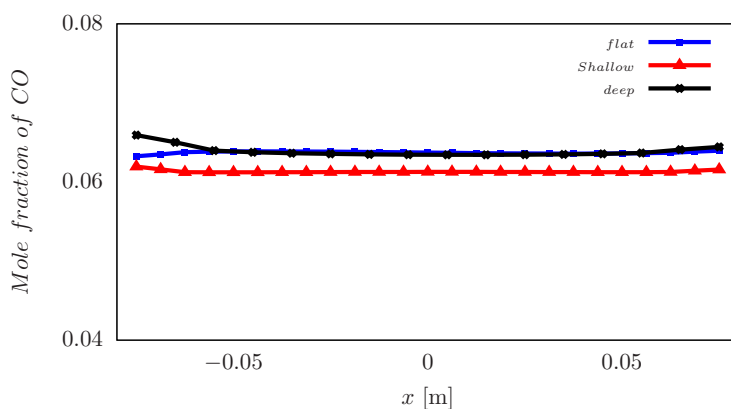


Figure 6.42: Outlet mean mole fraction profile of CO in flat, shallow and deep dimpled wall CFB reactors.

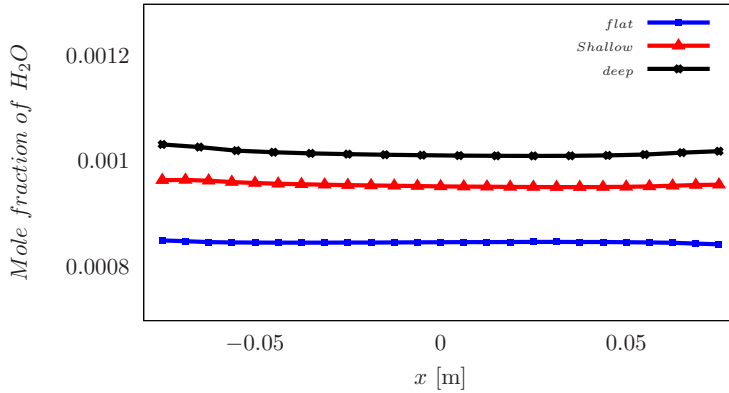


Figure 6.43: Outlet mean mole fraction profile of  $\text{H}_2\text{O}$  in flat, shallow and deep dimpled wall CFB reactors.

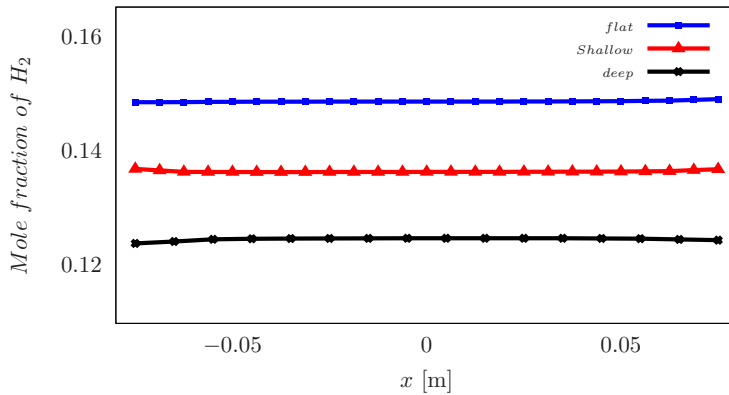


Figure 6.44: Outlet mean mole fraction profile of  $\text{H}_2$  in flat, shallow and deep dimpled wall CFB reactors.

Fig. 6.41 shows mole fractions of the  $\text{CO}_2$ . The higher mole fraction in the dimpled wall reactors is due to the good mixing of the char and coal with the gaseous products and their increased residence time. On Fig. 6.42 is presented the mole fraction of the CO which for all cases is almost the same. The mole fraction of  $\text{H}_2\text{O}$  is high in the dimpled wall reactor as shown in Fig. outletH<sub>2</sub>O. The reason for that is the lower concentration of the char and coal at the outlet as a result of the better mixing, clusters break down the clusters, increased contact area of the char and coal with surrounding gaseous products and increased residence time. The consumption of  $\text{H}_2$  occurs only due to reactions R4 and R6, where  $\text{H}_2$  reacts with the char and  $\text{O}_2$ . In the dimpled wall reactors, the char and  $\text{O}_2$  are kept longer at the bottom and middle of the reactor and are consumed there. This may explain the highest  $\text{H}_2$  concentration in the deep dimpled wall case (Fig. 6.44).

#### 6.4.8 Conclusion and summary

In the CFB reactor, CFD proved to be an effective tool for predicting the gasification products. The simulation results are in good agreement with the experimental data [Zhou et al. (2011)]. Whilst many simulation results for the gasification of BFB type reactors are available [Armstrong et al. (2011a); Yu et al. (2007); Gerber et al. (2010)], they are limited for CFB reactors with air. This work shows that it is possible to compute such a complex model as CFB with coal gasification using CFD. We can conclude that wall modifications influence the behaviour of the system. Dimple walls increase some of the gaseous products consumption in the reactor and convert them to different products. Therefore, the modification of the wall has a slight influence on gasification products. The reason for that can be the higher mixing efficiency which helps increase the contact area between fuel and O<sub>2</sub>. Recirculation facilitates the increase of the residence time of the fuel and oxygen in the reactor. Moreover, except for the fuel resistance time, the dimple structures increase the residence time of the gaseous products, which helps the reactions, like water-gas shifting [R8], to enhance their reaction rate in the dilute region of the reactor. Due to water-gas shifting and char combustion, CO and CO<sub>2</sub> are the dominant products in the coal gasification in CFB reactors. Further investigations for dimpled structures are needed. Also, a parametric (i.e. depth of dimples, editing reactions, different fuel types, adding limestone etc.) study of the gasification of CFB type reactors can be very beneficial.



# Chapter 7

## Conclusions

This chapter summarises all the work done during this study, concludes with key findings and highlights the novelties. Future suggestions are made for the extension of the study.

### 7.1 Conclusions

The gas-solid four-way coupled  $k_s-k_{gs}$  isotropic turbulence model is fundamentally studied by modifying the full equation model [Peirano and Leckner (1998)]. The model is in good agreement with the DNS data available from the literature [Elghobashi and Truesdell (1993)]. Further investigations have been performed by varying the solid volume fraction and the Stokes number. As expected from the four-way coupling mechanism, where particle-particle interaction plays a key role, the model is very sensitive to the solid volume fraction. When the solid volume fraction increases then the turbulent kinetic energy starts to decay more quickly due to particle-particle collision. Also, a higher Stokes number shows lower decay in the particle turbulent kinetic energy, although there is still no fair agreement in the literature about the Stokes number impact on turbulence.

The study continued by applying the full  $k_s-k_{gs}$  model to ANSYS Fluent 14.5 and its UDF utility. The 2D calculations were performed in a classical backward-facing step geometry and the code was validated with experimental data from the literature [Fessler and Eaton (1995, 1999); Benavides and van Wachem (2009)]. Different size particles, mass loading, velocity, and turbulence intensities are presented. Particle velocity profiles as well as primary phase turbulent intensities proved to be in good agreement with the experimental data. The particle turbulent intensities and classical granular temperature [Gidaspow (1994)] models are compared and both models show similar behaviour. They are in fair agreement with the experimental results as well. The study shows that the full  $k_s-k_{gs}$  model gives similar results with the most accurate existing model - the classical granular temperature model [Gidaspow (1994)]. The  $k_s-k_{gs}$  model has the potential for

even more accurate predictions with further improvements. In particular, the inclusion of particle-particle interaction into the velocity covariance transport equation which may have a vital impact on the entire model. Overall, the gas-solid four-way coupled  $k_s-k_{gs}$  model gives good predictions and good agreement with the experiments.

Two studies of the dense gas-solid flow, followed by dilute gas-solid turbulence cases were investigated. The current models experience problems with the near wall phenomenon for low Reynolds number flows as described in the literature [[Peirano and Leckner \(1998\)](#)]. They are using damping and wall functions to capture this wall behaviour. A totally new dispersed  $v^2 - f$  model for multiphase turbulence is derived here. This model includes a particle-fluid interaction term and an elliptic function for the wall region which is novel for gas-solid flows. The 2D model is applied in ANSYS Fluent 14.5 via UDF utility and the standard backward-facing step geometry is used to calculate and validate the code with experimental data from the literature [[Fessler and Eaton \(1995, 1999\)](#)]. The preliminary results were in fair agreement with the experimental data. However, in the recirculation zone, a slight overprediction of the turbulent intensity was observed. Nevertheless, the results indicate that it is worth to further develop the model for dense cases. Additional source terms may be needed to capture dissipation due to the fluid-particle interaction in the  $v^2$  transport equation. The model has an advantage over Reynolds stress models (RSM) due to lower computational cost, too.

A further novelty here is the application of dimpled structures to the wall of the cold flow CFB reactors. One of the main problems in the CFB reactors is the particle accumulation near the wall region which decreases the combustion efficiency in the reactor. Moreover, clusters lead higher energy losses and disturbances in the reactor. In order to deal with the clustering effect, the novel dimpled structures are implemented to the walls of the reactor. The dimple structures are widely used in the aerodynamical and the heat transfer applications. Here, the aim is to apply the dimpled structures to boost recirculation and to break down the clusters near the wall and push them back to the main flow. The results show that the dimpled structures help decrease the clustering effect near the wall significantly. Two depths of dimples were used during this study, with the deep dimpled structure giving more promising results than the shallow ones. However, further parametric and optimisation studies are needed to find the optimal design. Moreover, by breaking down the clusters the dimpled structures promote the mixing in the reactor which increases the contact between fuel and oxygen. Also, after clusters are broken down, the drag inside the reactor increases as well. Another benefit is the increased residential time of the fuel and gasification products in the reactor. The increase of the residential time may give the opportunity for the fuel to stay in contact with the oxygen and gasification products longer. As dimples are used to clean the wall surface, dimples can have the cleaning role in fluidised bed applications as well. Dimples increase the surface of the reactor which may enhance the heat transfer, too. To

capture the inhomogeneous distribution of the particles in the CFB reactors, an EMMS drag model was implemented in ANSYS Fluent 14.5 using UDF. Also, a UDF code was developed to keep the solid mass flow rate constant without a cyclone. The UDF code helped save a reasonable computational effort.

Moreover, hot CFB and BFB reactors were simulated by including the chemical reactions and two-way coal devolatilisation. The gasification products were validated with the experimental results from the literature [Armstrong et al. (2011a); Yu et al. (2007); Gerber et al. (2010)]. The results from the flat BFB type reactor were in fairly good agreement with the experimental results. The reason for the slight difference was the absence of the limestone in the reactor [Armstrong et al. (2011a); Yu et al. (2007); Gerber et al. (2010)]. The same reaction kinetic was applied also to the BFB type reactor with dimpled wall modification. The dimpled structures produce slightly different gasification products by keeping the gasification products in the reactor longer and letting the water-shift reaction to function backwards. This is very dominant in the upper region of the reactor, producing more CO by keeping the CO<sub>2</sub> longer inside the furnace. As are CO and CO<sub>2</sub> the dominant products of coal combustion, the rate of these products is vital. The dimpled simulations indicate that the wall modification affects the gasification products which could be used to decrease the emission.

After the validation of the code, the CFB simulations were performed by including chemical reactions and coal devolatilisation, being one of the few CFD modelling and simulations. The experimental results and geometry were taken from the literature where it is applied for oxy-fuel reactors. The experimental results were chosen for oxy-fuel due to the lack of data for air combustion modelling for CFB reactors. In fact, it helps to compare pure oxygen combustion and air mixture combustion. The results for CO<sub>2</sub> were in agreement with the experimental data, but the amount of CO was higher in air mixture combustion, as expected, due to the existence of H<sub>2</sub>O. O<sub>2</sub> leaving the outlet was also lower in air combustion. This could be due to two reasons: the first one being dimpled wall which allows O<sub>2</sub> to come contact with fuel and gasification products. This leads to more consumption of the oxygen. The second reason could be more products in the air mixture than in oxy-fuel combustion to consume O<sub>2</sub>. The EMMS model was also used here and the UDF code was developed to avoid a cyclone. The results show that the CFD is capable to simulate such a complex CFB system even with chemical reactions and coal devolatilisation. A further modelling study of CFB reactors is essential for their development and efficiency improvements. A profound parametric study and additional chemical reactions can be included in the future.

## 7.2 Contributions

The summary of the contributions made to this work:

- Extensive literature review has been done for turbulence modelling of a gas-solid flow. The  $k_s - k_{gs}$  model is modified in order to analyse the isotropic turbulence with four-way coupling where particle-particle interaction takes place. Matlab code is developed to calculate isotropic  $k_s - k_{gs}$  model. Several cases are applied to analyse the effect of Stokes number, mass loading, etc and compared with DNS data from the literature.
- Entire  $k_s - k_{gs}$  model is applied to ANSYS Fluent 14.5 by using C-subroutines (UDF). The calculations are run in a classical vertical oriented backward-facing step geometry with different particle types and different mass loading in order to get clear understanding of the model and comparison with the experimental data.
- First time dispersed  $v^2 - f$  model is introduced here for dilute gas-solid flows and the C-subroutines (UDF) are developed in ANSYS Fluent 14.5. Similar to previous turbulence models, classical vertical oriented backward-facing step geometry is used to simulate the novel dispersed  $v^2 - f$  model. It is compared with data from the literature.
- Novel wall design is applied to the CFB type reactor in order to increase their efficiency and to avoid clusters near the wall. Aslo, EMMS drag model is vital to capture the inhomogeneous distribution of the solids (like clusters) in the reactor, so by using C-subroutines (UDF) EMMS model is applied to the ANSYS Fluent 14.5. Moreover, to avoid extra computational cost, a code is developed to keep the solid mass flow rate constant in the reactor. A wide literature review has been done about kinetic theory of granular flow, CFB and BFB type reactors.
- Two-step Kobayashi coal devolatilisation model, heterogeneous and homogeneous reactions are applied tin ANSYS Fluent 14.5 by using C-subroutines (UDF). The code has been run for a BFB type reactor with flat and dimpled walls. Also, the same code is used to implement gasification of the CFB type reactors. Moreover, dimpled structures are applied to the hot CFB simulations and the UDF code was modified for constant mass flow rate.

### 7.3 Future Work

- Further isotropic turbulence analysis can be performed by using the already developed matlab code and modify it to capture the near wall behaviour.
- The  $k_s - k_{gs}$  model code can be improved by including particle-particle interaction to the velocity covariance transport equation. Also, further parametric study is vital for improvement of the model.
- The dispersed  $v^2 - f$  model can be improved by derivation of the source term for  $v^2$  equation and further simplification of the UDF code to have better understanding

of the model (like isotropic dispersed  $v^2 - f$  model) and followed by parametric study.

- Finally, two models can be coupled in order to capture whole particle turbulence phenomenon, which means instead of standard dispersed  $k_g - \varepsilon_g$  model to use dispersed  $v^2 - f$  model in the  $k_s - k_{gs}$  model.
- Further optimisation of the dimpled geometry with parametric study is necessary and 3D simulation may be beneficial.



## Appendix A

# General averaging techniques

### A.1 Averaging

Instantaneous equations need to be averaged or alternatively, one differential ordinary equation can be solved for each particle using Lagrangian approach. Analytical solutions can be obtained only for simple cases. Hence, modelling of two-phase flow is a challenging task, from both mathematical and physical point of you due to the interaction between the phases. The mathematical difficulties appear in the formulation of two single phases with moving boundaries in the two phase flow.

Here averaging techniques [[Ishii \(1975\)](#); [Delhaye and Achard \(1977, 1978\)](#)] are applied to the previously presented local instantaneous equations in two phase flows. In the two fluid approach, a given parameter is approximated with a function  $f = f(x, t)$  to find a solution at a fixed point in space,  $x$  at any time,  $t$ . The averaging process is denoted as  $\langle \dots \rangle$ , then  $\langle f \rangle(x, t)$  is the corresponding averaged function. Several averagings are applied to the balance equations. Firstly, volume averaging is performed around the fixed point  $x$  at any time  $t$ , whereas time averaging is vice versa. The ensemble averaging is a statistical average of the parameter  $f_n$  over point  $x$  and time  $t$  over many experiments with the same boundary and initial conditions [[Enwald et al. \(1996\)](#)]. The volume averaging can be described as:

$$\langle f \rangle_V(x, t) = \frac{1}{V} \iiint_V f(x, t) du dv dw \quad (\text{A.1})$$

There are several conditions to be fulfilled before applying the volume averaging [[Whitaker \(1969\)](#)]:

- characteristic dimensions of phases;
- characteristic dimensions of averaging volume;

- characteristic dimensions of physical system.

The time averaging can be defined as

$$\langle f \rangle_t(x, t) = \frac{1}{T} \int_{t-T/2}^{t+T/2} f(x, t) dt \quad (\text{A.2})$$

The assumption applied in time averaging are [Delhayé and Achard (1977, 1978)]:

- turbulent fluctuations time scale;
- specific time interval for averaging;
- time scale of fluctuations of mean flow;

If the mean and turbulent fluctuations are not distinguishable, double time averaging operator can be used [Delhayé and Achard (1977, 1978)]. The most general averaging process is ensemble averaging, defined as [Enwald et al. (1996)]:

$$\langle f \rangle_e(x, t) = \int_b(x, t) dP(a) \quad (\text{A.3})$$

where  $b$  is all possibilities and  $dP(a)$  is probability of observing processes. Practically, there is no need to know the exact location for each particle nor the exact velocity of the fields at the beginning. The ensemble averaging is just a statistical mean value of any parameters which are measured by performing set of experiments in given time and space with the same initial conditions. The averaging rules must satisfy the Reynolds' (see B), Leibniz'

$$\langle \frac{\partial f}{\partial t} \rangle = \frac{\partial}{\partial t} \langle f \rangle \quad (\text{A.4})$$

and Gauss' rules:

$$\langle \frac{\partial f}{\partial x_i} \rangle = \frac{\partial}{\partial x_i} \langle f \rangle \quad (\text{A.5})$$

When averaging is applied to an equation of motion for each phase, difficulties arise. In order to solve this phase function  $X_k(x, t)$  is introduced as

$$X_k(x, t) = \begin{cases} 1, & \text{if } x \text{ is in phase } k \text{ at time } t \\ 0, & \text{otherwise.} \end{cases} \quad (\text{A.6})$$

By using Reynolds averaging (see Appendix B), Eqs.A.4-A.6 and using the chain rule, the following equation can be derived

$$\frac{\partial \langle X_k f_k \rangle}{\partial t} = \langle X_k \frac{\partial f_k}{\partial t} \rangle + \langle f_k \frac{\partial X_k}{\partial t} \rangle \quad (\text{A.7})$$

$$\nabla \langle X_k f_k \rangle = \langle X_k \nabla f_k \rangle + \langle f_k \nabla X_k \rangle \quad (\text{A.8})$$

$$\nabla \cdot \langle X_k f_k \rangle = \langle X_k \nabla \cdot f_k \rangle + \langle f_k \cdot \nabla X_k \rangle \quad (\text{A.9})$$

One of the fundamental relations, from which the material derivative of the phase indicator is derived, is defined as [Drew (1983)]:

$$\frac{\partial X_t}{\partial t} + \mathbf{u}_i \cdot \nabla X_k = 0 \quad (\text{A.10})$$

By applying these averaging techniques to the instantaneous equations (see sections 2.4.1, 2.4.2 and 2.4.3), the averaged balanced equations can be derived.



## Appendix B

# RANS

### B.1 Reynolds averaged Navier-Stokes Equation (RANS)

The derivation of the RANS equations is based on the original Navier-Stokes(NS) equations. Continuity for incompressible flow

$$\frac{\partial u_i}{\partial t} + \frac{\partial u_1}{\partial x_1} + \frac{\partial u_2}{\partial x_2} + \frac{\partial u_3}{\partial x_3} = 0, \quad (\text{B.1})$$

and momentum equation:

$$\frac{\partial u_i}{\partial t} + \frac{\partial u_i u_j}{\partial x_j} = F_i + \frac{1}{\rho} \frac{\partial \tau_{ij}}{\partial x_j}, \quad (\text{B.2})$$

where  $F_i$  are the body forces,  $\tau_{ij}$  is the viscous stress which can be defined as:

$$\tau_{ij} = \rho \nu \left( \frac{\partial u_i}{\partial x_j} + \frac{\partial u_j}{\partial x_i} \right). \quad (\text{B.3})$$

By using Reynolds averaging, the fluctuating quantity  $f$  (i.e. the pressure and velocity in x, y, z-direction) can be defined as the sum of its averaged value ( $\bar{f}$ ) and its fluctuation ( $f'$ ):

$$f = \bar{f} + f'; \quad (\text{B.4})$$

where the averaged part can be described as follows:

$$\bar{f} = \frac{1}{T} \int_0^T f dt; \quad (\text{B.5})$$

The assumptions here are that averaged fluctuating value is zero,

$$\bar{f}' = 0, \quad (\text{B.6})$$

and the double averaged quantity is equal to one time averaged one:

$$\bar{\bar{f}} = \bar{f}, \quad (\text{B.7})$$

The averaged sum is equal to the sum of the averaged values

$$\overline{\bar{f} + \bar{g}} = \bar{f} + \bar{g}, \quad (\text{B.8})$$

The averaging and differentiation combine as

$$\overline{\frac{\partial f}{\partial t}} = \frac{\partial \bar{f}}{\partial t}, \quad (\text{B.9})$$

Similarly, for the space:

$$\overline{\frac{\partial f}{\partial x}} = \frac{\partial \bar{f}}{\partial x}. \quad (\text{B.10})$$

One of the most important properties is that the product of the fluctuating quantity is not equal to zero:

$$\overline{f'g'} \neq 0, \quad (\text{B.11})$$

But the product of two averaged values is equal to

$$\overline{\bar{f}\bar{g}} = \bar{f}\bar{g}, \quad (\text{B.12})$$

and any product of averaged and fluctuating quantity is equal to zero

$$\overline{\bar{f}g'} = \bar{f}\bar{g}' = 0. \quad (\text{B.13})$$

Applying the fluctuating quantities (Eq.B.4) to Eq.B.2 takes the form:

$$\frac{\partial(\bar{u}_i + u'_i)}{\partial t} + \frac{\partial(\bar{u}_i + u'_i)(\bar{u}_j + u'_j)}{\partial x_j} = \bar{F}_i + F'_i + \frac{1}{\rho} \frac{\partial(\bar{\tau}_{ij} + \tau'_{ij})}{x_j}. \quad (\text{B.14})$$

After averaging both sides,

$$\overline{\frac{\partial(\bar{u}_i + u'_i)}{\partial t}} + \overline{\frac{\partial(\bar{u}_i + u'_i)(\bar{u}_j + u'_j)}{\partial x_j}} = \overline{\bar{F}_i + F'_i} + \frac{1}{\rho} \overline{\frac{\partial(\bar{\tau}_{ij} + \tau'_{ij})}{x_j}}, \quad (\text{B.15})$$

and applying the Reynolds averaging properties, Eq.B.2 is transformed into:

$$\frac{\partial \bar{u}_i}{\partial t} + \frac{\partial(\bar{u}_i \bar{u}_j + \overline{u'_i u'_j})}{\partial x_j} = \bar{F}_i + \frac{1}{\rho} \frac{\partial \bar{\tau}_{ij}}{x_j}. \quad (\text{B.16})$$

Finally, the unsteady Reynolds Averaged Navier Stokes Equation (URANS) (Eq.B.16) can be written as:

$$\rho \frac{\partial \bar{u}_i}{\partial t} + \rho \frac{\partial(\bar{u}_i \bar{u}_j)}{\partial x_j} = \rho \bar{F}_i \frac{\partial}{\partial x_j} (\bar{\tau}_{ij} - \rho \bar{u}'_i \bar{u}'_j). \quad (\text{B.17})$$

If we compare the features of URANS with NS, it can be concluded that URANS describes the average quantities, whereas NS the instantaneous ones. URANS has an additional term on the r.h.s  $-\rho \bar{u}'_i \bar{u}'_j$ , which is the so-called Reynolds stress  $R_{ij}$ :

$$R_{ij} = \begin{pmatrix} -\rho \bar{u}'_x \bar{u}'_x & -\rho \bar{u}'_x \bar{u}'_y & -\rho \bar{u}'_x \bar{u}'_z \\ -\rho \bar{u}'_x \bar{u}'_y & -\rho \bar{u}'_y \bar{u}'_y & -\rho \bar{u}'_y \bar{u}'_z \\ -\rho \bar{u}'_x \bar{u}'_z & -\rho \bar{u}'_y \bar{u}'_z & -\rho \bar{u}'_z \bar{u}'_z \end{pmatrix} \quad (\text{B.18})$$

Due to symmetrical conditions, the stress unknowns are six. The name 'stress' comes from the similarity of the NS viscous stress. The Reynolds stress appears due to flow fluctuations, whereas viscous stress is expressed through the molecular viscosity. We have the following unknowns: three averaged velocity components, one averaged pressure and six Reynolds stress components. It means that the system is not closed. In order to describe the Reynolds stresses, closure models of turbulence should be used. These models are based on Boussinesq approximation for turbulent flows, which is a modification of the Newton's hypothesis. Boussinesq uses the turbulent viscosity ( $\nu_t$ ) instead of kinematic viscosity ( $\nu$ ):

$$-\rho \bar{u}'_i \bar{u}'_j = \rho \nu_t \left( \frac{\partial \bar{u}_j}{\partial x_i} + \frac{\partial \bar{u}_i}{\partial x_j} \right) - \frac{2}{3} \rho \delta_{ij} k \quad (\text{B.19})$$

and the Reynolds stress is described through the strain rate tensor:

$$S_{ij} = \frac{1}{2} \left( \frac{\partial \bar{u}_j}{\partial x_i} + \frac{\partial \bar{u}_i}{\partial x_j} \right) \quad (\text{B.20})$$

The turbulent viscosity ( $\nu_t$ ) is not a property of the fluid, but depends on the flow behaviour.



# References

- Agrawal, K., Loezos, P. N., Symlal, M., and Sundaresan, S. (2001). The role of meso-scale structures in rapid gas-solid flows. *J. Fluid Mech.*, 445:151–185.
- Anderson, T. and Jackson, R. (1967). A fluid mechanical description of fluidized beds: Equations of motion. *Ind. Eng. Chem. Fundam.*, 6:527–539.
- Arastoopour, H., Pakdel, P., and Adewumi, M. (1990). Hydrodynamics analysis of dilute gas-solid flow in a vertical pipe. *Powder Technology*, 62.
- Armstrong, L. (2011). *CFD modelling of the gas-solid flow dynamics and thermal conversion processes in fluidised beds*. PhD thesis, University of Southampton.
- Armstrong, L., Gu, S., and Luo, H. K. (2011a). Parametric study of gasification processes in a BFB coal gasifier. *Industrial and Engineering Chemistry Research*, 50(10):5959–5974.
- Armstrong, L., Luo, K., and Gu, S. (2010). Two-dimensional and three-dimensional computational studies of hydrodynamics in the transition from bubbling to circulating fluidised bed. *Chem. Eng. J.*, 160:239–248.
- Armstrong, L., Luo, K., and Gu, S. (2011b). Effects of limestone calcination on the gasification processes in a BFB coal gasifier. *Chem. Eng. J.*, 168:848–860.
- Badzioch, S. and Hawksley, P. G. (1970). Kinetics of thermal decomposition of pulverized coal particles. *Ind. Eng. Chem. Process Design and Development*, 9:521–530.
- Balachandar, S. and Eaton, J. K. (2010). Turbulence dispersed multiphase flow. *Annu. Rev. Fluid Mech.*, 42:111–133.
- Baum, M. and Street, P. (1971). Predicting the combustion behaviour of coal particles. *Combust. Sci. Tech.*, 3(5):231–243.
- Benavides, A. and van Wachem, B. (2008). Numerical simulation and validation of dilute turbulent gas-particle flow with inelastic collisions and turbulence modulation. *Powder Technology*, 182:294–306.

- Benavides, A. and van Wachem, B. (2009). Eulerian-Eulerian prediction of dilute turbulent gas-particle flow in a backward-facing step. *International Journal of Heat and Fluid Flow*, 30.
- Benavides, A. G. (2009). *Eulerian-Eulerian Modeling of Turbulent Gas-Particle Flow*. PhD thesis, Chalmers University of Technology.
- Bi, H. T. and Grace, J. R. (1995). Flow regime diagrams for gas-solid fluidization and upward transport. *Int. J. Multiphase Flow*, 21:1229–1236.
- Bi, H. T., Grace, J. R., and Lim, K. S. (1995). Transition from bubbling to turbulent fluidization. *Ind. Eng. Chem. Res.*, 34:4003–4008.
- Bird, B. (1976). *Transport Phenomena*. Wiley, New York.
- Carnahan, F. and Starling, K. (1967). Equation of state for non-attracting rigid spheres. *J. Chem. Phys.*, 51:635–636.
- Chapman, S. and Cowling, T. G. (1970). The mathematical theory of non-uniform gases. *Cambridge Mathematic Library*, 2(10).
- Crowe, S. T., Troutt, T. R., and Chung, J. N. (1996). Numerical models for two-phase turbulent flows. *Annu. Rev. Fluid. Mech.*, 28:11–43.
- Delhaye, J. M. and Achard, J. L. (1977). On the use of averaging operators in two phase flow modeling. In *Thermal and Hydraulic Aspects of Nuclear Reactor Safety, 1: Light Water Reactors*. ASME Winter Meeting.
- Delhaye, J. M. and Achard, J. L. (1978). On the averaging operators introduced in two-phase flow. In *In Transient Two-phase Flow*, ed. S. Banerjee and J. R. Weaver. *Proc. CSNI Specialists Meeting*. Toronto, 3–4 August.
- Deutsch, E. and Simonin, O. (1991). Large eddy simulations applied to the modelling of particulate transport in turbulent two-phase flows. *Symp. on Turbl. shear Flows, Tech. Univ. Munich*.
- Ding, J. and Gidaspow, D. (1990). A bubbling fluidization model using kinetic theory of granular flow. *AICHE J.*, 32(1):523–538.
- Drew, D. A. (1983). Mathematical modeling of two-phase flow. *Ann. Rev. Fluid Mech.*, 15:261–291.
- Durbin, P. (1991). Near-wall turbulence closure modelling without damping functions. *Theoretical and Computational Fluid Dynamics*, 3:1–13.
- Durbin, P. (1993). Application of a near-wall turbulence model to boundary layers and heat transfer. *International Journal of Heat and Fluid Flow*, 14:316–323.

- Elghobashi, S. E. (1994). On predicting particle-laden turbulent flows. *Appl. Sci. Res.*, 52:309–329.
- Elghobashi, S. E. and Abou-Arab, T. W. (1983). A two-equation turbulence model for two-phase flows. *Phys. Fluids*, 26(4):931–983.
- Elghobashi, S. E. and Truesdell, G. (1992). Direct simulation of particle dispersion in decaying isotropic turbulence. *J. Fluid Mech.*, 242:655–700.
- Elghobashi, S. E. and Truesdell, G. C. (1993). On two-way interaction between homogeneous turbulence and dispersed solid particles I: turbulence modification. *Phys. Fluids A*, 5:1790–1796.
- Enwald, H., Peirano, E., and Almstedt, A. (1996). Eulerian two-phase flow theory applied to fluidization. *Int. J. Multiphase Flow*, 22:21–66.
- Ergun, S. (1952). Fluid flow through packed columns. *Chem. Eng. Prog.*, 48(2).
- Fede, P., Simonin, O., Villedieu, P., and Squires, K. D. (2006). Stochastic modeling of the turbulent subgrid fluid velocity along inertial particle trajectories. In *Proceedings of the Summer Program*. Center for Turbulence Research.
- Fessler, J. R. and Eaton, J. K. (1995). Particle-turbulence interaction in a backward-facing step flow. In *Rep. MD-70, Mech. Engng Dept. Stanford University*. Stanford, California.
- Fessler, J. R. and Eaton, J. K. (1999). Turbulence modification by particles in a backward-facing step flow. *J. Fluid Mech.*, 394.
- Fessler, J. R., Kulick, J. D., and Eaton, J. K. (1994). Preferential concentration of heavy particles in a turbulent channel flow. *Phys. Fluids*, 6:3742–3749.
- Fevrier, P., Simonin, O., and Squires, K. (2005). Partitioning of particle velocities in gas–solid turbulent flows into a continuous field and a spatially uncorrelated random distribution: theoretical formalism and numerical study. *J. Fluid Mech.*, 533:1–46.
- Garside, J. and Al-Duboni, M. (1977). Velocity-voidage relationship for fluidization and sedimentation in solid-liquid systems. *Ind. Eng. Chem. Process Des. Dev.*, 16:206–214.
- Geldart, D. (1973). Types of gas fluidization. *Powder Technol.*, 7:285–292.
- Gera, D., Syamlal, M., and O’Brien, T. (2004). Hydrodynamics of particle segregation in fluidized beds. *Int. J. Multiphase Flow*, 30.
- Gerber, S., Behrendt, F., and Oevermann, M. (2010). An Eulerian modeling approach of wood gasification in a bubbling fluidized bed reactor using char as bed material. *Fuel*, 89(10).

- Gibilaro, L., Felice, R. D., and Waldram, S. (1985). Generalized friction factor and drag coefficient correlations for fluid-particle interaction. *Chem. Eng. Sci.*, 40.
- Gidaspow, D. (1994). *Multiphase Flow and Fluidization, Continuum and Kinetic Theory Descriptions*. Academic Press, Inc.
- Gidaspow, D., Bezburuah, R., and Ding, J. (1992). Hydrodynamics of circulating fluidized beds:kinetic theory approach. In *Proceedings of the 7th fluidization conference*.
- Goldschmidt, M., Kuipers, J., and van Swaaij, W. (2001). Hydrodynamic modeling of dense gas-fluidized beds using the kinetic theory of granular flow: effect of restitution coefficient on bed dynamics. *Chem. Eng. Sci.*, 56.
- Gore, R. A. and Crowe, C. T. (1991). Modulation of turbulence by dispersed phase. *J. Fluids Engng*, 113:304–307.
- Grace, J. and Bi, H. (1997). *Circulating Fluidized Beds*, chapter Introduction to circulating fluidized beds, pages 1–20. Blackie Academic & Professional, London.
- Gungor, A. and Eskin, N. (2008). Two-dimensional coal combustion modeling of CFB. *Int. J. Thermal Sci.*, 47:157–174.
- Gunn, D. (1978). Transfer of heat or mass to particles in fixed and fluidized beds. *Int. J. Heat Mass Transfer*, 21:467–476.
- Hardalupas, Y., Taylor, A. M. K. P., and Whitelaw, J. H. (1992). Particle dispersion in a vertical round sudden expansion flow. *Proc. R. Soc. Lond.*, 341(A):411–442.
- Harnby, N., Edwards, M. F., and Nienow, A. W. (1992). *Mixing in the process industries*. Butterworth-Heinemann,Boston.
- Helland, E., Occelli, R., and Tadrist, L. (2000). Numerical study of cluster formation in a gas-particle circulating fluidized bed. *Powder Technology*, 110.
- Hetsroni, G. (1989). Particles-turbulence interaction. *Int. J. Multiphase Flow*, 15(5):735–746.
- Hetsroni, G. and Sokolov, M. (1971). Distribution of mass ,velocity and intensity of turbulence in a two-phase turbulent jet. *Trans. ASME Jl appl. Mech.*, 38:315–327.
- Horio, H., Morisita, K., Tachibana, O., and Murata, N. (1988). *Solid distribution and movement in circulating fluidised beds*. Circulating fluidized bed technology II: Pergamon press.
- Hrenya, C. M. and Sinclair, J. L. (1997). The role of particle-phase turbulence in gas-solid flows. *A.I.Ch.E. Journal*, 43:853–869.
- Huilin, L., Guangbo, Z., Rushan, B., Yongjin, C., and Gidaspow, D. (2000). A coal combustion model for circulating fluidized bed boilers. *Fuel*, 79:165–172.

- Huilin, L., Rushan, B., Lidan, Y., Guangbo, Z., and Xiu, T. (1998). Numerical computation of a circulating fluidized bed combustor. *Int. J. Energy Res.*, 22:1351–1364.
- Ibsen, C. H., Solberg, T., and Hjertager, B. H. (2001). Evaluation of a three-dimensional numerical model of a scaled circulating fluidized bed. *Ind. Eng. Chem. Res.*, 40:5081–5086.
- Ishii, M. (1975). *Thermo-fluid Dynamic Theory of Two-phase Flow*. Eyrolles, Paris.
- Jenkins, J. and Savage, S. (1983). A theory for the rapid flow of identical, smooth, nearly elastic, spherical particles. *Journal of Fluid Mechanics*, 130.
- Jiradilok, V., Gidaspow, D., Damronglerd, S., Koves, W., and Mostofi, R. (2006). Kinetic theory based CFD simulation of turbulent fluidization of FCC particles in a riser. *Chem. Eng. Sci.*, 61:5544–5559.
- Johnson, P. and Jackson, R. (1987). Frictional-collisional constitutive relations for granular materials, with application to plane shearing. *J. Fluid. Mech.*, 176:67–93.
- Kawaguchi, T., Tanaka, T., and Tsuji, Y. (1998). Numerical simulation of two-dimensional fluidized beds using the discrete element method. *Powder Technology*, 98.
- Kobayashi, H. (1976). *Handbook of Fluidization and Fluid-Particle Systems*. PhD thesis, Department of Mechanical Engineering, Massachusetts Institute of Technology, Cambridge, Mass.
- Kobayashi, H., Howard, J. B., and Sarofim, A. F. (1977). Coal devolatilization at high temperatures. *Symposium (International) on Combustion*, 16:411–425.
- Kolmogorov, A. (1941). The local structure of turbulence in incompressible viscous fluid for very large reynolds numbers. *Dokl. Akad. Nauk. SSSR*, 30:299–303.
- Kulick, J. D., Fessler, J. R., and Eaton, J. K. (1994). Particle response and turbulence modification in fully developed channel flow. *J. Fluid Mech.*, 277.
- Li, J., Chen, A., Yan, Z., Xu, G., and Zhang, X. (1993). Particle-fluid contacting in circulating fluidized bed. *AIChE*, 20(1).
- Li, J., Ge, W., Cui, H., and Ren, J. (1998). Dissipative structure in concurrent-up gas-solid flow. *Chem. Eng. Sci.*, 53(19):3367–3379.
- Li, Y. and Kwauk, M. (1980). *Fluidization*, chapter The dynamics of fast fluidization, pages 537–544. New York & Plenum Press.
- Lun, C., Savage, S., Jeffrey, D., and Chepurniy, N. (1984). Kinetic theories for granular flow: Inelastic particles in Couette flow and slightly inelastic particles in a general flow field. *J. Fluid Mech.*, 140:223–256.

- Luo, K. M. (1987). *Dilute, dense-phase and maximum solids-gas transport*. PhD thesis, Illinois Institute of Technology.
- Maeda, M., Hishida, M., and Furutani, T. (1980). Optical measurements of local gas and particle velocity in upward flowing dilute gas-solids suspension. In *Proc. Polyphase Flow and Transport Technology*, pages 211–216. Century 2-ETC, San Francisco.
- Maeda, M., Kiyota, M., and Hishida, M. (1982). Heat transfer to gas-solids two-phase flow in separated, reattached and redevelopment regions. In *Proc. 7th Intl Heat Transfer Conf.*, volume 5, pages 249–254. Munich, Hemisphere.
- Manceau, R., Wang, M., and Laurence, D. (2001). Inhomogeneity and isotropy effects on the redistribution term in Reynolds-Averaged Navier-Stokes modelling. *Journal of Fluid Mechanics*, 438:307–338.
- Ocampo, A., Arenas, E., Chejne, F., Espinel, J., Londono, C., Aguirre, J., and Perez, J. (2003). An experimental study on gasification of colombian coal in fluidised bed. *Fuel*, 82:161–164.
- Ocone, R., Sundaresan, S., and Jackson, R. (1993). Gas-particle flow in a duct of arbitrary inclination with particle-particle interactions. *A.I.Ch.E. Journal*, 39:1261.
- Owen, P. R. (1969). Pneumatic transport. *J. Fluid Mech.*, 39:407–432.
- Ozel, A., Fede, P., and Simonin, O. (2013). Development of filtered euler–euler two-phase model for circulating fluidised bed: High resolution simulation, formulation and a priori analyses. *Int. J. Multiphase Flow*, 55:43–63.
- Pain, C., Mansoorzadeh, S., and de Oliveira, C. (2001). A study of bubbling and slugging fluidised beds using the two-fluid granular temperature model. *International Journal of Multiphase Flow*, 27.
- Pannala, S., Syamlal, M., and O'Brien, T. J. (2011). *Computational Gas-Solids Flows and Reacting Systems: Theory, Methods and Practice*. IGI Global.
- Peirano, E. and Leckner, B. (1998). Fundamentals of turbulent gas-solid flows applied to circulating fluidized bed combustion. *Prog. Energy Combust. Sci.*, 24.
- Phillips, O. M. (1969). Shear-flow turbulence. *Annual Review of Fluid Mechanics*, 1:245–264.
- Pillai, K. (1981). The influence of the coal type on devolatilization and combustion in fluidized beds. *J. Inst. Energy*, page 142.
- Pope, S. (2010). *Turbulent flows*. Cambridge University Press.
- Popper, J., Abuof, N., and Hetsroni, G. (1961). Velocity measurement in a two-phase turbulent jet. *Int. J. Multiphase Flow*, 190:715–726.

- Radjai, F. and Dubois, F. (2011). *Discrete-Element Modelling of Granular Materials*. John Wiley & Sons.
- Reeks, M. W. (1991). On a kinetic equation for the transport of particles in turbulent flows. *Phys. Fluids A*, 3:446.
- Reh, L. (1971). Fluidized bed processing. *Chem. Eng. Prog.*, 67(2):58–63.
- Richardson, J. and Zaki, W. (1954). Sedimentation and fluidization. *Trans. Chem. Eng.*, 32.
- Richardson, L. F. (1922). *Weather prediction by numerical process*. Cambridge: Cambridge University Press.
- Riley, J. J. and Patterson, G. (1974). Diffusion experiment with numerical integrated isotropic turbulence. *Phys. Fluids*, 17:292–297.
- Saffman, P. G. (1962). On the stability of laminar flow of a dusty gas. *J. Fluid Mech.*, 13:120–128.
- Sammuelsberg, A. and Hjertager, H. (1996). An experimental and numerical study of flow patterns in a circulating fluidized bed reactor. *Int. J. Multiphase Flow*, 22(3):575–591.
- Samruamphianskun, T., Piumsomboon, P., and Chalermsinsuwan, B. (2012). Effect of ring baffle configurations in a circulating fluidized bed riser using cfd simulation and experimental design analysis. *Chemical Engineering Journal*, 210:237–251.
- Schaeffer, D. (1987). Instability in the evolution equations describing incompressible granular flow. *J. Diff. Equ.*, 66:19–50.
- Schmid, J. C., Proell, T., Kitzler, H., Pfeifer, C., and Hofbauer, H. (2011). Improvement of gas-solid interaction in dual circulating fluidized bed systems. In *Proc. 9th European Conf. on Industrial Furnaces and Boilers (INFUB)*. Estoril, Portugal.
- Schmid, J. C., Proell, T., Kitzler, H., Pfeifer, C., and Hofbauer, H. (2012). Cold flow model investigations of the countercurrent flow of a dual circulating fluidized bed gasifier. *Biomass. Conv. Bioref.*, 42:229–244.
- Shih, T. H., Liou, W. W., Shabbir, A., Yang, Z., and Zhu, J. (1995). A new  $k-\varepsilon$  eddy-viscosity model for high Reynolds number turbulent flows - model development and validation. *Computers Fluids*, 24(3):292–297.
- Sinclair, J. L. and Jackson, R. (1989). Gas-particle flow in a vertical pipe with particle-particle interactions. *A.I.Ch.E. Journal*, 35(9).
- Smoot, L. (1984). Modeling of coal-combustion processes. *Prog. Energy. Combust. Sci.*, 10:229–272.

- Souza-Santos, M. (1989). Comprehensive modeling and simulation of fluidized bed boilers and gasifiers. *Fuel*, 68:1509–1521.
- Sproull, W. T. (1961). Viscosity of dusty gases. *Nature*, 190:976–978.
- Squires, A. M. (1986). *The story of fluid catalytic cracking: First Circulating Fluidized Bed*. Circulating fluidized bed technology: Pergamon press.
- Squires, K. D. and Eaton, J. K. (1990). Particle response and turbulence modification in isotropic turbulence. *Phys. Fluids A*, 2:1191–1203.
- Squires, K. D. and Eaton, J. K. (1991). Measurements of particle dispersion obtained from direct numerical simulations of isotropic turbulence. *J. Fluid Mech.*, 226:1–35.
- Stickler, D., Gannon, R., and H.Kobayashi (1974). Rapid devoltilization modeling of coal. In *Eastern States Section, Fall Meeting of the Combustion Institute, Applied Physics Laboratory, Maryland*.
- Sun, J. and Battaglia, F. (2006). Hydrodynamics modeling of particle rotation for segregation in bubbling gas-fluidized beds. *Chem. Eng. Sci.*, 61.
- Sveningsson, A. and Davidsson, L. (2005). Computations of flow field and heat transfer in a stator vane passage using the  $v^2 - f$  turbulence model. *Journal of Turbomachinery*, 127:627–634.
- Syamlal, M. and O'Brien, T. (1989). Computer simulation of bubbles in a fluidized bed. *A.I.Ch.E. Symposium Series*, 85.
- Syamlal, M. and O'Brien, T. J. (1987). Derivation of a drag coefficient from velocity-vorticity correlation. In *U.S. Dept. of Energy, Office of Fossil Energy, National Energy Technology Laboratory, Morgantown, West Virginia*.
- Syamlal, M., Rogers, W., and O'Brien, T. (1993). *Mfix Documentation Theory Guide*. U.S. Dept. of Energy, Office of Fossil Energy, Tech. Note.
- Tsuji, Y. and Morikawa, Y. (1982). LDV measurements of an air-solid two-phase in horizontal pipe. *J. Fluid Mech.*, 120:385–409.
- Tsuji, Y. and Morikawa, Y. (1984). LDV measurements of an air-solid two-phase in vertical pipe. *J. Fluid Mech.*, 139:417–434.
- Tsuo, Y. P. (1989). *Computation of flow regime in circulating fluidised beds*. PhD thesis, Illinois Institute of Technology.
- van Wachem, B., van der Schaaf, J., Schouten, J., Krishna, R., and van den Bleek, C. (2001a). Experimental validation of Lagrangian-Eulerian simulations of fluidized beds. *Powder Technology*, 116:155–165.

- van Wachem, B. G. M., Schouten, J. C., van den Bleek, C. M., Krishna, R., and Sinclair, J. L. (2001b). Comparative analysis of cfd models of dense gas-solid systems. *AICHE Journal*, 47(5):1035–1051.
- Wang, W. and Li, J. (2007). Simulation of gas-solid two-phase flow by multi-scale cfd approach-extension of the emms model to the sub-grid level. *Chem. Eng. Sci.*, 62(208-231).
- Wang, X., Jin, B., and Zhong, W. (2009). Three-dimentional simulation of fluidised bed coal gasification. *Chem. Eng. Proc.*, 48:695–705.
- Wardag, A. (2013). *Hydrodynamic and heat transfer Study in corrugated wall bubbling fluidized bed, experiments and CFD simulations*. PhD thesis, Universite Laval.
- Wardag, A. N. K. and Larachi, F. (2012a). Bed expansion and disengagement in corrugated wall bubbling fluidized beds. *Chem. Eng. Sci.*, 81:273–284.
- Wardag, A. N. K. and Larachi, F. (2012b). Bubble behavior in corrugated-wall bubbling fluidized beds—experiments and cfd simulations. *AICHE J.*, 58(7):2045–2057.
- Warnatz, J., Maas, U., and Dibble, R. W. (1996). *combustion: physical and chemical fundamentals, modelling and simulation, experiments, pollutant formation*. Springer, Berlin.
- Wen, C., Chen, H., and Onozaki, M. (1982). *User's manual for computer simulation and design of the moving bed coal gasifier*.
- Wen, Y. and Yu, Y. (1966). Mechanics of fluidization. *Chem. Eng. Prog. Symp. Ser.*, 62:100.
- Whitaker, S. (1969). Advances in theory of fluid motion in porous media. *Ind. Eng. Chem.*, 61:14–28.
- Yan, H., Heidenreich, C., and Zhang, D. (1999). Modeling of bubbling fluidised bed coal gasifiers. *Fuel*, 78:1027–1047.
- Yang, N., Wang, W., Ge, W., Wang, L., and Li, J. (2004). Simulation of heterogeneous structure in a circulating fluidized-bed riser by combining the two-fluid model with the EMMS approach. *Ind. Eng. Chem. Res.*, 43:5548–5561.
- Yang, N., Wang, W., and Li, J. (2003). CFD simulation of concurrent-up gas-solid flow in circulating fluidized beds with structure-dependent drag coefficient. *Chem. Eng. J.*, 96:71–80.
- Yang, W.-C. (2003). *Handbook of Fluidization and Fluid-Particle Systems*. Taylor & Francis Group LLC.
- Yarushalmi, J. and Squires, A. (1977). The phenomenon of fast fluidization. *A.I.ChE Symp.*, 161(73):44–50.

- Yousfi, Y. and Gau, G. (1974). Aerodynamique de l'ecoulement vertical de suspensions concentrees gaz-solides—i. regimes d'ecoulement et stabilite aerodynamique. *Chem. Eng. Sci.*, 29(9):1939–1946.
- Yu, K., Lau, K., and Chan, C. (2004). Numerical simulation gas-particle flow in a single-side backward-facing step flow. *J. Comput. Appl. Math.*, 163.
- Yu, L., Lu, J., Zhang, X., and Zhang, S. (2007). Numerical simulation of the bubbling fluidized bed coal gasification by the kinetic theory of granular flow (KTGF). *Fuel*, 86:722–734.
- Zhang, D. and Rauenzahn, R. (1997). A viscoelastic model for dense granular flows. *J. Rheol.*, 41(6):1275–1298.
- Zhang, D. and Rauenzahn, R. (2000). Stress relaxation in dense and slow granular flows. *Journal of Rheology*, 44.
- Zhang, Y. and Reese, J. M. (2001). Particle-gas turbulence interactions in a kinetic theory approach to granular flows. *Int. J. Multiphase Flow*, 27:1945–1964.
- Zhao, F., George, W. K., and van Wachem, B. G. M. (2015). Four-way coupled simulation of small particles in turbulent channel flow: The effects of particle shape and stoke number. *Phys. Fluids*, 27(083301):1–37.
- Zhou, W., Zhao, C. S., Qu, C. R., and Chen, X. P. (2011). Two-dimensional computational fluid dynamics simulation of coal combustion in a circulating fluidized bed combustor. *Chemical Engineering Journal*, 166.